From the Institute of Cardiovascular Physiology

at Heinrich Heine University Düsseldorf

Role of Pericardial Cells in Response to Myocardial Infarction

Dissertation

to obtain the academic title of Doctor rerum medicarum (Dr. rer. med)

from the Faculty of Medicine at Heinrich Heine University Düsseldorf

submitted by

Olesia Omelchenko

2025

As an inaugural dissertation printed by permission of the
Faculty of Medicine at Heinrich Heine University Düsseldorf

Signed:
Dean: Prof. med. Nikolaj Klöcker

Examiners:
Prof. Dr. rer. nat. Axel Gödecke
Prof. Dr. rer. nat. Judith Haendeler

... to Mama and Papa

... to Marius-Aquarius

... to Arni-Balamut

Abstract

Ischemic heart diseases affect around 126 million individuals globally (1,655 per 100,000), representing approximately 1.72% of the world's population[1]. Acute myocardial infarction (MI) is a life-threatening condition, which can occur due to coronary vascular stenosis, resulting in acute coronary occlusion and cell death due to inadequate oxygen supply. Research of the past decade revealed that among a variety of cells involved in post-MI cardiac remodeling, epicardial cells building the visceral layer of the pericardium might play a significant role in the healing process. In contrast, the role of the parietal pericardium in post MI repair processes is less understood. Therefore, this project aimed at investigating structural and functional alterations of the partial pericardium in response to MI.

Foremost, the adult murine pericardium was characterized under basic conditions. Notably, the parietal pericardium contained abundant WT1-expressing cells, under basic conditions. WT1 (Wilms' tumor 1) is known, among others, as a prominent marker of epicardial cells that is typically expressed during cardiac development or re-activated in response to MI in adulthood. The finding of WT1 expression in the pericardium under basic conditions was confirmed by a lineage-tracing mouse model (WT1CreERT2;Rosa26-Tomato), in that tdTomato expression is controlled by the WT1 promoter. Bioinformatic analysis of single cell RNA sequencing data revealed two clusters of pericardial Wt1-expressing cells, the mesothelial cells (MCs; characteristic markers: *Muc16, Upk3b, Msln, Lrrn4, Krt19, Nkain4*) and mesenchymal cells (pMSCs; characteristic markers: *Pdgfra, Dpt, Pi16, Postn, Dpep1*). Furthermore, both clusters expressed progenitor markers and genes commonly associated with tissue development (*Tbx18, Aldh1a1, Sema3d, Gata6, Cd34, Isl1, Hand2*). Additionally, there was an indication of MCs and pMSCs involvement in mesothelial-to-mesenchymal transition already under basic conditions and in lipid metabolism related rather to pMSCs (*Pparg, Apod, Cebpd, Sult1e1, Pla1a, Ebf1* and *Ebf2*).

Upon ischemia/reperfusion injury (I/R) in a closed pericardium model performed in mice, pericardial WT1-expressing cells proliferated from day 2 to 5, leading to a substantial thickening of the parietal pericardium and exhibited a significant upregulation of the genes associated with differentiation processes (T*msb4x,* Tacc2, *Rbm3, Sfrp2, Runx1, Aff3, Actg1, Ripor2*). Moreover, the lineage-tracing model revealed that after I/R, tdTomato+ cells, most likely originating from the parietal pericardium, were present in the epicardium and in the scar, where they co-expressed fibroblast markers such as ACTA2, DDR2, and POSTN. Thus, the pericardial WT1+ cells proliferate, migrate and change their phenotype in response to MI.

Additionally, there was a significant expansion of the fat-associated lymphoid clusters (FALCs) integrated into the pericardium, suggesting an activation of immune cells as well. This correlated with sc-RNA seq data that showed an increase in myeloid and lymphoid populations. In line with this finding, cell communication analysis showed that MCs and pMSCs might facilitate immune cell infiltration via numerous interactions associated with cell adhesion and recruitment.

Taken together, this thesis elucidated that mesothelial and mesenchymal WT1-expressing cells residing in the parietal pericardium actively contribute to post-MI cardiac remodeling by migrating into the myocardium and their potential to modulate the immune response. Thus, this study sheds new light on the function of the pericardium necessitating further investigations addressing the cells' functionality under physiological and pathophysiological condition.

Zusammenfassung

Weltweit sind rund 126 Millionen Menschen (1.655 pro 100.000) von ischämischen Herzerkrankungen betroffen, was annähernd 1,72% der Weltbevölkerung entspricht. Ein akuter Myokardinfarkt (MI) ist ein lebensbedrohlicher Zustand, der durch eine Koronargefäßstenose verursacht werden kann, und einen akuten Koronarverschluss und Zelltod aufgrund unzureichender Sauerstoffversorgung hervorruft. Forschungen des vergangenen Jahrzehnts haben gezeigt, dass unter den verschiedenen Zellentypen, die am kardialen Remodeling nach einem MI beteiligt sind, epikardiale Zellen, welche die viszerale Schicht des Perikards bilden, eine bedeutende Rolle im Heilungsprozess spielen könnten. Im Gegensatz dazu ist die Rolle des parietalen Perikards bei Reparaturprozessen nach einem MI weniger verstanden. Daher zielte dieses Projekt darauf ab, strukturelle und funktionelle Veränderungen des partiellen Perikards als Reaktion auf einen MI zu untersuchen.

In erster Linie wurde das Perikard erwachsener Mäuse unter basalen Bedingungen charakterisiert. Interessanterweise enthielt das parietale Perikard unter diesen Bedingungen auffallend viele WT1-exprimierende Zellen. WT1 (Wilms-Tumor 1) ist unter anderem als Marker epikardialer Zellen bekannt, der in der Regel während der Herzentwicklung exprimiert oder im Erwachsenenalter als Reaktion auf einen Herzinfarkt reaktiviert wird. Der Nachweis der WT1-Expression im Perikard unter basalen Bedingungen wurde durch ein Lineage-Tracing-Mausmodell (WT1CreERT2; Rosa26-Tomato) bestätigt, in dem eine tdTomato-Expression unter Kontrolle des WT1-Promoters erfolgt wird. Die bioinformatische Analyse vom single-cell RNA-Sequenzierungsdaten ergab zwei Cluster perikardialer Wt1-exprimierender Zellen: Mesothelzellen (MCs; charakteristische Marker: *Muc16, Upk3b, Msln, Lrrn4, Krt19, Nkain4*) und mesenchymale Zellen (pMSCs; charakteristische Marker: *Pdgfra, Dpt, Pi16, Postn, Dpep1*). Darüber hinaus exprimierten beide Cluster Progenitormarker und Gene, die üblicherweise mit der Gewebeentwicklung assoziiert sind (*Tbx18, Aldh1a1, Sema3d, Gata6, Cd34, Isl1, Hand2*). Außerdem gab es bereits unter basalen Bedingungen Hinweise auf eine Beteiligung von MCs und pMSCs an der mesothelialen-mesenchymalen Transition (MMT) sowie auf eine Rolle im Lipidstoffwechsel, die eher mit pMSCs in Zusammenhang steht (*Pparg, Apod, Cebpd, Sult1e1, Pla1a, Ebf1* und *Ebf2*).
Nach chirurgisch induzierter Ischämie/Reperfusion (I/R) bei geschlossenem Perikard in Mäusen, proliferierten WT1-exprimierende Perikardzellen von Tag 2 bis 5, was zu einer deutlichen Verdickung des parietalen Perikards führte und eine signifikante Hochregulation der mit Differenzierungsprozessen assoziierten Gene (*Tmsb4x, Tacc2, Rbm3, Sfrp2, Runx1, Aff3, Actg1, Ripor2*) zeigte. Darüber hinaus zeigte das Lineage-Tracing Modell, dass nach I/R, tdTomato+ Zellen, die höchstwahrscheinlich aus dem parietalen Perikard stammten, im Epikard und in der Narbe vorhanden waren, wo sie Fibroblastenmarker wie ACTA2, DDR2 und POSTN ko-exprimierten. Somit proliferieren, migrieren und verändern perikardiale WT1+ Zellen ihren Phänotyp als Reaktion auf einen Herzinfarkt.
Darüber hinaus kam es zu einer signifikanten Vergrößerung der in das Perikard integrierten, fettassoziierten lymphatischen Cluster (FALCs), was auf eine Aktivierung von Immunzellen hindeutet. Dies korrelierte mit sc-RNA Sequenzdaten, die einen Anstieg myeloider und lymphatischer Populationen zeigten. In Übereinstimmung mit diesem Befund zeigte eine Zellkommunikationsanalyse, dass MCs und pMSCs die Infiltration von Immunzellen über zahlreiche Interaktionen im Zusammenhang mit Zelladhäsion und -rekrutierung erleichtern könnten.

Zusammenfassend verdeutlicht diese Arbeit, dass mesotheliale und mesenchymale WT1-exprimierende Zellen im parietalen Perikard aktiv zum kardialen Remodeling nach einem Herzinfarkt beitragen, indem sie in das Myokard migrieren und die Immunantwort modulieren. Somit wirft diese Studie neues Licht auf die Funktion des Perikards und erfordert weitere Untersuchungen zur Funktionalität der Zellen unter physiologischen und pathophysiologischen Bedingungen.

List of Abbreviations

7-AAD	7 Amino-Actinomycin D
AD	Adipocytes
AMI	Acute myocardial infarction
Arg1	Arginase-1
AT	Adipose tissue
CCL	C-C motif chemokine ligand
CD	Cluster of Differentiation
cDC1/2	Convenient dendritic cells type 1 /2
cDNA	complementary DNA
Col III	Collagen (III)
CRB	Crumbs complex comprising crumbs protein
Cre	Causes recombination
Ctnnb1	β-Catenin
CVD	Cardiovascular disease
Cxcl	C-X-C Motif chemokine ligand
DAPI	4',6-diamidino-2-phenylindole
DDR2	Discoidin domain receptor 2
DEG	Differentially expressed genes
DLG	Discs large homolog 1
EC	Endothelial cells
ECG	Electrocardiography
ECM	Extracellular matrix
EMT	Epithelial-to-mesenchymal transition
EPDC	Epicardium-derived cells
ERT	Estrogen receptor
FACS	Fluorescence Activated Cell Scanning
FALC	Fat-associated lymphoid cluster
FC	Fold change
FGF	Fibroblast growth factor receptor
FITC	Fluorescein isothiocyanate

FN1	Fibronectin
FSC	Forward scatter
gDNA	genomic DNA
I/R	Ischemia/Reperfusion
ICAM	Intercellular adhesion molecules
IF	Immunofluorescence
IGF	Insulin-like growth factors
IL	Interleukin
Itgb1	Integrin beta-1
LAD	Left anterior descending
LGL	Lethal giant larvae
LoxP	Locus of crossing over
LV	Left ventricle
LVa	Left ventricle, apex
LVb	Left ventricle, basis
MC	Mesothelial cells
MF	Macrophages
MI	Myocardial infarction
MM	Master Mix
MMP	Matrix metalloproteinases
MMT	Mesothelial-to-mesenchymal transition
Msln	Mesothelin
NaCl	Sodium Chloride
NCAM	Neural cell adhesion molecule
NF	Neutrophils
NK-cells	Natural-killer cells
NO	Nitric oxide
Nudc	Nuclear distribution protein
PALS1	Protein associated with Lin-7 1
PAR	Partitioning-defective complexes
PATJ	PALS1-associated tight junction protein

PBS	Phosphate buffered saline
PC	Plasma cells
PCR	Polymerase chain reaction
pDC	Plasmacytoid dendritic cells
PDGF	Platelet-derived growth factor
Pdpn	Podoplanin
Peri	Pericardium
PFA	Paraformaldehyde
pMSCs	Pericardial mesenchymal cells
Postn	Periostin
PPARγ	Peroxisome proliferator-activated receptor-γ
Retnla	Resistin like alpha
RT	Room temperature
RV	Rigth ventricle
RVa	Right ventricles, apex
RVb	Right ventricles, basis
sc-RNA seq	Singe cell RNA sequencing
SCRIB	Scribble planar cell polarity protein
SNAI	Snail Family Transcriptional Repressor
SSC	Side scatter
SVF	Stromal vascular fraction
Tbx18	T-box transcription factor 18
TGF-β	Transforming Growth Factor β
TIMP	Tissue inhibitor proteinases
Upk1b	Uroplakin-1b
VCAM-1	Vascular adhesion molecules
VEGF	Vascular endothelial growth factor
Wt1	Wilms' tumor 1
ZEB	Zinc finger E-box binding homeobox
α-SMA	α-Smooth Muscle Actin

Table of Content

List of Figures

List of Tables

1. Introduction

1.1. Basic structure of the pericardium

The pericardium is a pliable structure that envelops the heart and the roots of the big vessels. It consists of two layers: the visceral pericardium (referred to as epicardium) builds the outer cell layer of the heart and is adjacent to the myocardium; the parietal (serous) pericardium is firmly adherent to a stabilizing layer of fibrous connective tissue[2] (Figure 1A). Together, the parietal and fibrous layers form the sac-like structure enveloping the heart. The layers are separated by a cavity containing pericardial fluid, and their juncture occurs at the level of the atria.

Additionally, the murine pericardium contains adipose tissue integrated into the parietal layer, which harbors a stromal vascular fraction distributed between adipocytes and densely clustered immune cells, known as fat-associated lymphoid clusters (FALCs)[3,4] , Figure 1B.

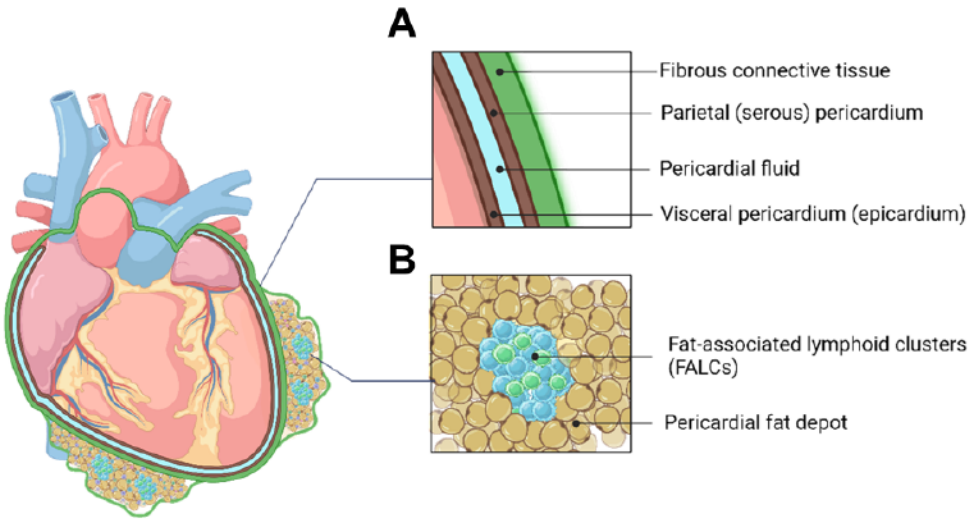

Figure 1. Schematic presentation of the adult murine pericardium.

[A] Murine pericardium consists of two layers - visceral pericardium (epicardium) and parietal (serous) pericardium, adjacent to the fibrous connective tissue. The pericardial fluid along the cardiac surface separates the leaflets, which are connected at the atrium level. [B] Fat depots, integrated in the parietal pericardium, contain fat-associated lymphoid clusters (FALCs). The scheme was created with BioRender.com

One of the primary functions of the pericardium is providing mechanical support for the heart by anchoring it within the thorax at 5 major attachment points[2]: (1) sterno-pericardial ligaments connect pericardium to the sternum at the anterior side; (2) at the anterocaudal side pericardium is in direct contact to the costal cartilages of the 5th and 6th ribs; (3) inferiorly, the pericardium is connected to the diaphragm via pericardiophrenic ligaments; (4) at the dorsal part the pericardium connects to the primary bronchi and at the area of descending thoracic aorta it binds to the vertebral column; (5) laterally, pericardium is surrounded by the mediastinal part of the parietal pleura, which is also covered by mesothelium and is in direct contact with the pericardium.

In addition to the mechanical aspect, the pericardium has a broad functional range dictated by a variety of cells, which reside in the tissue: mesothelial cells, forming the single cell layer stretching along the entire pericardial surface, immune cells that are mainly concentrated within FALCs and adipocytes, arranged into depots. The following chapters will describe in detail the major pericardial cells and their contribution to the functional spectrum of the pericardial tissue.

1.1.1. Mesothelium and its functions

Mesothelial cells (MCs) are a subset of epithelial cells, which line cavities such as peritoneum, pericardium, pleura and their corresponding organs[5]. Additionally, mesothelial cells can be found in parenchymal organs such as liver[6], “milky spots” of the omentum[7] or at the peritoneal side of the diaphragm[5,8] . The main features that mesothelial cells share with epithelial cells is cuboidal form, apical/basal polarity, presence of cytokeratin-formed intermediate filaments and well-developed junctional elements such as tight junctions, adherens junctions, desmosomes and gap junctions[9,10]. The mesothelium derives from the embryonic mesoderm and contributes essentially to development and homeostasis of many organs such as heart, lungs and intestines as well as male or female reproductive systems[11].

One of the basic functions of mesothelial cells is to synthesize and release lubricants such as hyaluronan[12], lubricin[13] and phospholipids[14,15], which help to avoid organ frictions[9]. Furthermore, upon a serosa injury, these cells demonstrate procoagulant activity, releasing tissue factor and plasminogen activator inhibitors PAI-1 and PAI-2. On the other hand, MCs are prone to fibrinolysis, since they release tissue plasminogen activators (tPA) and urokinase PA (uPA) leading to enzymatic breakdown of fibrin deposits, which otherwise lead to hemothorax, infections[16], fibrosis and post-operative adhesion formation[9,17].

In addition to the aforementioned functions, MCs engage in other activities, which will be elaborated upon in the subsequent chapters due to their significance for the current project.

1.1.1.1. Regulation of inflammation

Mesothelial cells play a critical role in regulating inflammation through the synthesis of both pro- as well as anti-inflammatory mediators. Among them are prostaglandins, prostacyclin, nitric oxide (NO), reactive nitrogen and oxygen species, antioxidant enzymes, cyto- and chemokines, growth factors, and extracellular matrix (ECM) molecules[12]. Upon tissue infection, an influx of various leukocytes that release mediators such as TNF-α, IL-1β, and interferon-gamma (IFN-γ) occurs[18,19]. This initial immune response, in turn, stimulates MCs to release cytokines such as monocyte chemotactic protein-1 (MCP-1)[18], C-C motif chemokines (CCL5)[18], Interleukin-6 (IL-6)[20] and IL-8[21,22]. Moreover, adhesion molecules, such as intercellular and vascular adhesion molecules (ICAM-1 and VCAM-1)[23-25] are upregulated facilitating leukocyte recruitment and adhesion to the site of inflammation[9].

1.1.1.2. Extracellular matrix components production

Furthermore, mesothelial cells play a significant role in synthesizing a variety of extracellular matrix (ECM) components, which can be categorized into two types[9]. The first type is the interstitial ECM, encompassing collagen type I, III and V, elastin, and fibronectin. These components not only modulate cellular differentiation and migration processes, but also contribute to the organization of tissue architecture, forming a three-dimensional network around the cells and binding them to the second type of ECM, known as the basement membrane[26-28]. The basement membrane, characterized as a more stable and dense structure, consists of collagen IV and laminins interconnected via nidogen and heparan sulphate proteoglycans[29]. It lines the surface of epithelial/mesothelial cells and is vital for maintaining their polarity[29]. Additionally, mesothelial cells regulate the turnover of ECM during tissue repair by secreting matrix metalloproteinases (MMPs), which are capable of degrading the entire range of ECM components, and tissue inhibitor of matrix metalloproteinases (TIMPs)[9] that have the ability to modulate the proteolytic activity of MMPs[30].

1.1.1.3. Mesothelial-to-mesenchymal transition

The mesothelial-to-mesenchymal transition (MMT) is a pivotal process through which mesothelial cells undergo morphological and functional alterations akin to the well-established epithelial-to-mesenchymal transition (Figure 2)[9,31-33]. This transition entails the loss of characteristic epithelial traits and the acquisition of a mesenchymal phenotype, affording the cells motility and capacity for differentiation. Research works of the past decades showed that in the heart this mechanism underlies MCs contribution to the generation of vascular smooth muscle cells[34], cardiac fibroblasts[31] and pericytes[35] during embryonic development.

MMT includes a series of overlapping and sequential steps regulated by transcription factors from the following families – zinc finger Snail (SNAI1, SNAI2, also known as SLUG), basic helix–loop–helix (Twist1), and zinc finger E-box binding homeobox (ZEB1 and ZEB2)[9,36]. The initial step of MMT involves the loss of junctional complexes, accomplished through the deconstruction of tight junctions (claudins, occludin, zonula occludens ZO-1, -2, -3), adherens junctions (E-Cadherin, p120-catenin, α-, β-catenin), and desmosomes (plakoglobins, plakophilins, desmoplakins)[36,37].

Next, the junctional complex destruction results in loss of the apical-basal polarity. This step is accompanied by suppression of the proteins, which represent apical and basal compartments:

- apical: partitioning-defective complexes PAR-3, -6 and atypical protein kinase C (aPKC)[38,39], crumbs complex comprising crumbs protein (CRB)[40,41], protein associated with Lin-7 1 (PALS1) and PALS1-associated tight junction protein (PATJ)[41,42]
- basal: Scribble complexes (scribble planar cell polarity protein (SCRIB), discs large homolog 1 (DLG) and lethal giant larvae (LGL))[41,42].

Simultaneously, the transitioning cells reorganize their actin cytoskeleton to acquire front-rear polarity[43,44]. At this phase, the transitioning cells commence expression of N-cadherin, which initiates interactions facilitating the assembly of focal adhesions and migration. Thus, N-Cadherin connects to α-, β-catenin, platelet-derived growth factor (PDGF), fibroblast growth factor receptors (FGFRs), and neural cell adhesion molecule (NCAM) [36].

Furthermore, suppression of keratins that form intermediate filaments in epithelia, is accompanied by increased expression of the filamentous protein vimentin (VIM), which is characteristic for mesenchymal cells[36]. Additionally, the cells express fibronectin (FN1) that interacts with α5β1 integrin thereby facilitating cell motility and migration[45]. Moreover, the transitioning cells acquire projections that serve as sensory extensions for directional movement[36], and they show upregulated expression of proteases and matrix metalloproteinases (MMP2 and MMP9), aiding in ECM degradation and promoting cellular migration[36,46].

One of the most studied primary inducers of EMT/MMT are TGF-β family members, particularly Tgfb1 and Tgfb2, eliciting this transition postnatally in the context of wound healing, fibrosis, and cancer. Additionally, epidermal growth factor receptor (EGFR) signaling[47,48], insulin-like growth factors (IGFs)[49] and fibroblast growth factor-2 (FGF-2)[50] can exhibit this function. On the other hand, it was shown that TGF-β induced EMT can also be reversed by FGF-1 and bone morphogenetic protein-7 (BMP7) leading to a process called mesenchymal-to-epithelial transition (MET)[51-53].

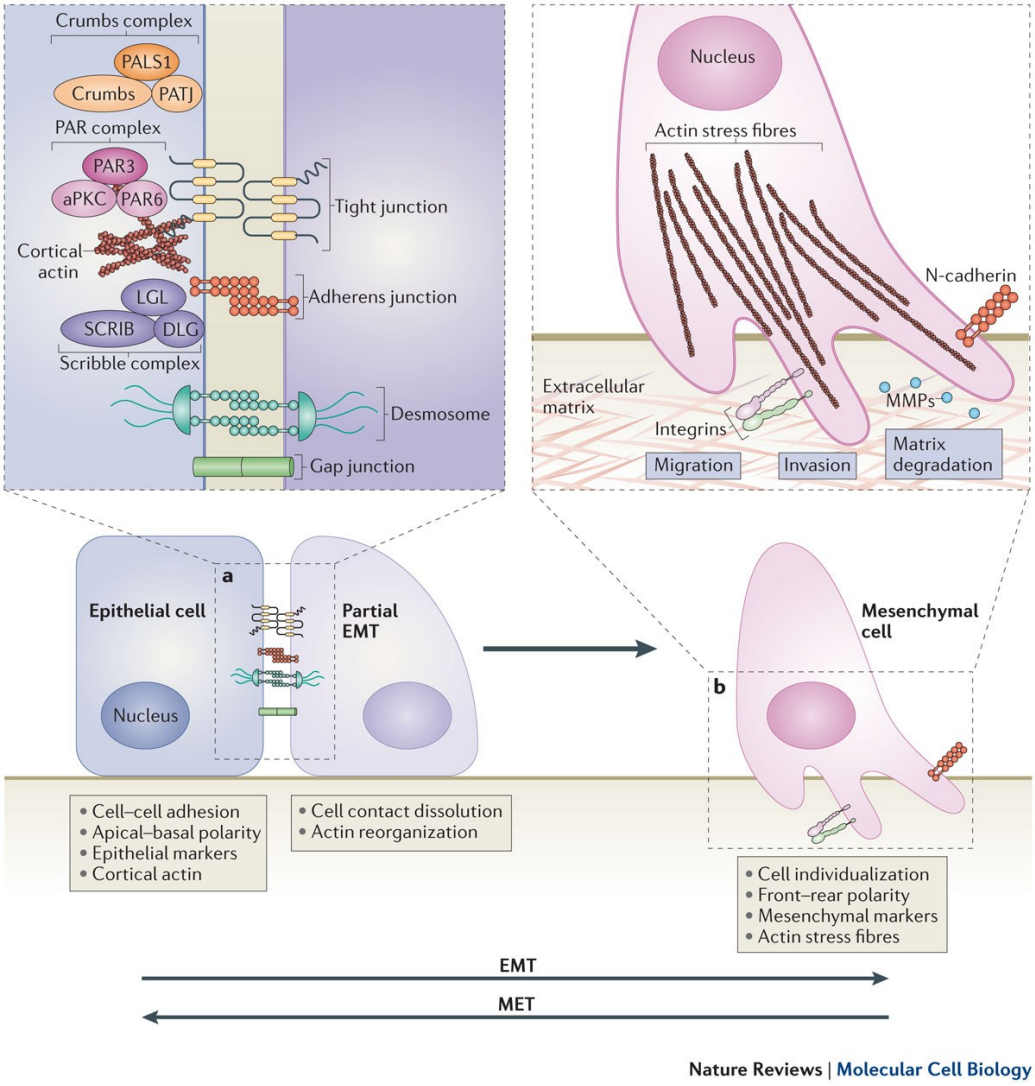

Figure 2. Epithelial-to-mesenchymal transition of epithelial cells.

Schematic representation of the major characteristics of epithelia-to-mesenchymal transition process (Lamouille, Derynck et al. 2014).

[a] Demonstration of the junctional complexes, characteristic for epithelial phenotype. Tight junctions, represented by partitioning-defective complexes PAR-3, -6 and atypical protein kinase C (aPKC), and crumbs protein complex which includes crumbs protein (Crumbs), associated with Lin-7 1 (PALS1) and PALS1-associated tight junction protein (PATJ). Adherens junctions, represented by Scribble complexes (scribble planar cell polarity protein (SCRIB), discs large homolog 1 (DLG) and lethal giant larvae (LGL). Finally, desmosomes and gap junctions. [b] shows mesenchymal type characteristics after the transformation, where the cells acquired projections, rich in actin stress fibers, they express N-Cadherin, integrins and ECM degradation components such as metalloproteinases (MMPs), which facilitate the migration process.

1.1.2. Fat-associated lymphoid clusters and their contribution to immune response

Fat-associated lymphoid clusters (FALCs) are a unique type of lymphoid tissue that is primarily inhabited by T- and B-cells and present in visceral fat[4]. In humans, epicardial fat and the myocardium are in direct contact. Therefore, it is hypothesized that lymphocytes may be partially recruited to the heart from the epicardial fat upon myocardial infarction (MI), thereby contributing to the inflammatory response to (MI)[4]. Accordingly, the studies in patients with coronary artery disease have revealed an increase in the size of FALCs in the epicardial adipose tissue[4].

In mice, FALCs are rather located in the pericardial fat. It was demonstrated that in murine models after MI pericardial FALCs were expanded - a change that was linked to a significant increase in granulocyte-macrophage colony-stimulating factor–producing B cells, dendritic cells (DC), and T-cells[4]. A similar trend was observed in the studies in the peritoneal fat, which also harbors an abundance of FALCs. It was shown that upon immunological challenges, FALCs support B-cell proliferation and germinal center formation, thus functioning as a secondary lymphoid organ[3].

1.1.3. Pericardial fluid – protective cushion and reservoir of resident macrophages

The pericardial cavity, replete with fluid, conventionally serves as a protective cushion, shielding the heart from mechanical damage and acting as a barrier against potential infectious agents. Extensive research has revealed that the pericardial fluid comprises an array of enzymes, glucose, lactate dehydrogenase (LDH), and albumin, along with a diverse population of cells, including mesothelial cells, leukocytes, and macrophages[54]. Notably, recent investigations using a murine mouse model have demonstrated the presence of Gata6+(MHCII^{-}CD102^{+}) macrophages within the pericardial space under steady-state conditions[55]. It was shown that the resident macrophages were recruited to the heart following myocardial infarction, thereby preventing deleterious cardiac fibrosis. Removal of the subset via *Lyz2^{cre};Gata6$^{fl/fl}$* mouse model showed that after MI the heart exhibited adverse cardiac fibrosis, hinting at the reparative relevance of the Gata6+ population[55]. On the contrary, at 4 weeks post-MI the animals, which had preserved pericardium and intact pericardial fluid showed better LV hemodynamics, reduced left ventricle stiffness and improved left ventricle relaxation capacity.

This finding has broadened the understanding of the functional spectrum of pericardial fluid and underscored the significance of preserving the pericardium in various experimental procedures, such as myocardial infarction surgery, where it has conventionally been incised.

1.2. Pericardial involvement into pathological conditions

Despite its modest size, the pericardium contains many structural components and various cell types, which collectively orchestrate numerous processes protecting the heart from pathological conditions. The pericardium is not essential for the normal functioning of the heart[56]. However, the research findings of the past decades showed that the pericardium contributes essentially to the damaged myocardium as well as the diseased pericardium itself may imperil the heart[55,56]. Nevertheless, the mechanisms that drive response of pericardial cells to pathological conditions remain to be elucidated. This chapter provides an overview of the most common pathological conditions associated with the pericardium and, consequently, with the heart.

1.2.1. Pericarditis

Pericarditis is a characteristic pathological condition of the pericardium and can be associated with pericardial effusion, cardiac tamponade, or constrictive pericarditis[57]. Pericarditis involves inflammation of the pericardium, which can arise from various sources, including infections, autoimmune diseases, trauma, or malignancy. Pathological conditions associated with pericarditis often manifest as severe chest pain due to the rich innervation of the pericardium. The gradual accumulation of pericardial fluid may allow structural adjustments, but in cases of rapid fluid accumulation, as seen in malignancy, a life-threatening cardiac tamponade can develop, resulting in impaired heart function due to increased fluid pressure[57].

One type of pericarditis results from a wide range of pathogens, including viruses (coxsackieviruses A and B, echovirus, adenoviruses, parvovirus B19, HIV, influenza), less commonly bacteria (such as tuberculosis), and in rare cases, fungi or parasites[57]. In these cases, pericarditis involves the activation of the inflammasome NOD-like receptor family pyrin domain containing 3 (NLRP3) and subsequent release of IL-1, predominantly driven by the innate immune response[58]. Alternatively, pericarditis can be non-infectious (or autoimmune) and may be associated with conditions such as malignancy (especially in metastatic cases), connective tissue diseases (such as lupus erythematosus or rheumatoid arthritis), or metabolic disorders (e.g., uremia and myxedema). Furthermore, post-myocardial infarction injury can lead to Dressler syndrome (DS) – pericardial inflammatory condition, or “late post-myocardial infarction syndrome” that develops several weeks after the initial injury[57].

Research on inflammatory pericardial effusion (PE), associated with pericarditis, has revealed that this pathological condition is characterized by elevated vascular permeability, leading to the accumulation of pericardial fluid.

This phenomenon is affiliated with upregulated expression of vascular endothelial growth factor (VEGF), which plays a pivotal role in promoting the formation of the excessive pericardial fluid[59]. Furthermore, the pericardial fluid has been found to contain increased levels of basic fibroblast growth factor (bFGF), interleukin-1β (IL-1β), and tumor necrosis factor-α (TNF-α), which are believed to, at least partially, originate from pericardial cells, although further investigation has to be performed to elucidate this aspect[59]. In addition to the cytokines, there is a significant increase of neutrophils in the pericardial fluid - an observation which in terms of neutrophil-to-lymphocyte ratio (NLR) may serve as a marker in acute pericarditis[60,61].

Treatment options for pericarditis available nowadays include colchicine, corticosteroids, azathioprine, and anakinra, each with its own set of advantages and potential adverse effects[62]. Colchicine, for instance, inhibits NLRP3 inflammasome activation, thereby exerting an anti-inflammatory effect and reducing the risk of recurrence[57,58]. Corticosteroids offer symptomatic relief and aid in pericardial effusion resolution by inhibiting pro-inflammatory mediators such as nuclear factor-kappa B (NF-κB) and activator protein-1 (AP-1)[63]. Azathioprine, a purine mimic anti-metabolite, is used to manage recurrent pericarditis but comes with potential adverse effects, such as liver dysfunction or leukopenia[64]. Anakinra, an IL-1 receptor antagonist, has shown promising results in improving symptoms after just a few days of treatment[65].

1.1.1. Epicardium activation in response to myocardial infarction

Research works of the past decades showed that during cardiac diseases, such as myocardial infarction, there is an activation of cells residing on the visceral part of the pericardium, the epicardium. As displayed in Figure 3, foremost, a pronounced thickening of the epicardium was observed, particularly around the areas of injury. The transformation of the single cell layer to a multicellular layer may be explained by proliferation, which is limited under basic conditions, however, in adulthood, proliferating cells appear upon an injury[66].

Additionally, in response to damage epicardial cells release proangiogenic factors, such as Fibroblast Growth Factor 2 (Fgf2) and VEGFA[67,68] and undergo EMT[67]. Thus, epicardium-derived cells (EPDC) acquire mesenchymal lineage characteristics and express Fibroblast-Specific Protein 1 (FSP1), Procollagen I (ProCol), Collagen III (ColIII), Fibronectin (FN1), α-Smooth Muscle Actin (α-SMA), Smooth Muscle Protein 22 Alpha (SM22α), and Smooth Muscle Myosin Heavy Chain (SM-MHC) [67].

A similar tendency of epicardium activation was also documented in other cardiac injuries, such as a mouse model for acute cardiomyopathy, where epicardium-derived fibroblasts expressed one of the major EMT inducers - Transforming Growth Factor Beta 1 (TGF-β1)[69]. In some cases epicardial cells after EMT also adopt an adipocyte fate via expression of the metabolic regulator peroxisome proliferator-activated receptor-γ (PPARγ)[70] or transcription factor TFAP2A (activating enhancer-binding protein 2 alpha), which serves as a trigger promoting this process[71].

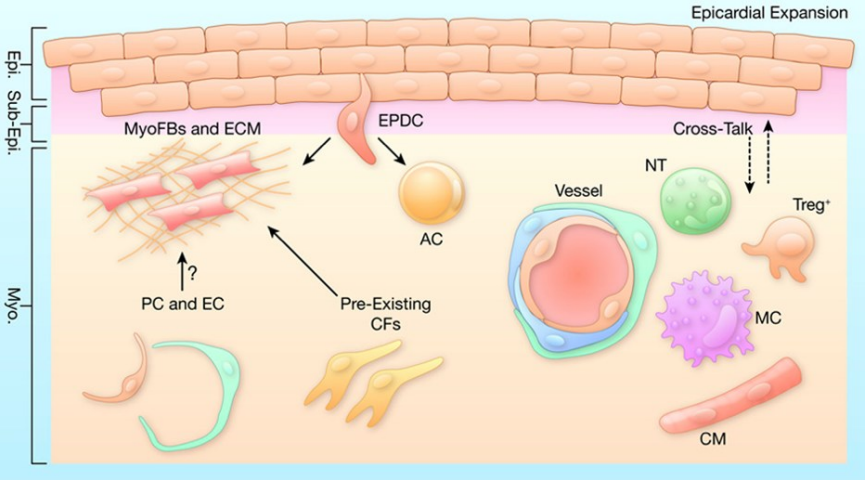

Figure 3. Epicardial cells activation in response to myocardial infarction.

Schematic description of epicardial cell activation in response to myocardial infarction. 1. Substantial thickening of the epiardium. 2. Differentiation of epicardium-derived cells (EPDC) to myofibroblasts (MyoFB), adipocytes (AC), production of extracellular matrix (ECM) components. 3. EPDCs exhibit intercommunication with the myocardium, and modulate the recruitment of neutrophils (NT), regulatory T-cells (Treg), and macrophages (MC). The scheme was represented by Pearl Quijada et al. 2020. License number 5862511044211.

However, the chief characteristic of the epicardial cells activation is a significant upregulation of markers that are highly expressed during embryogenesis and often attributed to various developmental program. Among them are WT1, TBX18, RALDH2, SEMA3D, and TCF21 [67,72-74]

Notably, it is well-established that during embryonic development the aforementioned activities are exerted by pro-epicardial and, eventually, epicardial cells during embryonic development[67,75]. At this period the cells proliferate, undergo EMT, migrate into the developing myocardium and subsequently differentiate into cell types, that constitute myocardium, including interstitial fibroblasts, smooth muscle cells, pericytes, and to a minor extent, cardiomyocytes [67,76-79]. One of the most distinctive and strongly expressed markers during this period is Wilms' tumor 1 (WT1), which is crucial for development since its loss results in embryonic lethality[66,67].

Notably, WT1 plays an essential role in EMT regulation since studies, involving mouse models with loss of WT1 function in the heart, demonstrated that epicardial cells fail to undergo EMT[80]. However, in the post-natal period murine epicardium contains a scarce amount of WT1-expressing cells - the condition referred to as "dormant"[81]. Therefore, it is proposed that the WT1+ cells detected in the visceral part of the pericardium have been activated in response to the cardiac injury. There cells may recapitulate, at least partially, the gene expression pattern detected during embryonic development. This finding represents a potential target for cardiac repair or regenerative interventions.

1.3. Animal models used in investigations of epicardial cells.

The epicardium has been the subject of extensive research over the past decades due to its crucial role in providing essential signals for heart growth and its contribution to cardiac cell lineages and coronary vasculature. As a result, numerous models and experimental setups have been developed to investigate its cellular contributions and molecular mechanisms in cardiac development and disease. The following chapter is focused on a chronological overview of animal models, which contributed to the essential findings described above. It is important to note, that the research works of past decades examined various epicardial markers (*Tbx18:nlacZ,* Tbx18:Cre/R26R^{lacZ}*; Tcf21^{iCre}*/ R26R^{YFP} or R26R^{tdTomato}; Sema3d^{GFPCre} [77] [82] [83]), however, the following overview is based on WT1 as one of the most studied markers.

Initially, researchers observed a high activity of epicardial cells during embryonic development, leading to majority of research works dedicated to this period. Early models utilized vectors based on different viruses, such as spleen necrosis virus (SNV) or adenovirus[34,84,85]. The vectors incorporated *lacZ* gene (e.g. AdCMVlacZ), encoding β-galactosidase (β-gal) – an enzyme enabling tracking of the cells that were infected by the virus[86]. The analysis was based on a histochemical reaction, where β-gal cleaves the substrate X-gal (5-bromo-4-chloro-3-indolyl β-D-galactopyranoside), resulting in a product whose oxidation is accompanied by blue-colored precipitation. Firstly, the viral vectors were injected in avian proepicadium and were analyzed histologically, revealing that *in ovo*, at least a subset of epicardial cells enters the myocardium and contributes to formation of coronary smooth muscle cells[87,88].

Concomitant with this observations, it was noticed, that at this period of embryogenesis (E9 in mice, HH17 in chicken (Hamburger–Hamilton stage)), mesothelial cells lining pericardial, pleural and peritoneal cavities as well as in the enclosed organs, the lungs, heart, and gut highly express the transcription factor WT1, which was originally considered as crucial factor for kidney development[89-91].

Moreover, it was suggested that WT1 plays a central role in transitioning of cells between epithelial and mesenchymal phenotypes[89]. This finding attracted attention to WT1 and furthered its investigations in the heart using mouse models with targeted mutation of *Wt1* gene.

Inactivation of the *Wt1* gene by deletion of the first exon and 0.5 kb of upstream sequence showed that the animals, heterozygous for the mutation, appeared to be normal. On the other hand, the homozygous mice developed an extreme heart pathology with edema, pericardial bleeding, rounded apex, smaller ventricles size, dilation, and extremely thin ventricular walls leading eventually to death on days 13-15 of gestation[92]. Additionally, the *Wt1* homozygous null mice exhibited the failure of the kidney and gonad development[93].

Later linage tracing studies included improved mouse models based on yeast artificial chromosome (YAC) carrying the human *Wt1* locus promoter directing expression of a *β-galactosidase* reporter gene (WT470LZ^{H})[94-96]. The models allowed confirming the *Wt1* expression pattern as well as it was shown that the heart phenotype characteristic for homozygous *Wt1* KO mice could be rescued. The observation was reported by A. W. Moore at al., where firstly the transgenic lines were generated using 280 kb YAC (WT280) spanning the human-derived WT1 locus (WT280^{WA,WC,WW}). Next, the transgenic lines (WA, WC and WW) were crossed onto the Wt1 null background (Wt1-/-; WT280$^{WA,\ WC,\ WW}$+/-). As a result, the WT1 YAC construct rescued epicardial and diaphragm defects, however, not the urogenital defects[93,96,97].

In 2008, a tamoxifen-inducible heterozygous Wt1$^{CreERT2/+}$ (Wt1tm2(cre/ERT2)Wtp/J) and eventually Wt1$^{GFPCre/+}$ (Wt1tm1(EGFP/cre)Wtp) mouse models were introduced, which allowed a temporal and tissue-specific gene modification[78]. This system was helpful for studying Wt1 gene in cells or tissues, which specifically express it, and avoiding lethality at early embryonic stages caused by the constitutive Wt1 deficiency. Thus, *Wt1* gene function was abolished via replacement of the coding portion of exon 1 with a fusion protein of Cre-recombinase and enhanced green fluorescent protein (GFPCre), allowing tracing Wt1-expressing cells and their descendants[78,97].

Within the past decades among the implicated models, the following reporter variations were used:

- *Rosa26^{fsLz}* known as *Gt(ROSA)26^{tm1Sho}* [78,98], where β-gal-neomycin resistance fusion gene (βgeo) is integrated in ROSA26 locus[99] and upon the excision of a floxed STOP sequence by activated Cre-recombinase, β-gal expression would be activated and confined to WT1-expressing cells and their descendants (*Wt1^{CreERT2}*;*Rosa26^{fsLz})*[78].

- *Z/Red (Tg(CAG-Bgeo,-DsRed*MST)1Nagy/J)*[100]. In this model, mice expressed β-gal under the control of the chicken beta actin promoter coupled with the cytomegalovirus (CMV) enhancer. When crossed with a Cre-expressing strain, lacZ expression was replaced with red fluorescent protein (DsRed*MST) expression in Wt1+ cells, (*Wt1*$^{GFPCre/+}$;*Z/Red)*[78].
- *Rosa26*^{mTmG} *(Gt(ROSA)26Sortm4(ACTB-tdTomato,-EGFP)Luo/J)*[101]. This strain includes mice which expresses membrane-targeted tdTomato (‘‘mT’’) prior to Cre excision, whereas after Cre-excision, Wt1+ cells expressed membrane-targeted EGFP (‘‘mG’’) due to replacement of the red fluorescence (*Wt1*$^{CreERT2/+}$;*Rosa26*$^{mTmG/+}$*)*[102].

The Cre-LoxP technology, in combination with expression of fluorescent proteins allowed WT1-specific lineage tracing that confirmed the significance of epicardial cells for embryonic development as well as in adulthood under physiological and pathophysiological conditions (described in 1.1.1). Additionally, it was shown that during embryonic development a small subset of Wt1-expressing population might differentiate into cardiomyocytes, since *Wt1*-derived cells demonstrated co-expression of the lineage tracers and cardiomyocyte markers such as cardiac troponin T2 (Tnnt2) and sarcomeric alpha-actinin-1 (Actn1)[78]. Furthermore, a fate map of EPDCs in annulus fibrosis showed that epicardial cells migrate to this region and partially contribute to periostin-expressing cells and platelet derived growth factor receptor β (PDGFR) – expressing smooth muscle cells[78]. The advanced analyses demonstrated that in response to myocardial infarction, epicardial cells of adult mice do not differentiate into endothelial cells (EC) but rather release various paracrine factors (Vegfa, Angpt1), contributing ECs development[103].

1.4. Aim and objectives

According to the World Health Organization (WHO), cardiovascular diseases (CVDs) accounted for 17.9 million deaths in 2019, representing 32% of global mortality (https://www.who.int). The pericardium significantly contributes to cardiac homeostasis and its close relationship to the heart makes it relevant also in response to a range of cardiac damages. However, the meachanisms that orchestrate these responses remain to be understood.

Whereas numerous studies focused on the epicardium and its activation in response to cardiac damage, the role of the parietal pericardium is less understood. Therefore, the primary aim of this thesis was to establish structure and cellular compartment of the adult murine parietal pericardium under basic conditions and to study its response to myocardial infarction.

To achieve the aim the following objectives were planned:

- Characterization of the pericardial elements under basic conditions, including morphological description, spacial distribution across the entire cardiac surface and establishement of cell types residing in the perietal pericardium.

- Exploring the response of the pericardium to ischemia/reperfusion (I/R) injury, employing I/R and sham techniques with the closed pericardium, which allow maintaining the cells in their natural milieu and preserving potential interconnections between cardiac and pericardial cells.

- Obtain intricate description of the pericardial cells behaviour under basic and pathological conditions, detect their involvement into possible interconnections and signaling pathways incorporating a lineage-tracing model WT1CreERT2 Rosa26-tdTomato and single-cell RNA sequencing analysis.

2. Materials

The following chapter lists the laboratory equipment, technical devices, chemical materials, kits as well as software, which were used in the project.

2.1. Laboratory equipment and technical devices

Table 1. Materials applied in the experiments.

Product name	**Manufacturer**
1 ml syringe	Braun AG, Melsungen, Germany
6 wells cell culture plates	Greiner Bio-One, Germany
15/50 ml Falcon tubes	Greiner Bio-One, Germany
5/10/25 ml stripettes	Corning Costar®, Germany
EASYstrainerTM 40/100 µm cell filter	Greiner Bio-One, Germany
FACS tubes	Falcon, Germany
Eppendorf tubes	Eppendorf AG, Germany
Cell scraper	VWR, Germany
Gilson Pipetman classic pipet (10-1000 µl)	Fisher Scientific, UK
Microscope slides	Marienfeld Superior™, Germany
Cover slips (24x50mm; 18x18 mm)	Engelbrecht, Germany
Microtome Blade - C35	Feather® Safety Razor Co. Ltd.
Lubricating gel Aquagel	Parker Laboratories, USA
Mouse retractor set	Kent Scientific, USA
Surgery instruments (Scissors, Moria Iris Forceps, Vannas Spring Scissors, Micro Needle Holder)	Fine Science Tools (F.S.T.), Germany
Improved Neubauer chamber	Laboroptik, Germany
BETAISODONA® solution	Mundipharma, Germany
Mono-lumen tubing (0,76x1,65x0,45mm)	Freudenberg Medical, Germany
Buprenorphin (Temgesic)	Indivior Europe Limited, Ireland
Hair removal creme - Veet sensitive	Reckitt Benckiser Group, UK
Dry silica beads	Carl Roth, Germany

Table 2. Technical devices applied in the experiments.

Product name	**Manufacturer**
-20 °C Freezer Premium NoFrost	Liebherr, Germany
-80 °C Freezer	Thermo Fisher Scientific, USA
Autoclave maschine	Systec, Germany
Centrifuges	Eppendorf (5415R), Eppendorf (5402), VWR (Mega Star 1.6R), Labnet (Spectrafuge Mini Centrifuge), Roth (Rotilabo)
Cryostat microtome Rotation CM1860	Leica Biosystems, GErmany
Electrical shaver	Contura, Germany
FACS	MoFlo XDP, Beckman-Coulter
FACS Canto II	BD Bioscience, USA
Fluoresence microscope BZ 9000	Keyence, Japan
Fridge +4°C	Liebherr, Germany
Homogenizer TissueRuptor II	Qiagen, Germany
Ice Maschine	Ziegra, Germany
Incubator	Heraeus (B6120), Infors HAT (Ecotron)
Isoflurane vaporizer	Vet Equipment Inc., USA
Light microscope M60	Leica, Germany
Liquid nitrogen tanks Apollo	Cryothem, Germany
Magnetic stirrer MR3001	Heidolph, Germany
PCR plate spinner 521-1648E	VWR, USA
qTOWER Real-Time PCR Thermal Cycler	Analytik Jena, Germany
Thermoshaker OV 3	Biometra, Germany
Combination shaker KL 2	Edmund Bühler, Germany
Temperature controller dTRON 316	Jumo, Germany
MEB 200-2 series precision balances	KERN & SOHN, Germany
PowerLab 26T, ECG	ADInstruments, USA
GasMixer GME-2802	Föhr Medical Instruments, Germany
VaporGuard™ Activated Charcoal Filter	Vet Equipment Inc., USA
MiniVent Ventilator for mice (Model 845)	Hugo Sachs Elektronik, Germany
Cold light source KL 1500 LCD	Schott, Germany
Hot Bead Sterilizer 250	Fine Science Tools (F.S.T.), Germany
Vortexer	Heidolph, Germany
Water purification system	Merck Millipore (MilliQ)

2.2. Chemicals and Kits

Table 3. Chemicals applied in the experiments.

Chemicals	**Manufacturer (Cat. No.)**
Gelatin powder from porcine skin	Sigma-Aldrich (G2500; 9000-70-8)
BSA Fraction V	Sigma-Aldrich (10775835001)
Collagenase Type II, CLS II	Sigma-Aldrich (C2-22-1g)
OCT Embedding Matrix	Cellpath, (KMA-0100-00A)
Ethylendiamintetraacetic acid (E9884)	Sigma-Aldrich, (E9884)
Isoflurane	Piramal Critical Care (1182097)
Isopentane	Carl Roth, Germany
Normal goat serum	Biozol (LIN-ENG9010)
Normal donkey serum	Sigma-Aldrich (D9663)
Ethanol, 99%	Roth (9065.3)
Fetal Bovine Serum (FBS)	Biochrom (S0615)
Paraformaldehyd (PFA 4%)	Sigma Aldrich (16005)
Saponin	Carl Roth (6857.1)
Tamoxifen	Sigma-Aldrich (H6278)
Trizol	Thermofisher Scientific (15596018)
Chloroform	Merck (67-66-3)
Isopropanol	Carl Roth (CP41.3)
Xylol	Carl Roth (9713.3)
Trypsin-EDTA Solution	Sigma-Aldrich (T3924)
Tween 20	Sigma-Aldrich (11332465001)
Triton-X100	Sigma-Aldrich (T8787)
Mounting medium DAPI Fluoromount-G	Southern Biotechnology (0100-20)
Bouin Solution	Sigma-Aldrich (HT10132-1L)
Masson staining solutions (Hematoxylin, Ponceau Acid Fuchsin (Goldner I), Phosphorus molybdenum acid - Orange G (A) (GOLDNER II), Light green 0.2% (GOLDNER III)	Morphisto (11092.0025)
Entellan	Sigma-Aldrich (107960)

Table 4. Kits applied in the experiments.

Product name	**Manufacturer**
Maxima SYBR green/ROX qPCR master mix (K0221)	Thermo Fisher Scientific, USA
Fix & PERM™ Cell Permeabilization Kit (GAS004)	Invitrogen, USA
Quantitect Reverse Transcription kit (205311)	Qiagen, Germany
MACS Separation colums + CD31, CD45 Microbeads (130-042-201, **130**-097-418, 130-052-301)	Miltenyi Biotec, Germany

2.3. Antibodies and primers.

Table 5. Primary antibodies used in histology analysis.

Primary Antibody	**Host**	**dilution**	**Manufacturer (Cat. No.)**
Fab Fragment Goat Anti-Mouse IgG (H+L)	goat	1:10	Jackson ImmunoResearch (115-007-003)
WT1	rabbit	1:100	Abcam (ab89901)
WT1	mouse	1:100	Merk (MAB4234)
TBX18	rabbit	1:100	Thermo Fisher Scientific (PA5-101921)
Perilipin (D1D8) XP	rabbit	1:1000	Cell Signaling Technology (CS #9349)
Ki-67	goat	1:500	Santa Cruz Biotechnology (sc-7846)
CD31	rat	1:400	BD Pharmingen (553370)
CD31	rabbit	1:100	Abcam (ab222783)
CD19	rabbit	1:100	Abcam (ab245235)
CD19	rat	1:100	eBioscience (14-0194-82)
UPK1B	mouse	1:100	Abcam (ab237777)
CD68	rat	1:100	Abcam (ab53444)
F4/80	rat	1:100	eBioscience (14-4801)
α-Tomato	goat	1:100	Sicgen Antibodies (ab8181-200)
α-Tomato	rabbit	1:100	Rockland (600-401-379)
DDR2	rabbit	1:100	Abcam (ab76967)
POSTN	rabbit	1:100	Abcam (ab14041)
ACTA2	mouse	1:100	Thermo Fisher Scientific (MA5-11547)

Table 6. Secondary antibodies used in histology analysis.

Secondary Antibody	dilution	Manufacturer (Cat. No.)
Goat-anti-rabbit Alexa488	1:500	Jackson ImmunoResearch (111-545-114)
Goat-anti-rat Rhodamin Red X	1:300	Jackson ImmunoResearch (112-295-167)
Goat-anti-mouse CY3	1:300	Jackson ImmunoResearch (115-165-062)
Goat-anti-rabbit CY3	1:300	Jackson ImmunoResearch (111-165-144)
Donkey-anti-mouse CY3	1:300	Jackson ImmunoResearch (705-165-147)
Donkey-anti-rabbit CY3	1:300	Jackson ImmunoResearch (711-165-152)
Donkey-anti-rat Alexa 488	1:500	Jackson ImmunoResearch (712-545-153)

Table 7. Antibodies applied in flow cytometry analysis.

Antibody	Clone	Dilution	Channel	Manufacturer
CD16/32 Fc-block	93	1:20	-	Biolegend (101302)
Ter-119	Ter-119	1:100	PE	Miltenyi Biotec (130-102-336)
Ter-119	Ter-119	1:100	FITC	Miltenyi Biotec (130-102-257)
7AAD	-	1:100	PerCP-Cy5-5	Biolegend (420404)
CD45	30-F11	1:100	V-500	BD Biosciences (563891)
CD45	30-F11	1:100	PE-Cy7	BD Biosciences (552848)
CD3	17A2	1:100	FITC	BD Biosciences (561798)
CD19	1D3	1:100	PE	BD Biosciences (557399)
CD31	390	1:100	PE-Cy7	Biolegend (102528)

Table 8. qPCR-Primers.

Primer	Direction	Sequence 5`-3`	Manufacturer
Wt1	fwd	GTAAAACAAGTGAAAAGCCC	Sigma-Aldrich
	rev	TCAGATTTGGAAGCAGTTTG	
Tbx18	fwd	GAACAGAATGGGTTTGGAAG	Sigma-Aldrich
	rev	AGGGATATCTTCAAAGGTGAG	
Ym1/Ym2 ≙ Chi3l3	fwd	TCACAGGTCTGGCATTCTTCTG	Invitrogen
	rev	TTTGTCCTTAGGAGGGCTTCCTCG	
Resistin-like molecule α	fwd	GATGAAGACTACAACTTGTTCC	Sigma-Aldrich
	rev	AGGGATAGTTAGCTGGATTG	
Mrc1	fwd	CTCTGTTCAGCTATTGGACGC	Sigma-Aldrich
	rev	CGGAATTTCTGGGATTCAGCTTC	
Adipoq	fwd	CCACTTTCTCCTCATTTCTG	Sigma-Aldrich
	rev	CTAGCTCTTCAGTTGTAGTAAC	
Col III	fwd	CTGTAACATGGAAACTGGGGAAA	Sigma-Aldrich
	rev	CCATAGCTGAACTGAAAACCACC	
Nudc	fwd	AGAACTCCAAGCTATCC	Sigma-Aldrich
	rev	CTTCAGGATTTCCTGTTC	

2.4. Software

Table 9. List of applied software.

Software	Manufacturer
BD FacsDiva Software v.8.0.2	BD Biosciences
Endnote X7	Clarivate Analytics, Philadelphia, USA
GraphPad Prism 10	GraphPad Software, Inc., La Jolla, USA
LabChart	ADInstruments, USA
Microsoft Office	Microsoft Corporation, Redmond, USA
qPCRsoft V3.2	Analytik Jena, Germany
ImageJ (Fiji)	National Institutes of Health (NIH), Laboratory for Optical and Computational Instrumentation
IPA	Qiagen, USA
RStudio	Posit PBC, USA

3. Methods

3.1. Lineage tracing mouse model Rosa26-tdTomato, WT1CreERT2

The animal experiments were conducted in accordance with the national guidelines of the National Institute of Health (NIH) and were authorized by the local animal care and use committee (LANUV, Recklinghausen License No. AZ.:81-02.04.2017.A401, 81-02.04.2020.A171. Felasa certificate (ID: F048/16_#_0468) was obtained on 29.11.2019 at the Central Institution of Animal Research and Scientific Animal Welfare (ZETT) of the Heinrich-Heine-University Düsseldorf.

Mice (*mus musculus*) were kept at the animal stables of the ZETT under controlled temperature (20-22 °C) and in a 12 -hour light/dark cycle, receiving water and food *ad libitum*. The Institute for Molecular Cardiology, HHU, under the direction of Prof. Dr. Jürgen Schrader, kindly provided the mice with Rosa26-tdTomato, WT1CreERT2 genotype.

The lineage-tracing model mouse Rosa26-tdTomato, WT1CreERT2 was introduced in 2008 by Zhou B et al[104]. It was generated using mice with an inbred C57BL/6J background. *Cre/loxP* is a well-established system and extensively used in the past decades system allowing to delete, insert or inverse specific genes in the DNA of cells[98]. It consists of the enzyme *Cre-recombinase,* derived from Escherichia coli P1 bacteriophage, which induces deletion, insertion or inversion of the *loxP*-flanked ("floxed") DNA region[105,106].

In the applied model, a function of the *Cre-recombinase* and the ligand-binding domain (LBD) of the estrogen receptor with three-point mutations (G400V/M543A/L544A) was used (Cre-ERT2). The Cre-ERT2 allows activation of the Cre recombinase by Tamoxifen but does not respond to endogenous estrogen[107]. To confine the expression of Cre-ERT2 to Wt1-expressing cells, the fusion gene replaced the coding exon1 of *Wt1* locus (Figure 4).

Furthermore, a construct of a floxed (flanked by *loxP* sites) a STOP cassette positioned in front of tdTomato cDNA was placed between exons 1 and 2 of the Gt(ROSA)26Sor locus[108]. Thus, once Cre-ERT2 is activated, it deletes the STOP codon resulting in tdTomato expression in $Wt1^+$ cells and their descendants.

The lineage tracing strain was generated by crossing the reporter mice containing ROSA26-loxP-stop-loxP-tdTomato with mice containing the Wt1-CreERT2 knock-in allele. The offspring carrying both modifications, were intraperitoneally injected for five days with the estrogen antagonist, 4 Hydroxytamoxifen (4OHT, 500 µg/d dissolved in 100 µL peanut oil). Upon the injection, 4OHT binds to LBD of the modified estrogen receptor leading to the translocation of Cre-ERT2 protein into the nucleus, where it recognizes the loxP sites, excises the STOP codon and activates tdTomato, selectively in $Wt1^+$ cells and their descendants (Rosa26-tdTomato; Wt1-CreERT2).

As controls, litter mates lacking Cre-ERT2 were treated equally to exclude any tamoxifen related effects. After a recovery period of nine days, the animal experiments were performed.

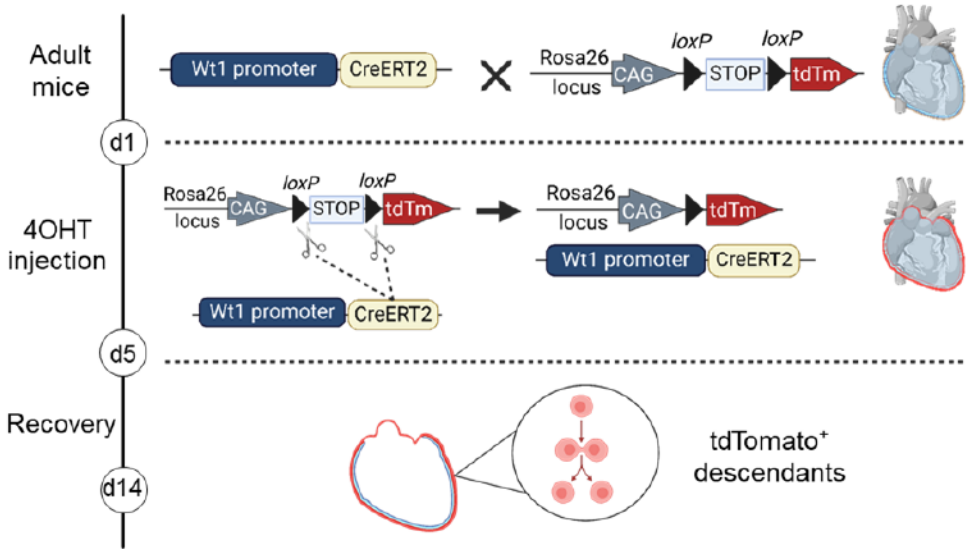

Figure 4. Schematic presentation of tamoxifen-inducible lineage tracing model Rosa26-tdTomato, WT1CreERT2.

Murine model used for the tracing of the pericardial WT1-expressing cells and their descendants. Mice containing CreERT2 at Wt1 locus were crossed with mice containing STOP cassette, flanked by *loxP* sites in front of the fluorescent protein tdTomato at Rosa26 locus. The Cre-recombinase was activated by injecting the adult offspring with 4 Hydroxytamoxifen (4OHT) for 5 days followed by a recovery period of 9 days.

3.2. *In vivo* ischemia-reperfusion and sham surgery

Firstly, mice were anesthetized by isoflurane inhalation at a flow rate of 2 % (v/w) (isoflurane vaporizer, *VetEquip*), intubated and ventilated with oxygen-enriched gas (air flow rate 200 Nml/min, O_2 flow rate 100 Nml/min, tidal volume 260 µl/stroke, ventilation rate 170 strokes per minute). Analgesic buprenorphine was injected subcutaneously at 0.1 mg/kg body weight. Furthermore, to keep the core temperature at 37.5°C mice were placed on a warm pad (temperature set to 40-42°C) and monitored using a rectal thermometer. To access the third intercostal space, the corresponding area was shaved (*Contura*) and hair remover lotion (*Veet*) was applied. Upon thoracotomy, left anterior descending coronary artery (LAD) was positioned and a 7-0 surgical prolene suture with a tapered needle was passed underneath the LAD coronary artery. For ischemia-reperfusion surgery (I/R), both ends of the suture were passed through mono-lumen tubing and the artery was tightened inducing ischemia for 45 min (Figure 5C).

Successful ligation of the artery was confirmed electrocardiographically (ECG) by elevated ST-segment (Figure 5D)[109-111]. Sham operation included the same steps, except for LAD ligation. (Figure 5 A, B). Subsequently, the suture was removed leading to reperfusion and the chest was closed. After surgery, mice obtained buprenorphine (0.1 mg/kg subcutaneously) every 4 hours and in drinking water (0.009 mg/mL) over night and for 3 days for analgesia.

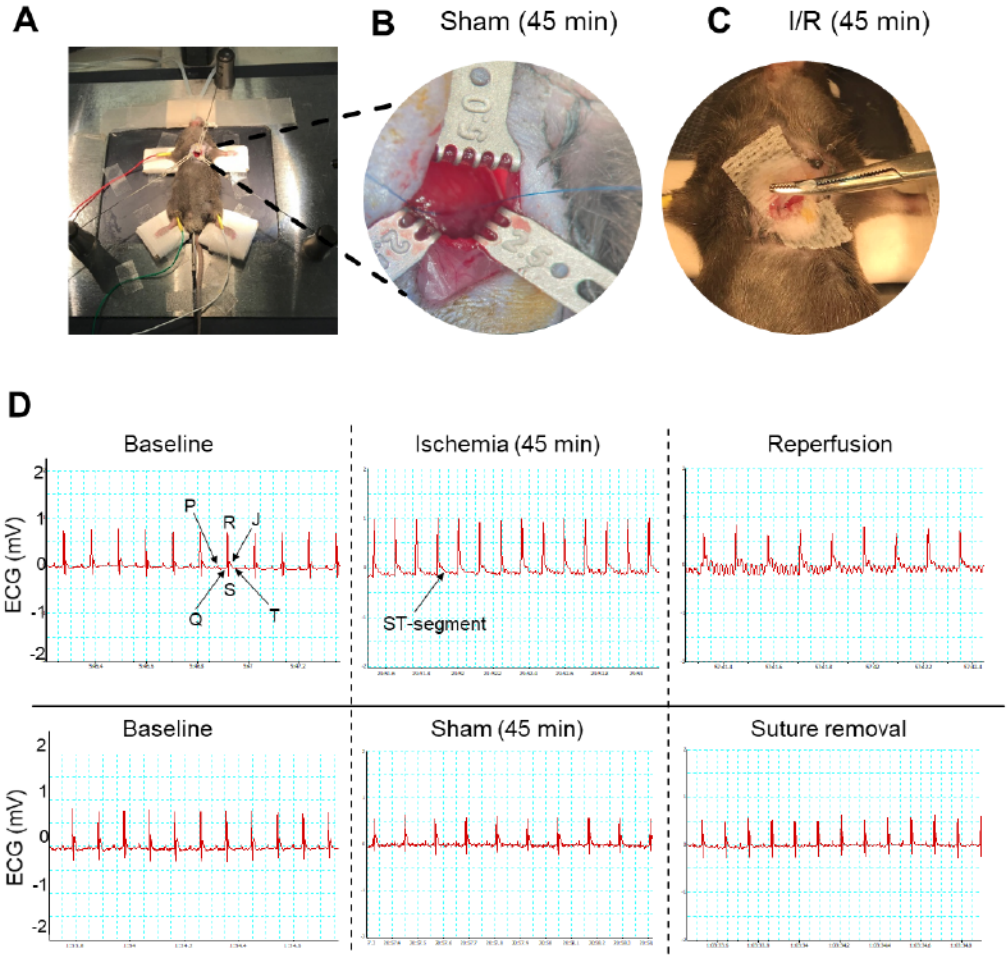

Figure 5. I/R and Sham surgeries performed with closed pericardium.

[A] Mouse was placed on a surgery table, undergone to the opening of the 3rd intercostal space, where the pericardium was maintained closed across the entire surgery. The limbs are connected to electrocardiogram (ECG) electrodes. [B] Representative image of a sham experiment where a suture is placed in the myocardium for 45 min. [C] An image of the ischemia where LAD is ligated, and the opened chest is covered by moistening pads to prevent tissue from drying. [D] Electrocardiogram monitoring before coronary artery occlusion (Baseline), during ischemia or sham lasting 45 min and reperfusion.

3.3. *In vitro* methods

3.3.1. Isolation of the pericardium

The mice were sacrificed by cervical dislocation and the thorax, including its intact compartments as well as the attached diaphragm, was isolated (Figure 6A). This step is necessary to obtain an access to the pericardium, its anterior and posterior anchoring ligaments[2] as well as to facilitate an accurate isolation, avoiding an excision of tightly positioned surrounding organs and obtaining the maximal possible amount of the pericardial tissue. Next, the ribcage was opened at the posterior wall by excision of the thoracic spine followed by fixation of the ribcage and diaphragm on the table with needles. After cleaning from blood via dropwise supply of 0.1 M phosphate buffered saline (PBS; pH 7.4) lungs were excised (Figure 6B). Finally, the pericardium was separated from the heart by cutting along the circumference of the heart near the roots of the big vessels and at the anchoring points, where the pericardial ligaments connect the tissue to the diaphragm, the vertebral column, and the sternum (Figure 6 C-D). The following steps vary depending on the following experiments.

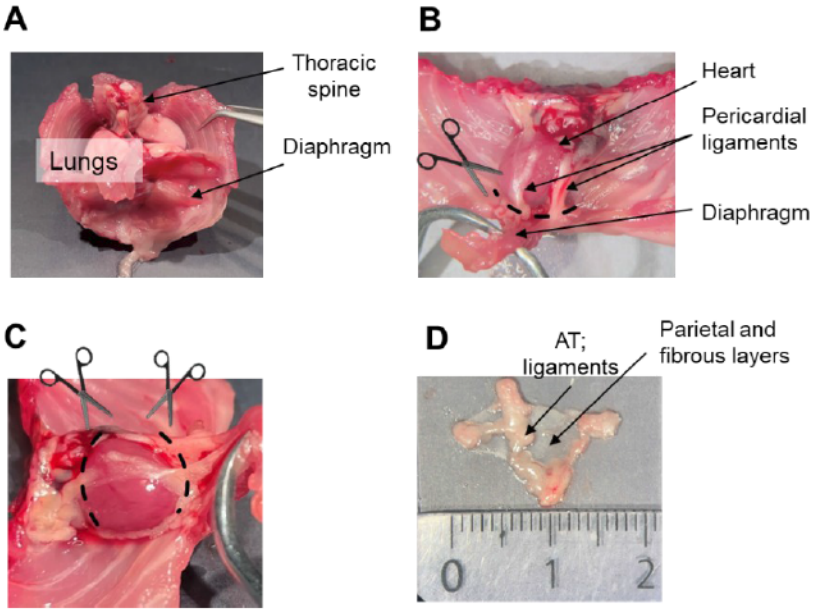

Figure 6. Stepwise representation of the pericardial isolation method.

[A] Isolated thorax, attached to the diaphragm including the heart, pericardium, and surrounding organs. [B-C] Images of in the ribcage opened posteriorly, which contains the heart surrounded by the intact pericardium. The scheme includes excision points: along the circumference of the heart near the atria and at the positions of the pericardial ligaments. [D] Parietal pericardium isolated separately from the heart including the ligaments and the adipose tissue integrated in it.

3.4. Histological analysis

3.4.1. Tissue preparation

For histological analysis, two tissue preparation methods were used. Firstly, the pericardium isolated from the heart (Figure 6D). Secondly an intact pericardium surrounding the heart and connected to the ribcage at the anterior part (Figure 7B). The isolated tissue was washed in PBS solution and was embedded in O.C.T. compound-filled mold (Figure 7 A, C). The molds were put in cold isopentane (-40°C) until the tissue was completely frozen and stored henceforth at -80°C. Since the pericardium is an amorphous and thin structure, it is critical to straighten it after separation from the heart. Proper arrangement of the tissue in the mold allows obtaining cryosections that include maximal surface information (Figure 7A). If the pericardium was isolated with the heart, the heart was positioned with a perspective to obtain cryosections with coronal plane view (Figure 7B). The cryosectioning was performed at -22°C. Therefore, the frozen tissue was relocated to the pre-cooled cryostat (-22 °C) for 1 hour. The tissue was sectioned into 5 µm thick slices and each object slide contained two tissue slices. The slices were dried with cold-air hairdryer and were stored in microscope slide boxes with dry silica beads to remove humidity. The boxes were stored at -20°C for a short-term or -80°C for a long-term storage. Before re-opening, the box was kept at 4°C over night and on the day of experiment for 30 minutes at room temperature. Upon multiple freezing and thawing cycles the beads may absorb humid (color change from blue to pink); in this case it is necessary to replace the beads.

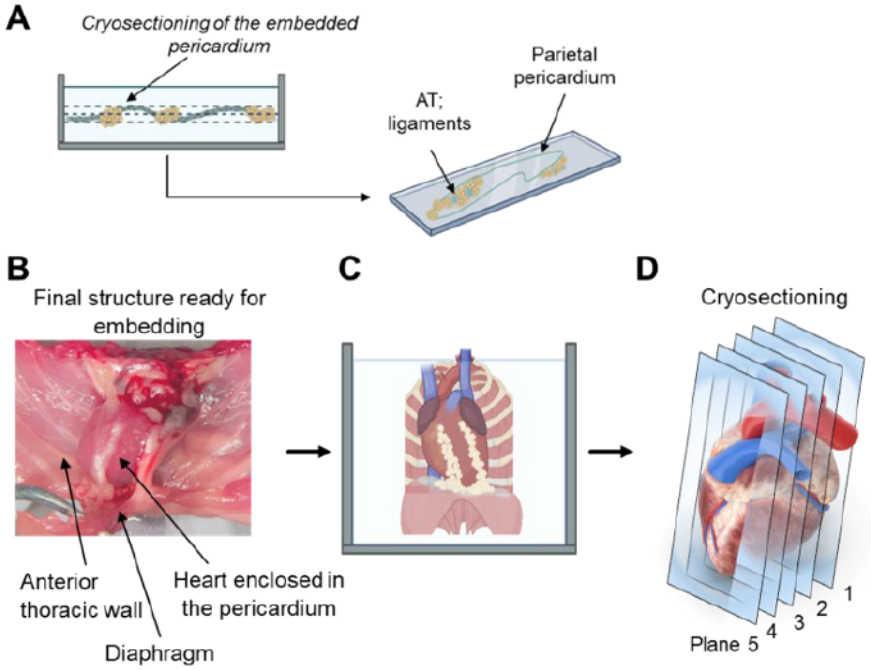

Figure 7. Scheme of the pericardial tissue preparation for the histological analysis.

[A] Pericardium isolated separately from the heart and placed into O.C.T. compound-filled mold. Proper positioning of the tissue in the mold contributes to the cryosections embracing most of the surface. [B] The heart, enclosed in the intact pericardium, was positioned in the O.C.T. compound-filled mold with a perspective for the coronal plane view. [C] Following cryosectioning of the heart into five coronal planes (slices thickness - 5µm; plane 5-anterior wall, plane 1 - posterior wall).

3.4.2. Immunofluorescence staining

Firstly, the tissue slices were fixed with in paraformaldehyde (PFA) solution (4% in PBS) for 10 minutes at room temperature (RT). Then the sections were washed in PBS twice for 10 minutes and, subsequently, permeabilized with 0,5% Triton-X100 in PBS (20min incubation, RT). Afterwards, the sections were washed (2x10 min, PBS).

For the next steps PBS and Saponin 0.2%, solution was used. The sections were incubated (RT) for 2h in a blocking solution (10% NGS (normal goat serum) in PBS/Saponin). The primary antibody was diluted in PBS/Saponin + 2% NGS, pipetted on the tissue slices and incubated over night at 4 °C. On the next day, the samples were washed two times in PBS/Saponin and the secondary antibody, diluted in PBS/Saponin 0.2% + 2% NGS, was added. The slices were incubated for 3h, RT in the darkness. Finally, the samples were washed 3x 10 min in PBS in the darkness and stocked with Fluoromount-G with DAPI (4',6-diamidino-2-phenylindole) fluorescent complex binding to adenine–thymine-rich regions in DNA). After overnight drying (4°C) the slices were analyzed using Keyence BZ 9000 fluorescence microscope.

3.4.3. Immunofluorescence staining (mouse on mouse)

The tissue slices were fixed with 4% PFA/PBS and were incubated for 10 minutes (RT). Then the sections were washed in PBS two times for 10 minutes and, subsequently, permeabilized using 1% Triton-X100 in PBS (1h incubation, RT). Afterwards, sections were blocked for 1h (RT) in 10% NGS/PBS + 1% Triton-X and washed two times for 10 minutes in PBS/Tween20 (0,2%) solution and 1x 10 min in PBS. In order to prevent background staining of endogenous immunoglobulins the tissue slices were incubated with Fab-Fragment Goat Anti-Mouse antibody for 3h RT. Prior to addition of the primary antibody, the samples were washed two times for 10 minutes in PBS/Tween20 (0.2%). The primary antibody was diluted in PBS/Tween20 + 2% NGS, and pipetted to the tissue slices (incubation over night at 4°C).

On the next day the samples were washed two times in PBS/Tween20 (0.2%) followed by incubation with the secondary antibody solution prepared in PBS/Tween20 + 2% NGS. The incubation lasted for 3h at RT in the darkness. Finally, the slices were washed (3x15 minutes in PBS), and stocked with Fluoromount-G/DAPI. It is crucial to keep the samples in the darkness throughout all the steps, once the secondary immunofluorescence antibody was applied. After overnight drying (4°C) the slices were analyzed using Keyence BZ 9000 fluorescence microscope.

3.4.4. Masson's trichrome stain

Tissue slices were incubated in Bouin fixative (Sigma-Aldrich, HT10132) for 15 min and washed afterwards for 5 min under constantly flowing tap water. The staining solutions used in the following steps were obtained from Morphisto (11092.0025). The samples were incubated for 5 min in Hematoxylin solution (11717) and were washed again under constantly flowing tap water for 10 min. Next, the sections were incubated for 2 min in Ponceau Acid Fuchsin (Goldner I, 10366) and were washed two times for 30 seconds in distilled water. Then, the samples were incubated for 2 min in phosphorus molybdenum acid-Orange G (11195) and again washed two times for 30 seconds in distilled water. Afterwards, the slices were incubated for 20 min in Light green (GOLDNER III; 102180) and washed shortly in tap water until the staining solution vanished. The object slides were then shortly immersed in acetic acid 1% (10180), distilled water, twice in ethanol 96% (Carl Roth, 9065.3), once in isopropanol (Carl Roth, CP41.3) and two times for 5 min in Xylol (Carl Roth, 9713.3). Finally, the slices were stocked with Entellan (Sigma-Aldrich, 107960) and were kept overnight in RT for drying.

3.4.5. Microscope image processing

The images obtained with fluorescence microscope Keyence BZ 9000 (Keyence) were analyzed using the Fiji app based on ImageJ software.

The thickness of the pericardial layer was measured in the coronal plane slices after Masson's trichrome stain. To take into account a possible heterogeneous distribution of the pericardium around the heart, measurements were taken from planes 1 and 2 representing the posterior wall of the heart, planes 3 and 4 corresponding to the middle part and plane 5 that represents the anterior wall. The measurements were performed on the images taken with 20x magnifications. In each plane, three measurements were taken along the left ventricle and three measurements along the right ventricle (Figure 8). An average of the three measurements per image was considered as a thickness of the pericardium.

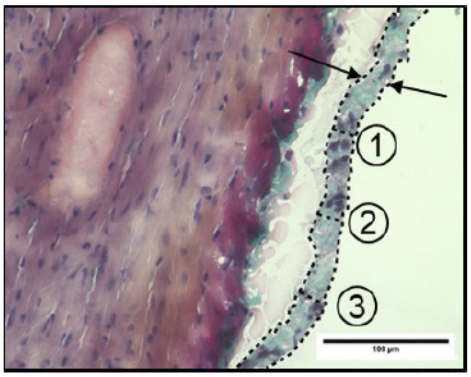

Figure 8. Microscope image processing. Pericardial thickness.

The thickness of the pericardium was measured in Fiji (ImageJ) on images with 20x magnifications at three locations. An average of the three measurements was taken as a pericardial thickness.

Measurement of an area of interest in the pericardium was implemented via 4-step processing in Fiji, as it is demonstrated on Figure 9A, where the pericardium isolated separately from the heart was analyzed. (1) After the original image with Masson's trichrome stain was uploaded in the program, (2) it was converted into 8-bit image, (3) inverted to a grayscale image to obtain black background and enhance the contrast. (4) Then a threshold was set and the area of interest was measured, for example, the total area of the pericardium (A_{peri}) in one cryosection.

The areas of pericardial adipose tissue (A_{AT}) and of fat-associated lymphoid clusters (A_{FALC}), were measured in a similar workflow including 8-bit conversion and image inversion. However, AT and FALCs were distributed randomly across the entire pericardial surface, therefore, the areas of interest were selected manually and measured (Figure 9B).

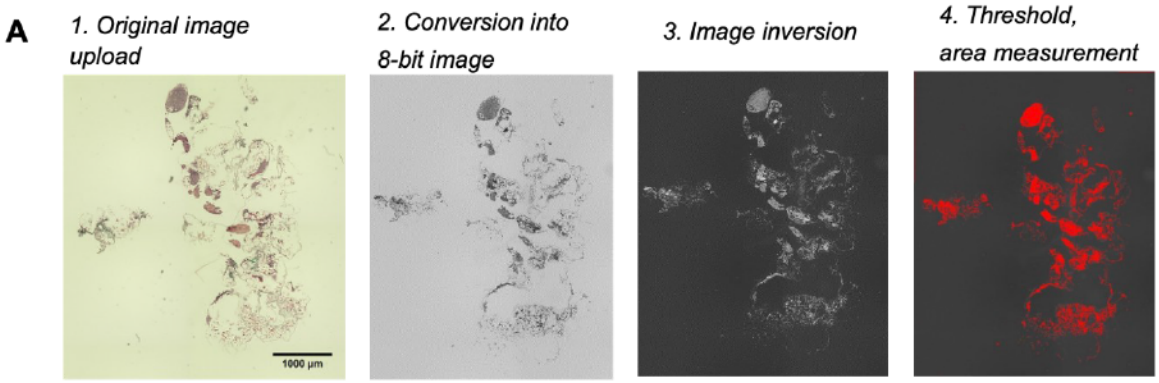

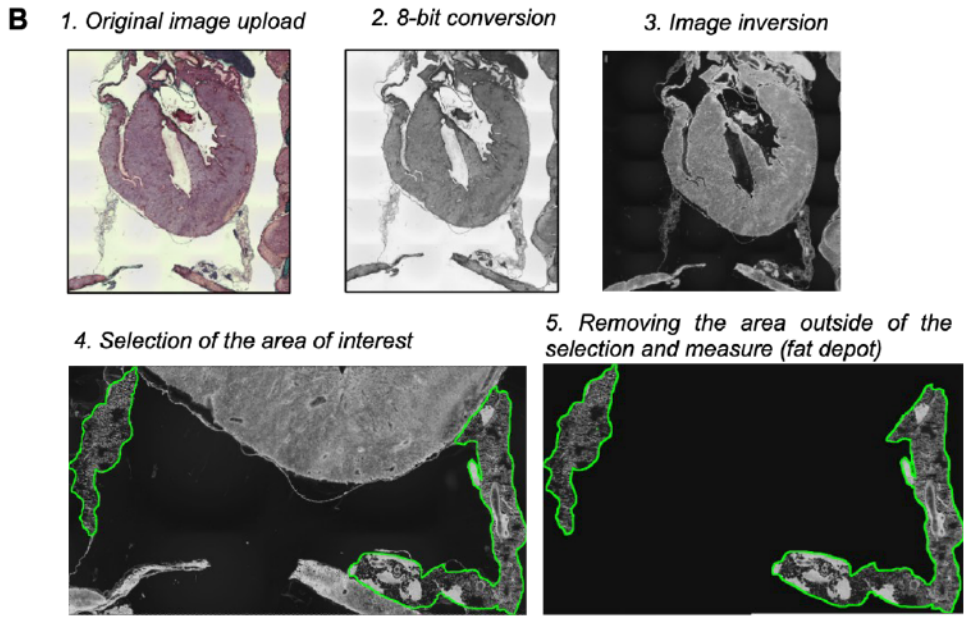

Figure 9. Analysis of pericardial cryosections after Masson's trichrome staining.

[A] Cryosections of the pericardium isolated separately from the heart after Masson's trichrome staining. Using Fiji program the image was processed in three steps, including conversion to 8-bit image, inversion and threshold establishment, for measuring an area of the pericardium in one cryosection. [B] Coronal view of a cardiac cryosection after Masson's trichrome staining, processed in Fiji via 8-bit conversion, image inversion, manual selection of an area of interest, for example, fat depot, followed by automatic measurement.

3.5. Culture of mesothelial cells

In the project, the primary WT1-expressing cells of murine pericardium were cultured. After isolation of the pericardium, described stepwise in Figure 6, the pericardial tissue was digested for 25 min in 0.6% Collagenase II (Sigma-Aldrich, C2-22-1g) solution. To facilitate digestion, the solution was pipetted up and down every 5-10 min.

To avoid immune and endothelial cells contamination, the cell suspension was supplied with CD45 and CD31 Microbeads (Miltenyi Biotec, Germany) for removal of immune and endothelial cells, respectively. The suspension was filtered via a MS Columns that contained a matrix with ferromagnetic spheres. The Columns were placed in the magnetic field of a MACS® Separator and the cell suspension was filtered. The filtrate was cultured on 48-well plate at 37 °C and 5% CO_2, at 0,1-0,3 x 10^6 cells/ml. The growth media was changed once on the third day. The total culture period was 5 days. It is crucial to incubate (at least 20 min before seeding) the plate wells with 0,1% gelatin solution, which provides adhesion of mesothelial cells to the well bottom.

Table 10. Composition of the growth medium for pericardial mesothelial cells

DMEM + GlutaMAX, Dulbesco's Modified Eagle Medium	89%
Fetal bovine serum	10%
Penicillin/Streptomycin (Gibco, 15140122, ThermoFisher)	1%

3.6. Flow cytometry analysis

Flow cytometry is a technology that allows analyzing the compositions of a cell mixture based on cell structure and protein expression. The instrument has various lasers that are applied to analyze each cell separately while the solution in a single-file line passes through the flow cells. Thus, each cell is analyzed for the visible light scatter, which when measured in the forward direction (forward scatter, FSC), indicates the relative size of the cell, and when measured at 90° (side scatter, SSC) indicates granularity of a cell. Furthermore, the system is equipped with excitation and collection optics (lasers and photomultiplier tubes) allowing measurement of various fluorochromes in the analyzed sample treated with fluorescence-labeled antibodies specific for different cell types. Thus, the lasers excite the fluorescent reagents bound to the cells resulting in emitting of the light. The emitted light is directed to the fluorescence detectors specific for a particular wavelength. Next, the photomultiplier tubes amplify the fluorescence signal and generate an electrical current. The electronic system can convert the obtained signals into digital signals, which can be read by a computer and be plotted as histograms or dot pots[112].

PEB buffer (pH 7.5) that was used in cell suspensions, contained the following ingredients:

Table 11. Composition of PEB buffer for FACS analysis

PBS	0.2 g KCl (potassium chloride)
	0.2 g KH_2PO_4 (potassium dihydrogen phosphate)
	8 g NaCl (sodium chloride)
	1.17 g Na_2HPO_4 (disodium hydrogen phosphate)
	1 l ddH_2O
	4 ml EDTA (500 mM)
	5 g BSA

3.6.1. Sample preparation

The animals were sacrificed by cervical dislocation and the pericardial tissue was isolated according to Figure 6 and digested for 25 min in 0.6% Collagenase II (Sigma-Aldrich, C2-22-1g) solution at 37°C. To facilitate digestion, the solution was pipetted up and down every 5-10 min. After the digestion, the samples were filtered through 100 µm and 40 µm using Easystrainer (Greiner Bio-One, Germany) and centrifuged for 10min, 800xg at 4°C. The supernatant was discarded and the pellet re-suspended in PEB. The cell suspension was incubated for 10 min at 4°C with Fc-block (CD16/32) to avoid unspecific binding. Next, 100 µl of each sample was transferred to a FACS tube and stained with antibodies listed in

Table 7. For intracellular staining, the samples were additionally incubated with 100 µl of fixation medium (Medium A) for 15 min in the darkness at RT and were washed with 2 ml of PEB (centrifugation at 1400 rpm/450xg, 7 min). Then the supernatant was discarded, and the cell pellet was dissolved in 100 µl permeabilization medium (Medium B) and incubated for 20 minutes in the darkness at RT. The final washing step was preformed as described above, and cells were dissolved in 100 µl PEB. The cells were measured using a BD FACSCanto II. Data were analyzed using the associated software, BD FACSDiva version 8.0.2. Results for cell populations are shown as dot plots, where each dot is equivalent to one measured cell in the flow cell. The individual dots were combined to populations with the aid of gates.

3.7. Real-time Quantitative Polymerase Chain Reaction (qPCR)

3.7.1. Isolation of RNA

The animals were sacrificed by cervical dislocation, and the pericardial tissue was isolated according to Figure 6. Next, a cold Trizol Reagent (Invitrogen, Thermofisher #15596018), 1 mL per 50-100 mg of tissue, was added to the samples and was homogenized with the TissueRuptor from Qiagen, Germany. For cell culture, the media was removed and Trizol was added to the samples (0.75 mL Trizol per 0.25 ml sample 5-10 x 10^6 cells), pipetted up and down and incubated for 5 min at RT. After lysis, 0.2 ml chloroform was added per 1 ml Trizol, incubated for 5 min RT and the sample was centrifuged 15 min, 4°C, 12 000rpm. Next, the upper aqueous phase containing the RNA, was transferred to a new Eppendorf tube and 0.5 ml isopropanol per 1ml Trizol used for the lysis was added. The sample was vortexed and was incubated for 10 min at -20°C, vortexed again and followed by the centrifuge step.

Afterwards, the supernatant was discarded and the pellet was re-suspended in 1 ml of 75% Ethanol. The sample was votexed and centrifuged again for 10 min, 4°C. The supernatant containing Ethanol was discarded and the pellet was kept at 50°C for 5-10 min for drying. Then, the pellet was re-suspended in 30µl of RNase-free water and was incubated on heat block at 55°C for 10 min.

3.7.2. cDNA Transcription

RNA was transcribed into complementary DNA (cDNA) using QuantiTect Reverse Transcription Kit from Qiagen. According to the manufacturer's protocol, 1 µg of RNA was diluted in RNase-free water up to a reaction volume of 20 µl and genomic DNA was eliminated using gDNA buffer. Next, RNA was transcribed into cDNA by reverse transcriptase in a reaction for 15 minutes at 42 °C. The sample was heated to 95 °C for 3 minutes to inactivate the reverse transcriptase. The synthesized cDNA may be stored at -20 °C for a long-term.

3.7.3. Polymerase Chain Reaction and cDNA detection via SYBR Green

For the quantitative polymerase chain reaction (qPCR), cDNA expression was detected using Maxima SYRB Green/ROX qPCR Master Mix (Thermo Scientific). The Master Mix (MM) contained Maxima Hot Start Taq DNA Polymerase and desoxyribonucleosidtriphosphates (dNTPs) and the primers of interest (listed in Table 8) as well as prepared cDNA were added as follows:

Table 12: Composition of the cDNA reaction medium.

SYBR Green MM (2x)	10 µl
RNase-free H_2O	7.2 µl
cDNA (25-40 ng/µl)	1 µl
Fwd Primer	1 µM
Rev Primer	1 µM
Total	20.2 µl

qPCR experiments presented in the project were performed using a real-time PCR thermal cycler qTOWER (AnalytikJena). In the first cycle, the Taq-polymerase was activated by heating up the samples up to 95 °C for 10 min. Next, the system performed 40 cycles at 95 °C for 15 secs and 60 °C for 60 secs. The specificity of amplicons was verified by a melting curve analysis, where the samples were kept to 95 °C for 15 secs, then at 60 °C for 60 sec. Finally, the temperature was increased every 15 sec by 0.3 °C until 95 °C was reached.

3.7.4. Data analysis

Analysis of the data obtained in the experiments was based on X_0 method using general equation for PCR amplification[113].

$$X_n = X_0(1 + E_{amp})^n$$

X_0 = amount of transcript in the sample at cycle 0
X_n = amount of transcript after n-cycles (defined by Ct-value)
E_{amp} = efficiency of amplification
n = number of cycles to reach X_n

When E_{amp} equals 1, which indicates a 100% qPCR efficiency, the equation can be solved for X_0 and therefore simplified:

$$X_0 = \frac{X_n}{2^n}$$

Samples from different conditions were normalized by dividing the X_0 value of a gene of interest by the X_0 value of an endogenous reference gene. In all represented experiments, NUDC (uclear distribution C, dynein complex regulator) was used as the reference gene. Normalized X_0 values were used in the graphical representation of the results.

3.8. Singe cell RNA sequencing analysis

Pericardial tissue from the healthy mice, on day 6 after sham as well as I/R surgeries was analyzed with single cell RNA sequencing analysis (sc-RNA seq). The surgeries were performed as it was described in the chapter 3.2 and the isolation of the pericardium was performed according to the workflow described in Figure 6. To avoid the influence of daily variability, on each experimental day one pericardium from a healthy mouse (basic conditions), one from a mouse after sham and one from a mouse after I/R was prepared and considered as one sample. In total three samples were analyzed.

The isolated pericardium was digested for 25 min in 0.6% Collagenase II solution at 37°C (2ml per pericardium). To facilitate digestion, the solution was pipetted up and down every 5 min. After the digestion, the samples were filtered through 100 µm and 40 µm and were centrifuged for 10min, 800xg at 4°C. The supernatant was discarded and the pellet re-suspended in 100 µl PEB and incubated for 10 min at 4°C with Fc-block (CD16/32) to avoid unspecific binding.

Next, each sample was transferred to a FACS tube and stained with Ter-119 (APC) antibody that targets mature erythrocytes. Additionally, to differentiate all three conditions, different TotalSeq hashtag antibodies (2ml per sample) were added and incubated for 15 minutes. The cell suspension was repeatedly washed and propidium iodid was added to identify dead cells. Consequently, living and single cells were sorted by FACS (MoFlo XDP, Beckman-Coulter) and an equal amount of cells from each sample was combined. The quality of obtained cells was reviewed using trypan blue staining. If the cells were of good quality, single-cell RNA sequencing was started, which was performed in cooperation with the BMFZ (Dr. Tobias Lautwein).

Approximately ~20.000 cells per sample were applied as an input for microfluidics-based 10X Chromium Controller, where single cells were partitioned into GEMs (Gel Beads-in-emulsion) using the Chromium Single Cell 3' NextGEM Reagent Kit v3.1 (10X Genomics, Pleasanton, CA, USA). Generated GEMs, enable production of barcoded, full-length cDNA, where cDNA from a single cell share a common 10x Barcode. The produced cDNA was processed, including purification from reaction leftovers with silane magnetic beads, amplification via PCR and enzymatic fragmentation as well as adapter ligation, resulting in the final sequencing library. Furthermore, the samples contained TruSeq Read 1 and TruSeq Read 2 (read 1 and 2 primer sequence), served as sequencing primers. Sequencing was executed on a NextSeq 550 system (Illumina Inc. San Diego, USA) based on SBS (sequencing-by-synthesis) chemistry. After another round of denaturation, the second DNA strand was synthesized, where the nucleotides contained a fluorescent label, enabling its detection by the sequencer. The fluorescence signals were converted into digital data and raw BLC-files were eventually generated. An average sequencing depth was ~50.000 reads/ cell.

The raw sequencing data was analysed with the 10X Genomics CellRanger software (v3.1), mkfastq pipeline, where the BCL-files were demultiplexed according to the individual barcode sequences and were processed to Fastq-files. Next, the obtained reads were aligned to the mm10 mouse genome provided by 10x Genomics and UMIs were counted in order to generate the gene-barcode matrix. Consequently, applying the cellranger aggr pipeline, the gene barcode matrices were combined and normalized for the sequencing depth.

Further analysis was performed based on Seurat v3.2 R package[114,115]. The cells with less than 200 detected genes, genes expressed in less than 3 cells, as well as dead or damaged cells, which were identified by > 10% mitochondrial , were removed from the analysis. Additionally, cell doublets were removed via the DoubletFinder v2.0 tool[116].

Next, dimensionality reduction was performed via PCA (Principal Component Analysis), followed by the data visualization using UMAP (Uniform Manifold Approximation and Projection). The UMAP analysis allows projecting the data into a 2D model, where the relationship between the neighboring cells as well as relationship between larger clusters is preserved. To identify differentially expressed genes between the clusters Wilcoxon Rank Sum test was applied.

3.9. Ingenuity Pathway Analysis (IPA)

Ingenuity Pathway analysis (IPA) software from Qiagen was applied to analyze sc-RNA seq data. As an input, an excel file containing differentially expressed genes (DEG) between various cell groups (Log2 Ratio), p-value and False discovery fate (FDR) or q-value, was used. Across the entire set of functions, QIAGEN OmicSoft Suite and Canonical pathways analysis were applied to define cell type and canonical pathways associated with analyzed DEGs. As a part of the core analysis, IPA applies two statistical evaluations: p-value and z-score. P-values were calculated using Right-Tailed Fisher's Exact Test, which reflects the likelihood to what extent an association identified by the program in the given dataset is due to a random chance. Consequently, smaller the p-value, less the probability that the identified association is random. Z-score reflects the directional effect of an identified process or a change of molecules in the dataset. Z-score represents the number of standard deviations from the mean of a normal distribution of activity edges.

3.10. Cell-cell communication analysis

Potential interaction between cells of different clusters was analyzed with the CellChat tool (http://www.cellchat.org/), which infers intercellular communication analyzing by single-cell RNA-sequencing (scRNA-seq) data via R package (https:// github.com/sqjin/CellChat). ChellChatDB is a manually curated database based on the KEGG Pathway database (Kyoto Encyclopedia of Genes and Genomes; (https://www.genome.jp/kegg/pathway.html) and other publicly available peer-reviewed experimental studies. CellChatDB considers known ligand-receptor interactions including multimeric complexes, their soluble agonists, antagonists along with stimulatory and inhibitory membrane-bound co-receptors. To infer possible intercellular communications, firstly, differentially expressed signaling genes in the given sc-RNA seq were identified, using Wilcoxon rank sum test (significance level <0.05).

Secondly, an average gene expression in a given cell cluster was calculated:

$$EM = \frac{1}{2}Q2 + \frac{1}{4}(Q1 + Q3)$$

EM – ensemble expression of a signaling gene

Q1-3 quartiles of expression levels of a signaling gene in a cell group.

Next, the ligand-receptor interaction was modeled using the law of mass action. The given gene expression profile was projected onto protein-protein interactions, obtained from STRINGdb, using random walk-based network propagation technique. The communication probability was modeled using the following formula:

$$P_{i,j}^{k} = \frac{L_i R_j}{K_h + L_i R_j} \times \left(1 + \frac{AG_i}{K_h + AG_i}\right) \cdot \left(1 + \frac{AG_j}{K_h + AG_j}\right) \times \frac{K_h}{K_h + AN_i} \cdot \frac{K_h}{K_h + AN_j} \times \frac{n_i n_j}{n^2},$$

$$L_i = \sqrt[m1]{L_{i,1} \cdots L_{i,m1}},\ R_j = \sqrt[m2]{R_{j,1} \cdots R_{j,m2}} \cdot \frac{1 + RA_j}{1 + RI_j}.$$

$P_{i,j}^{k}$ – communication probability from cell groups i and j, for a particular ligand-receptor pair.

L_i, R_j – expression level of ligand and receptor in a cel group I and j respectively.

($L_{i,l} \ldots L_{i,m}$) ($R_{j,l} \ldots R_{j,m}$)– expression level of a ligand (L) or receptor (R) with subunits, which was approximated by their geometric mean, implying that zero expression of any subunit leads to an inactive ligand.

RA and RI – average expression of co-stimulatory and co-inhibitory membrane-bound receptors, respectively, which were used in a linear function to model positive modulation of the receptor expression.

K_h – Hill function parameter set to 0.5 by default.

AG, AI – average expression of extracellular soluble agonists and antagonists respectively, which was used in Hill function to model positive or negative ligan-receptor interaction.

n, n_i, n_j – total cell number in the given dataset, cell number in cluster i or j.

The significance of a potential binding was evaluated via permutation test by randomly permuting the group labels of cells, and then recalculating the communication probability $P_{i,j}$ between cell group i and cell group j through a pair of ligand L and receptor R. p-value was calculated using the following formula:

$$p\text{-}value = \frac{\left\{\#m | P_{i,j}^{(m)} \leq P_{i,j}, m = 1, 2, \cdots, M\right\}}{M}$$

$P_{i,j}^{(m)}$ – communication probability for the m-th permutation

M – total number of permutations (set to 100 by default).

Interactions with p-value <0.05 are considered significant.

4. Results

4.1. Pericardial structure under basic conditions

4.1.1. Characterization of the basic pericardial composition

The first set of experiments was aimed at analyzing histologically the composition of the murine pericardium under basic conditions, separately from the heart. Due to pericardial fragility and its modest size, the separation of the pericardium from the heart and preservation of its entirety required a specific excision approach, which is described in detail in the chapter 3.3.1, Figure 7. For microscopic inspection, the isolated tissue was embedded in a plastic base mold filled with Tissue-Tek compound, followed by cryosectioning and Masson's trichrome staining (Figure 7A).

The microscopy images of the pericardial cryosections are represented in Figure 10. Murine pericardium appears as a flexible and heterogeneous tissue consisting of the fibrous layer, tightly connected to the parietal layer resided by cells along its perimeter (Figure 10-1) and integrated adipose tissue (Figure 10-2). Moreover, at several locations the pericardial fat depots harbored (Figure 10-3) groups of densely arranged cells. Later immunofluorescence staining (IF) showed that these clusters are fat-associated lymphoid clusters (FALCs)[117], containing primarily CD19 expressing B-cells (Figure 18C).

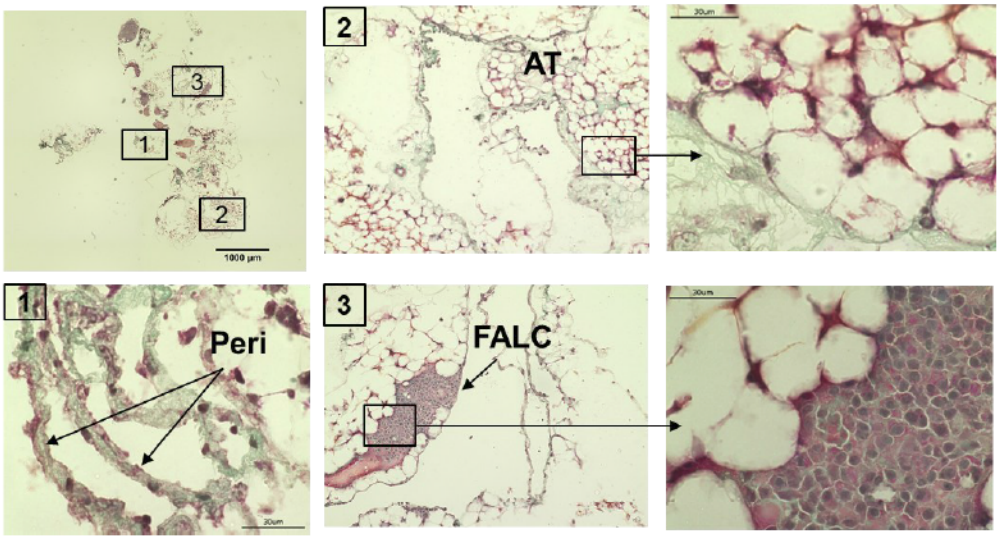

Figure 10. Histological representation of the murine pericardial structure under basic conditions.

Representative microscopy images of a pericardial cryosection after Masson's trichrome staining with [1] x100 magnification of the adjacent parietal and fibrous layers (Peri). [2] adipose tissue (AT) integrated in the parietal pericardium (20x and 100x). [3] a group of densely arranged cells, integrated in the pericardial fat depots defined as fat-associated lymphoid clusters (FALCs), 20x and 100x.

Due to the extensive folding of the filigree structure visible in the image of the entire pericardium (Figure 10), the cryosections could reflect only partially the information about surface area of the pericardium and incorporated fat depots with FALCs. To acquire semi-quantitative data from the obtained micrographs, the ImageJ (Fiji) program was used. The stepwise description of the image processing is presented in the chapter 3.4.5, Figure 9. Firstly, the total area of the pericardium (A_{peri}) was measured. Next, the areas of AT or FALCs (A_{AT} , A_{FALC} respectively), were obtained via manual selection of each structure, followed by automatic measurement. Since AT and FALCs were distributed randomly across the entire pericardial surface, surface areas of each AT or FALC were summarized and represented as a percentage of $A_{peri.}$ The result showed that A_{AT} represented 60% ±8.9 of A_{peri} , meanwhile A_{FALC} – 0.088% ± 0.020 of A_{peri} (Figure 11).

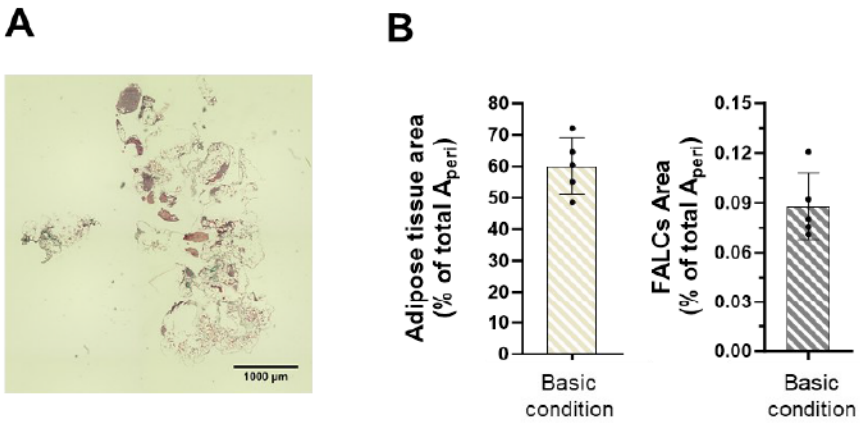

Figure 11. Image analysis of the adipose tissue and lymphoid clusters integrated in the adult murine pericardium under basic conditions.

[A] Microscopy image of the pericardium isolated separately from the heart, after Masson's trichrome staining. [C] Quantification of the adipose tissue (A_{AT}) and FLACs (A_{FALC}) area, represented as a

To gain an additional insight into fractions of fibrous and adipose parts of the pericardium under basic conditions, qPCR analysis was performed (Figure 12). For AT characterization adiponectin *(Adipoq),* an adipokine secreted by adipocytes[118,119] was used, whereas for the fibrous layer - collagen type 3 (*Col3*), since it serves as one of the main components of the fibrous pericardial scaffold.[120] The gene expression was compared between freshly isolated pericardium, heart and subcutaneous fat in case of *Adipoq*.

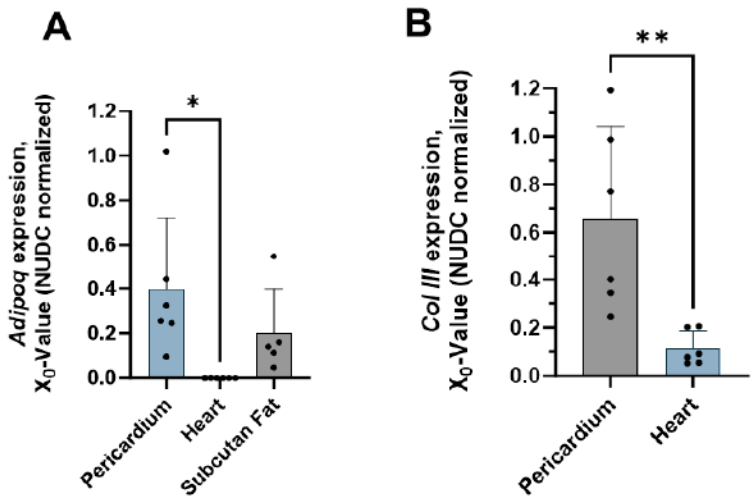

Figure 12. qPCR analysis of the pericardial fat and fibrous layer under basic conditions.

Quantitative PCR analysis (qPCR) of Adiponectin (Adipoq) and Collagen type 3 (Col3) expression in the pericardium, myocardium and subcutaneous fat under basic conditions. Data are presented as mean ±SD, n=6. Statistical significance was calculated with [A] one-way ANOVA and [B] Unpaired t test (*p<0.05, **p<0.01).

4.1.2. Spatial description of the pericardium.

Since the isolation of the pericardium resulted in the loss of information about spatial distribution of AT and FALCs in relation to the heart, an alternative setup of tissue preparation was introduced, (Figure 7), which left the parietal pericardium intact and in its proper alignment with the myocardium. The adjusted isolation method contained analogous initial steps, depicted in Figure 6 , where the thorax was isolated and posteriorly opened, however, the connection of the pericardium to the anterior wall of the ribcage as well as to the diaphragm were maintained and embedded along with the pericardium enclosing the heart (Figure 7B). The isolated tissue was cryosectioned into five coronal planes as it is shown on Figure 7C and Figure 14C:

- planes 1-2 represent posterior wall of the heart with nearly no ventricular cavities visible;
- planes 3 and 4 correspond to the middle part, where both ventricles were detectable;
- plane 5 represents the anterior wall, where primarily the right ventricle was depicted.

To obtain detailed morphological characteristics of the pericardium along the entire cardiac surface the crysections representing each plane were stained with Masson's trichrome (Figure 13). The described experimental setup (Figure 7) allowed a precise detection of the parietal pericardium, the pericardial cavity as well as the epicardium (i.e. the visceral layer of the pericardium), which was barely detectable under basic conditions, however, clearly separated from the outer pericardial layers by the pericardial cavity (Figure 13, B-C). Moreover, the analysis showed that adipose tissue was detectable along the left as well as the right ventricles (Figure 13A). It was integrated into the adjacent parietal and fibrous layers, since the pericardial cell layers appear to branch at the edges of the adipose tissue and to enclose it (Figure 13D). In addition, the microscopy showed that fat depots were distributed around the cardiac surface and some of them encapsulated FALCs (Figure 13E).

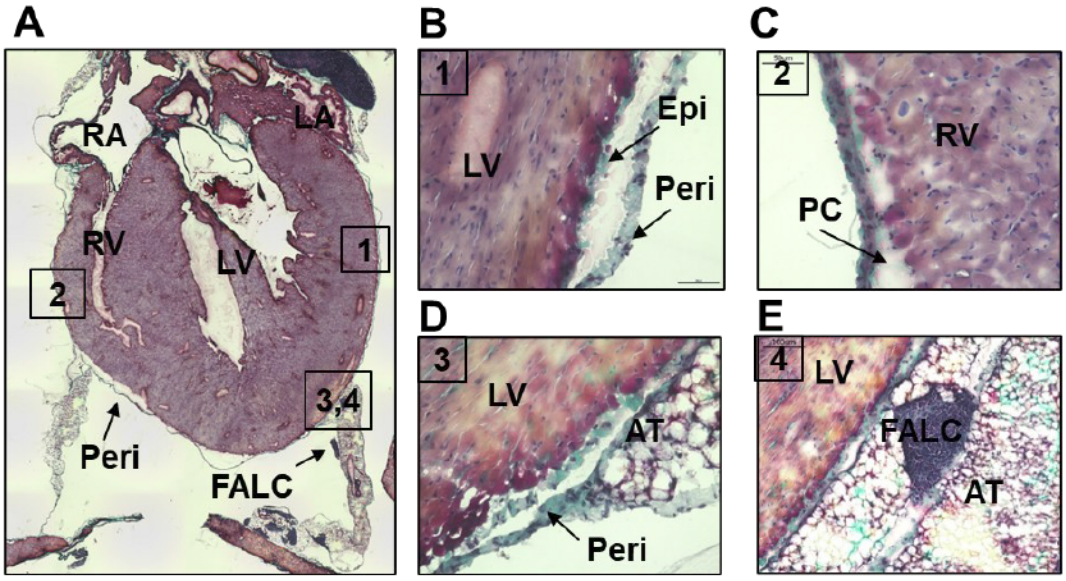

Figure 13. Histological representation of the heart surrounded by the pericardium and its integrated elements.

[A] Coronal view of a middle section of the heart after Masson's trichrome staining. [B] Magnification x40 of the pericardial layer along LV at the position [1]. [C] Pericardial layer along RV (40x) at the position [2]. [D] Image representing a direct integration of AT into the parietal pericardium (40x), position [3]. [E] pericardial AT along LV, with an integrated FALC (20x), position [4]. RV: right ventricle, LV – left ventricle, RA – right atrium, LA – left atrium, Peri – pericardium, Epi – epicardium, PC – pericardial cavity, FALC – fat-associated lymphoid cluster, AT – adipose tissue.

4.1.3. Distribution and proportions of pericardial adipose tissue and FALCs.

Image analysis showed that the average thickness of the adjacent parietal and fibrous layers (further referred as pericardium), at positions free of the fat depots, does not substantially vary in thickness around the myocardium, with no significant differences neither between posterior, middle and anterior regions nor between the areas along the left and right ventricles (Figure 14). Posterior (plane 1): LV 10.63 µm ± 2.59, RV 10.68 µm ± 5.99; middle (plane 3): LV 10.04 µm ± 3.33, RV 11.22 µm ± 5.64; anterior (plane 5): LV 13.47 µm ± 4.03, RV 12.43 µm ± 2.18 µm.

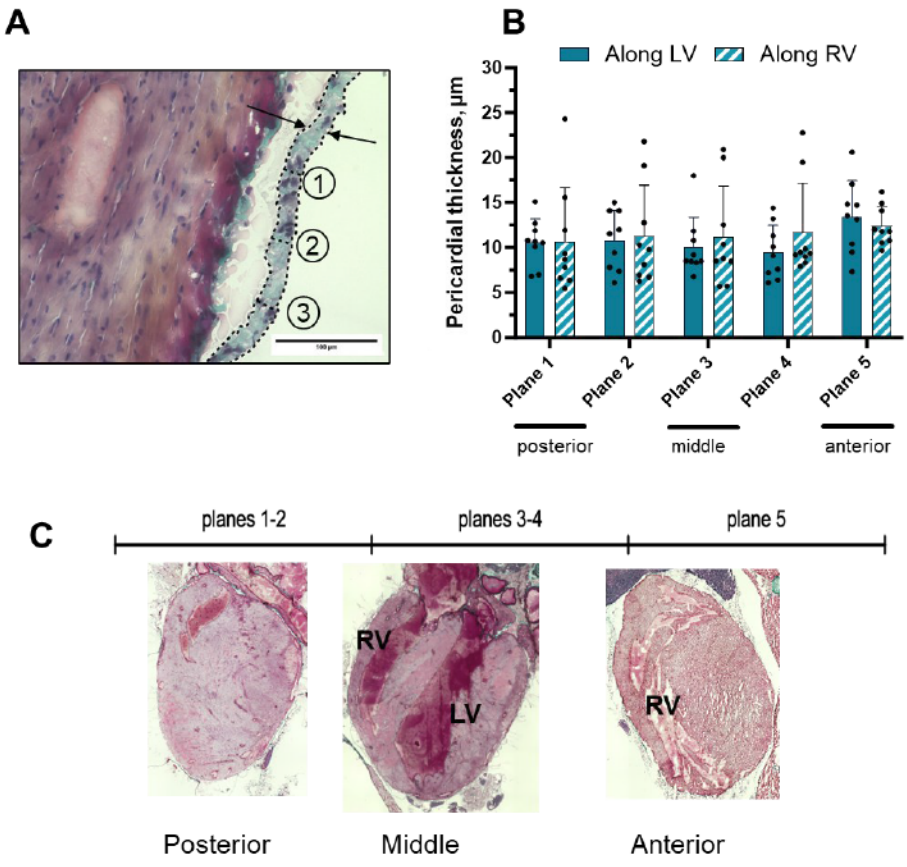

Figure 14. Image analysis of the parietal pericardium thickness under basic conditions.

[A] Micrograph with a marking including three measurements, which average value was used as thickness. [B]. [C] Spatial orientation of the cryosectioned tisue: planes 1-2 correspond to the posterior wall of the heart, planes 3-4 represent the middle part and plane 5 is the anterior wall of the heart. The values represented in the graph were obtained from the areas free of fat and FALC. Data are presented as mean ±SD, n=9.

Subsequently, the area of integrated fat depots (A_{AT}) was evaluated via the image processing workflow described in Figure 9, chapter 3.4.5. The measurements were taken from one cryosection selected from each plane and represented as a percentage of the measured pericardial area A_{peri}: posterior (plane 1) 59.4% ± 0.92; middle (plane 3) 59.7% ± 4.03; anterior (plane 5) 76.2% ± 20.7, (Figure 15A).

Since AT was detected along both ventricles, AT distribution between RV and LV was examined as well. To do this the area of AT located at LV or RV was represented as a percentage of the entire fat area detected in each plane. The analysis showed that compared to RV, the fat depots were primarily located in the region along LV, with a significant difference in planes 3 and 4 (Figure 15, B):

- plane 3 – 73.3% of A_{AT} (along LV) and 26.69% ±7.9 of A_{AT} (along RV),
- plane 4 – 71.3% of A_{AT} (along LV) and 28.64% ±13.5 of A_{AT} (along RV).

Since the plane 5, where the pericardium covers the anterior part of the heart, represents mainly RV region (Figure 14C), A_{AT} in the 5th plane was assigned to RV only.

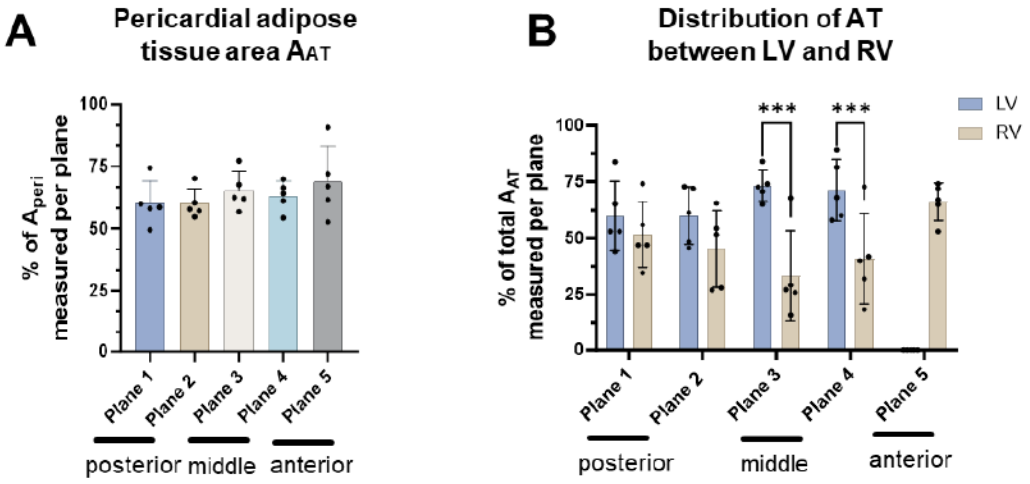

Figure 15. Image analysis of the adipose tissue proportion and distribution throughout the entire pericardial surface under basic condition.

[A] Area of the pericardial adipose tissue (A_{AT}) represented as a percentage of the entire pericardial area (A_{Peri}), measured in each plane separately. [B] Evaluation of the fat depots distribution between the areas along LV and RV, represented as a percentage of A_{AT} per plane. Data are presented as mean ±SD, n=5. Statistical significance was calculated with one-way [A] and two-way [B] ANOVA (***p<0.001).

FALCs, as a compartment of AT, were correspondingly detected in the pericardial regions along the posterior, middle and anterior cardiac walls. Image analysis, analogous the one of fat depots (Figure 15) showed that there was a significant difference between the area of FALCs (A_{FALC}) in the posterior (13.34% ±8.1 of A_{AT}) and anterior regions (2.2% ±2.7 of A_{AT}), Figure 16A. Moreover, FALCs demonstrated a similar behavior, concentrating preferentially along LV rather than RV, corresponding to the distribution pattern of AT, Figure 16B:

- plane 2 (posterior): 83.4% of A_{FALC} (along LV) and 16.6% ±19.3 of A_{FALC} (along RV),
- plane 3 (middle): 92.8% of A_{FALC} (along LV) and 7.2% ±16.0 of A_{FALC} (along RV),
- plane 4 (middle): 78.5% of A_{FALC} (along LV) and 21.5% ±14.1 of A_{FALC} (along RV).

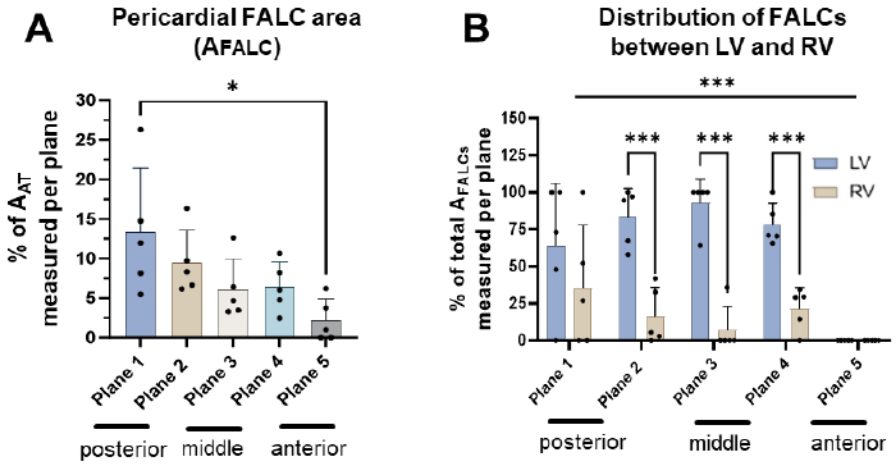

Figure 16. Image analysis of FALCs proportion and distribution throughout the entire pericardial surface under basic condition.

[A] Area of the pericardial FALC (A_{FALC}) represented as a percentage of adipose tissue area (A_{AT}), measured in each plane separately. [B] Evaluation of the FALCs distribution between the areas along LV and RV, represented as a percentage of A_{FALC} per plane. Data are presented as mean ±SD, n=5. Statistical significance was calculated with one-way [A] and two-way [B] ANOVA (* $p<0.05$, ***$p<0.001$).

4.2. Cellular composition of the pericardium under basic conditions

4.2.1. Characterization of Upk1b and WT1-expressing mesothelial cells.

Following experimental steps were aimed at defining the pericardial cell composition under basic conditions via IF staining using both setups of the tissue preparation described above in Figure 6 and Figure 7. Initially, the analysis was implemented using an antibody directed against Uroplakin-1b (Upk1b), a well characterized marker for mesothelial cells delineating visceral surfaces[9,121-123].

The microscopy images shown in Figure 17 demonstrate a monolayer of Upk1b$^+$ cells, distributed throughout the entire perimeter of the parietal pericardium. However, Upk1b signaling was not detected in epicardium – the neighboring visceral layer tightly connected to the myocardium. Moreover, Upk1b expressing cells were detected in the FALCs amongst the densely packed cells. There, Upk1b$^+$ cells occurred as small groups of cells rather clustering together than being distributed evenly (Figure 17C).

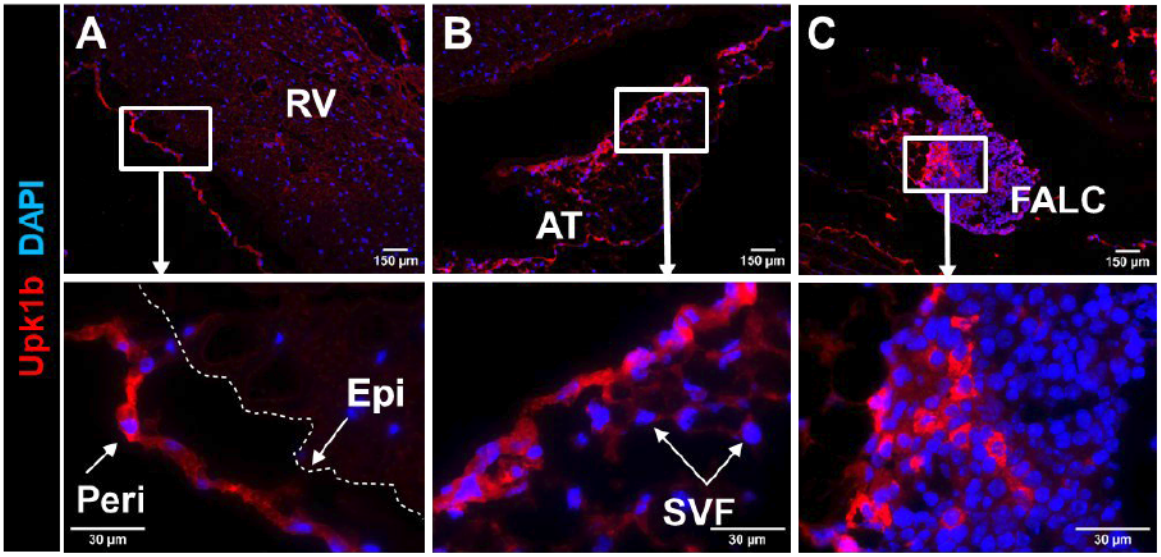

Figure 17. Histological presentation of Upk1b+ mesothelial cells residing on the parietal pericardium and FALCs.

Microscopy images of the pericardium under basic conditions after the immunofluorescence staining with anti-Upk1b and DAPI. 20x and 100x magnification of [A] parietal pericardium (peri) and epicardium (epi), [B] pericardial adipose tissue (AT) including stromal vascular fraction (SVF) and [C] FALC integrated in the pericardial fat depot.

Since it is known that the epicardial cell population exhibits a pronounced expression of Wilms' tumor-1 (WT1) upon MI[10,11], WT1 was also included in the conducted IF analysis of the adult murine pericardium (Figure 18). Microscopy revealed that that the pericardium already under basic conditions contained abundant WT1-expressing cells, located mainly in the parietal pericardium rather than epicardium (Figure 18A). Additionally, a counterstaining of WT1 with anti-Perilipin 1 (Plin1), which is a known as adipocytes marker[124], showed that WT1 expressing cells were interspersed between the large adipocytes, presumably representing a part of stromal vascular fraction (Figure 18B). Upon IF staining with CD19 (B-cells marker) WT1$^+$ cells were detected within FALCs distributed equally in a single cell manner (Figure 18C).

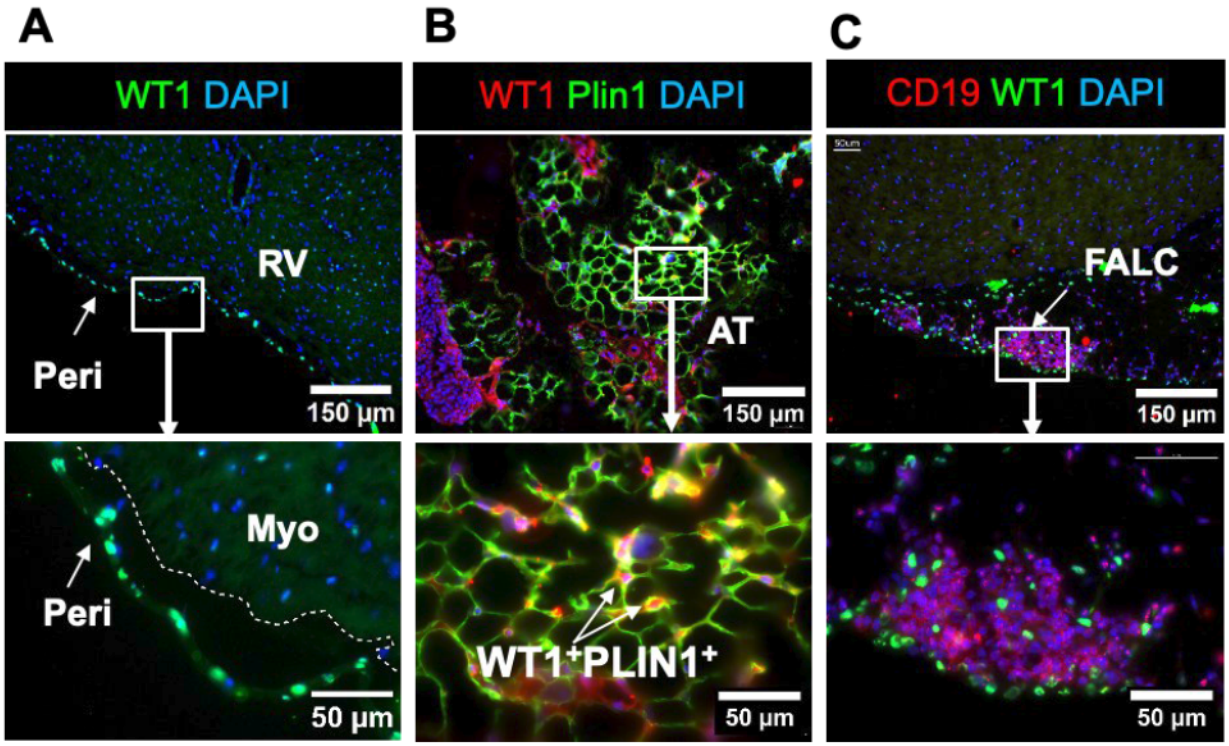

Figure 18. Distribution of WT1-expressing cells in the adult murine pericardium under basic conditions.

Microscopy images (20x and 100x magnification) of the pericardium under basic conditions after the immunofluorescence staining with the antibody targeting [A] WT1 and DAPI. [B] Adipocytes marker Perilipin1 (Plin1) and WT1 and [C] B-cells marker CD19 and WT1. Peri - parietal pericardium; AT – adipose tissue; SVF - stromal vascular fraction; FALC – fat-associated lymphoid cluster.

To confirm the presence of $WT1^+$ cells in the adult murine pericardium under basic conditions a quantitative PCR (qPCR) analysis was performed. *Wt1* expression was compared between freshly isolated pericardium (the protocol is depicted on Figure 6) and myocardium. The kidney was used as a positive control since WT1 expression can be detected in podocytes (visceral epithelial cells) of the mature glomerulus[125].

According to the result shown in (Figure 20), the pericardium of adult mice under basic conditions has a significantly higher *Wt1* expression than the myocardium and kidney, whereas expression of *Tbx18* (a member of the T-box transcription factor family), which is known for its expression in in the proepicardium, epicardium and epicardium-derived cells was relatively low[14,15].

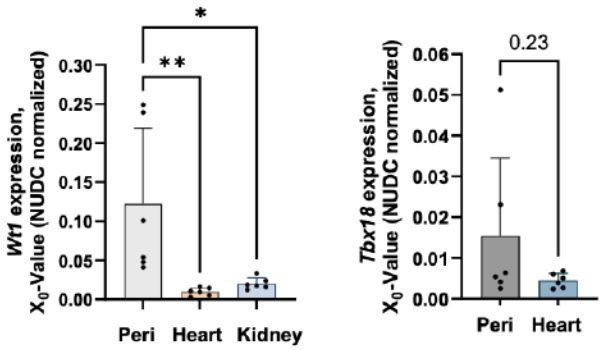

Figure 20. qPCR analysis of *Wt1* and *Tbx18* in adult murine pericardium under basic conditions.

qPCR analysis of *Wt1* and Tbx18 expression in the freshly isolated pericardium, myocardium and kidney, used as a positive control for *Wt1* expression. Data are presented as mean ±SD, n=6. Statistical significance was calculated with one-way ANOVA (*p<0.05, **p<0.01).

In the next step, the experiments were focused on establishment of a protocol for culturing pericardial Wt1-expressing cells, which is described in chapter 3.5. Upon the pericardium isolation as described in Figure 6, and 5 days of culturing, the pericardial cells were used for IF staining with the antibody targeting WT1. DAPI staining was used for nuclei detection. Next, the stained cells (Figure 19A) were counted using ImageJ (Fiji). The result showed that the cultured cells contained a high amount of Wt1-expressing cells, which represented 78.74% ±13.9 of all DAPI$^+$ cells (Figure 19B). To confirm the observation, qPCR analysis was preformed (Figure 19C). The analysis showed that *Wt1* was significantly higher expressed in the cultured cells compared to the freshly isolated pericardium and myocardium under basic conditions.

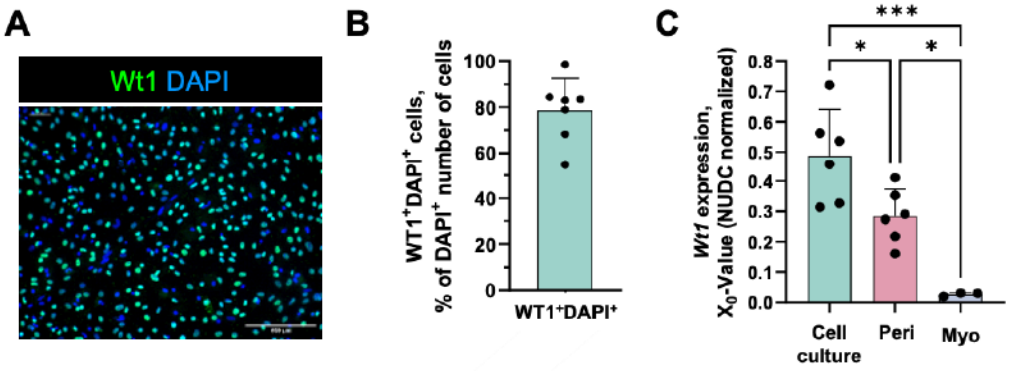

Figure 19.Culturing of WT1-expressing pericardial cells under basic conditions.

[A] 20x magnification microscopy image of the pericardial cells cultured for 5 days (staining with WT1-targeting antibody); [B] Count of WT1$^+$DAPI$^+$ cells represented as a percentage of DAPI$^+$ cells per image. [C] qPCR analysis of *Wt1* expression in the isolated pericardium (peri), cultured pericardial cells and myocardium (myo). Data are presented as mean ±SD, n=3-6. Statistical significance was calculated with one-way ANOVA (*p<0.05, ***p<0.001).

4.2.2. Identification of the pericardial myeloid and lymphoid cell populations under basic conditions

Histological analysis (Figure 16) showed that FALCs represent a significant part of the pericardium and immunofluorescence staining with anti-CD19 antibody revealed a high number of B-cells within the clusters. This is in line with data from Horckmans, Michael, et al. who showed that due to the abundance of activated B-cells residing in FALCs, the clusters play an important immunological role in the response to myocardial infarction[4]. Based on this perspective, the next set of experiments focused on characterizing other types of the pericardial immune cells, in addition to B-cells (Figure 18) that were already detected. The result obtained with IF staining showed that pericardium also contains immune cells of the myeloid lineage (Figure 21). Thus, FALCs, SVF and the parietal pericardium contain $CD68^{+}$ macrophages (MF)[126-129], whereas, $F4/80^{+}$ MFs[126-129] were present in FALCs and in the parietal part, however, not in SVF.

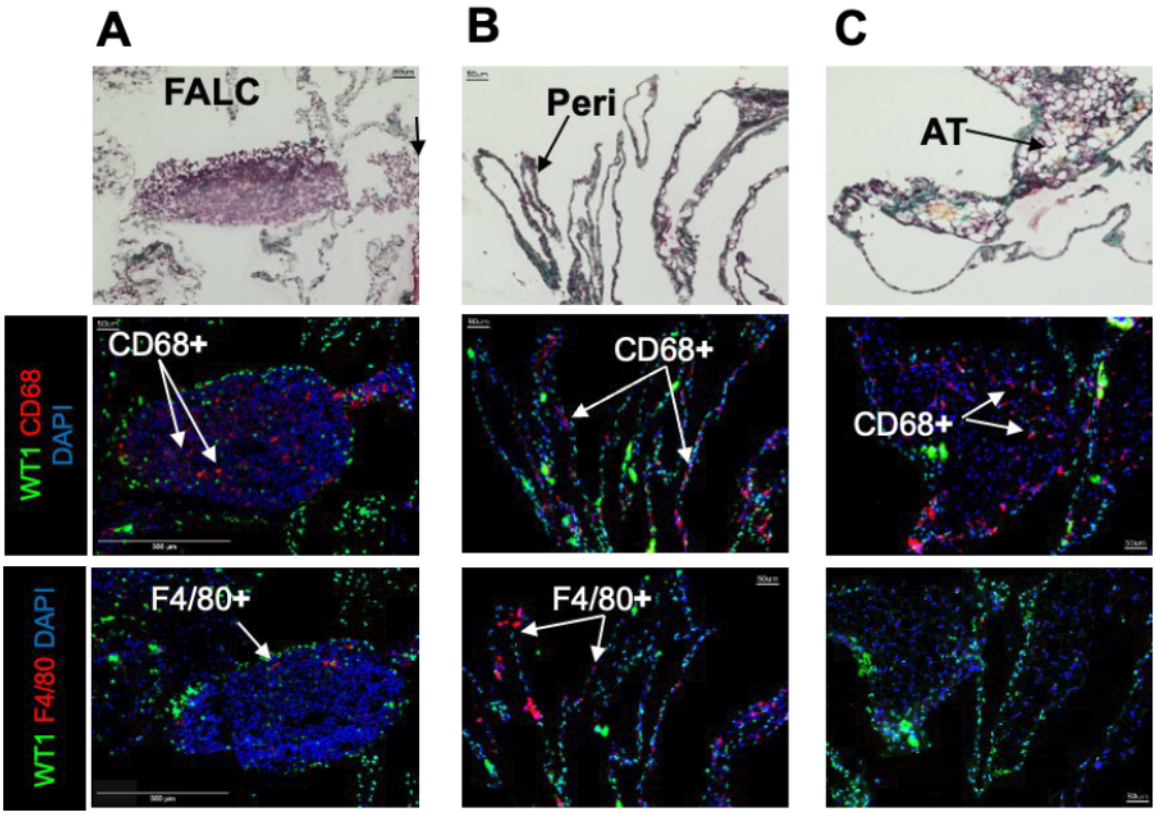

Figure 21. Histological detection of macrophages in the parietal pericardium, FALCs and adipose tissue.

Representative images of the pericardium isolated separately from the heart and stained with Masson's trichrome and antibodies targeting WT1 and MFs markers CD68 and F4/80. [A] 20x magnification of FALCs, [B] adjacent fibrous and parietal layers and [C] adipose tissue (AT) integrated in the pericardium.

Additionally, freshly isolated pericardium was analyzed via qPCR analysis. Expression of marker genes for myeloid lineage cells was compared between pericardium, myocardium and spleen, used as a positive control. The pericardium demonstrated a significantly higher expression of resistin like alpha *(Retnla)*[129-131] in comparison to heart and spleen, whereas the expression of mannose receptor C-type 1 *(Mrc1)*[130,132,133] and chitinase-3-like protein 3 *(Chil3 or Ym1)*[129,134,135] were expressed to a significantly lower extent (Figure 22).

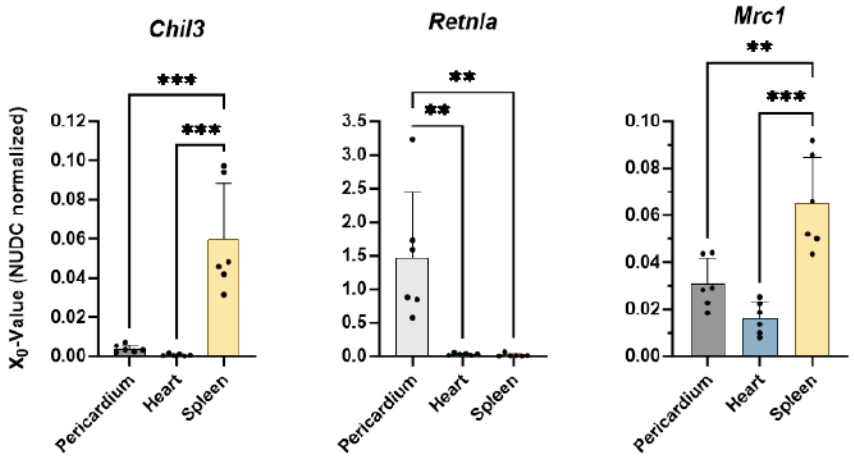

Figure 22. qPCR analysis of macrophage (MF) marker genes expression in the adult murine pericardium under basic conditions.

qPCR analysis of the MFs marker genes *Chil3* (chitinase-3-like protein 3), *Retnla* (resistin like alpha) and *Mrc1* (mannose receptor C-type 1). The analysis included freshly isolated pericardium, myocardium and the spleen, used as a positive control. Data are presented as mean ±SD, n=6. Statistical significance was calculated with one-way ANOVA (**p<0.01, ***p<0.001).

Presence of immune cells in the parietal pericardium was also confirmed via FACS analysis (Fluorescence Activated Cell Scanning). The workflow of the analysis and tissue preparation is described in the chapter 3.6.

According to the results, represented on Figure 23, $CD45^+$ leukocytes reach 48.12% ±19.87 of the total pericardial cell number. Among them were B-cells that expressed CD19 as one of the most characteristic markers. CD19+ B-cells represent a large fraction accounting for 23.71% ±10.92 of all pericardial cells. Additionally, the pericardium contained $CD3^+$ T-cells that amounted to 15% ±5.45 (Figure 23B). Notably, a fraction of $CD45^+$ pericardial cells also expressed CD31 (Clone 390), which is commonly known as endothelial cells marker, representing 25.10% ±10.13 of the total number of pericardial cells, Figure 23C.

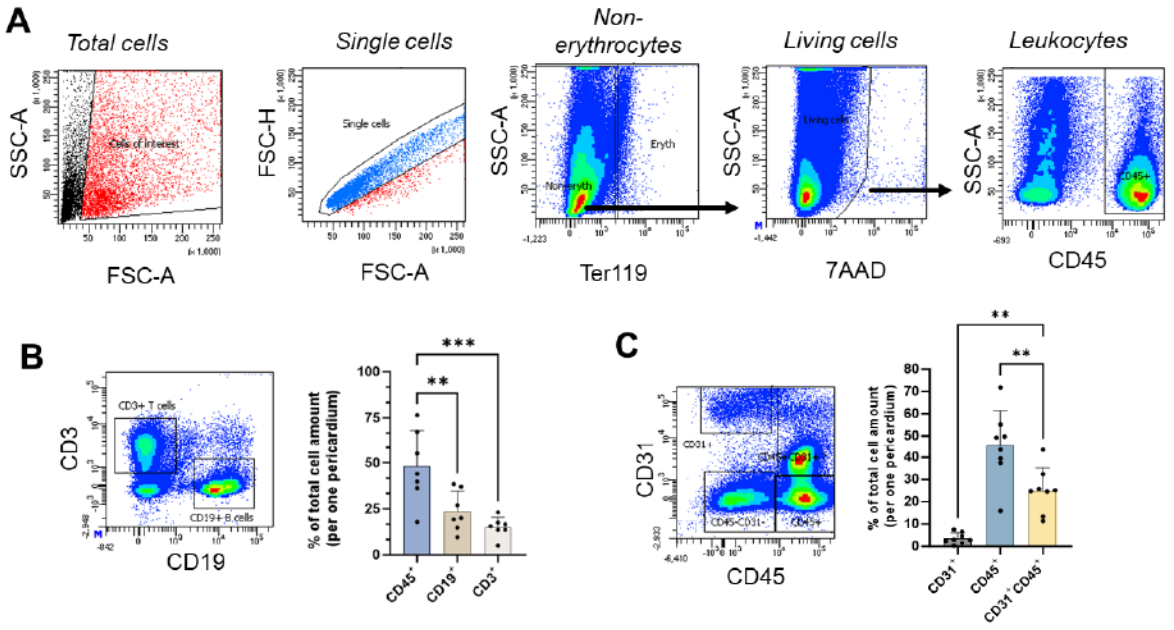

Figure 23. FACS analysis of the pericardial cells under basic conditions

[A] Gating workflow using the erythrocyte marker Ter-119, live/dead dye 7AAD and leukocytes marker CD45. [B] Selection of CD19 and CD3 expressing population serving as B- and T-cells markers respectively; data are represented as a percentage of the total pericardial cell number. [C] Detection of $CD31^{+}CD45^{+}$ cell population, using CD31 Clone 390 and representing the cell ratio as a percentage of the total pericardial cell number. Data are presented as mean ±SD, n=6. Statistical significance was calculated with one-way ANOVA (**p<0.01, ***p<0.001).

4.2.3. Analysis of WT1+ cells using lineage tracing Rosa26-tdTomato, WT1CreERT2 mice

To confirm Wt1 expression in the parietal part of the adult murine pericardium by an independent approach, a tamoxifen-inducible lineage-tracing model for Wt1 expressing cells (WT1CreERT2 Rosa26-tdTomato, henceforth referred as WT1-tdTm)[104] was used (Figure 24). Description of the model development is presented in chapter 3.1. Adult WT1CreERT2 Rosa26-tdTomato mice were subjection to intraperitoneal injected for five consecutive days with the estrogen antagonist, 4 Hydroxytamoxifen (4OHT, 500 µg/d dissolved in 100 µL peanut oil), Figure 24B. Upon injection, 4OHT mediated translocation of the CreERT2 into the nucleus, where it excised the STOP cassette, activating tdTomato selectively in $Wt1^{+}$ cells (WT1-tdTm). Littermates lacking Cre-ERT2 were treated equally to control for any tamoxifen related effects.

After a recovery period of nine days tdTomato expression was analyzed using histological analysis of the heart surrounded by the pericardium. Since WT1 is also expressed by podocytes of the adult kidney, kidney cryosections were used as positive controls. In order to increase the signal intensity, anti-tdTomato antibodies were used to stain WT1-expressing cells as well as their descendants. As shown in Figure 24C, cardiac tissue of WT1-tdTm mice did not contain tdTomato$^+$ cells after immunofluorescence staining. In contrast, the parietal pericardium, but not the epicardium demonstrated a pronounced tdTomato expression, which was found along the entire pericardial surface including posterior, middle and anterior sides of the heart. The specificity of the staining was verified in kidney sections, which displayed extensive staining of the glomeruli, which is in line with the well-known expression of WT1 in podocytes. Importantly the sections from control mice lacking CreERT2 expression contained no tdTomato$^+$ cells neither in the kidney nor in the pericardium or myocardium (Figure 24D). Thus, the lineage tracing confirmed the expression of WT1 by cells of the adult pericardium but not epicardium under basic conditions.

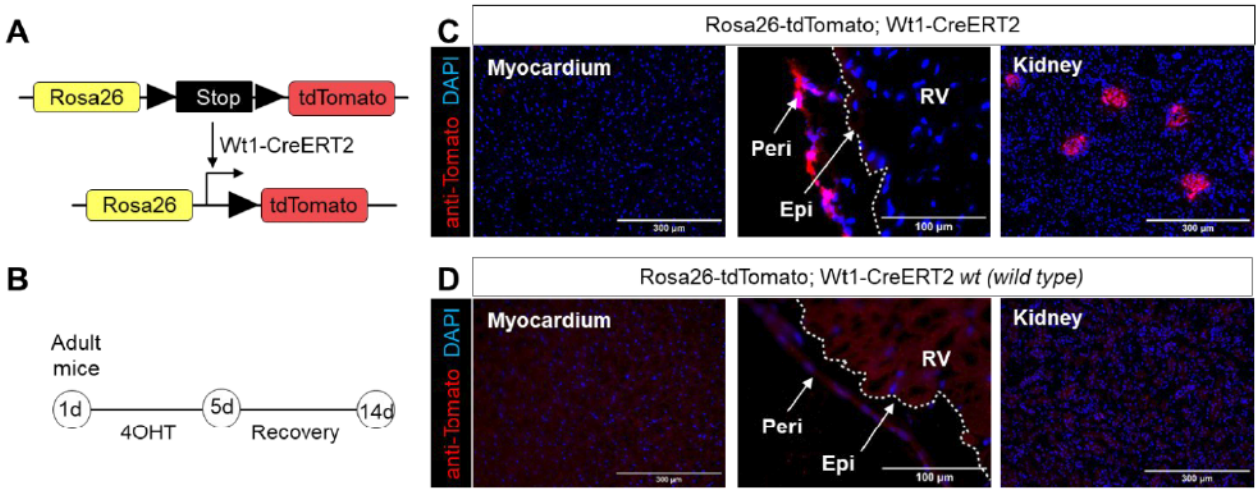

Figure 24. Tamoxifen-inducible lineage tracing model Rosa26-tdTomato; Wt1-CreERT2.

[A] Murine model used for the lineage tracing of the pericardial WT1-expressing cells and their descendants. Mice expressing CreERT2 under control of the WT1 promoter were crossed with mice containing an expression casstte consisting of the CAG promoter followed by a floxed STOP cassette in front of a tdTomato; the coding sequence was integrated into the Rosa26 locus. The Cre-recombinase was activated by injecting the adult offspring with 4 Hydroxytamoxifen (4OHT) for 5 days [B] followed by a recovery period of 9 days. [C] Immunofluorescence staining with antibody targeting tdTomato. The images represent myocardium, pericardium as well as the kidney, obtained from Rosa26-tdTomato; Wt1-CreERT2 adult mice and [D] control mice lacking Cre-ERT2 protein.

Furthermore, the area of tdTomato-expressing cells at the level of epicardium and pericardium was compared via image analysis of cryosections from the third plane representing the middle area along the heart (cryosections orientation Figure 14C). To gain a detailed insight into the spatial distribution of tdTomato expression, the regions along the left and right ventricles at the basis (LVb, RVb) and apex (LVa, RVa) of the heart were evaluated (Figure 25A). The result supported the earlier observation showing that tdTomato+ area is primarily confined to the parietal pericardium but not epicardium. IF co-staining with anti-WT1 antibody, showed that pericardium of WT1-tdTm 2 mice but not epicardium contains $Wt1^{+}tdTomato^{+}$ cell population. (Figure 25B).

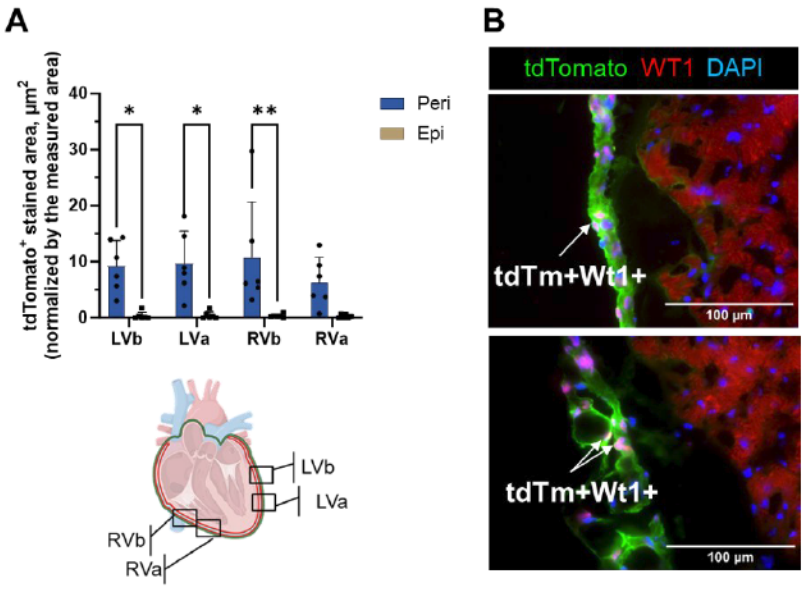

Figure 25. Wt1-expressing cell under basic conditions are confined to the parietal pericardium but not epicardium (Rosa26-tdTomato, Wt1-CreERT2).

[A] Image analysis (ImageJ/Fiji) of tdTomato expression in the epicardium and parietal pericardium in the following areas: LVb and LVa – along the area of the left ventricle basis and apex respectively; RVb and RVa – along the right ventricle basis and apex respectively. Data are presented as mean ±SD, n=6. Statistical significance was calculated with two-way ANOVA (*p<0.05, **p<0.01). [B] Microscopy images of the heart surrounded by pericardium after immunofluorescence staining with the antibodies against WT1 (red staining) and tdTomato (green staining).

Figure 26 summarizes the first characteristics of the pericardium under basic conditions. Thus, the pericardium comprises various cell types. Surprisingly, a myriad of Wt1-expressing cells was detected in the parietal pericardium under basic conditions. Furthermore, the parietal pericardium contained Upk1b+ mesothelial cells, immune cells of myeloid and lymphoid lineages, and adipocytes, which were arranged as depots integrated into the parietal layer.

Many of the cells showed a broad distribution pattern; for example, WT1+ cells were located in the parietal part of the pericardium as well as within FALCs and between adipocytes of the fat depots. The same tendency was observed for immune cells. The highest density of immune cells was found in FALCs, but the parietal pericardium and SVF also contained a minor fraction. Such a diversity may imply a diversity of pericardial functions. Therefore, to obtain an insight into the functional aspect of the adult murine pericardium, the next set of experiments was based on an analysis of the pericardial structure and cell composition upon cardiac damage, such as myocardial infarction.

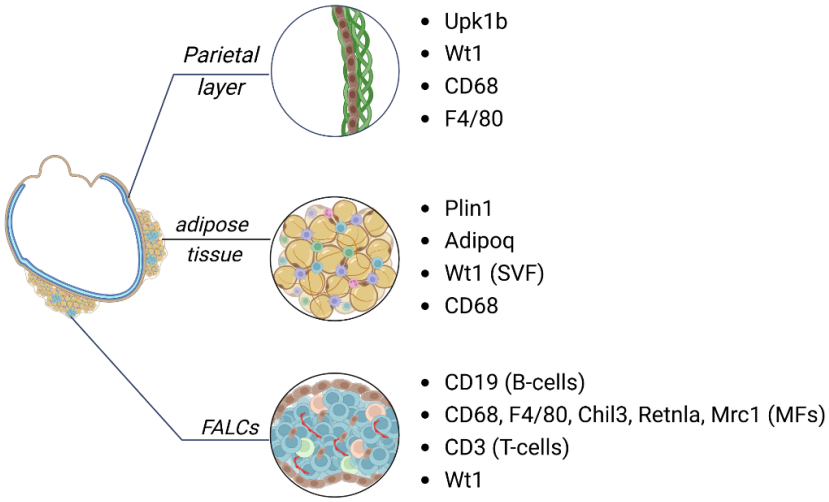

Figure 26. Schematic overview of the cell types composing the pericardium.

The scheme is based on the experiments described in the current chapter and summarizes the main elements of the pericardium as well as the markers expressed by the cells found in the tissue. The scheme was created in https://BioRender.com

4.3. Pericardial response to I/R and Sham injuries

4.3.1. Proliferative activation of pericardial cell in response to I/R.

To characterize the behavior of the described pericardial cells upon cardiac damage, an ischemia/reperfusion (I/R) surgery with a closed pericardium was implemented. In contrast to the commonly performed I/R surgery with opened pericardial sac, the setup with closed pericardium allowing to minimize the damage caused by the surgery was introduced in this project. This approach kept the cells in their environment, preserved the pericardial fluid, and maintained a possible communication of the cells within the pericardium as well as between the pericardium and the heart.

To induce myocardial infarction, the left anterior descending artery (LAD) was ligated for 45 min followed by reperfusion of the ischemic area after removal of the ligature. Successful ligation of the artery was confirmed by ST-segment elevation in the continuously recorded ECG (the protocol is described in 3.2). To take into account the mechanical damage, sham experiments were included, where all operation steps identical to I/R were conducted, omitting LAD ligation.

In a pilot experimental series the most favorable duration between the surgery and harvesting of the pericardial tissue was defined. This included six I/R surgeries, followed by recovery for 1, 2, 3, 4, 5, or 6 days. The pericardium including the heart, was isolated as outlined in Figure 7, and the structural changes after I/R were examined histologically using Masson's trichrome, Figure 27. Additionally, due to the detection of a high number of WT1-expressing cells in the parietal pericardial layer under basic conditions, anti-WT1 and anti-Ki67 (proliferating cell marker[136,137]) antibodies were used to examine possible activation in response to I/R.

Microscopy of cryosections from plane 3 (along the middle part of the heart, cryosections orientation Figure 14C) demonstrated that the pericardium underwent the following structural changes:

- Already on the second day, the parietal layer developed from the single-cell layer, which was still observed at day one after I/R, into a multicellular layer. Immunofluorescence staining revealed WT1-expressing proliferating cells as well as other KI67+ cells located in the parietal pericardium. Moreover, Masson's trichrome staining helped to detect adipocytes integrated into the parietal layer, which did not belong to the fat depots.

- Days 3-4 were associated with continued proliferation. Ki67+ cells were ubiquitously distributed around the parietal surface, whereas the pericardial cavity appeared more filled with floating cells that are not detectable under basic conditions.

- Apparently, on day five, a slight subsidence in Ki67 signaling was observed, suggesting that day 4 could be a potential climactic point in the pericardial cell proliferation.

- Finally, the pericardium on day 6 after I/R surgery revealed no Ki67+ cells throughout the entire surface, indicating a termination of the proliferation phase induced by the injury.

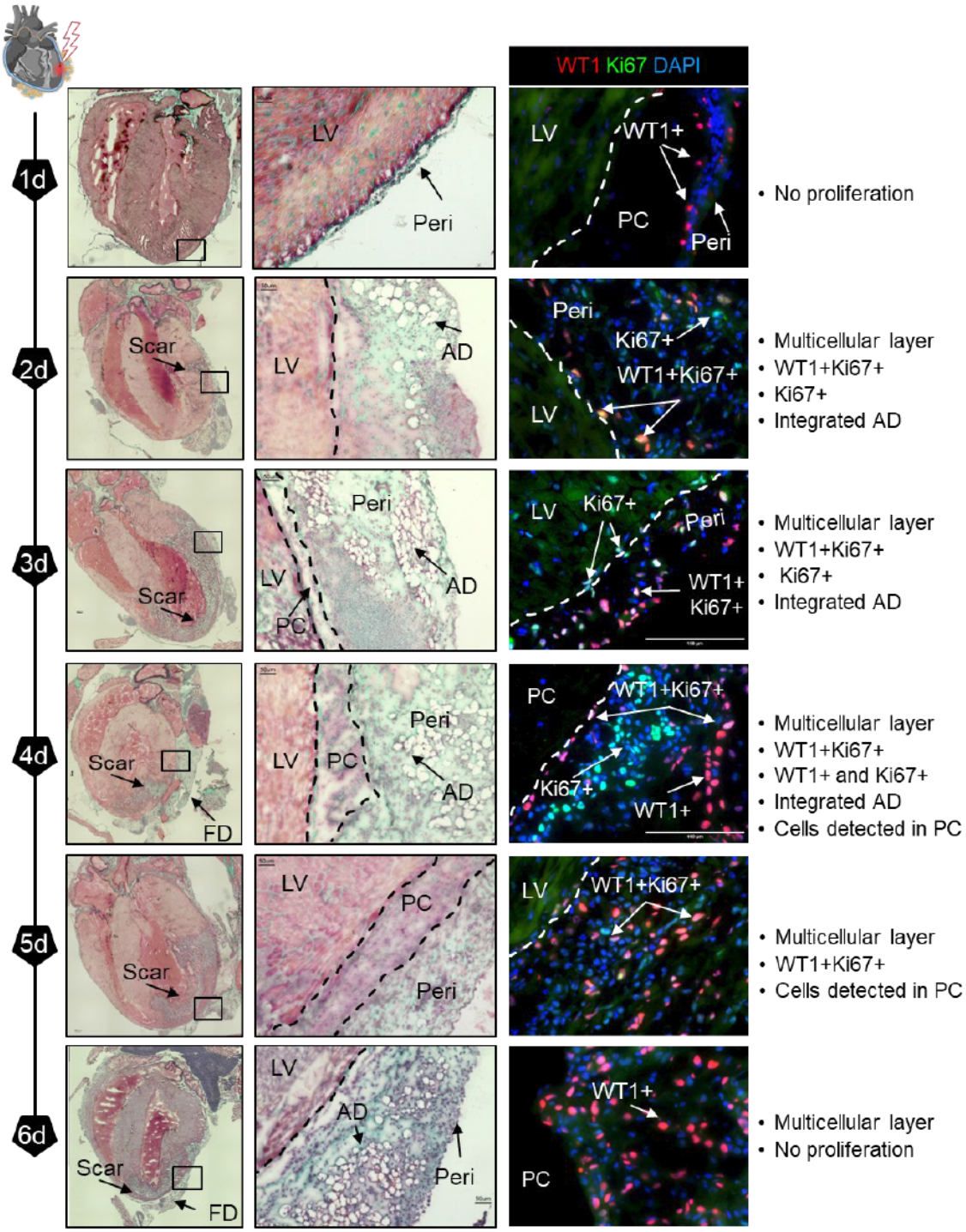

Figure 27. Overview of the pericardial alterations occurring after day 1-6 after I/R.

Representative images of the cryosections of the pericardium enveloping the heart. First column are images after Masson's trichrome staining, made with 4x and showing a total overview of the coronal plane; 2nd column are 20x images showing LV (scar proximity); the 3rd column are images after immunofluorescence staining with anti-Ki67 (proliferation marker) and anti-WT1 antibodies. The tissue was harvested on days 1, 2, 3, 4, 5 and 6 days after I/R, according to the method described in **Figure 7**. LV – left ventricle, Peri – pericardium, PC – pericardial cavity, AD – adipocytes, FD – fat depot.

Interestingly, cell proliferation also occurred in FALCs indicated Ki67+ cells already on the second day after surgery. The proliferation lasted up to the fifth day (Figure 28). The presented microscopy shows abundance of Ki67+ cells within FALCs and among them also WT1+Ki67+ population. The proliferative activity in FALCs also decreased by day five and vanished on day 6.

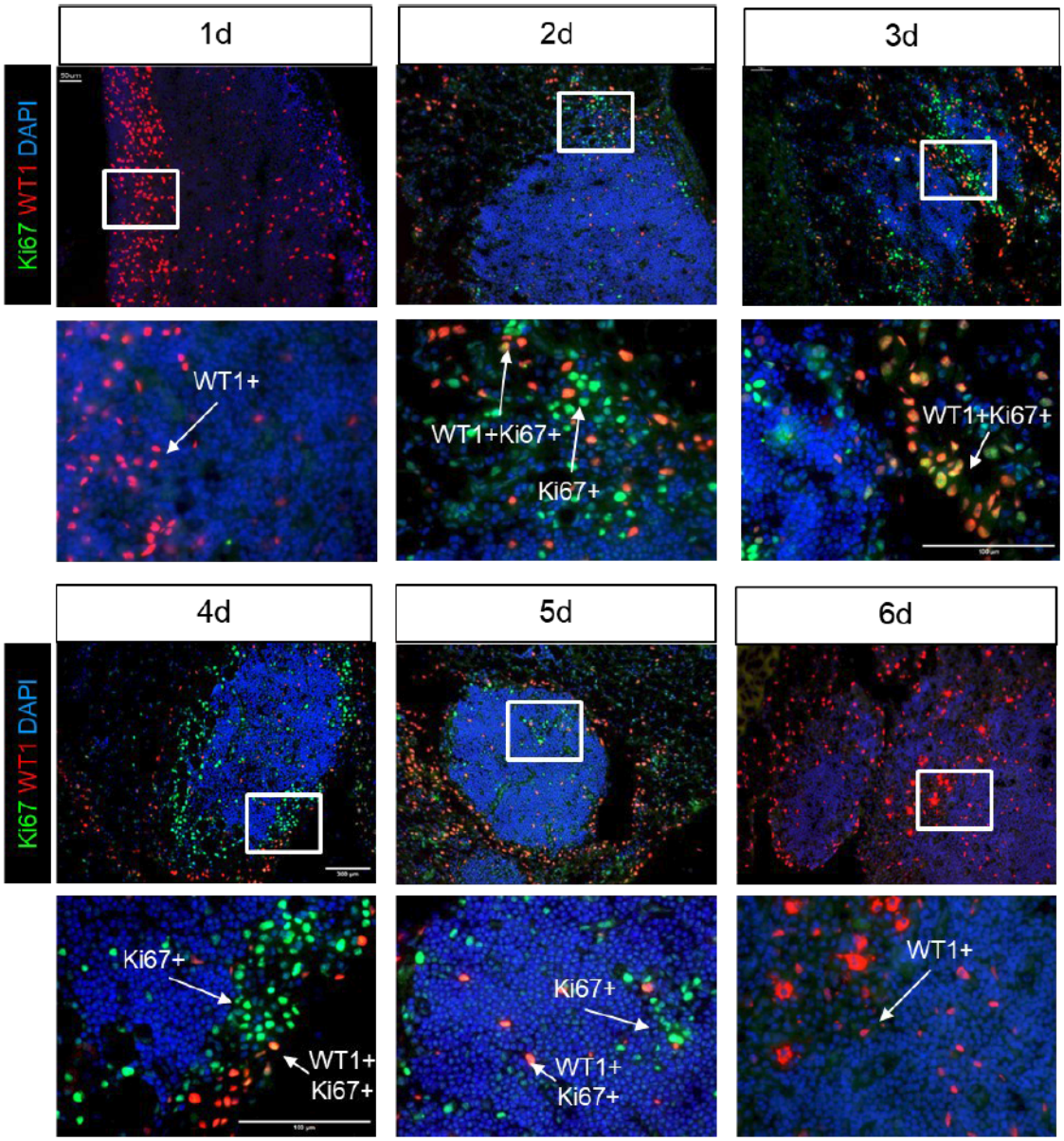

Figure 28. Timespan of proliferation in pericardial FALCs in response to I/R.

The microscopy images (20x, 40x) after immunofluorescence staining with DAPI, anti-Ki67 and WT1 antibodies that show FALCs regions with x60 and x20 magnifications at days 1, 2, 3, 4, 5 and 6 days after I/R.

4.3.2. Increase of the pericardial thickness in response to I/R and sham

According to the pilot experiment (Figure 28), day 6 after I/R showed the end-stage of the pericardial cell activity. Therefore, the next set of experiments were aimed at analysis of the pericardium on day 6 after I/R and sham surgeries, including the record of structural changes and cellular composition. To gain spatial information about the pericardial morphology after the cardiac injuries, the pericardium, alongside the heart, was sectioned and analyzed using the planes that correspond to the anterior, middle and posterior part of the heart, as described in Figure 7.

Firstly, to pursue the observations obtained via the timeline experiment, the thickness of the pericardium near the scar was compared between basic conditions, I/R and sham (Figure 29). For the measurements, the pericardial areas, free of fat and FALCs, were selected. Analogously to the previous measurement, depicted on Figure 14, at least three measurements were conducted in each image and average value was taken as a thickness value. The analysis revealed that the pericardium after I/R significantly thickened along the posterior and anterior parts of the heart (posterior: basic 12.9µm ±5.6, sham 45.48µm ±5.6 and I/R 145.6 ±46.3; middle: basic: 11.0µm ±4.1, sham: 77.9µm ±46.6, I/R: 163.8 ±53.1; anterior: basic: 12.9µm ±2.9, sham: 92.2µm ±62.8, I/R: 192.0µm ±68.4), Figure 29A.

Interestingly, after the cardiac injuries, particularly after I/R, the visceral part of the pericardium (epicardium) became more pronounced (Figure 29C). Measurement of the epicardium showed that between sham and I/R there was no significant difference in the thickness, which was in a range of 8.3µm ±1.5 (sham) and 20.7µm ±15.4 (I/R) respectively, Figure 29B. It is important to note that the evaluation was accompanied by a high standard deviation, resulting from a heterogeneous distribution of pericardial elements across the surface. Moreover, in some samples, an extreme proximity of the visceral and parietal layers, which occurred during embedment of the pericardium, caused difficulties in distinguishing and measuring the layers.

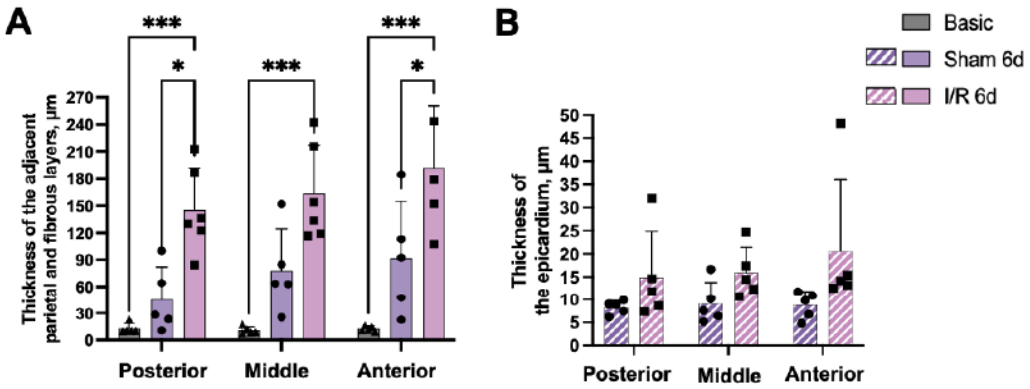

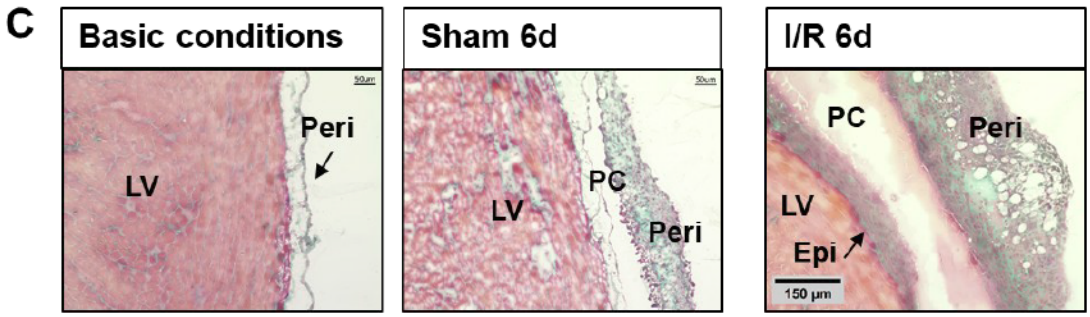

Figure 29. Expansion of the parietal and visceral layers in response I/R injury and Sham.

Image analysis of the parietal and [A] and visceral [B] pericardial layers comparing the thickness under basic conditions and on day 6 after sham and I/R. The measurements were made along the posterior, middle and anterior cardiac walls. Data are presented as mean ±SD, n=5. Statistical significance was calculated with two-way ANOVA (*p<0.05, ***p<0.001). [C] Representative images of the cryosections after Masson's trichrome staining demonstrating the structure of the pericardium under basic conditions, and on day 6 after sham and I/R.

4.3.3. Activation of pericardial tdTomato-expressing cells in WT1-tdTm mice in response to I/R and sham

Since the timeline experiment showed that WT1+ cells might contribute to the pericardial expansion by their proliferation from day 2 to 5 after I/R surgery, the lineage tracing model WT1-tdTm was used to test the hypothesis. Therefore, the following set of experiments consisted of histological analyses to visualize the spatial distribution of tdTomato+ cells throughout the examined tissue after I/R and sham. The area occupied by tdTomato$^+$ cells was measured along LV and RV followed by normalizing the values to the length of the measured part of the pericardium.

Figure 30A demonstrates that in comparison to the basic condition, the damage caused by sham led to a 3-fold expansion of the tdTomato stained area in the proximity of the injury along the LV, whereas I/R resulted in 5-fold increase. On the other hand, the area along RV, exhibited 2-fold increase of the area occupied by tdTomato+ cells.

Moreover Figure 30B reveals that the epicardium that becomes more pronounced after the injuries, also exhibited tdTomato+ signaling. After sham, the area occupied by tdTomato+ cells was 15.64µm^2 ±18.72 along LV, and 5.93µm^2 ±3.9 along RV. Similarly, after I/R the area was 16.14µm^2 ±7.9 and RV 3.71µm^2 ± 2.75.

According to these observations, tdTomato signals, which occur in the epicardial part of the pericardium after the cardiac damage might suggest that Wt1-expressing cells or their descendants may originate from the cells of the parietal pericardium.

Additionally, counterstaining with anti-tdTomato and anti-CD31 (endothelial cells (EC) marker) represented on Figure 30D revealed that after the cardiac damage the thickened parietal pericardium contained CD31+ ECs, which were not detected under basic conditions. However, there was no co-expression of tdTomato and CD31, ruling out that the CD31+ ECs could be derived from tdTomato+ cells, but it rather reflects angiogenesis in the thickened pericardium.

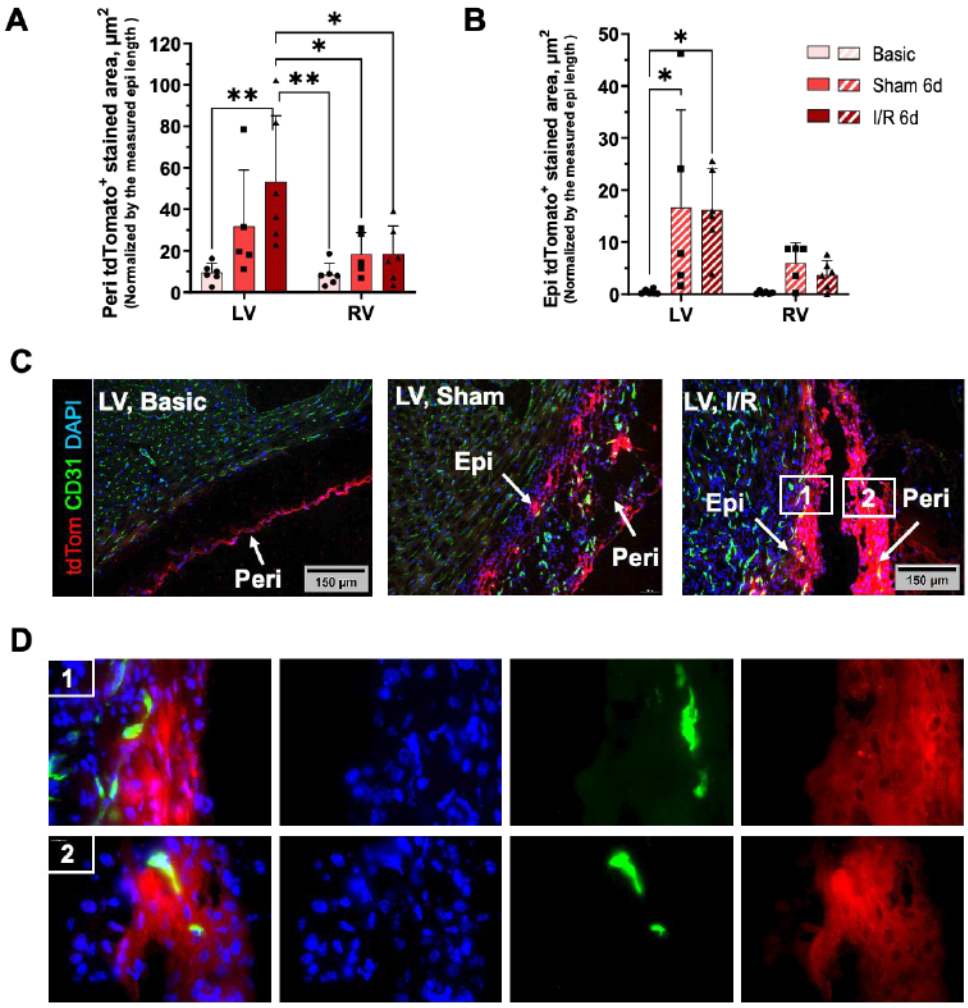

Figure 30. Activation of tdTomato-expressing cells of WT1-tdTm mice in response to sham and I/R injury.

Image analysis of the parietal [A] and visceral [B] pericardium, showing tdTomato stained area under basic conditions, on day 6 after sham and I/R injury. Data are presented as mean ±SD, n=5. Statistical significance was calculated with two-way ANOVA (*p<0.05, **p<0.01). [C] Representative images of the immunofluorescence counterstaining with anti-tdTomato and CD31 (endothelial cells marker). [D]100x magnification of the visceral [1] and parietal [2] pericardium on day 6 after I/R injury.

4.3.4. Pericardial tdTomato+ cells may differentiate in response to I/R

To examine whether tdTomato expressing cells preserve their mesothelial characteristics, a counterstaining with anti-Upk1b was performed. On one hand, similar to the basic conditions the parietal pericardium after I/R and sham contained tdTomato+Upk1b+ cells, which were present throughout the perimeter of the parietal pericardium. However, after I/R there were also areas, particularly in the scar proximity, where only tdTomato+ cells were present (Figure 31). This observation could imply a potential differentiation of tdTomato+ cells and their progress towards a cell lineage, which has lost typical mesothelial characteristics as indicated by the loss of Upk1b expression.

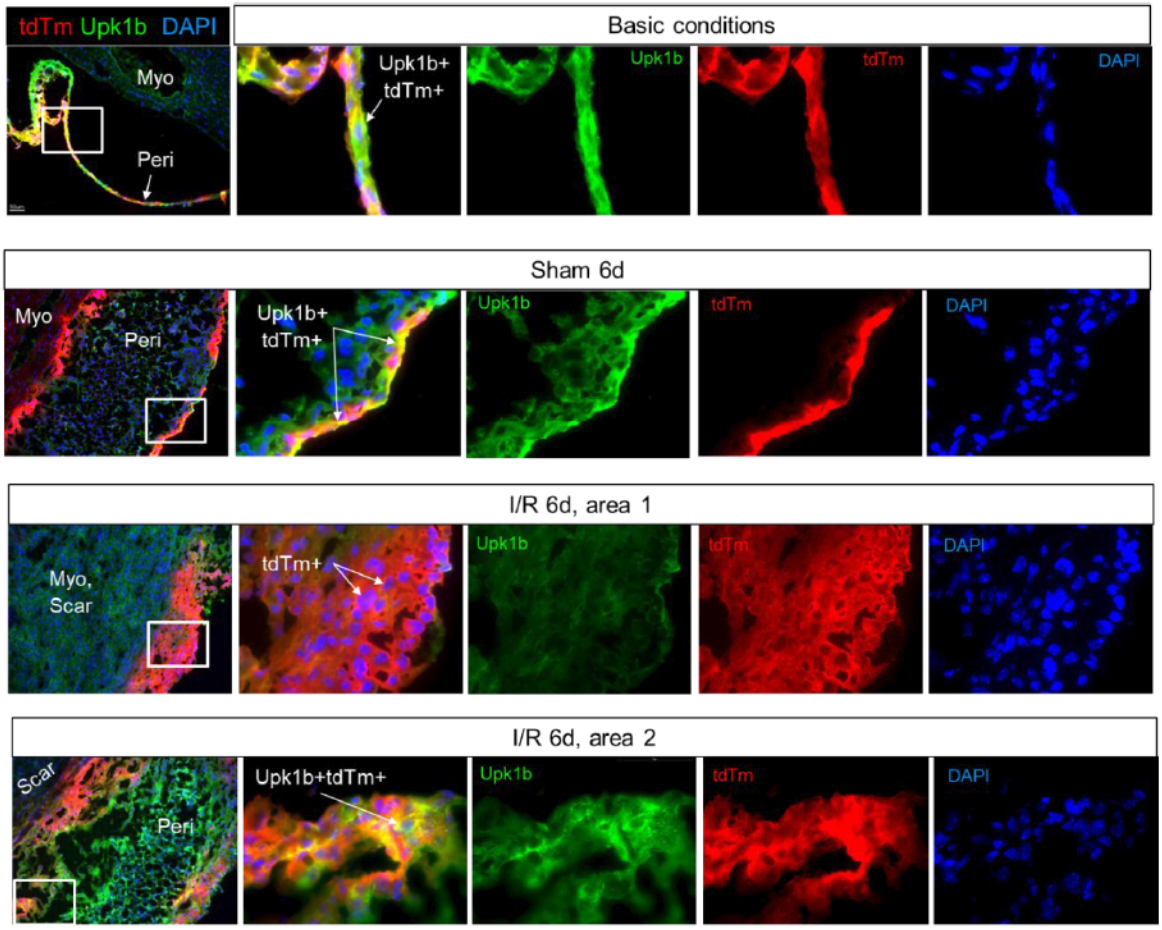

Figure 31. Expression of tdTomato by pericardial cells of WT1-tdTm in mice after I/R and sham.

Microscopy images after the immunofluorescence staining with the antibodies targeting tdTomato and Upk1b (mesothelial cells marker) made at 20x and 100x magnification. The images represent pericardium under basic conditions, on day 6 after sham and I/R surgery. Myo – myocardium, Peri – pericardium.

4.3.5. Upk1b+tdTomato+ cells were not detected within pericardial adipose tissue after sham and I/R

Furthermore, the IF co-staining of the pericardium with anti-Upk1b and anti-tdTomato antibodies in WT1-tdTm mice showed that under basic conditions Upk1b+tdTomato+ signal was detected among the pericardial adipocytes (Figure 32). However, upon sham and I/R tdTomato signal was not detected, containing only Upk1b-expressing mesothelial cells as a part of SVF.

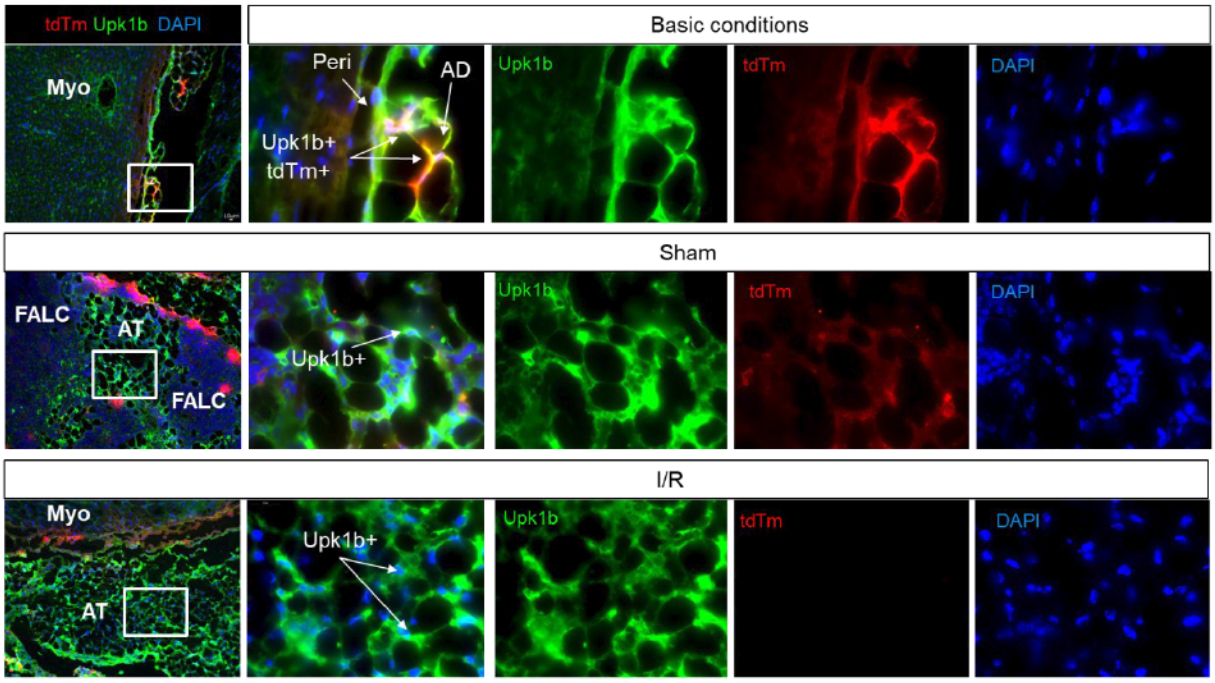

Figure 32. Expression of mesothelial cells in pericardial fat of WT1-tdTm mice under basic conditions, after I/R and sham.

Microscopy images (20x, 100x magnification) of the pericardial adipose tissue after the immunofluorescence staining with the antibodies targeting tdTomato and Upk1b (mesothelial cells marker) under basic conditions and on day 6 after sham. Myo – myocardium, AD – adipocytes, Peri- pericardium, AT – adipose tissue.

4.3.6. Pericardial tdTomato+ cells possibly migrate toward the scar after I/R and differentiate into fibroblasts

It was striking that further histological analysis of the myocardium after I/R in WT1-tdTm mice, revealed that the scar formed by day 6 after I/R contained tdTomato-expressing cells. The microscopy images represented in Figure 33 show that the cardiac tissue in the region of LV (apex proximity) under basic conditions contains no tdTomato signal.

After sham there were minor tdToamto+ signals detected in the corresponding area, whereas I/R injury caused formation of a significant scar that certainly contained tdTomato-expressing cells. This finding supports the hypothesis that the pericardial cells migrate towards the area of damage.

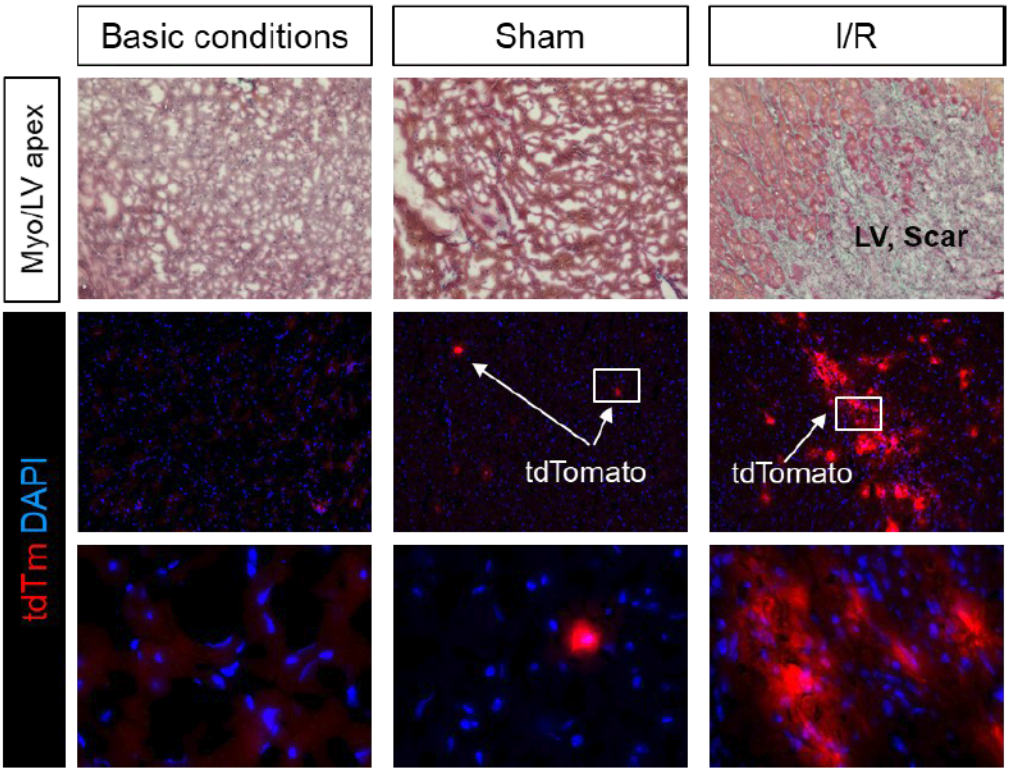

Figure 33. Myocardial scar after I/R in WT1-tdTm mice contains tdTomato signals.

Microscopy images (20x, 100x) of the damaged myocardium after I/R and of the areas that correspond to scar region in healthy hearts (left ventricle, close to apex) and sham after Masson's trichrome and immunofluorescence staining with anti-tdTomato antibody.

To identify a type of cells that express tdTomato within the scar an additional immunofluorescence staining was performed. Since it is known that infarcted myocardium contains a high amount of activated fibroblasts, the analysis included antibodies targeting fibroblasts-associated markers such as Periostin (Postn)[138], discoidin domain receptor 2 (DDR2)[139] and α-smooth muscle actin (α-SMA or Acta2)[140]. According to the microscopy images (Figure 34), which depict the scar regions, occurred on day 6 after I/R, some of these areas contained signals of the applied antibodies, which localized with tdTomato staining. The observation suggests a potential differentiation of the pericardial tdTomato-expressing cells into cells of a fibroblastic type, which reside in the damaged myocardium and might contribute to the scar remodeling process.

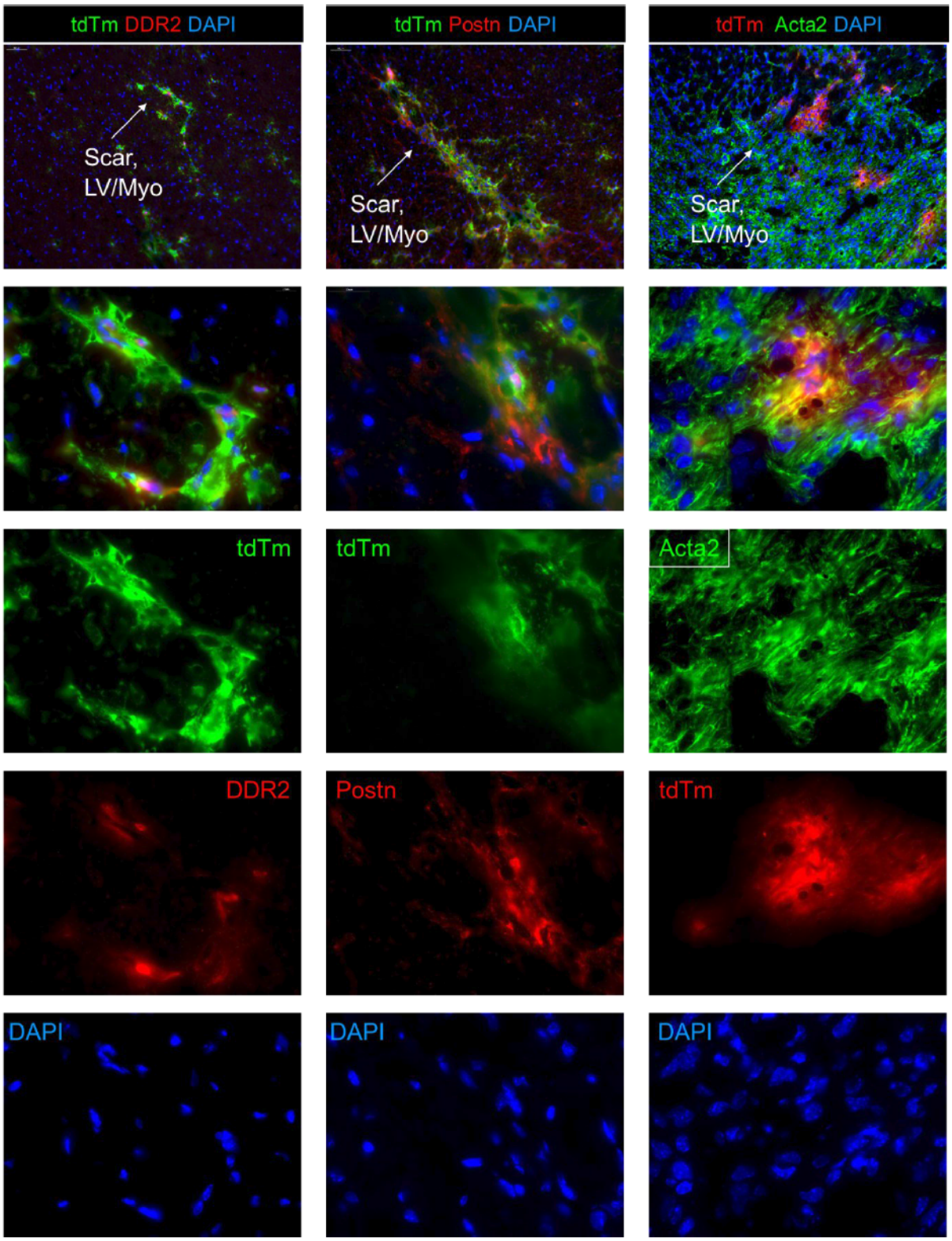

Figure 34. tdTomato+ cells from WT1-tdTm mice, detected within the scar after I/R express fibroblasts markers.

Microscopy images after the immunofluorescence staining with the antibodies targeting tdTomato and fibroblast markers DDR2, Postn and Acta2. 20x and 100x magnification images demonstrate scar region in the myocardium on day 6 after I/R. Myo – myocardium, LV – left ventricle.

4.3.7. On day 6 after I/R and sham pericardium contains less adipose tissue than under basic conditions.

Since the adipose tissue and integrated lymphoid clusters represent an essential part of the pericardium, evaluation of their structural changes in response to the cardiac injury were included in the image analysis.

The measurement of adipose tissue was performed analogously to the workflow used for the basic conditions (Figure 9, chapter 3.4.5) where the area of adipose tissue (A_{AT}) was represented as percentage of the pericardial area (A_{peri}), measured in each plane separately. The analysis demonstrated that A_{AT} along the anterior wall of the heart, which represents the scar region, was significantly smaller after sham or I/R surgery in comparison to basic conditions (anterior basic: 66.2% ±8.3; sham: 45.8% ±24.1; I/R: 42.58 ±24.4), Figure 35A. Thus, both types of the cardiac damage induced a similar biological effect, although both interventions potentially have different severity levels. Comparison of the fat depots distribution throughout the pericardial surface showed that, similar to the basic conditions, the pericardial AT after sham or I/R injury is primarily located along LV rather than RV, particularly along the middle section of the heart (Figure 35B). The relative distribution of AT was similar across all three conditions: basic 71.4% ±5.4 was detected along LV, and 28.5% ±5.5 along RV, sham 75% ±18.2 was found at LV, and 24.9% ±18.1 at RV, and after I/R surgery LV was surrounded by 74.4% ±13.8 and RV - 25.5% ±14.0.

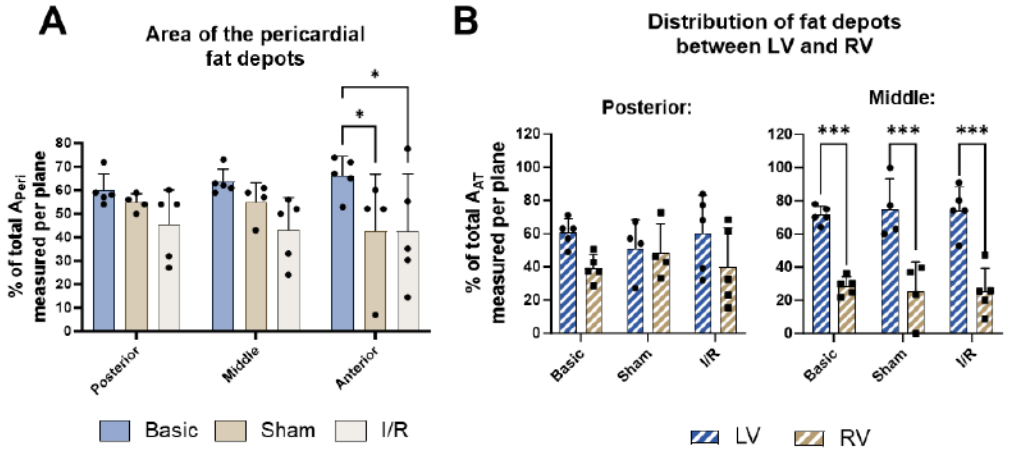

Figure 35. Spatial distribution of the pericardial adipose tissue in response to I/R and sham.

[A] Surface area of the pericardial adipose tissue (A_{AT}) represented as a percentage of the pericardial area (A_{Peri}), measured in each plane separately (workflow described in chapter 3.4.5). [B] AT distribution between the areas along LV and RV, represented as a percentage of the entire A_{AT} per plane. Data are presented as mean ±SD, n=5. Statistical significance was calculated with one-way [A] and two-way [B] ANOVA (*p<0.05, *** p<0.001).

4.3.8. Expansion of pericardial FALCs in response to sham and I/R.

Further image analysis was aimed at evaluation of FALCs area under basic conditions, after sham and I/R using Masson's trichrome staining (Figure 36). In Figure 36A the area of FALCs (A_{FALC}) is represented as a percentage of the adipose tissue area (A_{AT}). The areas were measured in each plane separately.

Figure 36A shows that the surgeries induced an increase in the FALCs area, particularly in the planes obtained from the middle of the heart. Under basic conditions, FALCs composed only 6.2% ±3.2 of fat, after sham it was increased up to 20.8%±11.9, whereas I/R caused an increase up to 29.9% ±14.9. Furthermore, along the anterior part of the heart the area of FALCs was very low with no significant changes upon the cardiac damage.

Figure 36B shows distribution of FALCs between LV and RV. In the plains obtained from the middle of the heart the distribution of FALCs was similar to the distribution of fat depots, primarily concentrating along LV across all three conditions (Figure 35B).

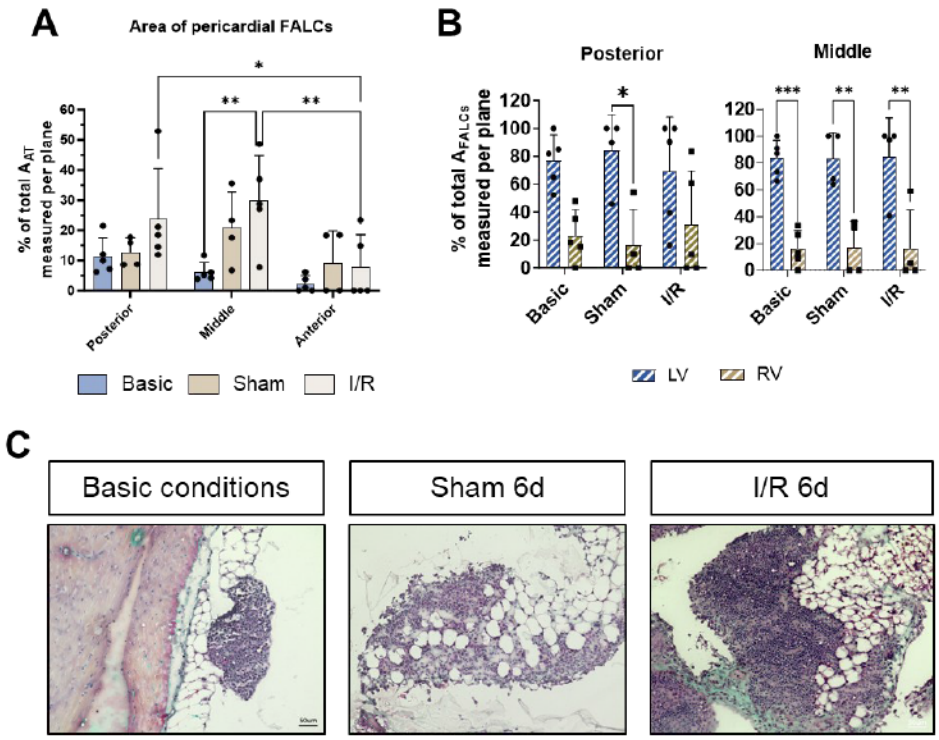

Figure 36. Expansion of the pericardial FALCs after I/R and sham.

[A] Area of FALCs (A_{FALC}) represented as a percentage of adipose tissue area (A_{AT}), measured in each plane separately. [B] Evaluation of the FALCs distribution between the areas along LV and RV, represented as a percentage of A_{FALC} per plane. Data are presented as mean ±SD, n=5. Statistical significance was calculated with one-way [A] and two-way [B] ANOVA (* $p<0.05$, ** $p<0.01$). [C] Microscopy images after Masson's trichrome staining representing pericardial FALCs.

Immunofluorescence staining with antibodies targeting CD68+ macrophages and CD19+ B cells, demonstrated that both, myeloid and lymphoid cell lineages were present within FALCs across all three conditions (Figure 37), although B-cells represent a predominant subset. According to the microscopy, the cardiac damage did not cause any changes in the distribution pattern of the immune cells within FALCs. However, the staining revealed that by day 6 after I/R the pericardial fluid contained floating CD19+ and CD68+ immune population.

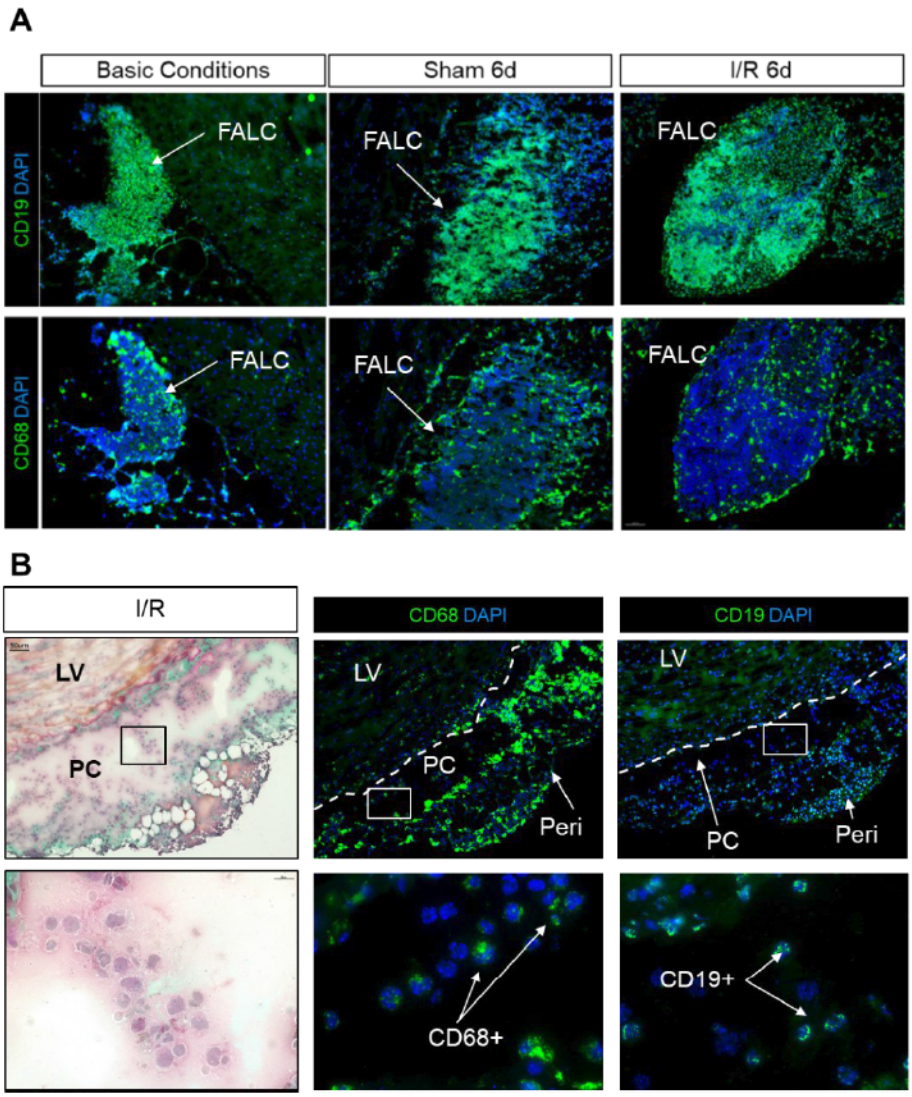

Figure 37. Immune cells distribution within FALCs after sham experiment and I/R injury.

Immunofluorescence staining with anti-CD68 (MFs marker) and CD19 (B-cells marker) of the pericardium. [A] Microscopy images (20x) of FALCs under basic conditions, on day 6 after sham experiment and I/R surgery. [B] Microscopy images (20x, 100x) of pericardial fluid after Masson's trichrome and after IF, on day 6 after I/R.

The histological analyses of the pericardium after I/R and sham showed that the pericardium undergoes pronounced changes on the morphological and cellular level (schematic summary Figure 38). Wt1-expressing cells, as well as other cells residing in the pericardium, proliferate from day 2 to 5 after I/R. Interestingly, the proliferation was detected throughout the entire pericardium, including FALCs. In addition, the lineage-tracing in WT1-tdTm mice showed that under basic conditions, tdTomato+ cells are confined to the parietal part of the pericardium, whereas after sham, the signals expand, to a small extent, to the visceral layer. After I/R, however, a pronounced expression is detected even within the damaged myocardium. The IF staining of the hearts after I/R with anti-Acta2, DDR2, and Postn antibodies showed that within the scar, some cell populations express tdTomato as well as the selected markers, which hints at possible migration of the pericardial cells towards the scar and differentiation into activated myofibroblasts. Finally, significant expansion of the FALCs upon I/R and sham suggests a strong immune response. Therefore, to gain an advanced understanding of the significant changes and to obtain a comprehensive description of the pericardial cell diversity the following experiments included single-cell RNA sequencing analysis.

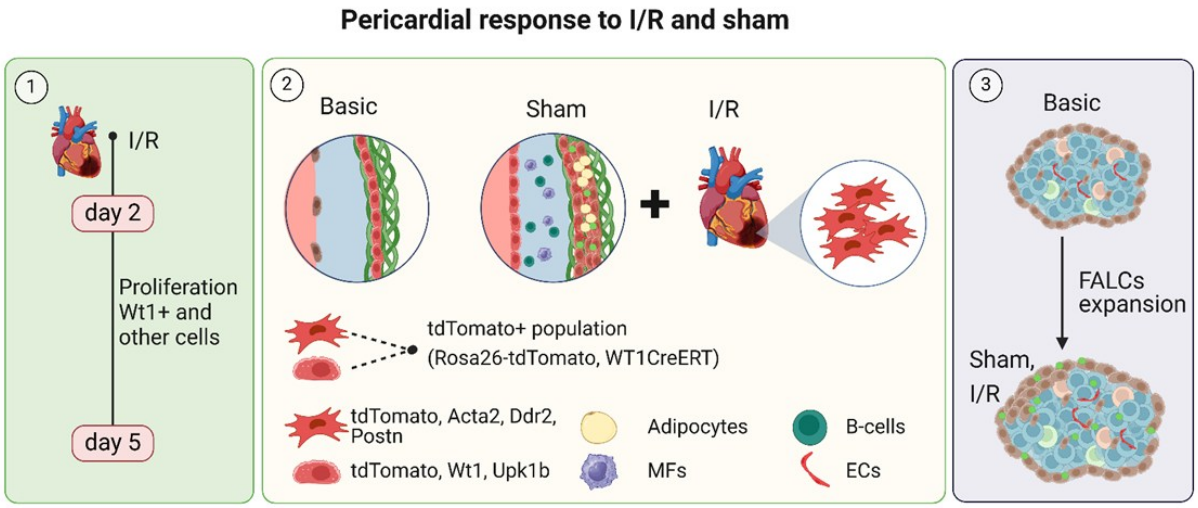

Figure 38. Schematic overview of the pericardial cells' behavior in response to I/R and sham.

The scheme is created with Biorender.com

4.4. Analysis Pericardial cell composition and response to I/R using single-cell RNA sequencing.

The main pericardial changes upon I/R and sham, which were revealed by the previous experiments, suggest that there is a strong immune response supported by FALCs and activation of Wt1-expressing cells which might play a role of progenitor cells. In this respect, the aim of single-cell RNA sequencing analysis (scRNA-seq) was to examine the activity and diversity of pericardial cells and with focus on the response of Wt1-expressing cells to the cardiac damage.

For the analysis, the male C57BL/6J (Janvier Labs, Le Genest-Saint-Isle, France) animals, 10-12 weeks old, underwent to the I/R and sham surgeries, as described in chapter 3.2. The pericardium of mice on day 6 after I/R (n=3), sham (n=3), as well as of healthy animals (basic condition) (n=3) was isolated according to the scheme illustrated in Figure 6, A-D. The tissue was digested in Collagenase II to obtain the single-cell suspension, which was FACS sorted to remove erythrocytes and dead cells via FACS using Ter-119 antibodiy and propidium iodid respectively, Figure 39 (tissue preparation and analysis workflow are described in chapter 3.8).

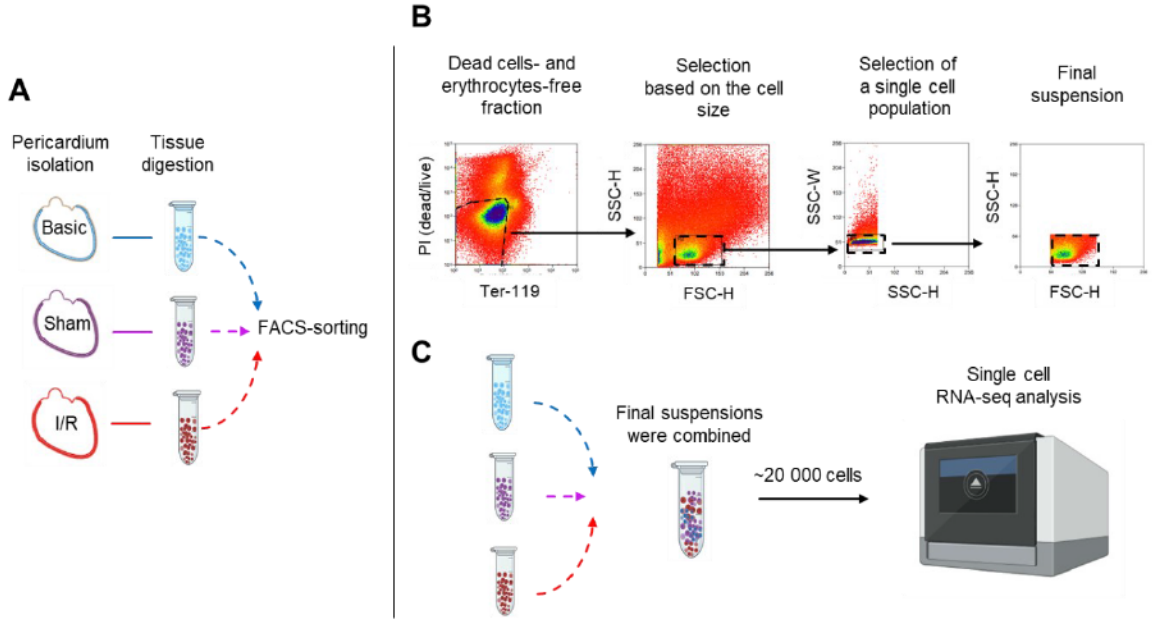

Figure 39. Pericardium preparation for scRNA-seq analysis.

[A] Schematic workflow for isolation of the pericardium separately from the heart under basic conditions, on day 6 after sham and I/R, followed by 25 min digestion in Collagenase II. [B] FACS sorting workflow using Ter-119 antibody (erythrocytes) and propidium iodid (PI) for removal of dead cell population, followed by selection of the cells based on forward scatter (FSC) and side scatter (SSC) measurements. FSC-Height vs SSC-Height – selection of the population of interest based on the cell size. SSC-Height vs SSC-Width – exclusion of cell clumps and doublets. [C] The final suspension, contained a mixture of FACS-sorted pericardial cells under basic conditions, after sham and I/R injury was used for scRNA-seq analysis

The single cell sequencing and following bioinformatics analysis of the obtained data was performed, as described in chapter 3.8, in cooperation with Dr. Tobias Lautwein at Biological-Medical Research Center (BMFZ), Heinrich Heine University Düsseldorf. detected that murine pericardium contains 21 cell cluster (Figure 40). The cell types, which were residing in each cluster, were identified in accordance to the predominant and specific gene expression patterns, which are shown in Figure 41 and will be revealed in detail in the following chapters. Thus, the clusters presented on the UMAP occur as separate populations or groups of sub-clusters that define a particular type of cells. Importantly, the numbering of the clusters occurs in the order of decreasing cell number in each cluster, implying that cluster 0 contains the highest and cluster 20 – the smallest number of cells.

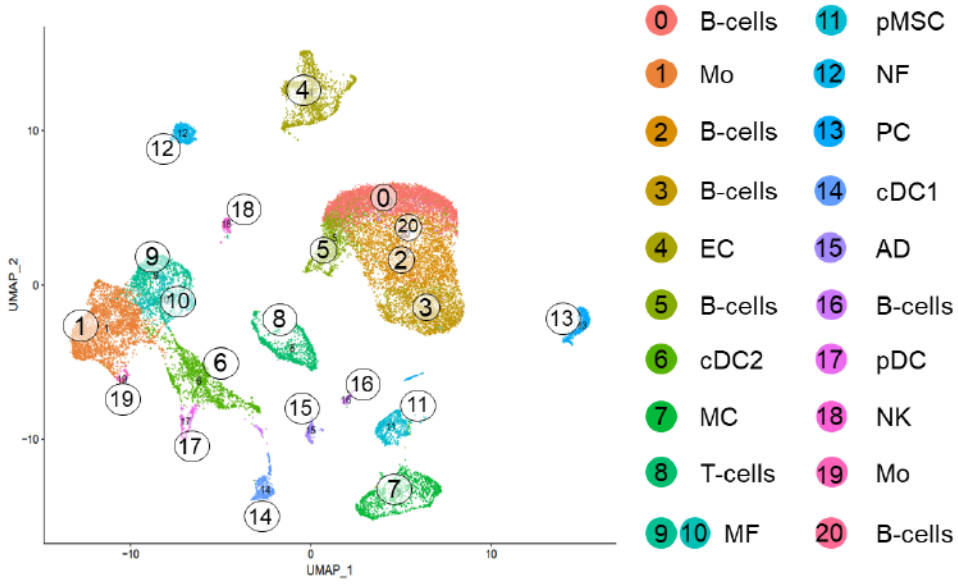

Figure 40. Pericardial cell populations and their distribution obtained with single-cell RNA sequencing analysis

[A] UMAP plot of pericardial cell clusters with combined conditions obtained via scRNA-seq analysis of 28385 cells, n=3 for each condition (basic, sham, I/R). Mo – monocytes, EC – endothelial cells, cDC1 (2) – conventional dendritic cells type 1 or 2, pDC – plasmacytoid dendritic cells, MC – mesothelial cells, MF – macrophages, pMSCs – pericardial mesenchymal cells, NF- neutrophils, PC – plasma cells, AD – adipocytes, NK – natural killer cells.

According to Figure 41, immune cells of the lymphoid as well as myeloid lineages constituted the largest part of the pericardium. Among the lymphoid cells, a variety of B-cell subsets represented by a group of four large sub-clusters 0, 2, 3, 5, and the small cluster 20. These cells are characterized by a high expression of *Cd19*[141,142], *Pax5*[143,144], *Ighd*[145], *Ly6d*, *Ms4a1*[146], *Cd79a*, *Cd79b*[147].

However, there were also several cell groups displayed separately on the UMAP, albeit they are related to B-cells. Among them was cluster 16, which expressed B-cell characteristic genes as well as genes indicating involvement in the cell cycle *(Mki67*[148]*, Ccne1, Ccne2, Aurka, Nusap1*[149]*)*. Plasma B cells (PC) were found in cluster 13 and expressed *Jchain*[150]*, Fkbp11, Mzb1* [151], *Prdm1, Irf4,* and *Xbp1*[152]. Furthermore, cluster 8 of the pericardium contains T-cells that expressed *Cd8a* [153]*, Cd4* [153]*, Foxp3* [154] as well as natural-killer cells (NK-cells) found in cluster 18 (*Itga2*[155]*, Klrk1*[156]*, Klrb1c, Gzma*[157]).

Another predominant group of pericardial cells was represented by myeloid cells that included a wide range of cell clusters, arranged as a group of sub-clusters or separated cell clusters. Hence, there were monocytes residing the clusters 1 and a small adjacent cluster 19 that expressed *Ly6c2*[133], *Fcgr1*[133]*, Chil3*[146]*, Cd68*[158]*,* and *Myd88*[159]. Furthermore, the analysis detected macrophages (MFs), supporting the previous histological finding (Figure 21). However, sc-RNA seq showed that there are two subsets that reside in clusters 9 and 10 that expressed *Arg1*[131]*, Folr2*[146]*, Lyve1*[151]*, Mrc1*[160]*, Adgre1*[160]*, Rentla*[161]*, Timd4*[146]*, Ccr2*[162]. Next, there were several types of dendritic cells including conventional dendritic cells type 1 (cDC1, cluster 14; *Clec9a*[163,164]*, Irf8*[164]*, Xcr1, Cadm1*[165]*, Itgae*[166]), cDC2 (cluster 6*; Itgam, Sirpa, Mgl2*[166]*, Clec10a*[163]*, Itgax*[167]*, H2-Ab1, H2-Eb*[167]) and plasmacytoid DC (pDC, cluster 17; *Siglech*[168]*, Ccr9*[169,170]*, Stat5a, Runx2*[164]*).* Finally, the analysis revealed the presence of neutrophils that were identified in cluster 12 (NFs; *S100a8/a9* [171,172]*, Ly6g, Cd11b*[173]*, Csf3r, Cxcr2*[172]).

In addition to the broad spectrum of immune cell populations, the pericardium contained non-immune cells. Among them, cluster 4 was annotated as endothelial cells (ECs) due to a high expression of *Cldn5, Pecam1, Vwf*[174]. Furthermore, there was a small group of adipocytes detected in cluster 15 (*Lipe*[172]*, Adipoq*[175]*, Plin1*[176]*, Ucp1*[177]). The small size of adipocyte cluster is in contrast to the histological observations showing abundance of the fat depots (Figure 15). This might be explained by a loss of adipocytes during the tissue preparation and several filtering steps of the cell suspension (chapter 3.8).

Importantly, the cluster analysis revealed two separate clusters of WT1-expressing cells (cluster 7 and 11). Cluster 7 contained mainly canonical mesothelial cells (*Msln, Upk3b, Lrrn4*[178]), whereas cluster 11 rather represented by fibroblasts-like cells (*Postn*[179] , *Pdgfrb*[180], *Pdgfra*[180], *Ddr2*[181]). A detailed characterization of the cluster will be presented in the chapter 4.1.1

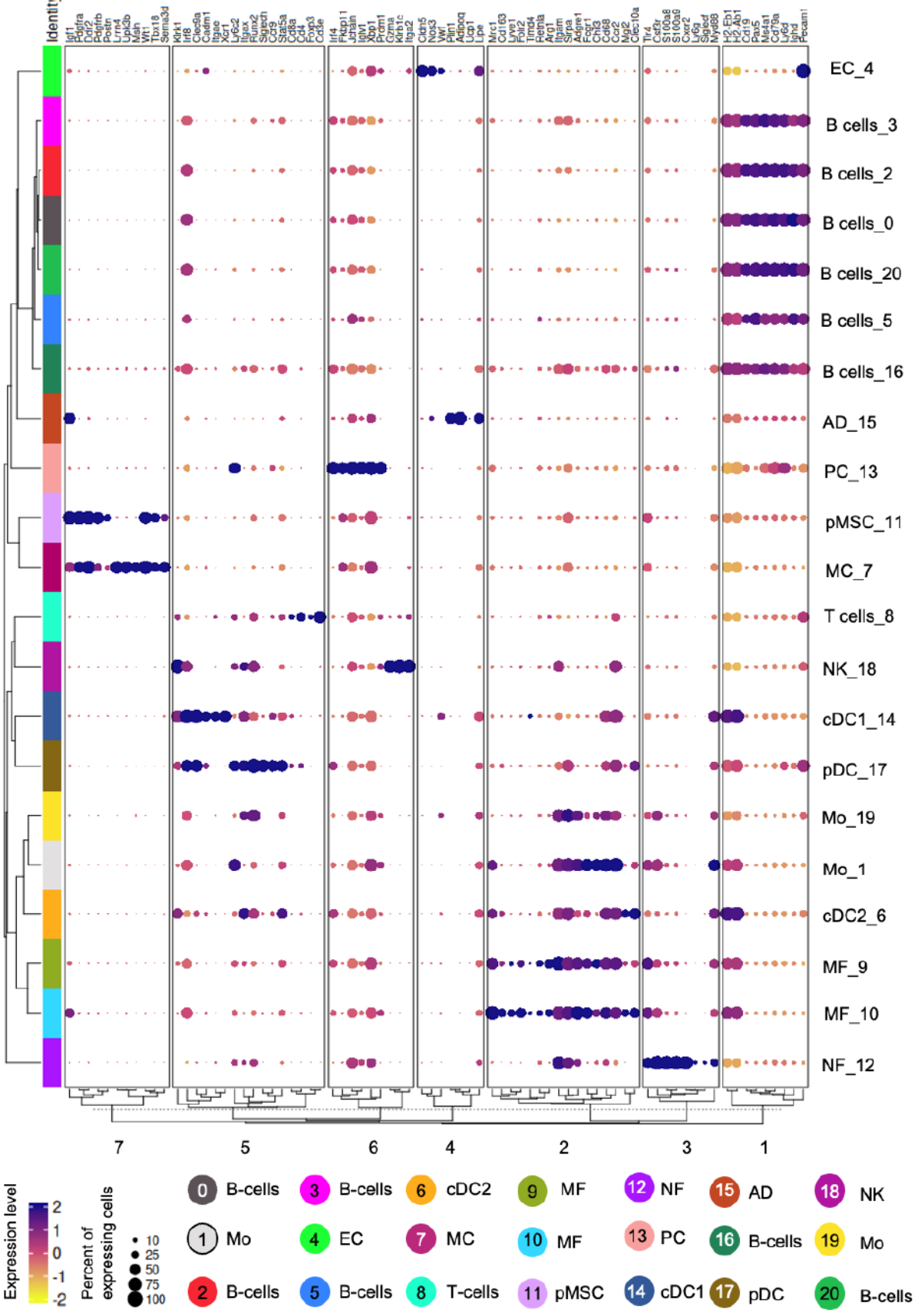
Identity
EC_4
B cells_3
B cells_2
B cells_0
B cells_20
B cells_5
B cells_16
AD_15
PC_13
pMSC_11
MC_7
T cells_8
NK_18
cDC1_14
pDC_17
Mo_19
Mo_1
cDC2_6
MF_9
MF_10
NF_12
7
5
6
4
2
3
1
Expression level
2
1
0
-1
-2
Percent of expressing cells
10
25
50
75
100
0 B-cells
3 B-cells
6 cDC2
9 MF
12 NF
15 AD
18 NK
1 Mo
4 EC
7 MC
10 MF
13 PC
16 B-cells
19 Mo
2 B-cells
5 B-cells
8 T-cells
11 pMSC
14 cDC1
17 pDC
20 B-cells

Figure 41. Dot plot showing the expression of markers characterizing the pericardial cell clusters.

Mo – monocytes, EC – endothelial cells, cDC1 (2) – conventional dendritic cells type 1 or 2, pDC – plasmacytoid dendritic cells, MC – mesothelial cells, MF – macrophages, pMSCs – mesenchymal, NF – neutrophils, PC – plasma cells, AD– adipocytes, NK – natural killer cells.

Additionally, the sc-RNA seq data also provided an insight into the relative proportion analysis of the pericardial cell clusters in response to the cardiac damage.

When the cells were analyzed separately for the basic, I/R injury, and sham condition, the UMAP plot showed a comparable pattern displaying all 21 clusters under all conditions. However, the plot also revealed quantitative difference occurring in some clusters. For example, neutrophils (NFs) were barely detected under basic conditions but increased substantially after I/R and apparently more after sham. Furthermore, macrophages (MFs) and monocytes (Mo) seemed to increase their proportions after I/R and profoundly more after sham. On the other hand, I/R was associated with the highest number of B-cells. The proportions of cell clusters were quantified, and data are represented in Figure 42B.

Under basic conditions B-cells constituted the largest population of the pericardial cells, where all the sub-clusters in total represented 41,4% of the entire cell number. On the other hand, T-cells amounted to 5,1%, plasma B-cells to 2,2%, and NK represented only 0,5%. Cells of the myeloid lineage occurred in smaller fractions under basic conditions and accounted for the following percentages: cDC2 - 8,5%, cDC1 – 2%, pDC – 0,5%, MFs - 6% (cluster 9 and 10), Mo (cluster 1) – 4,7% and NFs – 0,05% of the of the entire cell number.

Among non-immune cell populations endothelial (cluster 4) appeared as a predominant group with 15,9% of the total cell number, and adipocytes was the smallest cluster with 3,2%. The WT1-expressing cells of interest found in cluster 7 represented 6.5% and the cells of cluster 11 were only 2.9% of the total cell number.

Interestingly, both types of the cardiac damage implemented in the experimental set up induced a strong immune response within the pericardial tissue, which was, unexpectedly, different for I/R injury and sham, Figure 42.

As already visible in the UMAP plots, the pericardial cells of mice exposed to sham exhibited a preferential increase of myeloid cells on day 6 after the surgery. MFs (cluster 9, 10) reached 11,2%, Mo (cluster 1, 19) - 21,2%, cDC2 (cluster 6) – 6,1%, cDC1 (cluster 14) – 2,26%, pDC (cluster 17) – 1,17%. Moreover, sham surgery induced a pronounced infiltration of NFs (cluster 12) that increased their proportion up to 5.3%. There was also a minor change in WT1-expressing cells of cluster 11 that increased up to 3.7% and of cluster 7 – 6%.

I/R injury, on the other hand, induced rather activation of the lymphoid lineage cells, since B-cells increased significantly their proportion up to 62%, including all sub-clusters. T-cell did not exhibit a change 5,5%. This strong fractional increase of B-cells occurred along with a decrease of other pericardial cell clusters, such as PC population (cluster 13) was reduced to 1,12%, EC (cluster 4) to 2,8%, WT1-expressing cells of cluster 7 to 2,63% and cluster 11 to 1,67%, whereas adipocytes cluster nearly vanished and accounted only for 0,67% of all pericardial cells.

Importantly, that the proportion analysis does not give information on absolute quantitative analysis. The number of analyzed cells was set to 20,000 that included samples of all three conditions. A significant activation of immune cells, representing the most abundant population, might have substituted the minor groups of cells and concealed the changes upon I/R and sham.

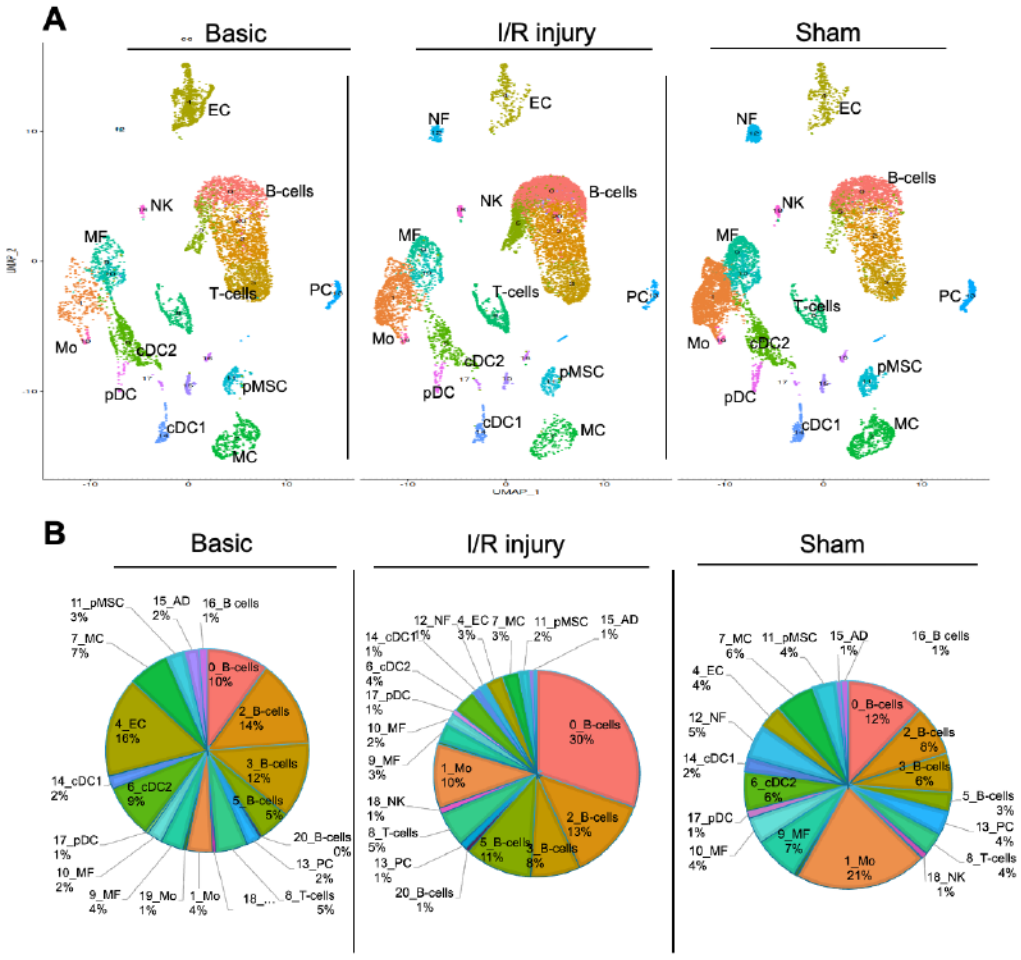

Figure 42. Proportions of the pericardial cell clusters under basic conditions, on day 6 after sham experiment and I/R surgery

Data is shown as a percentage of the total cell number. Mo–monocytes, EC–endothelial cells, cDC1 (2)–conventional dendritic cells type 1(2), pDC–plasmacytoid dendritic cells, MC–mesothelial cells, pMSC–mesenchymal cells, MF–macrophages, NF–neutrophils, PC–plasma cells, AD–adipocytes, NK –natural killer cells.

4.4.1. Adult murine pericardium contains two distinct populations of Wt1-expressing cells

Since Wt1-expressing cells are detected in the parietal pericardium already under basic conditions (Figure 18, Figure 20,Figure 25) and their activation upon the cardiac injury (Figure 27, Figure 30), the sc-RNA seq data was analyzed in detail to obtain a deeper insight into their functions. As it is shown in Figure 43, the majority of cells residing in clusters 7 and 11 express *Wt1* under basic conditions as well as on day 6 after sham and I/R injury. In cluster 11 under basic conditions, 66.36% of all cells expressed *Wt1*, whereas after sham and I/R the proportion increased up to 83.29% and 80%, respectively, with the average expression of 1.25, adjusted p-value 0. In cluster 7, 96.19% ±1.61 of cells expressed *Wt1* under each condition (average expression 2.73, adjusted p-value 0).

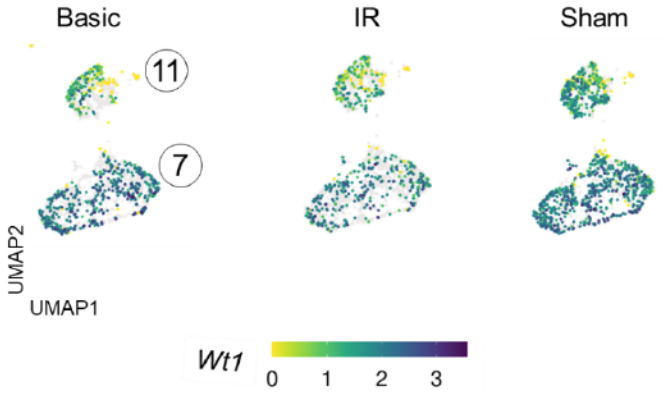

Figure 43. Parietal pericardium of adult mice contains two separate clusters of *Wt1*-expressing cells.

UMAP obtained from sc-RNA seq data, which shows distribution of Wt1-expressing cells in clusters 7 and 11 under basic conditions, on day 6 after sham and I/R injuries. Yellow-green-purple color-coding reflects expression level of *Wt1*.

On the basis of histological analysis, which showed that pericardial cells express the mesothelial cells marker Upk1b (Figure 17), foremost the canonical markers characterizing mesothelial and epithelial phenotypes were analyzed. As it is represented in Figure 44, the cells residing in cluster 7 displayed the mesothelial cell characteristics since they expressed *Upk3b* (uroplakin 3b), *Lrrn4* (leucine-rich repeat neuronal 4), glycoproteins *Msln* (mesothelin), *Muc16* (*mucin 16) and Pdpn* (podoplanin)[182-186] as well as *Krt19* (keratin-19) encoding intermediate filament protein of epithelial cells[187]. These genes are primary mesothelial cell markers, which play a critical role in maintaining the layer integrity and stabilizing mesothelial/epithelial cells[168-171].

On the one hand, the cells of cluster 11 expressed fibroblasts-associated markers such as *Postn* (periostin), *Fap* (fibroblast activation protein alpha)[209,210] *, Pdgfra*[188-191] (platelet-derived growth factor receptor A) and *Ddr2*[188,202-208] (discoidin domain receptor 2), *Dpt* (dermatoponin), *Pi16*[192-197] (peptidase inhibitor 16) and *Prrx1* (paired related homeobox 1).

Furthermore, under basic conditions, the cells of cluster 11 displayed expression of markers related to the metabolism and transport of lipids as well as adipocyte differentiation *Ebf2* (early B cell factor 2)[198], *Lpl*[199] (lipoprotein lipase)*, Apod*[200] (apolipoprotein D), *Cebpd*[201] (CCAAT/enhancer binding protein delta).

Interestingly, the cells of both clusters expressed a set of genes, which are known for their high expression during embryogenesis and contribution to cell proliferation, differentiation and vasculogenesis, thereby representing an essential part of the heart development. Among them were *Aldh1a1* (aldehyde dehydrogenase)[202-205], *Sema3d* (semaphorin class III)[206-209]*, Gata6* (*GATA binding protein 6)*[210-213] as well as progenitor marker genes *Cd34, Isl1* (Islet-1) and *Hand2* (heart and neural crest derivatives expressed 2)[173,180-183].

Thus, the first insight demonstrated that the cells of cluster 7 and 11 possess different phenotypes. Whereas the cells of cluster 7 correspond to a mesothelial phenotype and are engaged in structural integrity alongside lubrication, the cells of cluster 11 demonstrate fibroblast as well as pre-adipocytes characteristics, what might be referred to mesenchymal phenotype. In addition to the distinguishing characteristics, both subsets shared progenitor cell markers, and genes associated with tissue development, which suggests that the cells of cluster7 as well as 11 may have the potential to contribute to other cell lineages.

Figure 44. Two distinct subsets of Wt1-expressing cells in parietal pericardium of adult mice.

[A] Dot plot based on log2FC (fold change) in gene expression level between mesothelial cells (MC) residing in cluster 7 and pericardial mesenchymal cells (pMSCs), detected in cluster 11. Group of genes (1) represents mesothelial cell markers, (2) – genes involved in developmental program; (3) represents the markers of mesenchymal and fibroblasts-like cells, (4) signature of potential involvement in adipogenesis. [B] Corresponding values of log2FC in gene expression level between MCs and pMSCs. Proportion of cells expressing the gene of interest is represented as a percentage (pct) of all MCs or pMSC residing in cluster 7 and cluster 11, respectively.

A

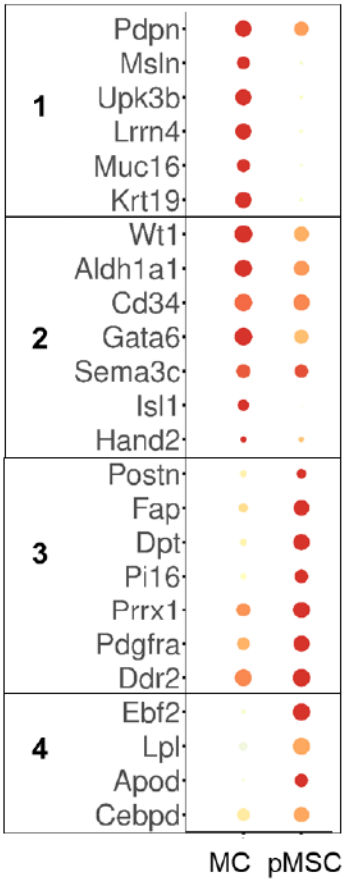

B

gene	avg_log2FC	pct in MC	pct in pMSC	p_val	p_val_adj
Pdpn	1.3119	89	73.1	7.87597E-85	2.0118E-80
Msln	4.6833	57.4	2.2	2.2882E-137	5.845E-133
Upk3b	5.4182	76.7	3.3	6.4995E-212	1.66E-207
Lrrn4	4.8096	81	2.8	1.4358E-233	3.668E-229
Muc16	5.2380	49.6	1	1.1374E-114	2.905E-110
Krt19	4.9517	74.4	3.1	2.4131E-202	6.164E-198
Wt1	1.4624	96.6	77.9	1.1631E-141	2.971E-137
Aldh1a1	1.0406	90.7	77.2	1.91281E-55	4.8861E-51
Cd34	0.3468	94.9	89.1	1.2569E-15	3.2106E-11
Gata6	1.4555	94.7	74	1.0639E-137	2.718E-133
Sema3c	0.4672	68.7	48.8	6.36381E-25	1.6256E-20
Isl1	2.0109	28	0.6	7.7888E-56	1.9896E-51
Hand2	0.6427	15.6	9.8	1.98864E-05	0.50797786
Postn	-2.7066	12.3	29	9.71376E-26	2.4813E-21
Fap	-1.8460	24.1	71.4	5.0583E-110	1.292E-105
Dpt	-4.3164	15.4	91	0	0
Pi16	-4.1141	14.4	60.2	6.9209E-129	1.768E-124
Prrx1	-1.1267	71.2	93.6	1.45178E-90	3.7084E-86
Pdgfra	-1.0557	60	88.8	1.12254E-86	2.8674E-82
Ddr2	-1.2558	90.6	94.9	8.26E-100	2.1099E-95
Ebf2	-5.6803	5.2	91.9	0	0
Lpl	-3.8652	26.2	91.2	4.4114E-260	1.127E-255
Apod	-4.4067	1	42	1.8388E-140	4.697E-136
Cebpd	-0.9468	58.5	78	3.42469E-32	8.748E-28

To complement this characteristic with more objective approach, a set of differentially expressed genes (DEGs) between clusters 7 and 11 was analyzed using IPA software (Ingenuity Pathway Analysis, Quagen). The application matches the sc-RNA-seq analysis data, used as an input, against publicly available studies allowing exploring, interpreting and visualizing various biological processes. Figure 45 represents 581 genes, which were upregulated in cluster 7 (red marking), and 605 genes, which were downregulated (blue marking). Since the DEGs that were used as an input are derived from a comparison of cluster 7 and 11, the genes upregulated in 7 correspond to the genes with low expression in cluster 11. Vice versa, the genes “downregulated” in cluster 7 are expressed at the highest level in cluster 11. For an initial overview of the genes with the strongest difference in expression level, the plot contains manually highlighted genes with expression log2 ratio <-4.0 and >4.0 and False discovery fate (FDR) or q-value -log10 above 100.

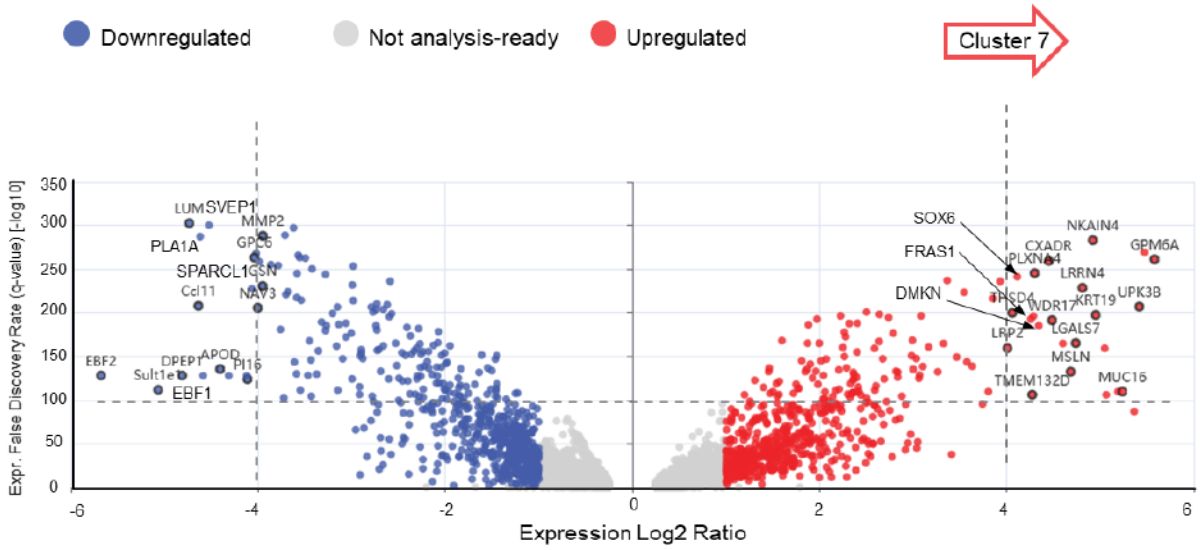

Figure 45. Two distinct subsets of Wt1-expressing cells in parietal pericardium (IPA analysis).

Differentially expressed genes (DEGs) between cluster 7 and 11 analyzed in QIAGEN Ingenuity Pathway Analysis (IPA). Upregulated expression of genes refers to cluster 7 (red), blue refers to the genes downregulated in cluster 7 and, therefore, characterize cluster 11. Y-axis: expression false discovery rate (q-value) transformed via –log10 function (threshold 0.05). X-axis: Expression Log2 Ratio with cutoff <-1.0 and >1.0. q-value was obtained using Benjamini-Hochberg (BH) method. As an initial overview of the genes with the strongest expression level difference, the manual labeling of single genes was based on the Expr.Log2 Ratio 4> and <-4 and expr. False Discovery Rate (q-value) [-log10] cutoff of is 100.

In addition to already described canonical markers for mesothelial cells, the analysis revealed that the cells of cluster 7 expressed to a high extent *Nkain4* (sodium/potassium transporting ATPase interacting 4), which was reported as an alveolar and small airway epithelial cells marker[178]. Furthermore, there was a set of highly upregulated genes, involved in vasculogenesis and cell differentiation (*Plxn4*; plexin)[214,215]; *Sox6*[216] (SRY-box transcription factor 6), *Gpm6a*[217] (glycoprotein M6A), *Dmnk*[218] (dermokine) and *Lrp2*[219] (low density lipoprotein-related protein 2). Finally, mesothelial cells were involved in ECM organization as well as cell-cell and cell-matrix interactions *Thsd4*[220] (thrombospondin type 1 domain containing 4), *Fras1*[221] (fraser subunit 1), *Lgals7*[222] (galectin 7) and *Cxadr*[223] (coxsackie and adenovirus receptor).

The genes characteristic for cluster 11 (blue marking) were reported to be expressed in fibroblasts, involved into actin filaments organization, control of cell adhesion and cell motility. Among them were *Dpep1*[187] (dipeptidase 1), *Sparcl1*[192] (SPARC-like protein 1), *Ccl11*[196] (C-C motif chemokine ligand 11), *Lum*[224] (lumican), *Gpc6*[225] (glypican 6), *Gsn*[226] (gelsolin), *Svep1*[227] (sushi, von Willebrand factor type A, EGF and pentraxin domain containing 1) and *Nav3*[228] (neuron navigator 3).

Furthermore, the cells of cluster 11 expressed genes, which contribute to lipid metabolic processes *Ebf1*[229] and *Ebf2*[230] (early B-cell factor), *Sult1e1*[231] (sulfotransferase family 1E, member 1), *Pla1a*[232] (phospholipase A1), *Apod*[233] (apolipoprotein D).

To confirm the observed phenotypical differences between clusters 7 and 11, DEGs displayed on the volcano plot were analyzed using the “Similar and dissimilar analyses” tool (IPA Interpret). DEGs were compared to >200 000 datasets obtained from public sources using QIAGEN OmicSoft Suite. Figure 46 displays top 100 datasets with the most significant similarities to the analyzed data (positive match z-score) and top 100 datasets that are most "anti-similar" (negative match z-score). Thus, the most significant matches revealed a high similarity of the cells in cluster 7 with epicardial (study GSE132658[234]; p-value 4.68E-25) and mesothelial cells (GSE129605[235]; p-value 1.02e-14). The detected anti-matches, on the other hand, suggested with high significance that the cells of cluster 11 have a phenotype akin to cardiac fibroblasts (TabulaSapiens; p value 1.69e-31) and mesenchymal stem cells (TabulaSapiens; p value 1.69e-15).

Conclusively, based on the gene expression profiles described in Figure 44, Figure 45 and Figure 46, the cells residing in cluster 7 are referred to as mesothelial cells (hereafter **MC**), and the cells of cluster 11 referred to as pericardial mesenchymal cells (hereafter **pMSC**).

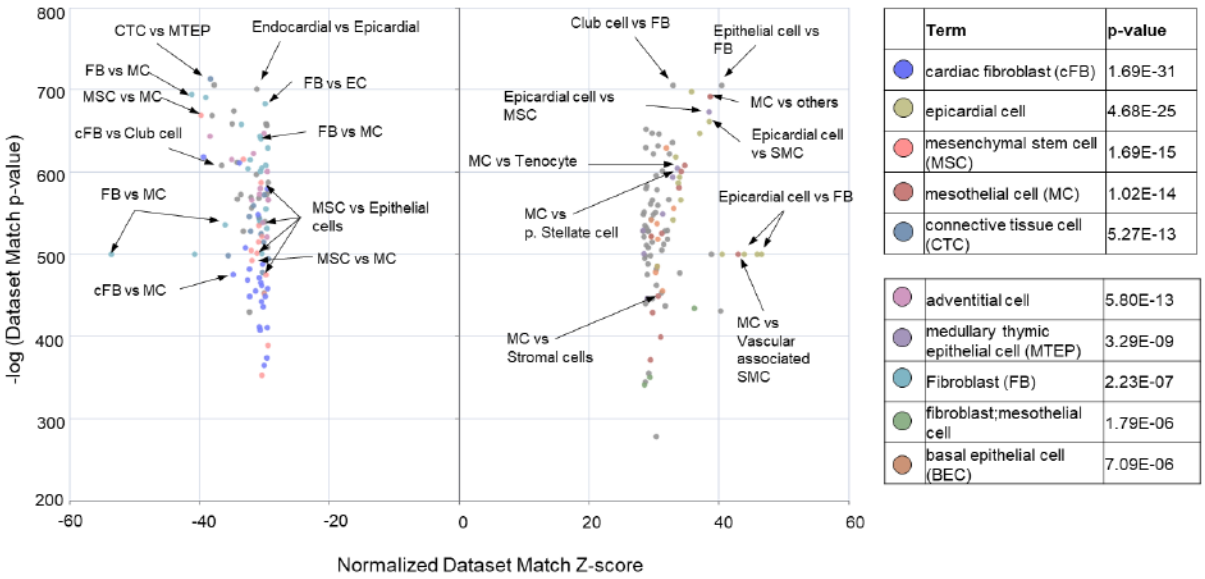

Figure 46. Annotation of WT1-expressing pericardial cells via IPA Interpret.

The plot obtained via “Similar and dissimilar analyses” tool (IPA Interpret), which compared DEGs between clusters 7 and 11 with the datasets from public sources using QIAGEN OmicSoft Suite. On the right side of the plot are top 100-curated datasets with significant similarities; on the left side are the top 100 that are most "anti-similar". Y-axis: p-value calculated with right-tailed Fisher's Exact Test; X-axis: z-score, which increases when direction of the gene expression matches most of the overlapping genes of the comparator dataset and negative score defines opposite direction in expression of the overlapping genes.

4.4.2. Signaling cascades related to the mesothelial and mesenchymal cells

According to the description of clusters 7 and 11 based on canonical markers (Figure 44) as well as DEGs processed in IPA (Figure 45), MCs and pMSC are, presumably, involved in a variety of signaling cascades influencing biological processes such as cell differentiation, vascularization, cell motility and eventually lipid metabolism. Therefore, in the next step, the DEGs were processed using IPA tool “Pathway Activity Analysis” detecting canonical pathways, which, according to the combination of highly upregulated and downregulated genes, might be activated in the analyzed cell clusters (Figure 47).

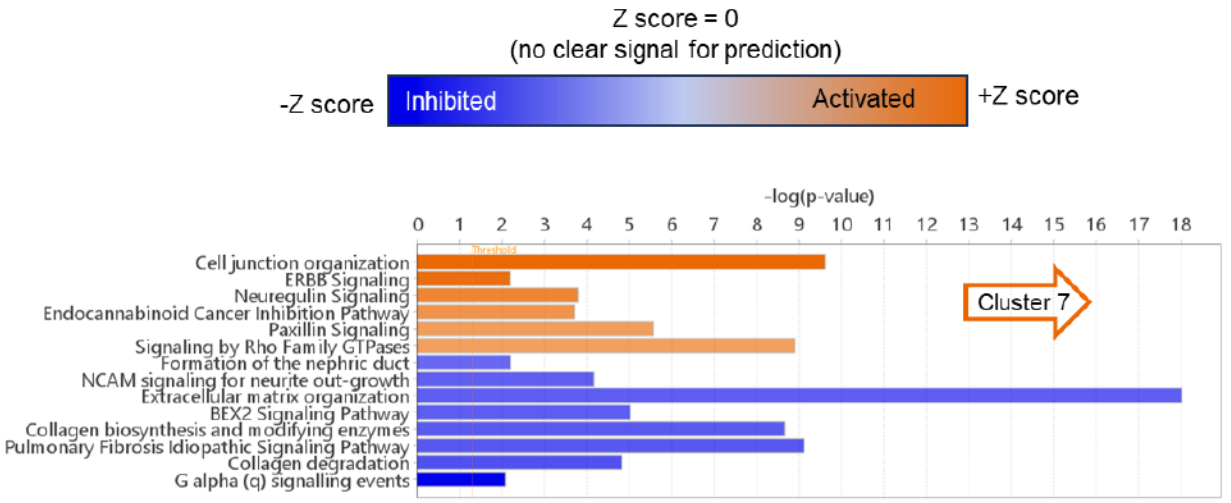

Figure 47. Signaling cascades associated with DEGs between cluster 7 (MCs) and 11 (pMSCs).

The plot is generated with the IPA tool “Pathway Activity Analysis”, which evaluates association of the differentially expressed genes (DEG) with canonical pathways. The plot is based on DAGs between cluster 7 (MCs) and 11 (pMSCs). The significance was calculated using the right-tailed Fisher's Exact Test (-log(p-value)>2.0) and prediction of inhibition or activation was based on a z-score algorithm (absolute value z-score >2.0). Orange color defines activation of a signaling cascade in MCs, whereas blue refers to a strong downregulation in MCs and thereby activation in pMSCs.

According to the detected signaling cascades, represented in Figure 47, MCs were involved in cell adhesion and cell junction organization processes although they might be also in a transitional state (Neuregulin, ErbB[236], Cell junctions organization, Paxillin[237] and Rho Family GTPases[238]). The detected cascades were mainly associated with the upregulated genes characteristic for basal and apical polarity *(Cdh11, Cd151, Cldn15, Cldn10, Parvb, Pard6b, Patj),* cell-ECM interactions *(Itga3, Itgb4, Cdh11, Ezr)*[239] and a transitional state of cells or MMT *(Pak3, Erbb4, Btc, Tgfa , Nck2)*[240-243].

The tool also revealed Endocannabinoid Cancer Inhibition Pathway, which is primarily characterized by inhibition of cell proliferation and arrest of the cell cycle[244] (*Ccnd1, Mapk10, Adcy9, Smpd3*)[245,246].

Simultaneously, the chart displays the pathways, which were significantly downregulated in MCs (cluster 7) and, thereby, characterize pMSCs (cluster 11). In comparison to MCs, pMSCs were in a motile state and involved in differentiation process. The signaling cascades NCAM signaling for neurite outgrowth[247] and ECM organization were based on high expression of ECM components and genes responsible for cell adhesion (*Plcb1, Tnxb , Lamc1, Lama2 , Aspn, Vtn, Pcdh19 , Ednra , Acvr2a*)[248-254]. The signaling cascades IPF Signaling[255] (Idiopathic Pulmonary Fibrosis), BEX2[256], G alpha (q)[257,258] signaling and formation of the nephric duct[259], correlated with genes involved in cell differentiation (*Ngf, Vegfd, Pdgfrb, Notch1 , Notch3, Fzd4, Plcb4, Chrm3 , Lpar1, Cacna1c, Prnp, Gng11, Grk5)* [260-266].

Collectively, the analyses showed that Wt1-expressing cells of the adult murine pericardium could be classified into two distinct subsets: mesothelial cells (MC) and mesenchymal stem cells (pMSCs). MCs of cluster 7 were defined by the MCs specific gene signatures and developed lateral cell interactions. In addition, the pathways associated with actin cytoskeleton reorganization that might indicate a transitional state. On the other hand, pMSCs demonstrated motile phenotype and active phase of differentiation process, potentially towards fibroblast-like cells due to expression of a range of genes characteristic for fibroblasts, Figure 48.

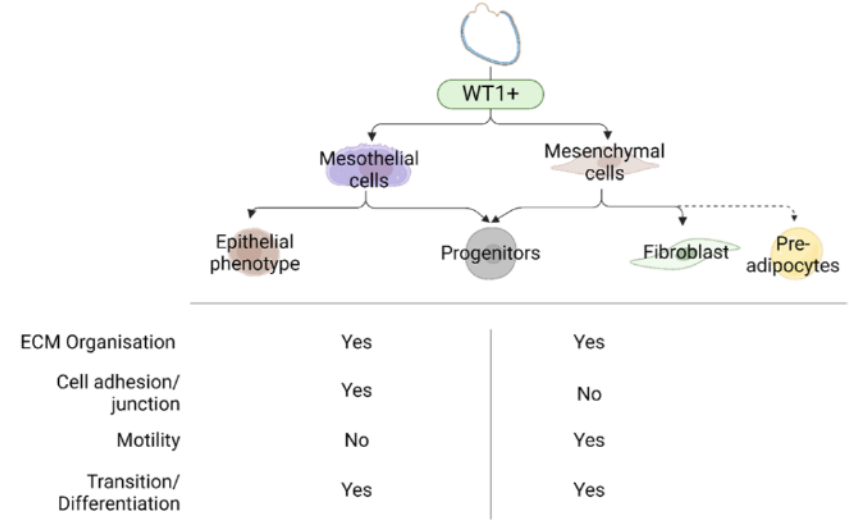

Figure 48. Classification of WT1- expressing cells of adult murine pericardium.

The scheme is created with Biorender.com and is based on the findings described in the chapter 4.4.1 and 4.4.2. Dotted lines indicate potential annotation based on gene expression profiles (Figure 44, Figure 45).

4.4.3. Wt1-expressing cells display upregulation of genes involved in proliferation, migration and differentiation in response to I/R

In the next step, the determined Wt1-expressing cell subsets MCs and pMSCs were analyzed under pathological conditions. Since sc-RNA seq analysis included I/R and sham surgeries, DEGs obtained from the comparison of basic conditions, sham and I/R in clusters 7 (MCs) and 11 (pMSCs), were identified and represented in Figure 49 and Figure 50 for MCs as well as Figure 51 for pMSCs, respectively.

Thus, according to the analysis, MCs were activated already after sham injury in comparison to the basic conditions. The majority of the upregulated genes in sham was the same as in response to I/R. Among them were genes associated with tissue damage and pro-survival mechanisms (*Clu, Lcn2, Mt1, Cfb*)[267-270] including IFN-γ induced molecules *(Ifi27l2, Bst2, Isg15, Irf7)*[271-274]. Furthermore, both injuries induced upregulation of genes contributing to cell migration (*Chl1, Serpinh1, Ctsl, Cdh2, Actg1, Tpm4, Sparc)*[274-277], alongside a range of genes encoding ECM re-organization components, that presumably contribute to remodeling process as well as they may facilitate migration process (*Loxl2*[278], *Saa3*[279], *Slit3*[280] *Adamts2, Col1a1, Col3a1, Col4a1, Col5a3, Col6a1, Col6a5, Timp1, Timp3*).

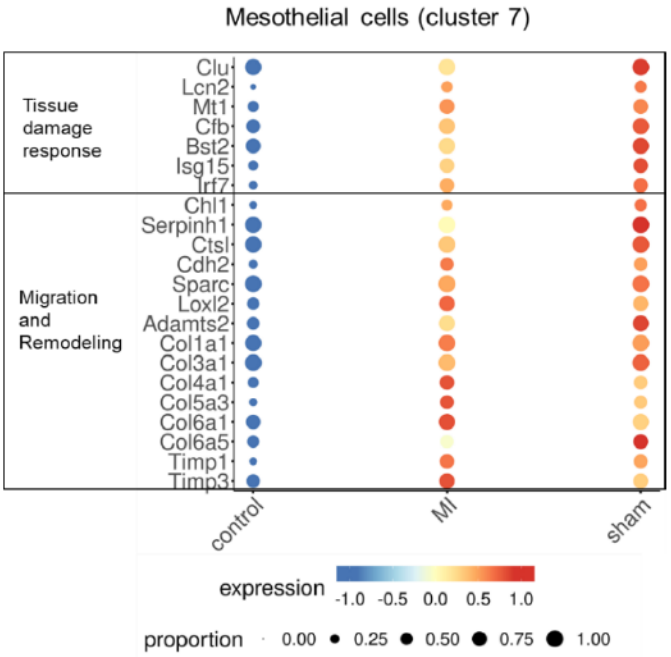

Figure 49. Differentially expressed genes compared in pericardial mesothelial cells between basic conditions, sham and I/R (continues on Figure 50).

Dot plot, obtained from sc-RNA seq data, shows the expression level of various genes in mesothelial cells that is represented as log2FC (fold change) obtained from comparison of basic conditions, day 6 after sham and I/R and is coded by the color. The size of dots corresponds to the proportion of cells that express the

Furthermore, in response to the injuries there was a range of upregulated genes that are involved in processes such as proliferation, cellular transition, MMT, and eventually differentiation. Interestingly, the analysis showed a group of genes that were highly expressed after both injuries, sham and I/R. Among them were *Ly6a, Rhoj, Mgp, Dmkn, Basp1, Dynll1, Gas7, Actn1, Pfn1, Plac8, Prg4*[218,281-291]. However, there was also a group of genes that was upregulated specifically after I/R: *Tmsb4x, Tmsb10 , Tacc2, Rbm3, Actg1, Gpr39, Tpm4, Hnrnpd*) [292-299].

Interestingly, in mesothelial cells sham induced significant upregulation of the genes associated with endoplasmic reticulum stress (*Manf, Herpud1, Creld2, Hspa5, Hspa8 Hspb1 Hsp90b1, Dnajc3, Dnajb9)*[300-308].

Also pMSCs responded to the tissue injury. Surprisingly, after sham but not I/R, there was an upregulation of genes characteristic for tissue damage response (*Clu, Lcn2, Hif1a, Hspa5, Il33).*

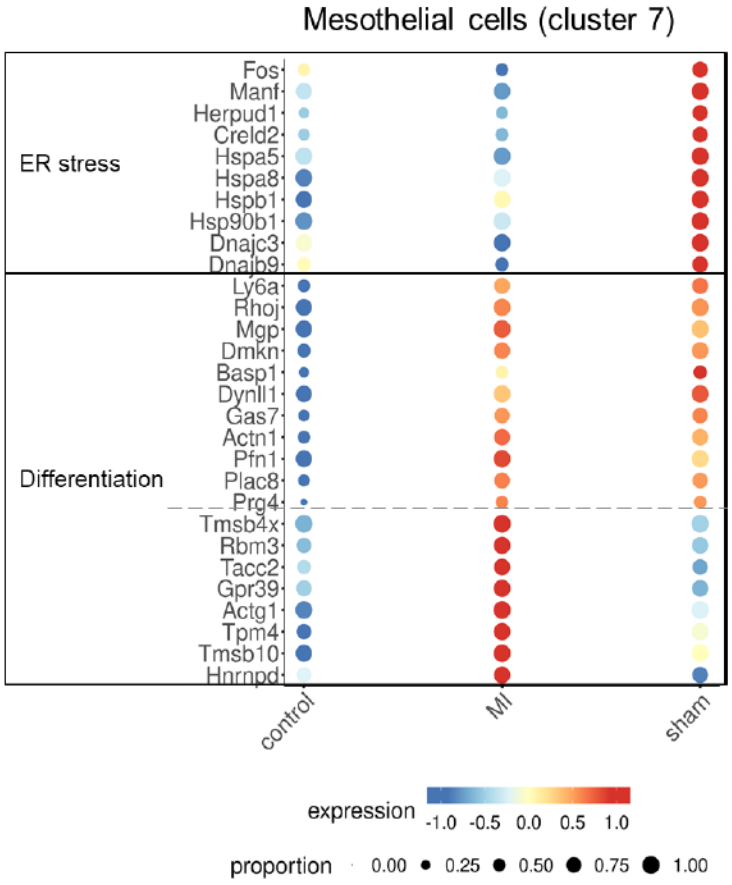

Figure 50. Differentially expressed genes compared in pericardial mesothelial cells between basic conditions, sham and I/R.

Dot plot, obtained from sc-RNA seq data, shows the expression level of various genes in mesothelial cells that is represented as log2FC (fold change) obtained from comparison of basic conditions, day 6 after sham and I/R and is coded by the color. The size of dots corresponds to the proportion of cells that express the given gene.

On the other hand, after I/R increased expression of *Lsp1,* known as an intracellular filamentous-actin binding protein that can modulate cell motility and often associated with immune cells infiltration [267,268,309-312].

Moreover, there was a higher expression of ECM associated genes *Col1a1, Col3a1, Mfap2, Mfap4, Adamts15, Chl1* that contribute to the tissue structure and potential wound healing, for example, via binding to TGF-β superfamily members, or other biological processes such as cell migration, proliferation and signal transduction[313-318].

Finally, the plot displays a set of genes related to differentiation process. Although all the listed genes are associated with cell transition process, there were genes that were upregulated rather in response to I/R (*Bach2, Sfrp2, Runx1, Aff3, Actg1, Mbnl1, Ripor2*)[319-325], whereas others exhibited higher expression level in sham (*Pdzrn3, Pabpc1, Gda, Ppic, Wnt4, Tgfb2, Mgp, Gem, Auts2, Enpp2*)[283,326-334].

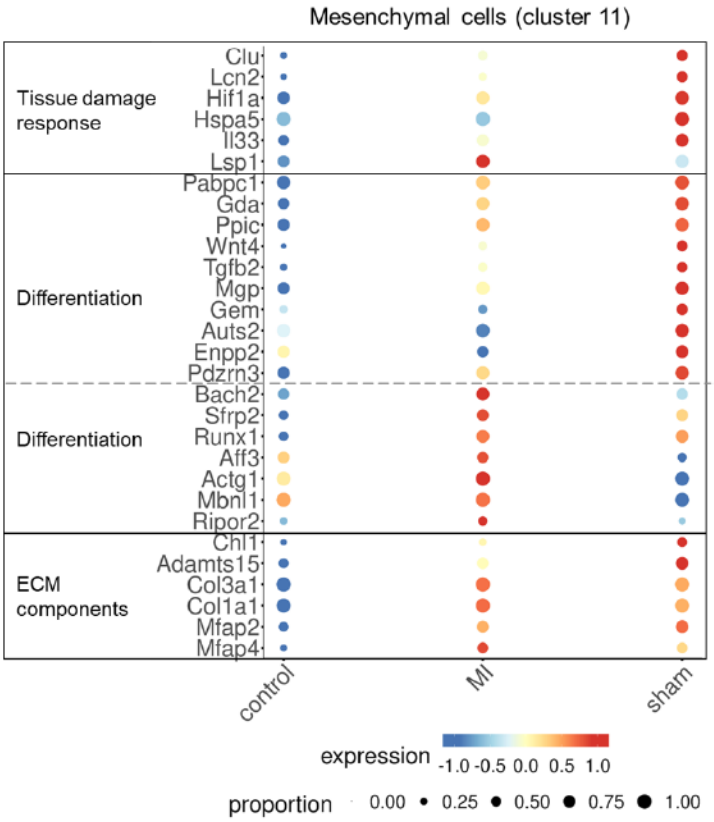

Figure 51. Differentially expressed genes between basic conditions, sham and I/R in mesenchymal cells.

Dot plot shows the expression level of genes in mesenchymal cells that is represented as log2FC (fold change) obtained from comparison of basic conditions, day 6 after sham and I/R. The size of dots corresponds to the proportion of cells that express the given gene.

Collectively, DEGs analysis showed that MCs and pMSCs exhibit a change in the gene expression pattern after sham and I/R. For example, in both clusters there are upregulated genes, associated with a tissue damage response. Moreover, there might be a change related to a transient state of cells because the analysis revealed upregulated genes associated with cell differentiation process. Finally, both clusters exhibited a pronounced expression of ECM components as well as the genes related to cell adhesion and cell motility. This might suggest a potential involvement in tissue remodeling process and cell migration.

4.4.4. WT1-expressing pericardial cells undergo mesothelial-to-mesenchymal transition under basic conditions and after I/R

Analysis of differentially expressed genes and canonical pathways demonstrated that MCs, as well as pMSCs, were involved in signaling cascades associated with a cellular transient state, change in cell shape, differentiation, and migration (Figure 44, Figure 47, Figure 49-Figure 51). The key mechanism that drives this phenotypic change in mesothelial cells is mesothelial-to-mesenchymal transition (MMT). Therefore, to detect possible signatures of MMT in pericardial Wt1-expressing cells, the genes corresponding to each step that comprise MMT (description in the chapter 1.1.1.3) were analyzed in sc-RNA seq data and represented in Figure 52.

The first step of MMT is an expression of master regulators, which induce the subsequent transitional state of cells. Surprisingly, both clusters expressed the key drivers of the process already under basic conditions. In MCs, the analysis detected transcription factors *Zeb1 and Zeb2* (zinc finger E-box binding homeobox 1/2) and to a minor extent *Twist2* (twist basic helix-loop-helix transcription factor 1/2). pMSCs, on the other hand, expressed even a broader range of regulators including *Snai1, Snai2* (snail family transcriptional repressor 1/2), *Zeb1, Zeb2, Twist1* as well as *Twist2*[335,336]. The finding indicates that the pericardial cells of adult murine pericardium express the genes involved in MMT already under basic conditions.

On day 6 after I/R, most of the transcription markers in MCs and pMSCs were downregulated, except for a small portion of MCs expressed *Snai1* and *Snai2*, suggesting that MMT at this point is terminated or subsides.

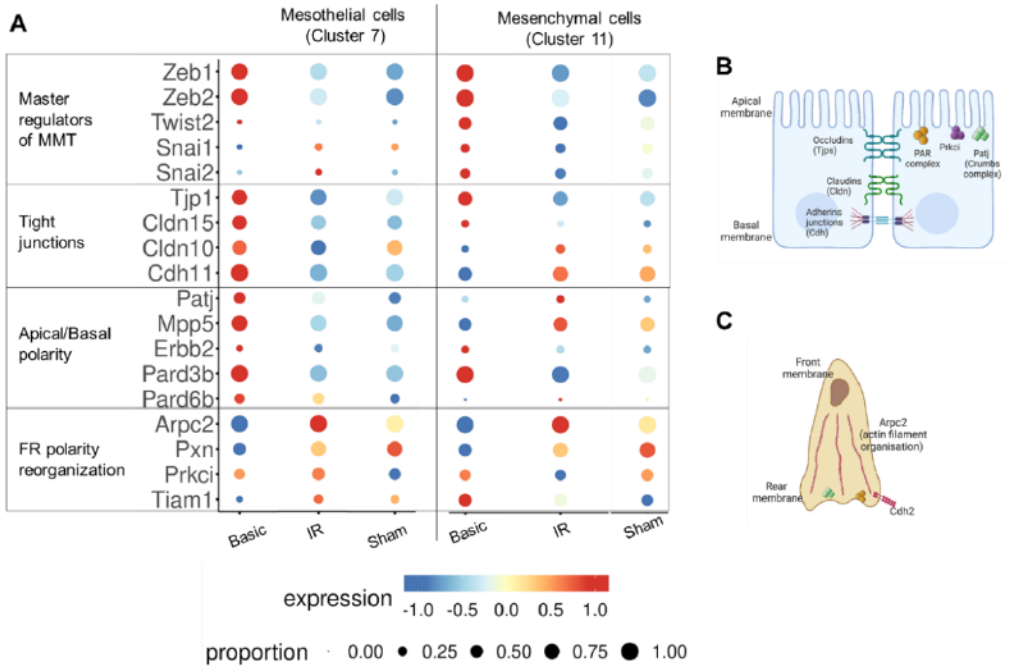

Figure 52. Wt1-expressing cells exhibit the gene expression pattern associated with mesothelial-to-mesenchymal transition.

[A] Dot plot based on log2FC (fold change) in gene expression level between basic conditions, day 6 after sham and I/R in mesothelial cells and mesenchymal cells. The listed genes are the hallmarks of mesothelial-to-mesenchymal transition (MMT) and characterize the major steps of the process. [B], [C] Schematic representation of mesothelial and mesenchymal phenotypes, respectively (Created using Biorender.com).

The next step of MMT is the disassembly of tight junctions between the neighboring cells and the detachment of the cells from the basal membrane, resulting in the downregulation of the corresponding genes. In MCs, under basic conditions, the genes encoding tight proteins *Tjp1* (or zonula occluden1) as well as claudins *Cldn11, Cldn15,* and *Cldn10*, were highly expressed, indicating that the cells exhibit lateral cell connection. On the contrary, pMSCs expressed only *Tjp1* and to a small extent, *Cldn15*, suggesting only a partial cell contact that might result from the transient state.

Along with the detachment from the membrane, the cells in transition lose apical/basal polarity and obtain front-rear polarity. Thus, MCs expressed marker genes encoding proteins, which stabilize apical and basal poles[336,337]. Among them were *Patj* (Pals1-associated tight junction), *Mpp5* (Pals1, protein associated with LIN7), *Pard3b* and *Pard6b* (par-3 family cell polarity regulator beta) and *Erbb2* (Erb-B2 Receptor Tyrosine Kinase 2).

In pMSCs, on the other hand, only *Erbb2* and *Pard3b* were present, and, additionally, pMSCs expressed *Tiam1* (T lymphoma invasion and metastasis), which upon association with a *Pard3/Prkci* (protein kinase C iota) complex, leads to stabilization of the front-rear cell polarization and facilitates cell migration[337]. This gene expression pattern suggests that in contrast to MCs, pMSCs are in a transient state already under basic conditions.

On day 6 after I/R, the majority of key transcription factors driving the process were primarily downregulated, what might indicate an absence or reduced MMT. In MCs, genes encoding cell contact proteins, as well as the apical/basal polarity indicators, were downregulated. Instead, MCs expressed *Prkci, Tiam1* and *Arpc2,* which participates in assembling actin filaments leading to the generation of membrane protrusions necessary for migration[44,338] and *Pxn* (Paxilin) and *Cdh2* (N-Cadherin) which are important for a connection of the cells with ECM allowing cells “to crawl” to their destination[336,339,340]. This might suggest that MCs acquired mesenchymal phenotype, whereas pMSCs still demonstrated a transient state expressing some of the genes characteristic for both phenotypes.

4.5. Analysis of potential interactions between pericardial cells.

To obtain a deeper insight into the activities revealed in pMSCs and MCs and to find key interactions with other pericardial cells, which might modulate these processes, cell-cell communication analysis (CellChat)[341] based on sc-RNA-seq data was performed. The tool predicts intercellular communications, indicating ligand-receptor pairs and their interaction probability, which in this analysis represents the interaction strength (the analysis workflow is described in chapter 3.10).

Figure 53 displays a general overview of detected interactions (A, D, G) accompanied by tables with the top 10 cell clusters exhibiting the highest number of interactions based on a source of ligands (B, E, H) and signal receivers serving as a target (C, F, I). Circle sizes are proportional to the number of cells in each cell group, and edge width (network lines) represents the number of potential interactions. In total, the analysis revealed 11.887 possible ligand-receptor pairs under basic conditions, 12.793 after sham, and 14.360 in response to I/R injury.

Interestingly, among all cell clusters serving as a source of ligands, MCs and pMSCs appeared to have the highest number of potential interactions under basic conditions, on day 6 after sham as well as I/R injuries (Figure 53 B, E, H). Moreover, in both clusters, the program detected predominant number of interactions based on receiving signals, where MCs and pMSCs serve as targets for ligands derived from other cells (Figure 53 C, F, I).

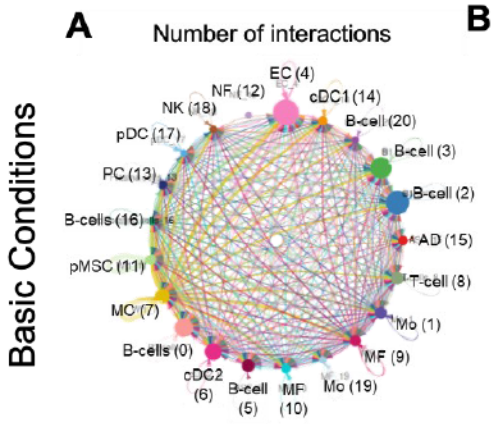

B

Source	Number of interactions
pMSC (11)	**1876**
MC (7)	**1798**
EC (4)	910
MF (9)	708
Mo (1)	616
B cells (16)	581
cDC2 (6)	526
B cells (2)	507
MF (10)	467
B cells (3)	442

C

Target	Number of interactions
MC (7)	**922**
MF (9)	902
pMSC (11)	**901**
cDC1 (14)	724
pDC (17)	723
NK (18)	722
cDC2 (6)	702
B cells (16)	671
EC (4)	671
MF (10)	617

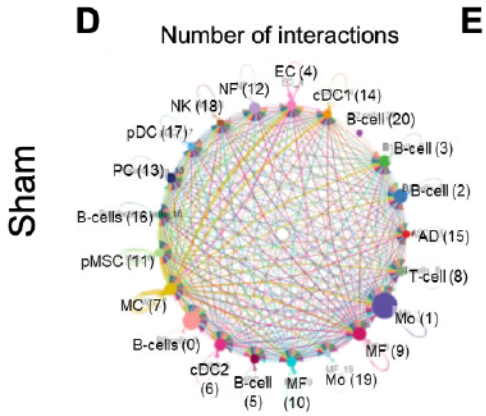

E

Source	Number of interactions
MC (7)	**2041**
pMSC (11)	**2035**
EC (4)	1116
MF (9)	772
MF (10)	728
Mo (1)	698
B cells (16)	522
cDC2 (6)	484
Mo (19)	473
B cells (3)	448

F

Target	Number of interactions
MC (7)	**1349**
pMSC (11)	**1018**
MF (9)	834
EC (4)	824
Mo (1)	800
cDC1 (14)	770
NK (18)	741
cDC2 (6)	728
MF (10)	723
B cells (16)	640

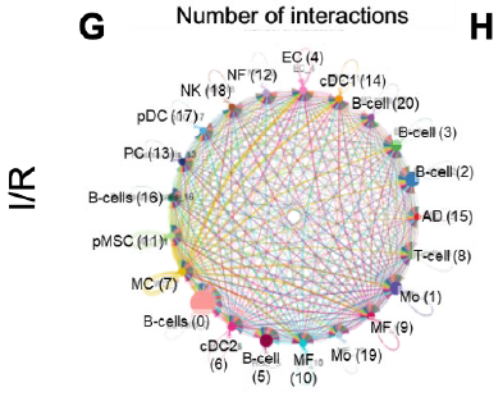

H

Source	Number of interactions
pMSC (11)	**2381**
MC (7)	**2174**
EC (4)	1207
MF (9)	873
MF (10)	831
Mo (1)	757
cDC2 (6)	616
cDC1 (14)	544
B cells (16)	512
Mo (19)	504

I

Target	Number of interactions
MC (7)	**1302**
pMSC (11)	**1021**
EC (4)	919
MF (9)	850
cDC1 (14)	823
MF (10)	791
Mo (1)	788
cDC2 (6)	722
Mo (19)	632
NK (18)	586

Figure 53. Predicted interaction network among pericardial cells under basic conditions, on day 6 after sham and I/R injury.

The interactions were predicted with CellChat tool, using sc-RNA seq data, the workflow is described in chapter 3.10. Circle plots reflect an overview of ligand-receptor interactions between pericardial cell clusters under basic conditions [A] on day 6 after sham [D] and I/R [G]. Circle sizes are proportional to the number of cells in each cluster and edge width represents the number of potential interactions. Next to each cluster a corresponding cluster number is displayed. [B, E, H] Top 10 cell clusters with the highest number of potential interactions based on the released ligands (source). [C, F, I] Top 10 cell clusters with the highest number of interactions. In the tables the clusters of interest, MC and pMSC, are manually highlighted.

4.6. Intercellular communication of mesothelial and mesenchymal cells.

Since MCs and pMSCs appeared to have the highest number of interactions, in the next step of the analysis, the cell clusters that communicated with both subsets were identified. Since the CellChat tool detected more than 12.000 interactions related to MCs and pMSCs, the analysis was narrowed down to the strongest interactions. Thus, the ligand-receptor pairs were sorted according to the interaction strength/probability and divided into three quartiles. Then, the 50 strongest interactions of the top quartile were selected and represented as network plots under basic conditions, on day 6 after sham and I/R (Figure 54).

Foremost, Figure 54 suggests that the networks of MCs and pMSCs include similar clusters. Next, the plots show that the majority of the signals were released by MCs or pMSCs to other cells, whereas only a few interactions were directed to them.

Furthermore, CellChat detected several clusters that were present in the network under all three conditions. Also altered interactions were detected, i.e., clusters that appeared in or disappeared from the network in response to the injuries. Among the preserved clusters that received signals from MCs and pMSCs were endothelial cells (cluster 4), macrophages (clusters 9 and 10), natural killer cells (cluster 18), monocytes (clusters 1 and 19). In addition, a strong autocrine loop was detected for MCs (cluster 7).

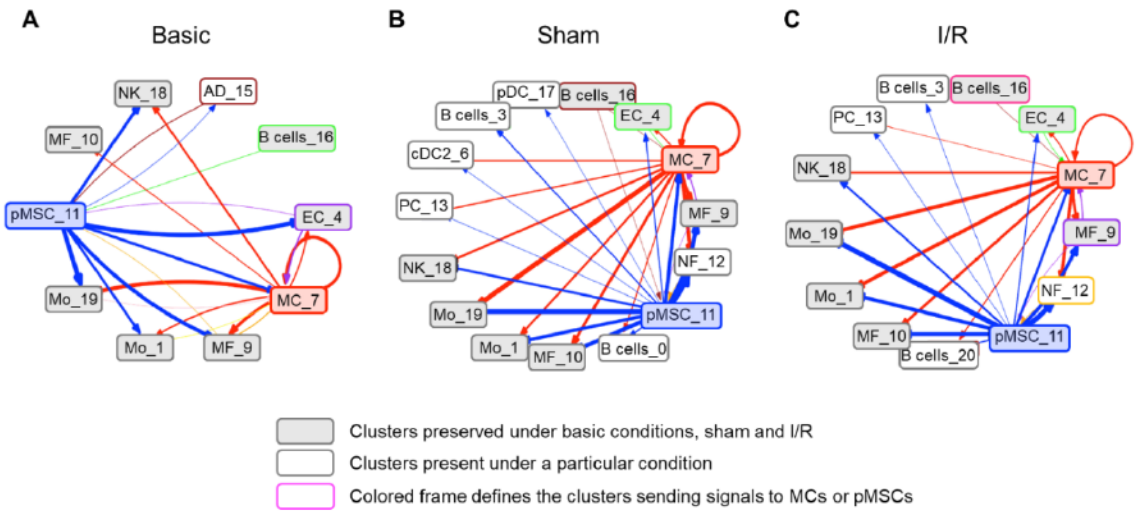

Figure 54. Potential cell-cell communication detected in pericardial mesothelial and mesenchymal cells.

The 50 strongest interactions involving mesothelial (MC) and mesenchymal (pMSC) were selected and presented as network plots for basic conditions [A], 6 days after sham [B], and I/R [C]. Edge width corresponds to the interaction number. EC–endothelial cells, MF–macrophages, NK–natural killer cells, Mo –monocytes, PC–plasma cells, cDC2–conventional dendritic cells type 2, pDC–plasmacytoid dendritic cells, NF–neutrophils, AD–adipocytes. Cluster names contain a corresponding cluster number. Plots are based on the CellChat analysis (description in chapter 3.10) and were generated with CCPlotR R package (Sarah Ennis et al).

Besides qualitative aspects of the interactions, the communication between the clusters is represented by edges, whose thickness corresponds to the number of interactions between a given cluster pair. The plots revealed that under basic conditions (Figure 54A), in MCs as well as pMSCs the predominant number of interactions was related to monocytes of sub-cluster 19 (MCs initiated 7 interactions, pMSCs – 9). Interestingly, the edges show that the intensity of communication (number of interactions) with the sub-clusters of monocytes varied. Thus, monocytes residing in cluster 1 exhibited fewer interactions (MCs initiated 3 interactions; pMSCs – 4). Similar concerned the communication with the macrophage subsets. Whereas cluster 10 exhibited only one interaction with MCs, cluster 9 had five interactions with MCs and six interactions with pMSCs.

After sham surgery, the network of MCs and pMSCs expanded involving additional clusters: neutrophils, plasmacytoid and type 2 conventional dendritic cells (pDCs and cDC2, respectively), B cells of sub-clusters 3 and 0 as well as plasma B-cells (Figure 54B). On the other hand, in contrast to the basic conditions, adipocytes were not in the range of the strongest interactions. The width of the edges sent by MCs and pMSCs shows that the most pronounced communication was still directed to the monocytes of cluster 19 (6 interactions in MCs and in pMSCs). However, neutrophils also had a strong network with both subsets (5 interactions in MCs and 6 in pMSCs). Overall, the extended network related to myeloid as well as lymphoid lineage cells may imply that after sham there is an immune response that is modulated by MCs and pMSCs.

In contrast to sham, the number of clusters within the network of MCs and pMSCs decreased after I/R (Figure 54C). Specifically, B-cells of cluster 0, pDCs and cDC2 were not in the range of the strongest interactions. Instead, B-cells of cluster 20 were present in the network.

Similar to sham, the predominant communication of MCs and pMSCs was directed to monocytes (cluster 19) and neutrophils. Moreover, after I/R, monocytes of cluster 1 and macrophages of cluster 10 also exhibited an increased number of interactions: the monocytes had 5 interactions with MCs and pMSCs, while the macrophages had 4 interactions with MCs and 5 with pMSCs.

4.6.1. The strongest ligand-receptor pairs detected in MCs and pMSCs

The initial insight into potential communication of MCs and pMSCs with other cells showed that the clusters expand their network in response to sham and I/R and they profoundly interact with immune cells, particularly, with monocytes and macrophages. To characterize these interactions, in the next step, 20 ligand-receptor pairs with the highest interaction probability were selected from the presented network (Figure 54) and displayed in Figure 55.

Firstly, according to Figure 55, the types of ligands and receptors did not vary significantly between the analyzed conditions. However, there was an increase in the number of clusters, between which they interacted. Next, the plots reveal that the predominant communication with monocytes and macrophages identified above (Figure 54), included interactions of the complement-integrin systems that are crucial for proper functioning of immune cells, phagocytosis, actin remodeling, degranulation and cytokine production[342,343]. Thus, MCs and pMSCs released C3 ligand that interacted with the integrin receptor complex Itgam_Itgb2 (known as CR3 or CD11b and CD18, respectively), expressed by monocytes (cluster 19) and macrophages (cluster 9).

Furthermore, the interactions with the immune cells included ECM-associated components that mediate cell-cell and cell-ECM interactions (collagens interacting with cell-surface glycoprotein Cd44[344] as well as fibronectin Fn1 interacting with various integrin complexes[345]). Whereas these interactions were identified as part of a cell-cell communication network, their regulatory role remains elusive.

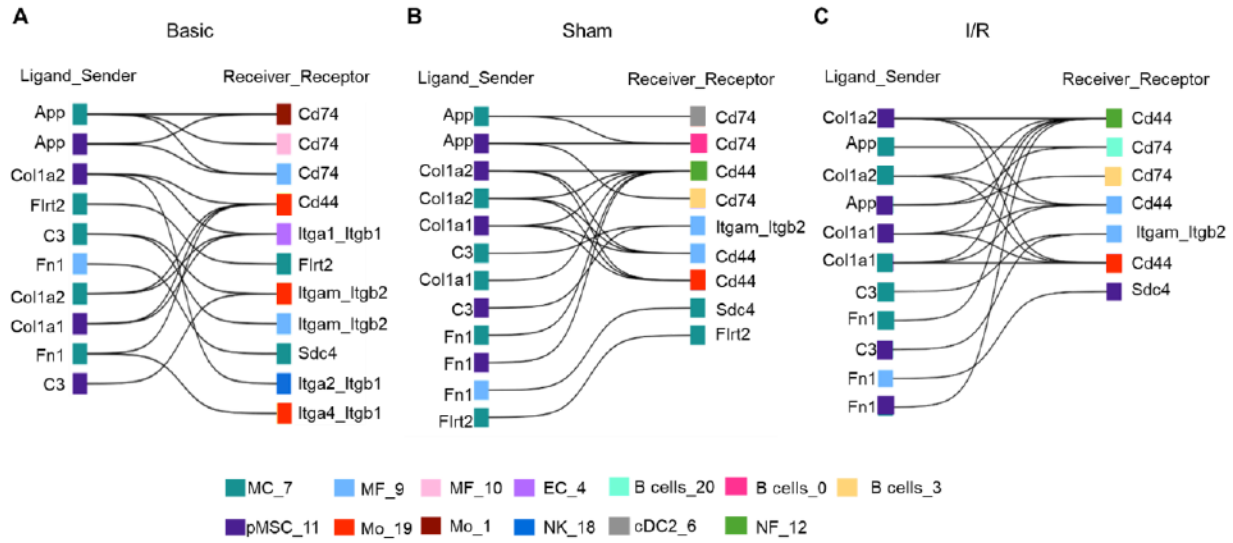

Figure 55. Strongest intercellular interactions detected in pericardial mesothelial and mesenchymal cells.

Ligand-receptor pairs with the strongest probability, related to mesothelial (MC) and mesenchymal (pMSC). The interactions were predicted by CellChat tool (description in chapter 3.10). The plots were generated with CCPlotR R package (Sarah Ennis et al). EC – endothelial cells, MF – macrophages, NK – natural killer cells, Mo – monocytes, cDC2 – conventional dendritic cells type 2, NF – neutrophils. Each cluster name contains a corresponding cluster number.

Additionally, CellChat detected App ligand (amyloid β precursor protein) released by MCs and pMSCs that could interact with Cd74 (major histocompatibility complex class II (MHCII) invariant chain) expressed by monocytes of cluster 1 and macrophages (clusters 9 and 10). Cd74 is known as MHC class II chaperone and it participates in non-MHC II protein trafficking[346]. It was reported that Cd74 binding inhibits App cleavage by β- and γ-secretase complexes and prevents production of amyloid-beta (Aβ) peptide that activates pro-inflammatory events, involving cytokine secretion and oxidative stress leading to vascular diseases[347-349].

Whereas MCs and pMSCs were origin of the ligand in most of the strongest interactions, MFs of cluster 9 appeared to interact with MCs via release of Fn1 possibly binding to Syndecan-4 (Sdc4). As shown in Figure 55, the interaction was also detected after sham, whereas after I/R, Fn1 released by MFs (cluster 9) appeared to target pMSCs. Sdc4 is a cell surface heparan sulfate proteoglycan that medicates cell interactions with ECM and is crucial for cell spreading, actin cytoskeleton organization and focal adhesion formation[350,351].

Finally, the profound autocrine interactions that were detected in MCs cluster (Figure 54) included the fibronectin leucine-rich repeat transmembrane protein, which formed a homophilic interaction Flrt2-Flrt2. As previously reported, Flrt2 plays an essential role in cell adhesion and basement membrane formation. It is strongly expressed in the pro-epicardium as well as the epicardium, while its loss results in abnormal epicardium disconnected from the heart[352,353].

4.6.2. Intercellular interactions specific for mesothelial and mesenchymal cells

The initial insight into the strongest interactions showed that MCs and pMSCs demonstrate many similarities, acting via the same ligand-receptor pairs and communicating with the same set of pericardial clusters. To find possible differences between MCs and pMSCs networks, the ligand-receptor pairs that were specifically related to MCs or pMSCs, were selected and displayed in Figure 56 and Figure 57, respectively. The following sub-chapters describe in detail the interactions detected in each cluster and their association with biological processes.

4.6.2.1. Ligand-receptor pairs detected in MCs

Firstly, according to Figure 56, the interactions specific for MCs were mainly either autocrine or were related to immune cell clusters. Figure 56A shows that the majority of the ligand-receptor pairs under basic conditions was involved in immunoregulation and support of cell homeostasis. To this category were related: apolipoprotein ApoE that interacted with Trem2 (triggering receptor expressed on myeloid cells 2) and the cytoplasmic adaptor for Trem2 – Tyrobp[354,355]; stem cell factor Kitl and tyrosine kinase receptor Kit[356]; Cd200 (type-1 cell membrane glycoprotein) and its receptor Cd200r1[357]; fibroblast growth factor 1 along with Fgfr1[358] and, finally, secreted glycoprotein Sema3c (semaphorin class 3 family) that interacted with nerophilin-plexin receptors Nrp1_PlxnA[359].

Interestingly, one of the predicted interactions targeted MCs. Monocytes of clusters 1 and 19, released Tgfb1 ligand that potentially interacted with MCs via activin receptor complex (Acvr1_Tgfbr). Importantly, among various functions, Tgfb1 is one of the primary inducers of MMT involving Smad2/3/4 proteins activation[360-362].

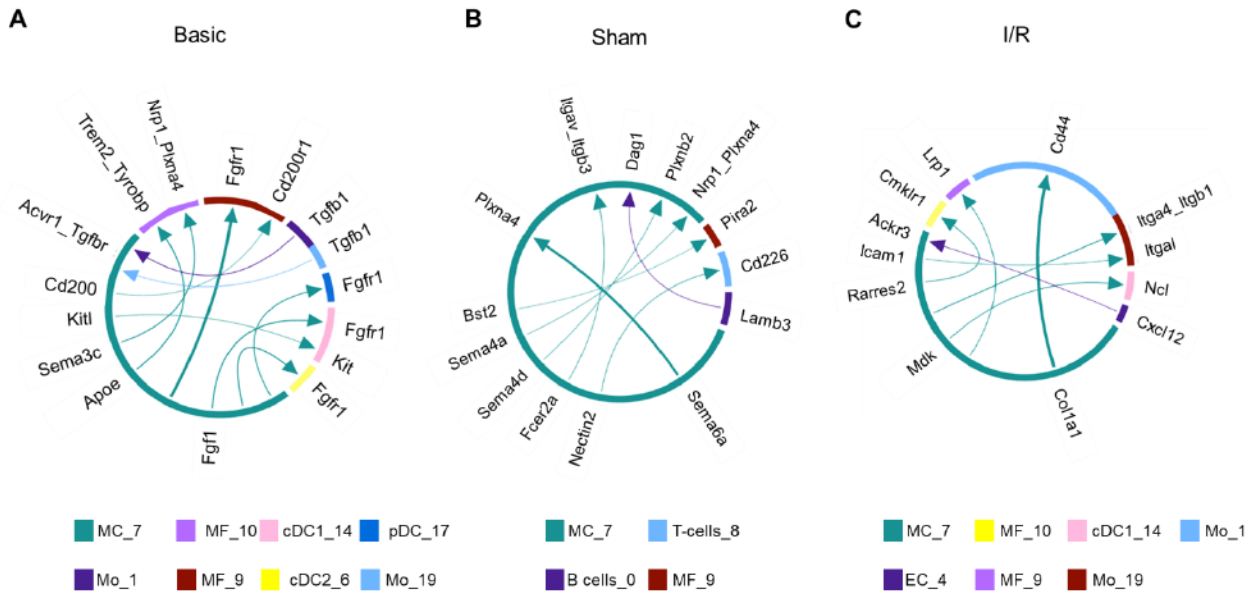

Figure 56. Intercellular network specific for pericardial mesothelial cells.

Ligand-receptor pairs specific for mesothelial cells (MC) under basic conditions [A], on day 6 after sham [B] and I/R [C]. The interactions were sorted according to their strength/probability and divided into three quartiles. The plots present interactions that were selected from the top quartile and were specific for MCs (ligand-receptor pairs that were present in all three conditions and in mesenchymal subset (pMSCs) were excluded). Plots are based on the CellChat-predicted interactions (description in chapter 3.10) and were generated with CCPlotR R package (Sarah Ennis et al).

In comparison to basic conditions, after sham, the MCs' network included more autocrine interactions (Figure 56B). Firstly, among them were the semaphorin family members with plexins (Plxna4, Plxnb2) and receptor complexes related to them (Nrp1_Plxna4) that are known to be crucial for tissue development since they contribute to tissue patterning, cell adhesion, and migration[363-365]. Secondly, MCs expressed Frer2a that interacted with integrin receptor complex Itgav_Itgb3. Fcer2a is known as a low-affinity receptor for immunoglobulin E (IgE) that plays a crucial role in B-cell differentiation[366,367]. However, in relation to mesothelial cells, a potential function of the autocrine Frer2a/Itgav_Itgb3 axis is not known.

Furthermore, MCs also interacted with immune cells. In comparison to basic conditions, sham induced interactions associated with migration and cell-ECM binding. Among them was Bst2 ligand (bone marrow stromal cell antigen 2) potentially interacted with Pira (paired-Ig-like receptor A1). For exapmple, in cancer studies it was shown that Bst2 has a pro-metastatic, invasive effect[363,368,]. Next, ECM protein Lamb3 (Laminin subunit beta-3) interacted with Dag1 (dystroglycan-1), that was shown to build dystrophin-glycoprotein complexes and link a cytoskeleton to ECM[364,369,370].

Additionally, MCs expressed Nectin2 (CD112, poliovirus receptor-related (PRR) family), which is known as a cell adhesion molecule. According to CellChat, Nectin-2 interacted with an activating receptor of the Ig superfamily, glycoprotein Cd226, expressed by T-cells. As it was reported, this interaction potentially mediates cytokines secretion by NK- and T-cells[371]. Therefore, this may also play an important role in pericardial immune response that could be mediated by MCs.

Figure 56C shows that after I/R, between MCs and monocytes were detected interactions associated with cell adhesion and migration (Icam1-Itgal and Col1a1-C -Cd44)[372]. Furthermore, MCs might have contributed to anti-inflammatory processes, facilitated by MCs-released growth factor Midkine (Mdk) that interacted with receptors Lrp1 (low-density lipoprotein-1), Ncl (nucleolin) and integrin receptor complex Itga4_Itgb1[373,374,372].

Next, MCs might have been involved in adipogenesis since they secreted a chemotactic adipokine Rarres2 (retinoic acid receptor responder-2 or chimerin) that interacted with Cmklr1 (chemokine like receptor-1) expressed by the macrophages of cluster 10[375].

Finally, the analysis revealed one ligand-receptor pair that targeted MCs. ECs released chemokine Cxcl12 (known as stromal cell-derived factor 1, SDF-1) that potentially interacted with Ackr3 (atypical Chemokine Receptor 3, Cxcr7).

This interaction might play an essential role in pericardial response to myocardial infarction since, as it was reported before, Cxcl12 affects proliferation, mobilization and angiogenesis in CD34+ progenitor cells. The Cxcl12/Ackr3 axis is also essential for recruitment of immune cells to the heart after myocardial infarction[376,377].

4.6.3. Intercellular interactions specific for pericardial mesenchymal cells (pMSC)

CellChat analysis showed that pMSCs also were involved in communication with immune cells. Figure 57A includes interactions detected under basic conditions that are essential for tissue homeostasis and support of cell proliferation, differentiation, and migration. Thus, pMSCs released Fgf10 (fibroblast growth factor-10) interacting with its receptor Fgfr1[378] as well as Mif (macrophage migration inhibitory factor) that interacted with receptor complex Cd74_Cd44. Although Mif is known as a pleiotropic inflammatory cytokine, it also supports cell survival and induces entrance of immune cells into the cell cycle[379,380].

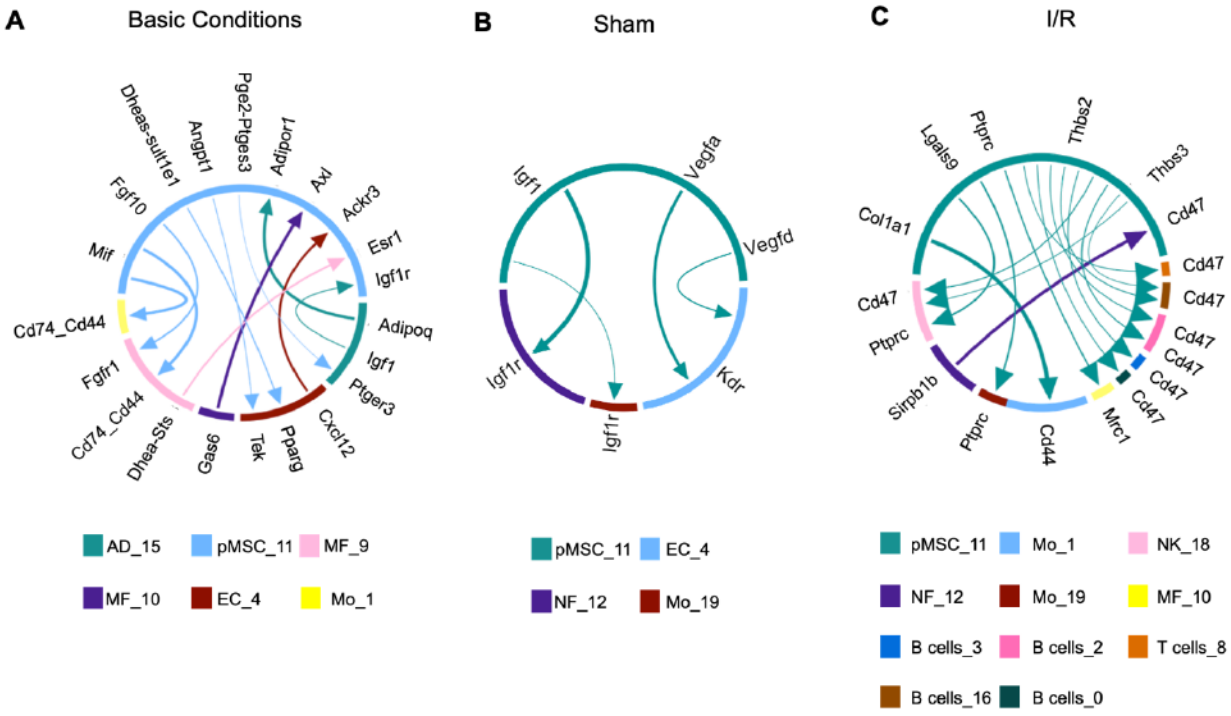

Figure 57. Intercellular network specific for pericardial mesenchymal cells.

Ligand-receptor pairs specific for mesenchymal cells (pMSC) under basic conditions [A], on day 6 after sham [B] and I/R [C]. The interactions were sorted according to their strength/probability and divided into three quartiles. The plots present interactions that were selected from the top quartile and were specific for pMSCs (ligand-receptor pairs that were present in all three conditions and in mesothelial subset (MC) were excluded). Plots are based on the CellChat-predicted interactions (description in chapter 3.10) and were generated with CCPlotR R package (Sarah Ennis et al).

There were also interactions that targeted pMSCs and might be essential for the regulation of proliferation, differentiation, and apoptosis in pMSCs. MFs (cluster 10) released Gas6 (growth arrest-specific 6) that has growth factor-like properties and interacts with Axl receptor tyrosine kinase[381]. Furthermore, MFs of cluster 9 expressed a hormone dehydroepiandrosterone along with steroid sulfatase enzyme (Dhea_Sts) that interacted with estrogen receptor Esr1, expressed accordingly by pMSCs[351,352].

Additionally, the CellChat analysis indicated in pMSCs a range of interactions involved in lipid metabolism and regulation of adipocyte function: Adipoq-Adipor1[382](adiponectin), Igf1-Igfr1[383-385], Dheas-Sult1e1-Pparg[386] and Pge2-Ptges3-Ptger3 (prostaglandin)[387,388].

Finally, pMSCs might communicate with endothelial cells via Cxcl12-Ackr3[389] and Angiopoetin1-Tek, which is crucial for vascular development as well as for support of stability of mature vessels[390].

After sham, pMSCs' network included primarily growth factors-based axes targeting immune and endothelial cells. For example, insulin-like growth factor Igf1 potentially interact with the Igf1r expressed by NFs and Mo (cluster 19). The vascular endothelial growth factors Vegfa and Vegfd released by pMSCs might bind to the receptor Kdr (kinase insert domain receptor) expressed by endothelial cells. This expression of these receptor-ligand pairs suggests that upon tissue damage, pMSCs contribute to immune cell modulation and vascular development[391].

After I/R, pMSCs exhibited a broad network for infiltration and adhesion of T and B cells residing in sub-clusters 0, 2, 3 and 16. This included thrombospondin ligands Thbs2 and Thbs3 that interact with Cd47 receptor. Additionally, the interaction between Sirpb1b (signal-regulatory protein beta-1) and Cd47 was reported to play a role in NFs infiltration[392-394].

Concomitantly, there was detected Ptprc, commonly known as CD45, a type 1 transmembrane protein tyrosine phosphatase. Interestingly, after I/R, Ptprc could participate in several interactions acting as a ligand or receptor. Firstly, it was expressed by pMSCs and interacted with Mrc1 (Mannose receptor C-type 1) detected on macrophages of cluster 10. Secondly, Ptprc was also expressed by NK-cells and monocytes of cluster 19. Here it could serve as a receptor for Lgals9 (galectin-9) released by pMSCs. Ptprc is known as an essential signaling molecule that regulates various processes including cytokine signaling, cell growth, differentiation and mitosis. Therefore, CD45 represents an important therapeutic target for many immune diseases[395]. In summary, the detected interactions might imply an essential role of pMSCs in the immune response of pericardial tissue to myocardial infarction.

5. Discussion

The pericardium is a double-layered structure that envelops the heart and provides mechanical support, lubrication, and protection. The inner visceral layer, known as the epicardium, is in direct contact with the myocardium, while the parietal layer, which is separated from the epicardium by the pericardial fluid, encloses the heart in a sac-like structure.

This project demonstrated that the parietal pericardium harbors various cell populations, including mesothelial and mesenchymal cells, endothelial cells, adipocytes, as well as a myriad of immune cells of myeloid as well as lymphoid lineages (T/B-cells, plasma B-cells, natural killer cells, monocytes, macrophages, dendritic cells and neutrophils). Moreover, it was demonstrated that the parietal pericardium responds to the cardiac damage caused by ischemia-reperfusion (I/R) and sham injuries. This response includes morphological changes of the pericardium as well as activation of mesothelial, mesenchymal, and immune cells of the innate and adaptive immune systems.

The observations made in this study add novel insight into the biology of the pericardium. Further, it expands the knowledge gained in other research works, which focused on the epicardium and indicated that this cell layer may play a significant role in cardiovascular diseases such as arrhythmogenic cardiomyopathy[71] and myocardial infarction (MI)[67]. In response to MI, epicardium-derived cells (EPDC) exhibit a temporal proliferative phase, differentiate into fibroblasts, and secrete paracrine factors such as vascular endothelial growth factor A (VEGFA), which induces vascular development following injury.

Moreover, activated epicardial cells reactivate gene expression programs linked to embryonic development and are characterized by the expression of genes such as Wt1 and Tbx18. Since activated epicardial cells were able to undergo transitions into other cell types it was suggested that these cells may contribute substantially to cardiac healing post MI.

Notably, the major findings of this project demonstrate that the pericardial cells may be of similar importance as epicardial cells for the healing process of the heart post myocardial infarction. Thus, in addition to the mechanical support, the pericardium appears to fulfil other functions critical to cardiac homeostasis.

The following critical findings related to the parietal pericardial cells have been elucidated:

1. Under basic conditions, the parietal pericardium of adult mice harbors two separate clusters of WT1-expressing cells, which include canonical mesothelial cells as well as cells with mesenchymal phenotype. Interestingly, both clusters express marker genes typical for progenitor cells, indicating that they might be prone to undergo mesothelial-to-mesenchymal transition.
2. In response to damage (I/R injury, sham surgery) the parietal pericardium transformed from a single-cell layer into a multicellular layer, and the associated lymphoid clusters (FALCs) significantly expanded. The cellular response included activation of immune cells and of both subsets of the WT1-expressing population.
3. Lineage tracing demonstrated that WT1+ cells of the pericardium not only proliferate but also migrate across the pericardial space. Migrated cells contribute substantially to thickening of the pericardium and enter the scar region. There they express the marker genes typical for fibroblasts.
4. Myeloid and lymphoid populations were activated in response to the cardiac injuries. Interestingly, sham induced a pronounced myeloid cell-driven response, whereas I/R induced a predominant increase of lymphoid cells, in particular B-cells.
5. sc-RNA seq analysis indicated that the Wt1 expressing cells secrete a large set of cytokines, growth factors and other ligands involved in cell-cell-communication and potentially mediate infiltration and adhesion of immune cells by Wt1-expressing cells.

Thus, this work demonstrates that pericardial cells due to their proximity to the myocardium appear to play an important role in the cardiac response to damage, which deserves a more intense investigation. The following sections discuss the interpretation of the experimental results, encountered study limitations, and potential perspectives.

5.1. Two types of WT1-expressing cells reside in parietal pericardium of adult mice under basic conditions.

One of the key markers of mesothelial cells is the zinc finger transcription factor WT1 (Wilms' tumor-1)[396-398]. The gene is indispensable for embryogenesis and is expressed by the tissues of mesodermal origin[399]. *Wt1*-null mice die due to lack of kidneys, adrenal glands, spleen and gonads, as well as heart failure[93,400-403]. In adulthood, WT1 expression is restricted to mesothelium, podocytes, gonadal cells, and minor fraction of bone marrow cells.

Deletion of *Wt1* in adult mice also had a lethal effect accompanied by widespread loss of fat and bone, podocyte foot processes and atrophy of the spleen and exocrine pancreas[404,405]. Additionally, the gene is associated with various pathological conditions, such as cancer and myocardial infarction. In the latter, the epicardial cells that are dormant under basic conditions, profoundly populate the visceral pericardium and highly express WT1[406].

Wt1 is a chameleon gene[407] that can activate or suppress numerous target genes regulating cell growth, differentiation, mesothelial-to-mesenchymal transition or apoptosis[400,408]. For example, it was reported that Wt1 suppresses *Pdgfa*[409], *Snai2*[410] and *Igf1r*[411], and, on the other hand, it can activate *Cdh1*[412] and *Nphs1*[413]. However, its effect can also be isoform dependent, where, for instance, the isoform of Wt1 that includes Lys-Thr-Ser (KTS) tripeptide was shown to repress the activity of *Igf2* promoter, whereas Wt1(-KTS) activates it[414,415]. Furthermore, the effect of Wt1 can be also organ or cell type dependent. Thus, it was reported that Wt1 activated *Wnt4* in the developing kidney and, concomitantly, repressed *Wnt4* in the epicardium[416].

Moreover, Wt1 is expressed during the mesothelial-to-mesenchymal transition (MMT), whereby mesenchymal progenitor cells can differentiate into osteoblasts, chondrocytes, adipocytes, and smooth muscle cells that contribute to the formation of various organs[403]. Studies involving the loss of Wt1 have shown that the mice exhibit disruption in MMT, suggesting that Wt1 plays a key role in maintaining mesothelial-to-mesenchymal balance[417,418].

In the current project, it was shown that under basic conditions, the parietal pericardium of adult mice contains an abundance of Wt1-expressing cells. This observation was confirmed on protein (Figure 18), and gene expression (Figure 20A, Figure 19B) levels as well as by analysis of the pericardium in genetically modified mice, allowing tracing of WT1-expressing cells due to expression of the fluorescent protein td-Tomato (Figure 24, Figure 25). Histological detection of tdTomato expression included an anti-tdTomato antibody for signal amplification. It is important to note that the staining against tdTomato was rather indistinct compared to the clear nuclear staining of Wt1 which was most likely due to the localization of the tdTomato protein in the cytoplasm. Nevertheless, microscopy could precisely define the localization of the WT1-expressing population throughout the entire pericardium. This finding is in clear contrast to the epicardial cells, which do not express WT1 under basic conditions but rather reactivate WT1 expression upon damage. Therefore, the visceral and parietal layers appear to be functionally different.

Wt1 expression has been demonstrated in mesothelial cell layers surrounding pleural, peritoneal, and pericardial cavities. In this work, a more detailed analysis revealed that the pericardium harbors two subsets of WT1-expressing cells (clusters 7 and 11) (Figure 40, Figure 43). One subset was represented by cells expressing canonical marker genes of mesothelial cells with epithelial phenotype *Muc16*, *Upk1b, Upk3b, Msln, Lrrn4*, *Krt19, Nkain4, Pdpn*, most of them being transmembrane proteins involved in defining the barrier functions of the mesothelial layer as well as a lubricious surface reducing friction during heart movement due to extensive glycosylation.

A hallmark of mesothelium is the formation of a single layer squamous epithelium. Like epithelial cells, mesothelial cells have an apical/basolateral polarity, which is defined by the formation of tight junctions and other adhesion complexes separating apical and basolateral parts of the epithelial cell and form lateral cell–cell contacts. MCs expressed several claudins as well as the regulator of cell polarity *Pard6b*. Therefore, cluster 7 was clearly defined as mesothelial cell cluster (MCs, Figure 44*,* Figure 45*,* Figure 46).

The second WT1+ subset (cluster 11) was represented by the cells with a phenotype akin to fibroblasts that expressed marker genes characteristic for mesenchymal cells (pMSCs) including *Pdgfra, Dpt, Pi16, Prrx1, Ddr2, Postn, Dpep1* (Figure 44*,* Figure 45*,* Figure 46). Many of the encoded proteins are involved in ECM remodeling and stability as well as regulation of cell proliferation and migration. Further genes contributing to the processes of cell adhesion, migration as well as ECM modulation include *Plcb1, Tnxb, Lamc1, Lama2, Aspn, Vtn, Pcdh19, Ednra,* and *Acvr2a*. These functions may be essential for the stability and flexibility of the fibrous layer, which, on the one hand must be flexible to withstand the stretching associated with the volume changes during the heart cycle. On the other hand, it must be rigid enough to inhibit overstretching of the heart and protect it from too large filling. Synthesis and modulation of the extracellular matrix is a canonical function of fibroblasts and mesenchymal cells.

The pMSCs express also a set of growth factors and receptors, indicating that they are actively involved in cell-cell communication and that cells of this cluster are in a transient or differentiating state (*Ngf, Vegfd, Pdgfrb, Notch1, Notch3, Fzd4, Plcb4, Chrm3 , Lpar1, Cacna1c, Prnp, Gng11, Grk5;* Figure 45, Figure 47). Particularly, Notch and Fzd receptors but also Lpar1 are components of cell differentiation programs, suggesting that pMSCs, at least in part, are prone to undergo transition or that such processes occur during the normal homeostasis of the pericardium.

Along the same line, pMSCs might exhibit adipogenic capacity. This hypothesis relies on the expression of pre-adipocyte markers *Lpl, Pparg, Apod, Cebpd, Sult1e1, Pla1a, Ebf1* and *Ebf2* (Figure 44, Figure 45).

Early B-cell factors 1 and 2 (Ebf1, Ebf2) turned out to be critical regulators of adipogenesis, controlling, among others, the expression of PPARγ, which was also elevated in pMSCs. The cell communication analysis also supported an adipogenic potential of pMSCs because interactions associated with lipid metabolism including Adipoq-Adipor1, Igf1-Igfr1, DHEAS-SULT1E1-Pparg and PGE2-PTGES3-Ptger3 were predicted (Figure 57).

The adipogenic potential of pMSC is reminiscent of mutated or activated epicardial cells. Earlier work revealed fibro-adipogenic characteristics in epicardial cells of mice with conditional deletion of Desmoplakin (*Dsp)* causing arrhythmogenic cardiomyopathy (ACM)[69] as well as in hiPSC-epicardial cells generated from patients with ACM[71].

Epicardium derived cells which are activated due to myocardial infarction are also able to form epicardial adipose tissue in mice, which is abundant in humans but rarely found in mice. Zangi et al. demonstrated that this response depended on the growth factor Igf1, when it was overexpressed in the scar region[419].

Furthermore, Westcott et al. showed that epididymal adipose tissue, which is also classified as visceral fat, contains a WT1+ cell population, which express mesothelial markers Krt19, Msln and Upk3b. However, a subset also expressed Pdgfra and Sca-1 and, therefore, was characterized by the authors as a pre-adipocyte population[420].

Besides the distinct features, both subsets of WT1-expressing cells showed features of cellular plasticity and could potentially contribute to formation of other cell lineages due to expressed progenitor cell markers. Among them, *Cd34, Isl1, Hand2,* as well as other genes known for their essential contribution to organ development during embryogenesis such as *Tbx18, Aldh1a1, Sema3d* and *Gata6* (Figure 20B*,* Figure 44) provide a hint for possible phenotypic changes by WT1 expressing cells. Such a gene expression pattern under basic conditions is rather surprising since the listed markers are known for their high expression level during embryogenesis or after injuries, such as myocardial infarction. It was also unexpected to detect Wt1-expressing subsets with two different phenotypes, which might hint at the transitional activity of cells already under basic conditions.

Summing up the findings of the basic characterization of the pericardial WT1+ cells demonstrates clear differences between parietal pericardial and visceral epicardial cells. Besides the finding of WT1 expression, pericardial WT1+ cells show under basic conditions already extensive similarities with activated epicardial cells post AMI. This is particularly true for the cells of pMSC fraction, which appear to be motile and show fibroblastic and adipogenic gene expression patterns and, therefore, may be derived from MCs, by MMT.

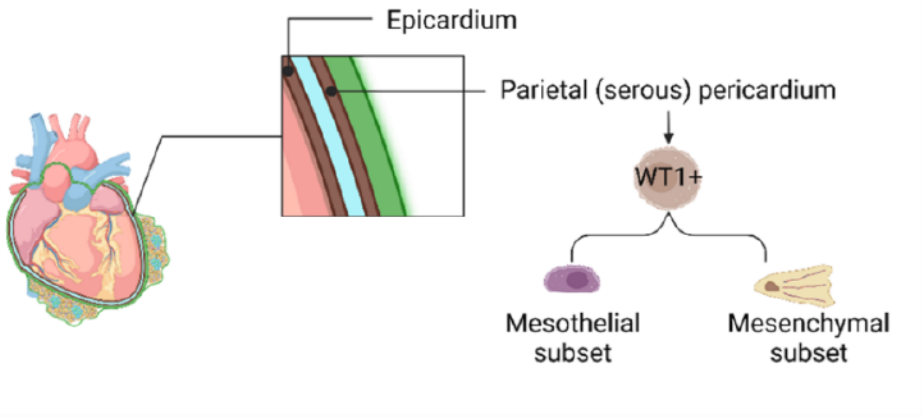

Figure 58. Subsets of Wt1-expressing cells in parietal pericardium of adult mice under basic conditions.

The scheme represents a preliminary Wt1+ cells classification based on the gene expression pattern obtained via sc-RNA seq analysis. The population of Wt1-expressing cells is subdivided into two groups with mesothelial and mesenchymal phenotype. The scheme was created in https://BioRender.com

5.2. Pericardial WT1-expressing cells are involved in mesothelial-to-mesenchymal transition already under basic conditions.

The finding of the marker gene expression related to progenitor cells and MMT prompted a more detailed analysis of MCs (cluster 7) and pMSCs (cluster 11) transcriptomes. considering the three commonly known types of EMT, which are often described as follows[421,422]: (1) EMT during development, such as embryogenesis, without resultant fibrosis or uncontrolled invasion;[423] (2) EMT associated with wound healing, fibrosis or tissue regeneration. In this case, EMT often resolves after the inflammatory phase;[423] (3) EMT in cancer allows tissue invasion and metastasis.

Since MMT (related to mesothelial cells) and well characterized EMT (related to epithelial cells) are closely related processes, the analysis focused on the gene expression patterns conforming to the major hallmarks of EMT (Figure 52, detailed description of the process is in chapter 1.1.1.3):

- expression of transcription factors controlling EMT,
- downregulation of cell-cell adhesion and apical-basal polarity markers,
- increased expression of the markers indicating front-rear polarity[424,425].

Cells of both clusters expressed the transcription factors that are important regulators of MMT, *Snai1* and *Snai2* (Snail Family Transcriptional Repressor 1/2), *Twist2* (twist basic helix-loop-helix transcription factor 2), *Zeb1* and *Zeb2* (zinc finger E-box binding homeobox 1/2). Among others, the epithelial marker E-Cadherin is repressed but mesenchymal markers such as N-Cadherin and vimentin are induced.

Thus, MCs and pMSCs express a network of transcriptional regulators, which promote MMT and enhance motility and invasiveness, where the latter is characteristic for various metastatic tumors including breast, pancreatic, ovarian and epidermal[426,427]. Transferred to pericardial Wt1+ cells, this might Indicate a tendency of pMSCs towards a motile phenotype acquirement (Figure 45, Figure 47, Figure 52). Of note, pMSCs expressed the focal adhesions marker *Tiam1* (T lymphoma invasion and metastasis), which, upon association with *Pard3* (par-3 family cell polarity regulator beta) and *Prkci* (protein kinase C iota) stabilizes front-rear cell polarization contributes to migration[337]. Furthermore, pMSCs expressed genes involved into actin filament organization and cell motility including *Sparcl1, Lum, Gpc6, Gsn, Svep1, Nav3.* Nevertheless, expression of tight junction proteins *Tjp1* and *Cldn15* was found in pMSCs, indicating that lateral cell-cell contacts occurred. The histological assessment of WT1+ cells in WT1-tdTm mice, demonstrated that tdTomato+ cells are mainly confined to the parietal pericardium, being embedded in the mesothelial cell layer and around FALCs. In contrast, the epicardium and myocardium next to the pericardium were free of tdTomato signals. This observation (Figure 30), implies that pMSCs may be prone to develop a migratory activity but appear to be stably integrated into the pericardium under basal conditions.

Interestingly, MCs, despite expression of MMT regulators clearly displayed the traits of the epithelial phenotype expressing genes encoding proteins determining apical/basal polarity such as *Pard3b*, *Mpp5* (Pals1, protein associated with LIN7), *Patj* (Pals1-associated tight junction)*, Prkci*. The expression patterns also indicate formation of the lateral cell contacts corroborated by expression of the genes encoding tight junction proteins (*Tjp1, Cldn10, 15)* and the adherens junction protein cadherin *Cdh11*). However, DEGs analysis also displayed upregulated expression of genes indicating transformative or differentiating phase in MCs *(Sox6, Dmkn, Lrp2).*

The regulation of MMT involves extracellular factors such as cytokines or growth factors acting on mesothelial cells. Regarding potential candidates that may induce MMT in pericardial cells, a first analysis of pericardial intercellular communication based on the CellChat tool revealed that immune cells may contribute to this process.

Accordingly, macrophages communicated with pMSCs via ligand-receptor pairs Gas6-Axl and DHEA_STS-Esr1, which are known to be involved in cell proliferation, differentiation, and apoptosis processes. However, the molecules were not yet profoundly studied in the given context. Also, for monocytes a strong interaction with MCs via Tgfb1 and receptor complex ACVR1_TGFbR was predicted. The TGFβ family of growth factors is essential for mesothelial cell functionality in healthy and pathological conditions. Among numerous biological processes, the TGFβ pathway is a principal inducer of the MMT/EMT process and is essential for cellular differentiation, proliferation, and cell motility[361].

Dysregulation and excessive activity of the TGFβ signaling cascade causes developmental disturbance and leads to fibrosis[428]. Ramachandran et al., who elaborated on the signaling cascade induced by Tgfb1[429] using the human breast cancer cell line MDA-MB-231 and the mouse mammary epithelial cell line NMuMG as model systems *in vitro*. It was established that Tgfb1 induces clustering of Acvr1 and Tgfbr1 receptors, leading to Smad1/5 activation and ID1 (Inhibitor of DNA Binding 1) expression, resulting in EMT.

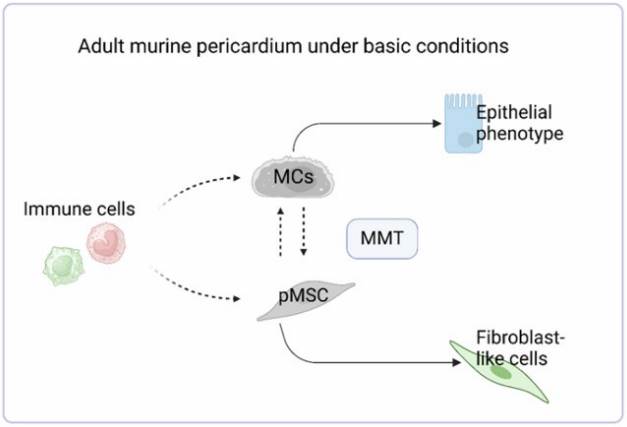

Figure 59. Mesothelial and mesenchymal cells potentially undergo MMT under basic conditions.

The scheme is based on sc-RNA seq analysis and summarizes a hypothesis that both populations of pericardial Wt1-expressing cells undergo mesothelial-to-mesenchymal transition (MMT) already under basic conditions, potentially resulting in a subset with epithelial phenotype and a subset that exhibits a gene expression pattern characteristic for fibroblasts. The scheme was created in https://BioRender.com

5.3. Activation of pericardial Wt1-expressing cells in response to I/R and Sham

Whereas under basic conditions the pericardial mesothelium represented a thin single-cell layer of WT1+ cells residing on a fibrous layer, I/R surgery initiated several processes:

1) An extensive cell proliferation between day 2 to 5 after I/R resulted in a significant expansion of the pericardium,
2) Pericardial WT1+ derived cells migrated towards the injured myocardium,
3) Migrated pericardial WT1+ cells in the infarct zone expressed fibroblasts markers suggesting a differentiation into activated fibroblasts.

The identification of the listed events is based on histological analyses of cardiac and pericardial tissue obtained from C57BL/6 mice, as well as the lineage-tracing model WT1-tdTm, along with sc-RNA seq performed on C57BL/6 mice.

The induction of the cell proliferation was related to WT1-expressing cells as well as other cells within fat-associated lymphoid clusters (FALCs), (Figure 27, Figure 28). In addition, also the visceral layer, i.e. the epicardium was affected (Figure 29, Figure 30). Collectively, this response correlates with a significant thickening of the parietal part of the pericardium, epicardium as well as expansion of the FALCs (Figure 36).

Interestingly, the proliferative phase of the pericardial cells coincided with the acute inflammation phase of the myocardium, which persists for up to 4 days following MI[430], as well as with the onset of the reparative phase, which reaches its peak at day 7 after the injury[430]. Thus, there is potentially a mutual exchange of signaling between the pericardium and myocardium, likely acting on the remodeling process in both tissues.

Moreover, DEGs analysis showed that in response to cardiac injury, MCs and pMSCs expressed a broad range of genes associated with tissue damage and pro-survival mechanisms (*Clu, Lcn2, Mt1, Cfb Ifi27l2, Bst2, Isg15, Irf7, Hif1a, Hspa5, Il33),* implying that the cells reacted to the stress and might be activated as a response (Figure 49-Figure 51).

Furthermore, the conditional tamoxifen-dependent activation of CreERT2 mediated tdTomato expression allowed lineage tracing of cells derived from pericardial WT1+ cells. The experimental protocol led to activation of tdTomato expression in WT1+ cells in healthy mice only in the pericardial but not epicardial cells. Thus, after the surgical induction of MI, only pericardial WT1+ cells and their descendants expressed tdTomato.

Therefore, it is assumed that after I/R, the abundance of tdTomato+ cells found in the thickened pericardium are the result of a local proliferation of these cells, which was demonstrated by WT1 – Ki67 co-staining in histology. Consequently, tdTomato+ cells that appeared in the epicardium, as well as in the myocardium were rather derived from the Wt1+ cells of the parietal pericardium (Figure 30, Figure 33). According to the data presented here, the well-known process of post-MI epicardial thickening is caused in part by migration of cells from the pericardium. Therefore, it is hypothesized that at least a portion of pericardial Wt1-expressing cells undergo MMT, acquire a motile phenotype and migrate across the pericardial cavity to infiltrate the epi- and myocardium.

According to DEGs analysis of the marker genes related to MMT, there was an indication that MCs potentially performed a conversion towards the mesenchymal phenotype since the mesothelium-characteristic genes were downregulated and the cells expressed marker genes indicating front-rear polarity and migration (S*nail1, Snail2*, *Arpc2*, *Pxn, Tiam,* and *Prkci*). On the contrary, pMSCs seemed to show only minor changes maintaining the transient state since they still expressed marker genes of both phenotypes *Cldn10, Cdh11, Mpp5*, suggesting at least partial lateral cell-cell contact as well as *Patj, Arpc2, Pxn*, indicating a motile phenotype.

Interestingly, a part of tdTomato+ cells detected within the scar co-expressed fibroblast markers such as Ddr2 (discoidin domain receptor tyrosine kinase 2), Acta2 (actin alpha 2; α-SMA), and Postn (periostin) suggesting that WT1+ cells invading from the pericardium possess the potential to differentiate into myofibroblasts (Figure 34). This may be also associated with the highly expressed genes indicating a differentiation process in pericardial MCs (Figure 50; *Tmsb4x, Tmsb10 , Tacc2, Rbm3, Actg1, Gpr39, Tpm4, Hnrnpd*) as well as in pMSCs (Figure 51; *Bach2, Sfrp2, Runx1, Aff3, Actg1, Mbnl1, Ripor2)*. Interestingly, although the gene set was mainly associated with cell differentiation, polarization, and re-organization of the cytoskeleton, MCs, and pMSCs expressed only the groups of genes specific for each subset and condition. This might suggest that although pMSCs and MCs differentiate after the applied injuries, the programs that drive those changes may not be the same and are aimed at different purposes. Collectively, the finding implies that pericardial Wt1-expressing cells and their derivatives contribute to post-MI cardiac remodeling process.

This hypothesis is consistent with the findings for epicardial cells published by Ruiz-Villalba et al., who observed that an epicardium-derived interstitial cell population differentiated into $CD90^{+}/CD31^{-}/\alpha\text{-}SMA^{low}$ cardiac fibroblasts, which were detected in the infarcted zone between day 7 and 14 after MI[431]. To what extent these cells were derived from pericardial cells is currently not clear, but answering this question will be an interesting topic for further investigation.

The interpretation of the lineage tracing data presented in this study has a minor limitation. It cannot be fully excluded, that, for example, pleural or peritoneal mesothelial cells, which also express WT1 could have migrated to the pericardium to give rise to tdTomato expression in pericardium, epicardium, and myocardium post MI. All of them can differentiate into fibroblasts [31,397] demonstrating the general, inherent plasticity of Wt1+ cells residing in visceral cavities.

However, the proximity and the extensive proliferation of pericardial cells after injury makes the pericardium the most likely source of tdTomato+ cells in the epicardium and the scar.

Histological analysis also detected sporadic endogenous tdTomato+ signals under basic conditions in vessels within the myocardium, which raises the possibility that a fraction of endothelial cells may have migrated to the site of inflammation, contributing to the activated fibroblasts detected in the scar. Verifying this observation will be an important future task.

Whereas histological analysis revealed a transformation of the pericardium towards a multicellular layer with substantial increase of WT1-expressing cells after I/R (Figure 27, Figure 29, Figure 30), the relative contribution of Wt1-expressing cells derived from sc-RNA seq analysis did not reflect elevated cell numbers for clusters 7 (MCs) and 11 (pMSCs). (Figure 42B), One possible explanation for the deceptive results is a technical aspect of the analysis. The number of analyzed cells across the three conditions - basic, I/R, and sham - was assigned to 20,000. Irrespective of cell proliferation, the equal cell numbers were analyzed, to avoid underrepresentation of minor cell fractions in the multiplex experiments. Therefore, the extensive increase of B-cell numbers reaching 60 % of all cells post MI reduced the relative contribution of the other cell clusters, including 7 and 11.

Furthermore, assuming that the migration of pericardial cells into the epi- and myocardium occurs after MI, this would also distort the cell numbers since the heart was not included in the sc-RNA seq analysis. Finally, sc-RNA seq analysis was performed using C57BL/6 mice, which compromised the opportunity to evaluate the differentiation potential of the pericardial cells by using tdTomato as a marker to identify WT1+ and, importantly, WT1+ cell-derived cells documented by the lineage tracing model. Therefore, it is crucial to evaluate the extent of the pericardial cells' participation in post-MI remodeling via quantitative evaluation of the MCs and pMSCs subsets in the pericardium, involving additional methods, which could confirm these preliminary findings.

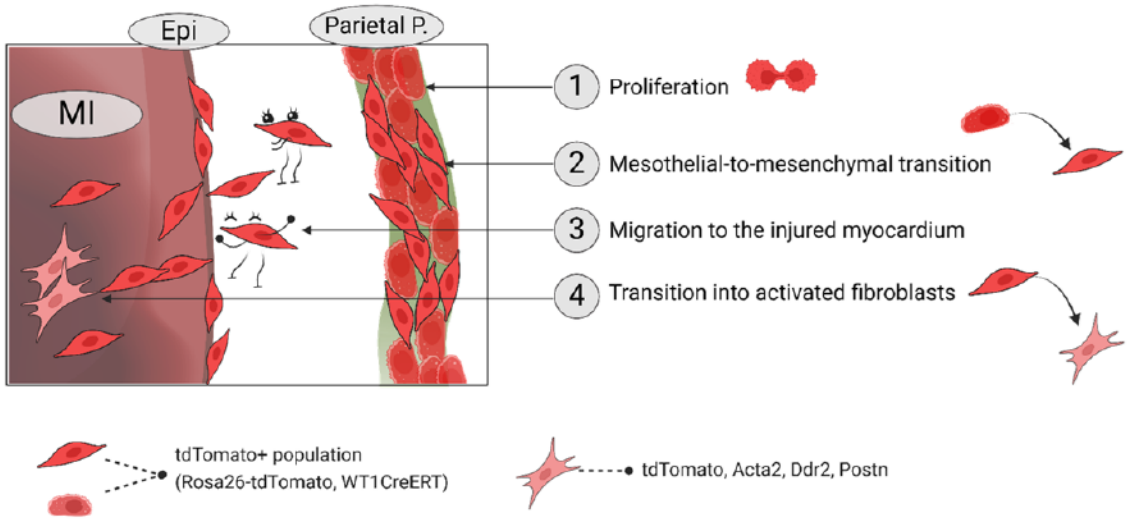

Figure 60. Concept of the activation of pericardial Wt1-expressing cells in response to myocardial infarction.

The scheme includes 4 potential steps comprising the activation of mesothelial cells in response to I/R: (1) Proliferation from day 2 to 5; (2) Mesothelial-to-mesenchymal transition; (3) Migration of mesenchymal subset toward the injured myocardium; (4) Differentiation into activated fibroblasts. MI – myocardial infarction; Epi – epicardium; Parietal. P – parietal pericardium. The image was created in https://BioRender.com

5.4. Response of the pericardial immune cells to the myocardial infarction

In the course of the project, there were several indications that the pericardium is a rich source of various immune cells. Firstly, histological analyses illustrated in Figure 18 and Figure 21 showed that the adipose tissue integrated within the parietal pericardium contains numerous fat-associated lymphoid clusters (FALCs) that are populated by lymphoid as well as myeloid immune cells. The presence of immune cells in the adult murine pericardium under basic conditions was further validated via qPCR (Figure 22) and FACS analyses (Figure 23). Moreover, scRNA seq analysis identified 17 groups of pericardial immune cells, which included T-cells, six subsets of B-cells and plasma B-cells, plasmacytoid and conventional cDC1 and cDC2 dendritic cells, two subsets of macrophages and monocytes, natural-killer cells as well as neutrophils that infiltrated following sham and I/R injuries.

This observation may complement earlier research works since the pericardium was already considered in 1985 as a reservoir for various immune cells responsive to cardiac injuries such as myocardial infarction[432-434]. However, this definition was primarily referred to the pericardial fluid until, in 2018, Horckmans et al. classified pericardial fat as a secondary lymphoid organ containing an abundance of T- and B-cells and dendritic cells concentrated in FALCs[4]. The research group reported that in response to MI, the FALCs expand in association with increased B-cell count as well as increase of DC and T-cell counts in the pericardial adipose tissue. Moreover, the removal of pericardial adipose tissue led to a beneficial post-MI outcome with mitigated cardiac fibrosis and cardiac function.

Within the current project, there was a series of histological analyses aimed at spatial description of the pericardial elements, including FALCs, under basic conditions, as well as after the cardiac injuries. The result showed that I/R and sham induced strong structural changes of the pericardial FALCs that were accompanied by increase in FALCs surface area, particularly along the lateral wall of the heart and less in the anterior and posterior parts (Figure 36). Furthermore, there was a significant immune response recorded by sc-RNA seq analysis (Figure 42). It is essential to note that the tissue preparation method was specifically designed to preserve the entire pericardium and to provide a comprehensive spatial overview of the pericardium surrounding the heart (Figure 7). However, this observation may still be influenced by the experimental setup used for the tissue isolation.

Interestingly, FALCs were delineated by WT1-expressing cells, and a portion of them was distributed within FALCs (Figure 21A, Figure 18C). This specific localization might suggest a potential communication between these cell groups.

This hypothesis is supported by cell-cell communication analysis that predicted an intricate network of MCs and pMSCs interacting with immune cells residing in the pericardium under basic conditions as well as after I/R and sham. As mentioned before, under basic conditions, many ligand-receptor pairs detected among MCs, pMSCs, and immune cells were associated with immunoregulation (Figure 55-Figure 57). For example, among interactions detected specifically in MCs were Apoe-Trem_Tyrobp, Kitl-Kit, Cd200-Cd200r1, Fgf1-Fgfr1, Sema3c-Nrp1_Plxna4, and interactions predicted in pMSC were Fgf10-Fgfr1 and Mif-Cd74_Cd44.

In response to sham, MCs initiated interactions with T-cells, B-cells of cluster 0, and MFs of cluster 9 suggesting a role in mediating cell recruitment, adhesion, proliferation, and phagocytosis via Bst2-Pira, Nectin2-Cd226, and Lamb3-Dag1 interactions.

Conversely, in pMSCs, among the prevailing interactions were insulin-like growth factor-1 (Igf1) ligand and Igf1 receptor expressed by neutrophils and monocytes (cluster 19).

Finally, after I/R injury, pMSCs exhibited extensive interactions via Thbs2, Thbs3 ligands, and Cd47 receptor expressed by T cells and B cells of clusters 0, 2, 3, and 16 as well as Sirpb1b ligand and Cd47 expressed by NFs that infiltrated in response to damage, since under basic conditions the cluster proportion represented less than 1%. Also, MCs showed a potential to contribute to leukocyte recruitment via Icam1-Itgal and Cxcl12 (SDF-1) – Ackr3 (Cxcr7). This observation aligns with the cell proportion analysis obtained from sc-RNA seq data, which indicated a significant increase in the immune cells proportion after the applied injuries, with I/R inducing a strong activation of lymphocytes, particularly B-cells, while, sham increased the proportion of myeloid cells (Figure 42).

Hence, the enlargement of the FALC area in response to the cardiac injury may result from the intricate communication with MCs and pMSCs, which potentially play a role in the immune cell recruitment. Additionally, this effect may result from the proliferative activity of cells found in FALCs spanning from day 2 to 5 after I/R (Figure 28).

This finding might expand other research works that also reported an intercommunication between mesothelial and immune cells in FALCs in other organs, such as omentum. Jackson-Jones et al. demonstrated that omental FALCs are enveloped by CD45−CD41−Ter119−CD31−PDPN+ mesothelial cells. These cells expressed the B-cell positioning chemokine Cxcl13 and served as a source of Cxcl1, thereby facilitating the accumulation of neutrophils at the initial phase of Zymosan-A-induced peritonitis[122].

Collectively, the observations made in this project show that the pericardial immune cells react to the cardiac injury and their response bay be mediated by MCs and pMSCs, what increases the necessity of studying the pericardial cells, their intercommunication, and mechanisms under pathological conditions.

6. Perspectives

The project offered a new perspective on the clinical relevance of the pericardium. According to the primary insight, Wt1-expressing cells could be characterized as a group of progenitor cells with tissue development or reparative potential. The population may play a pivotal role in inflammatory and remodeling processes that occur following myocardial infarction. Firstly, the cells demonstrated a possible contribution to the influx of immune cells that may modulate cardiac immune response; secondly, the cells possess plasticity and motility traits that may contribute to the heart remodeling process; finally, the cells are implicated into lipid metabolism that may be crucial for maintaining tissue function under both physiological and pathophysiological conditions.

6.1. Validation of MCs and pMSCs activation in response to cardiac injuries induced by non-invasive methods.

I/R and sham injuries used in the project as the cardiac injury models were improved compared to the commonly used myocardial infarction models with open pericardium. The presented surgeries were performed with the closed pericardium, preserving the cell environment and possible contact between the heart and parietal pericardium. However, the surgeries included steps of the suture entering the tissue, resulting in a minor, still present technical pericardial and myocardial disruption. Thus, the sham experiment showed that pericardial cells were activated in response to the minor damage already after sham surgery. Moreover, as the experiments showed, the tissue response to sham and I/R may differ, making it challenging to establish a baseline and infer the changes explicitly caused by the I/R condition, not a technical invasion. Therefore, it is critical testing the observed activation of MCs and pMSCs in models where non-invasive methods induce cardiac pathological conditions.

6.2. Transitional state of MCs and pMSCs already under basic conditions.

Already under basic conditions, MCs and pMSCs showed a signature of a transitional state that potentially linked to mesothelial-to-mesenchymal transition. The finding was rather surprising as MMT has traditionally been associated with embryogenesis, wound healing processes or cancer. Consequently, it would be relevant to investigate whether MCs can give rise to pMSCs cluster through this mechanism and to understand the functional implications of this transitional state in both cell populations under basic conditions.

The fundamental concept of MMT is to generate the cells that are able to migrate or differentiate into various cell types. Thus, it raises important questions regarding whether pMSCs maintain the motile phenotype or they exhibit directional migration. Furthermore, what is the differentiation capacity of pMSCs that expressed fibroblast-like markers as well as showed a potential involvement in adipogenesis. Finally, it is essential to explore how the transitional state of the clusters may influence the healing process following the myocardial infarction.

6.3. Immunoregulatory potential of pericardial MCs and pMSC.

Bioinformatics tools used to analyze sc-RNA seq data predicted that MCs and pMSCs are closely associated with the majority of immune cell clusters under basic conditions as well as in response to sham and I/R. Consequently, the programs identified potential ligand-receptor interactions and signaling cascades that may occur between the cells and facilitate various biological processes such as induction of MMT, cell recruitment, adhesion, and development. Therefore, a critical subsequent step is validating the candidate signaling and understanding how they govern immune cell behavior under basic conditions and in response to cardiac injury. Additionally, it is essential to investigate to what extent the immune cells influence the mesothelial and mesenchymal population of the adult murine pericardium.

7. References

1. Khan MA, Hashim MJ, Mustafa H, et al. Global Epidemiology of Ischemic Heart Disease: Results from the Global Burden of Disease Study. (2168-8184 (Print)).

2. Rodriguez ER, Tan CD. Structure and Anatomy of the Human Pericardium. Prog Cardiovasc Dis. 2017;59(4):327-340.

3. Benezech C, Luu NT, Walker JA, et al. Inflammation-induced formation of fat-associated lymphoid clusters. Nat Immunol. 2015;16(8):819-828.

4. Horckmans M, Bianchini M, Santovito D, et al. Pericardial Adipose Tissue Regulates Granulopoiesis, Fibrosis, and Cardiac Function After Myocardial Infarction. Circulation. 2018;137(9):948-960.

5. Mutsaers SE. The mesothelial cell. The International Journal of Biochemistry & Cell Biology. 2004;36(1):9-16.

6. Lua I, Asahina K. The Role of Mesothelial Cells in Liver Development, Injury, and Regeneration. (2005-1212 (Electronic)).

7. Krist LFG, Eestermans IL, Steenbergen JJE, et al. Cellular composition of milky spots in the human greater omentum: An immunochemical and ultrastructural study. The Anatomical Record. 1995;241(2):163-174.

8. Ohtani Y, Ohtani O Fau - Nakatani T, Nakatani T. Microanatomy of the rat diaphragm with special reference to the lymphatics and mesothelial stomata. (1122-6714 (Print)).

9. Mutsaers SE, Birnie K, Lansley S, Herrick SE, Lim CB, Prele CM. Mesothelial cells in tissue repair and fibrosis. Front Pharmacol. 2015;6:113.

10. Wu Y-J, Parker LM, Binder NE, et al. The mesothelial keratins: A new family of cytoskeletal proteins identified in cultured mesothelial cells and nonkeratinizing epithelia. Cell. 1982;31(3, Part 2):693-703.

11. Hiriart E, Deepe R, Wessels A. Mesothelium and Malignant Mesothelioma. LID - 10.3390/jdb7020007 [doi] LID - 7. (2221-3759 (Electronic)).

12. Mutsaers SE. Mesothelial cells: Their structure, function and role in serosal repair. Respirology. 2002;7(3):171-191.

13. Park DSJ, Regmi SC, Svystonyuk DA, et al. Human pericardial proteoglycan 4 (lubricin): Implications for postcardiotomy intrathoracic adhesion formation. The Journal of Thoracic and Cardiovascular Surgery. 2018;156(4):1598-1608.e1591.

14. Dobbie JW, Pavlina T, Lloyd J, Johnson RC. Phosphatidylcholine Synthesis by Peritoneal Mesothelium: Its Implications for Peritoneal Dialysis. American Journal of Kidney Diseases. 1988;12(1):31-36.

15. Beavis J, Harwood Jl Fau - Coles GA, Coles Ga Fau - Williams JD, Williams JD. Synthesis of phospholipids by human peritoneal mesothelial cells. (0896-8608 (Print)).

16. Zeiler J, Idell S, Norwood S, Cook A. Hemothorax: a review of the literature. Clinical pulmonary medicine. 2020;27(1):1-12.

17. Tsai JM, Sinha R, Seita J, et al. Surgical adhesions in mice are derived from mesothelial cells and can be targeted by antibodies against mesothelial markers. Science Translational Medicine. 2018;10(469):eaan6735.

18. Visser CE, Tekstra J Fau - Brouwer-Steenbergen JJ, Brouwer-Steenbergen Jj Fau - Tuk CW, et al. Chemokines produced by mesothelial cells: huGRO-alpha, IP-10, MCP-1 and RANTES. (0009-9104 (Print)).

19. Betjes MGH, Tuk CW, Struijk DG, et al. Interleukin-8 Production by Human Peritoneal Mesothelial Cells in Response to Tumor Necrosis Factor-α, Interleukln-1, and Medium Conditioned by Macrophages Cocultured with Staphylococcus epidermidis. The Journal of Infectious Diseases. 1993;168(5):1202-1210.

20. Topley N, Jörres A, Luttmann W, et al. Human peritoneal mesothelial cells synthesize interleukin-6: Induction by IL-1β and TNFα. Kidney International. 1993;43(1):226-233.

21. Topley N, Brown Z Fau - Jörres A, Jörres A Fau - Westwick J, et al. Human peritoneal mesothelial cells synthesize interleukin-8. Synergistic induction by interleukin-1 beta and tumor necrosis factor-alpha. (0002-9440 (Print)).

22. Goodman RB, Wood RG, Martin TR, Hanson-Painton O, Kinasewitz GT. Cytokine-stimulated human mesothelial cells produce chemotactic activity for neutrophils including NAP-1/IL-8. The Journal of Immunology. 1992;148(2):457-465.

23. Li FK, Davenport A, Robson RL, et al. Leukocyte migration across human peritoneal mesothelial cells is dependent on directed chemokine secretion and ICAM-1 expression. Kidney International. 1998;54(6):2170-2183.

24. Andreoli SP, Mallett C, Williams K, McAteer JA, Rothlein R, Doerschuk CM. Mechanisms of polymorphonuclear leukocyte mediated peritoneal mesothelial cell injury. Kidney International. 1994;46(4):1100-1109.

25. Liberek T, Topley N, Luttmann W, Williams JD. Adherence of neutrophils to human peritoneal mesothelial cells: role of intercellular adhesion molecule-1. Journal of the American Society of Nephrology. 1996;7(2).

26. Mutsaers SE, Prêle CM-A, Pengelly S, Herrick SE. Mesothelial cells and peritoneal homeostasis. Fertility and Sterility. 2016;106(5):1018-1024.

27. Saed GM, Zhang W, Chegini N, Holmdahl L, Diamond MP. Alteration of type I and III collagen expression in human peritoneal mesothelial cells in response to hypoxia and transforming growth factor-β1. Wound Repair and Regeneration. 1999;7(6):504-510.

28. Rennard SI, Jaurand M-C, Bignon J, et al. Role of pleural mesothelial cells in the production of the submesothelial connective tissue matrix of lung. American Review of Respiratory Disease. 1984;130(2):267-274.

29. Winkler J, Abisoye-Ogunniyan A, Metcalf KJ, Werb Z. Concepts of extracellular matrix remodelling in tumour progression and metastasis. Nature Communications. 2020;11(1):5120.

30. Ma C, Tarnuzzer RW, Chegini N. Expression of matrix metalloproteinases and tissue inhibitor of matrix metalloproteinases in mesothelial cells and their regulation by transforming growth factor-β1. Wound repair and regeneration. 1999;7(6):477-485.

31. Yang AH, Chen JY, Lin JK. Myofibroblastic conversion of mesothelial cells. Kidney International. 2003;63(4):1530-1539.

32. Sandoval P, Jiménez-Heffernan JA, Rynne-Vidal Á, et al. Carcinoma-associated fibroblasts derive from mesothelial cells via mesothelial-to-mesenchymal transition in peritoneal metastasis. The Journal of Pathology. 2013;231(4):517-531.

33. Yáñez-Mó M, Lara-Pezzi E, Selgas R, et al. Peritoneal Dialysis and Epithelial-to-Mesenchymal Transition of Mesothelial Cells. New England Journal of Medicine.348(5):403-413.

34. Dettman RW, Denetclaw W, Ordahl CP, Bristow J. Common Epicardial Origin of Coronary Vascular Smooth Muscle, Perivascular Fibroblasts, and Intermyocardial Fibroblasts in the Avian Heart. Developmental Biology. 1998;193(2):169-181.

35. Armulik A, Genové G, Betsholtz C. Pericytes: Developmental, Physiological, and Pathological Perspectives, Problems, and Promises. Developmental Cell. 2011;21(2):193-215.

36. Lamouille S, Xu J, Derynck R. Molecular mechanisms of epithelial–mesenchymal transition. Nature Reviews Molecular Cell Biology. 2014;15(3):178-196.

37. Hartsock A, Nelson WJ. Adherens and tight junctions: structure, function and connections to the actin cytoskeleton. (0006-3002 (Print)).

38. Zhang P, Wang S, Wang S, et al. Dual function of partitioning-defective 3 in the regulation of YAP phosphorylation and activation. Cell Discovery. 2016;2(1):16021.

39. Wodarz A. Establishing cell polarity in development. Nature Cell Biology. 2002;4(2):E39-E44.

40. Tepass U. Crumbs, a Component of the Apical Membrane, Is Required for Zonula Adherens Formation in Primary Epithelia ofDrosophila. Developmental Biology. 1996;177(1):217-225.

41. Pieczynski J, Margolis B. Protein complexes that control renal epithelial polarity. American Journal of Physiology-Renal Physiology. 2011;300(3):F589-F601.

42. Shin K, Fogg VC, Margolis B. Tight Junctions and Cell Polarity. Annual Review of Cell and Developmental Biology. 2006;22(Volume 22, 2006):207-235.

43. Nelson WJ. Remodeling epithelial cell organization: transitions between front-rear and apical-basal polarity. Cold Spring Harb Perspect Biol. 2009;1(1):a000513.

44. Ridley AJ, Schwartz MA, Burridge K, et al. Cell Migration: Integrating Signals from Front to Back. Science. 2003;302(5651):1704-1709.

45. Usman S, Waseem NH, Nguyen TKN, et al. Vimentin Is at the Heart of Epithelial Mesenchymal Transition (EMT) Mediated Metastasis. LID - 10.3390/cancers13194985 [doi] LID - 4985. (2072-6694 (Print)).

46. Taube JH, Herschkowitz JI, Komurov K, et al. Core epithelial-to-mesenchymal transition interactome gene-expression signature is associated with claudin-low and metaplastic breast cancer subtypes. Proceedings of the National Academy of Sciences. 2010;107(35):15449-15454.

47. Lo H-W, Hsu S-C, Xia W, et al. Epidermal Growth Factor Receptor Cooperates with Signal Transducer and Activator of Transcription 3 to Induce Epithelial-Mesenchymal Transition in Cancer Cells via Up-regulation of TWIST Gene Expression. Cancer Research. 2007;67(19):9066-9076.

48. Kim J, Kong J, Chang H, Kim H, Kim A. EGF induces epithelial-mesenchymal transition through phospho-Smad2/3-Snail signaling pathway in breast cancer cells. (1949-2553 (Electronic)).

49. Savagner P, Julien-Grille S, Moore R, et al. The role of insulin-like growth factors in the epithelial to mesenchymal transition. Rise and Fall of Epithelial Phenotype: Concepts of Epithelial-Mesenchymal Transition. 2005:215-235.

50. Strutz F, Zeisberg M Fau - Ziyadeh FN, Ziyadeh Fn Fau - Yang C-Q, et al. Role of basic fibroblast growth factor-2 in epithelial-mesenchymal transformation. (0085-2538 (Print)).

51. Nam MW, Kim CW, Choi KC. Epithelial-Mesenchymal Transition-Inducing Factors Involved in the Progression of Lung Cancers. (1976-9148 (Print)).

52. Kalluri R, Neilson EG. Epithelial-mesenchymal transition and its implications for fibrosis. The Journal of clinical investigation. 2003;112(12):1776-1784.

53. Ramos C, Becerril C, Montaño M, et al. FGF-1 reverts epithelial-mesenchymal transition induced by TGF-β1 through MAPK/ERK kinase pathway. American Journal of Physiology-Lung Cellular and Molecular Physiology. 2010;299(2):L222-L231.

54. Bizzi E, Picchi C, Mastrangelo G, Imazio M, Brucato A. Recent advances in pericarditis. European Journal of Internal Medicine. 2022;95:24-31.

55. Deniset JF, Belke D, Lee WY, et al. Gata6(+) Pericardial Cavity Macrophages Relocate to the Injured Heart and Prevent Cardiac Fibrosis. Immunity. 2019;51(1):131-140 e135.

56. Khandaker MH, Espinosa Re Fau - Nishimura RA, Nishimura Ra Fau - Sinak LJ, et al. Pericardial disease: diagnosis and management. (1942-5546 (Electronic)).

57. Dababneh E, Siddique MS. Pericarditis. BTI - StatPearls.

58. Xu B, Harb SC, Cremer PC. New Insights into Pericarditis: Mechanisms of Injury and Therapeutic Targets. Current Cardiology Reports. 2017;19(7):60.

59. Karatolios K, Moosdorf R, Maisch B, Pankuweit S. Cytokines in Pericardial Effusion of Patients with Inflammatory Pericardial Disease. Mediators of Inflammation. 2012;2012(1):382082.

60. Bayat A, Syed A, Ali AF, tornekar v, Dong T, Klein AL. Abstract 16555: Neutrophil to Lymphocyte Ratio: A Marker of Inflammation in Pericardial Disease. Circulation. 2023;148(Suppl_1):A16555-A16555.

61. Bonaventura A, Montecucco F. Inflammation and pericarditis: Are neutrophils actors behind the scenes? Journal of Cellular Physiology. 2019;234(5):5390-5398.

62. Hoffman M, Fried M, Jabareen F, et al. Anti-heart Antibodies in Postpericardiotomy Syndrome: Cause or Epiphenomenon? Autoimmunity. 2002;35(4):241-245.

63. Imazio M, Adler Y. Treatment with aspirin, NSAID, corticosteroids, and colchicine in acute and recurrent pericarditis. Heart Failure Reviews. 2013;18(3):355-360.

64. Vianello F, Cinetto F, Cavraro M, et al. Azathioprine in isolated recurrent pericarditis: A single centre experience. International Journal of Cardiology. 2011;147(3):477-478.

65. Jain S, Thongprayoon C, Espinosa RE, et al. Effectiveness and Safety of Anakinra for Management of Refractory Pericarditis. The American Journal of Cardiology. 2015;116(8):1277-1279.

66. Mutsaers SE, Whitaker D, Papadimitriou JM. Stimulation of Mesothelial Cell Proliferation by Exudate Macrophages Enhances Serosal Wound Healing in a Murine Model. The American Journal of Pathology. 2002;160(2):681-692.

67. Zhou B, Honor LB, He H, et al. Adult mouse epicardium modulates myocardial injury by secreting paracrine factors. The Journal of clinical investigation. 2011;121(5):1894-1904.

68. Winter EM, Grauss RW, Hogers B, et al. Preservation of Left Ventricular Function and Attenuation of Remodeling After Transplantation of Human Epicardium-Derived Cells Into the Infarcted Mouse Heart. Circulation. 2007;116(8):917-927.

69. Yuan P, Cheedipudi SM, Rouhi L, et al. Single-Cell RNA Sequencing Uncovers Paracrine Functions of the Epicardial-Derived Cells in Arrhythmogenic Cardiomyopathy. Circulation. 2021;143(22):2169-2187.

70. Yamaguchi Y, Cavallero S, Patterson M, et al. Adipogenesis and epicardial adipose tissue: a novel fate of the epicardium induced by mesenchymal transformation and PPARγ activation. Proceedings of the national academy of sciences. 2015;112(7):2070-2075.

71. Kohela A, van Kampen SJ, Moens T, et al. Epicardial differentiation drives fibro-fatty remodeling in arrhythmogenic cardiomyopathy. Science Translational Medicine. 2021;13(612):eabf2750.

72. Redpath AN, Smart N. Recapturing embryonic potential in the adult epicardium: Prospects for cardiac repair. Stem Cells Transl Med. 2021;10(4):511-521.

73. Lupu I-E, Redpath AN, Smart N. Spatiotemporal Analysis Reveals Overlap of Key Proepicardial Markers in the Developing Murine Heart. Stem Cell Reports. 2020;14(5):770-787.

74. Acharya A, Baek ST, Banfi S, Eskiocak B, Tallquist MD. Efficient inducible Cre-mediated recombination in Tcf21cell lineages in the heart and kidney. genesis. 2011;49(11):870-877.

75. Lavine KJ, Yu K, White AC, et al. Endocardial and epicardial derived FGF signals regulate myocardial proliferation and differentiation in vivo. Dev Cell. 2005;8(1):85-95.

76. Wu M, Smith CL, Hall JA, Lee I, Luby-Phelps K, Tallquist MD. Epicardial Spindle Orientation Controls Cell Entry into the Myocardium. Developmental Cell. 2010;19(1):114-125.

77. Cai C-L, Martin JC, Sun Y, et al. A myocardial lineage derives from Tbx18 epicardial cells. Nature. 2008;454(7200):104-108.

78. Zhou B, Ma Q, Rajagopal S, et al. Epicardial progenitors contribute to the cardiomyocyte lineage in the developing heart. Nature. 2008;454(7200):109-113.

79. Gittenberger-de Groot AC, Winter EM, Poelmann RE. Epicardium-derived cells (EPDCs) in development, cardiac disease and repair of ischemia. J Cell Mol Med. 2010;14(5):1056-1060.

80. von Gise A, Zhou B, Honor LB, Ma Q, Petryk A, Pu WT. WT1 regulates epicardial epithelial to mesenchymal transition through beta-catenin and retinoic acid signaling pathways. Dev Biol. 2011;356(2):421-431.

81. Smits AM, Dronkers E, Goumans MJ. The epicardium as a source of multipotent adult cardiac progenitor cells: Their origin, role and fate. Pharmacol Res. 2018;127:129-140.

82. Acharya A, Baek ST, Banfi S, Eskiocak B, Tallquist MD. Efficient inducible Cre-mediated recombination in Tcf21cell lineages in the heart and kidney. genesis. 2011;49(11):870-877.

83. Katz Tamar C, Singh Manvendra K, Degenhardt K, et al. Distinct Compartments of the Proepicardial Organ Give Rise to Coronary Vascular Endothelial Cells. Developmental Cell. 2012;22(3):639-650.

84. Mikawa T, Gourdie RG. Pericardial mesoderm generates a population of coronary smooth muscle cells migrating into the heart along with ingrowth of the epicardial organ. (0012-1606 (Print)).

85. Dougherty JP, Temin HM. High Mutation Rate of a Spleen Necrosis Virus-Based Retrovirus Vector. Molecular and Cellular Biology. 1986;6(12):4387-4395.

86. Turner Dl Fau - Cepko CL, Cepko CL. A common progenitor for neurons and glia persists in rat retina late in development. (0028-0836 (Print)).

87. <mikawa-fischman-1992-retroviral-analysis-of-cardiac-morphogenesis-discontinuous-formation-of-coronary-vessels.pdf>.

88. <82397575.pdf>.

89. Armstrong JF, Pritchard-Jones K, Bickmore WA, Hastie ND, Bard JBL. The expression of the Wilms' tumour gene, WT1, in the developing mammalian embryo. Mechanisms of Development. 1993;40(1):85-97.

90. Buckler AJ, Pelletier J, Haber DA, Glaser T, Housman DE. Isolation, Characterization, and Expression of the Murine Wilms' Tumor Gene (WT1) During Kidney Development. Molecular and Cellular Biology. 1991;11(3):1707-1712.

91. Park S, Schalling M, Bernard A, et al. The Wilms tumour gene WT1 is expressed in murine mesoderm–derived tissues and mutated in a human mesothelioma. Nature Genetics. 1993;4(4):415-420.

92. Kreidberg JA, Sariola H, Loring JM, et al. WT-1 is required for early kidney development. Cell. 1993;74(4):679-691.

93. Kreidberg JA, Sariola H Fau - Loring JM, Loring Jm Fau - Maeda M, et al. WT-1 is required for early kidney development. (0092-8674 (Print)).

94. Moore AW, Schedl A, McInnes L, Doyle M, Hecksher-Sorensen J, D. Hastie N. YAC transgenic analysis reveals Wilms' Tumour 1 gene activity in the proliferating coelomic epithelium, developing diaphragm and limb. Mechanisms of Development. 1998;79(1):169-184.

95. Sched A, Larin Z, Montoliu L, et al. A method for the generation of YAC transgenic mice by pronuclear microinjection. Nucleic acids research. 1993;21(20):4783-4787.

96. Menke A, McInnes L, Hastie ND, Schedl A. The Wilms' tumor suppressor WT1: Approaches to gene function. Kidney International. 1998;53(6):1512-1518.

97. Le Y, Miller JL, Sauer B. GFPcreFusion Vectors with Enhanced Expression. Analytical Biochemistry. 1999;270(2):334-336.

98. Mao X, Fujiwara Y, Orkin SH. Improved reporter strain for monitoring Cre recombinase-mediated DNA excisions in mice. Proceedings of the National Academy of Sciences. 1999;96(9):5037-5042.

99. Friedrich G, Soriano P. Promoter traps in embryonic stem cells: a genetic screen to identify and mutate developmental genes in mice. Genes & development. 1991;5(9):1513-1523.

100. Vintersten K, Monetti C, Gertsenstein M, et al. Mouse in red: Red fluorescent protein expression in mouse ES cells, embryos, and adult animals. genesis. 2004;40(4):241-246.

101. Muzumdar MD, Tasic B, Miyamichi K, Li L, Luo L. A global double-fluorescent Cre reporter mouse. genesis. 2007;45(9):593-605.

102. Zhou B, von Gise A, Ma Q, Hu YW, Pu WT. Genetic fate mapping demonstrates contribution of epicardium-derived cells to the annulus fibrosis of the mammalian heart. Developmental Biology. 2010;338(2):251-261.

103. von Gise A, Zhou B Fau - Honor LB, Honor Lb Fau - Ma Q, Ma Q Fau - Petryk A, Petryk A Fau - Pu WT, Pu WT. WT1 regulates epicardial epithelial to mesenchymal transition through β-catenin and retinoic acid signaling pathways. (1095-564X (Electronic)).

104. Zhou B, Ma Q, Rajagopal S, et al. Epicardial progenitors contribute to the cardiomyocyte lineage in the developing heart. Nature. 2008;454(7200):109-113.

105. <P1 Cre discovery.pdf>.

106. Zhang Y, Zeng F, Han X, Weng J, Gao Y. Lineage tracing: technology tool for exploring the development, regeneration, and disease of the digestive system. Stem Cell Res Ther. 2020;11(1):438.

107. <Inducible Cre mice.pdf>.

108. Soriano P. Generalized lacZ expression with the ROSA26 Cre reporter strain. Nature Genetics. 1999;21(1):70-71.

109. Scofield SL, Singh K. Confirmation of Myocardial Ischemia and Reperfusion Injury in Mice Using Surface Pad Electrocardiography. J Vis Exp. 2016(117).

110. <cm2010000443.pdf>.

111. Clasen L, Angendohr S, Becher S, et al. Cardiac ischemia and reperfusion in mice: a comprehensive hemodynamic, electrocardiographic and electrophysiological characterization. Sci Rep. 2023;13(1):5693.

112. McKinnon KM. Flow Cytometry: An Overview. Current Protocols in Immunology. 2018;120(1):5.1.1-5.1.11.

113. Premanandh J, George LV, Wernery U, Sasse J. Evaluation of a newly developed real-time PCR for the detection of Taylorella equigenitalis and discrimination from T. asinigenitalis. Veterinary Microbiology. 2003;95(4):229-237.

114. Butler A, Hoffman P, Smibert P, Papalexi E, Satija R. Integrating single-cell transcriptomic data across different conditions, technologies, and species. Nature Biotechnology. 2018;36(5):411-420.

115. Hao Y, Hao S, Andersen-Nissen E, et al. Integrated analysis of multimodal single-cell data. Cell. 2021;184(13):3573-3587.e3529.

116. McGinnis CS, Murrow LM, Gartner ZJ. DoubletFinder: Doublet Detection in Single-Cell RNA Sequencing Data Using Artificial Nearest Neighbors. Cell Systems. 2019;8(4):329-337.e324.

117. Elewa YHA, Ichii O, Nakamura T, Kon Y. Dual Effect of Bleomycin on Histopathological Features of Lungs and Mediastinal Fat-Associated Lymphoid Clusters in an Autoimmune Disease Mouse Model. Front Immunol. 2021;12:665100.

118. Eiras S, Teijeira-Fernandez E, Shamagian LG, Fernandez AL, Vazquez-Boquete A, Gonzalez-Juanatey JR. Extension of coronary artery disease is associated with increased IL-6 and decreased adiponectin gene expression in epicardial adipose tissue. Cytokine. 2008;43(2):174-180.

119. Antonopoulos AS, Margaritis M, Verheule S, et al. Mutual Regulation of Epicardial Adipose Tissue and Myocardial Redox State by PPAR-gamma/Adiponectin Signalling. Circ Res. 2016;118(5):842-855.

120. Filova E, Stankova L, Eckhardt A, et al. Modification of human pericardium by chemical crosslinking. Physiol Res. 2020;69(1):49-59.

121. Kendall TJ, Duff CM, Boulter L, et al. Embryonic mesothelial-derived hepatic lineage of quiescent and heterogenous scar-orchestrating cells defined but suppressed by WT1. Nat Commun. 2019;10(1):4688.

122. Jackson-Jones LH, Smith P, Portman JR, et al. Stromal Cells Covering Omental Fat-Associated Lymphoid Clusters Trigger Formation of Neutrophil Aggregates to Capture Peritoneal Contaminants. Immunity. 2020;52(4):700-715 e706.

123. Sousa IRF, Pereira ICC, Morais LJ, Teodoro L, Rodrigues MLP, Gomes R. Pericardial Parietal Mesothelial Cells: Source of the Angiotensin-Converting-Enzyme of the Bovine Pericardial Fluid. Arq Bras Cardiol. 2017;109(5):425-431.

124. Sohn JH, Lee YK, Han JS, et al. Perilipin 1 (Plin1) deficiency promotes inflammatory responses in lean adipose tissue through lipid dysregulation. J Biol Chem. 2018;293(36):13974-13988.

125. Guo J-K, Menke AL, Gubler M-C, et al. WT1 is a key regulator of podocyte function: reduced expression levels cause crescentic glomerulonephritis and mesangial sclerosis. Human Molecular Genetics. 2002;11(6):651-659.

126. Bajpai G, Schneider C, Wong N, et al. The human heart contains distinct macrophage subsets with divergent origins and functions. Nat Med. 2018;24(8):1234-1245.

127. Heidt T, Courties G, Dutta P, et al. Differential contribution of monocytes to heart macrophages in steady-state and after myocardial infarction. Circ Res. 2014;115(2):284-295.

128. Frantz S, Nahrendorf M. Cardiac macrophages and their role in ischaemic heart disease. Cardiovasc Res. 2014;102(2):240-248.

129. Shiraishi M, Shintani Y, Shintani Y, et al. Alternatively activated macrophages determine repair of the infarcted adult murine heart. The Journal of clinical investigation. 2016;126(6):2151-2166.

130. Yu T, Gan S, Zhu Q, et al. Modulation of M2 macrophage polarization by the crosstalk between Stat6 and Trim24. Nat Commun. 2019;10(1):4353.

131. Jablonski KA, Amici SA, Webb LM, et al. Novel Markers to Delineate Murine M1 and M2 Macrophages. PLoS One. 2015;10(12):e0145342.

132. Moskalik A, Niderla-Bielinska J, Ratajska A. Multiple roles of cardiac macrophages in heart homeostasis and failure. Heart Fail Rev. 2022;27(4):1413-1430.

133. Ma Y, Mouton AJ, Lindsey ML. Cardiac macrophage biology in the steady-state heart, the aging heart, and following myocardial infarction. Transl Res. 2018;191:15-28.

134. Mosser DM, Edwards JP. Exploring the full spectrum of macrophage activation. Nat Rev Immunol. 2008;8(12):958-969.

135. Kang Q, Li L, Pang Y, Zhu W, Meng L. An update on Ym1 and its immunoregulatory role in diseases. Front Immunol. 2022;13:891220.

136. Urruticoechea A, Smith IE, Dowsett M. Proliferation marker Ki-67 in early breast cancer. J Clin Oncol. 2005;23(28):7212-7220.

137. Kretzschmar K, Post Y, Bannier-Helaouet M, et al. Profiling proliferative cells and their progeny in damaged murine hearts. Proc Natl Acad Sci U S A. 2018;115(52):E12245-E12254.

138. Shimazaki M, Nakamura K, Kii I, et al. Periostin is essential for cardiac healing after acute myocardial infarction. J Exp Med. 2008;205(2):295-303.

139. Humeres C, Frangogiannis NG. Fibroblasts in the Infarcted, Remodeling, and Failing Heart. (2452-302X (Electronic)).

140. Shinde AV, Humeres C, Frangogiannis NG. The role of α-smooth muscle actin in fibroblast-mediated matrix contraction and remodeling. Biochimica et Biophysica Acta (BBA) - Molecular Basis of Disease. 2017;1863(1):298-309.

141. Zou Y-R, Grimaldi C, Diamond B. B Cells. 2017:207-230.e203.

142. Luo Y, Wang J, Li K, et al. Single-cell genomics identifies distinct B1 cell developmental pathways and reveals aging-related changes in the B-cell receptor repertoire. Cell Biosci. 2022;12(1):57.

143. <PIIS1074761301001534.pdf>.

144. <mcmanus-et-al-2011-the-transcription-factor-pax5-regulates-its-target-genes-by-recruiting-chromatin-modifying-proteins.pdf>.

145. Enders A, Short A, Miosge LA, et al. Zinc-finger protein ZFP318 is essential for expression of IgD, the alternatively spliced Igh product made by mature B lymphocytes. Proc Natl Acad Sci U S A. 2014;111(12):4513-4518.

146. Jung SH, Hwang BH, Shin S, et al. Spatiotemporal dynamics of macrophage heterogeneity and a potential function of Trem2(hi) macrophages in infarcted hearts. Nat Commun. 2022;13(1):4580.

147. Tkachenko AA-O, Kupcova KA-O, Havranek OA-O. B-Cell Receptor Signaling and Beyond: The Role of Igα (CD79a)/Igβ (CD79b) in Normal and Malignant B Cells. LID - 10.3390/ijms25010010 [doi] LID - 10. (1422-0067 (Electronic)).

148. Sobecki M, Mrouj K, Colinge J, et al. Cell-Cycle Regulation Accounts for Variability in Ki-67 Expression Levels. Cancer Res. 2017;77(10):2722-2734.

149. Riba A, Oravecz A, Durik M, et al. Cell cycle gene regulation dynamics revealed by RNA velocity and deep-learning. Nat Commun. 2022;13(1):2865.

150. Espinoza DA, Le Coz C, Cruz Cabrera E, Romberg N, Bar-Or A, Li R. Distinct stage-specific transcriptional states of B cells derived from human tonsillar tissue. JCI Insight. 2023;8(7).

151. Borchers A, Pieler T. Programming pluripotent precursor cells derived from Xenopus embryos to generate specific tissues and organs. Genes (Basel). 2010;1(3):413-426.

152. Wiggins KJ, Scharer CD. Roadmap to a plasma cell: Epigenetic and transcriptional cues that guide B cell differentiation. Immunol Rev. 2021;300(1):54-64.

153. Szabo PA, Levitin HM, Miron M, et al. Single-cell transcriptomics of human T cells reveals tissue and activation signatures in health and disease. Nat Commun. 2019;10(1):4706.

154. Reinhardt J, Sharma V, Stavridou A, et al. Distinguishing activated T regulatory cell and T conventional cells by single-cell technologies. Immunology. 2022;166(1):121-137.

155. Goh W, Huntington ND. Regulation of Murine Natural Killer Cell Development. Front Immunol. 2017;8:130.

156. Wensveen FM, Jelencic V, Polic B. NKG2D: A Master Regulator of Immune Cell Responsiveness. Front Immunol. 2018;9:441.

157. Crinier A, Milpied P, Escaliere B, et al. High-Dimensional Single-Cell Analysis Identifies Organ-Specific Signatures and Conserved NK Cell Subsets in Humans and Mice. Immunity. 2018;49(5):971-986 e975.

158. <2-10-973.pdf>.

159. McCarthy MK, Reynoso GV, Winkler ES, et al. MyD88-dependent influx of monocytes and neutrophils impairs lymph node B cell responses to chikungunya virus infection via Irf5, Nos2 and Nox2. PLoS Pathog. 2020;16(1):e1008292.

160. Willemsen L, de Winther MP. Macrophage subsets in atherosclerosis as defined by single-cell technologies. J Pathol. 2020;250(5):705-714.

161. <science.aai8132.pdf>.

162. Bajpai G, Bredemeyer A, Li W, et al. Tissue Resident CCR2- and CCR2+ Cardiac Macrophages Differentially Orchestrate Monocyte Recruitment and Fate Specification Following Myocardial Injury. Circ Res. 2019;124(2):263-278.

163. Vallejo J, Cochain C, Zernecke A, Ley K. Heterogeneity of immune cells in human atherosclerosis revealed by scRNA-Seq. Cardiovasc Res. 2021;117(13):2537-2543.

164. Merad M, Sathe P, Helft J, Miller J, Mortha A. The dendritic cell lineage: ontogeny and function of dendritic cells and their subsets in the steady state and the inflamed setting. Annu Rev Immunol. 2013;31:563-604.

165. Du X, Li M, Huan C, Lv G. Dendritic cells in liver transplantation immune response. Front Cell Dev Biol. 2023;11:1277743.

166. Brown CC, Gudjonson H, Pritykin Y, et al. Transcriptional Basis of Mouse and Human Dendritic Cell Heterogeneity. Cell. 2019;179(4):846-863 e824.

167. Weisheit CK, Engel DR, Kurts C. Dendritic Cells and Macrophages: Sentinels in the Kidney. Clin J Am Soc Nephrol. 2015;10(10):1841-1851.

168. Musumeci A, Lutz K, Winheim E, Krug AB. What Makes a pDC: Recent Advances in Understanding Plasmacytoid DC Development and Heterogeneity. Front Immunol. 2019;10:1222.

169. Stutte S, Ishikawa-Ankerhold H, Lynch L, et al. High-Fat Diet Rapidly Modifies Trafficking, Phenotype, and Function of Plasmacytoid Dendritic Cells in Adipose Tissue. J Immunol. 2022;208(6):1445-1455.

170. Pathak M, Lal G. The Regulatory Function of CCR9(+) Dendritic Cells in Inflammation and Autoimmunity. Front Immunol. 2020;11:536326.

171. Wang S, Song R, Wang Z, Jing Z, Wang S, Ma J. S100A8/A9 in Inflammation. Front Immunol. 2018;9:1298.

172. Norreen-Thorsen M, Struck EC, Oling S, et al. A human adipose tissue cell-type transcriptome atlas. Cell Rep. 2022;40(2):111046.

173. Grieshaber-Bouyer R, Radtke FA, Cunin P, et al. The neutrotime transcriptional signature defines a single continuum of neutrophils across biological compartments. Nat Commun. 2021;12(1):2856.

174. Kiss T, Nyul-Toth A, Balasubramanian P, et al. Single-cell RNA sequencing identifies senescent cerebromicrovascular endothelial cells in the aged mouse brain. Geroscience. 2020;42(2):429-444.

175. Burl RB, Ramseyer VD, Rondini EA, Pique-Regi R, Lee YH, Granneman JG. Deconstructing Adipogenesis Induced by beta3-Adrenergic Receptor Activation with Single-Cell Expression Profiling. Cell Metab. 2018;28(2):300-309 e304.

176. Agarwal AK, Tunison K, Vale G, et al. Regulated adipose tissue-specific expression of human AGPAT2 in lipodystrophic Agpat2-null mice results in regeneration of adipose tissue. iScience. 2023;26(10):107806.

177. Laurencikiene J, Ryden M. Liver X receptors and fat cell metabolism. Int J Obes (Lond). 2012;36(12):1494-1502.

178. Kanamori-Katayama M, Kaiho A, Ishizu Y, et al. LRRN4 and UPK3B are markers of primary mesothelial cells. PLoS One. 2011;6(10):e25391.

179. Snider P, Standley KN, Wang J, Azhar M, Doetschman T, Conway SJ. Origin of cardiac fibroblasts and the role of periostin. Circ Res. 2009;105(10):934-947.

180. Muhl L, Genove G, Leptidis S, et al. Single-cell analysis uncovers fibroblast heterogeneity and criteria for fibroblast and mural cell identification and discrimination. Nat Commun. 2020;11(1):3953.

181. Olaso E, Labrador JP, Wang L, et al. Discoidin domain receptor 2 regulates fibroblast proliferation and migration through the extracellular matrix in association with transcriptional activation of matrix metalloproteinase-2. J Biol Chem. 2002;277(5):3606-3613.

182. Astarita JL, Acton SE, Turley SJ. Podoplanin: emerging functions in development, the immune system, and cancer. Front Immunol. 2012;3:283.

183. Rudat C, Grieskamp T, Rohr C, et al. Upk3b is dispensable for development and integrity of urothelium and mesothelium. PLoS One. 2014;9(11):e112112.

184. Quintanilla M, Montero-Montero L, Renart J, Martin-Villar E. Podoplanin in Inflammation and Cancer. International journal of molecular sciences. 2019;20(3).

185. Acton SE, Astarita JL, Malhotra D, et al. Podoplanin-rich stromal networks induce dendritic cell motility via activation of the C-type lectin receptor CLEC-2. Immunity. 2012;37(2):276-289.

186. Rupert PB, Buerger M, Friend DJ, Strong RK. Structural elucidation of the mesothelin-mucin-16/CA125 interaction. (1878-4186 (Electronic)).

187. Xu J, Deng Y, Li G. Keratin 19 (Krt19) is a novel marker gene for epicardial cells. (1664-8021 (Print)).

188. Trempus CS, Papas BN, Sifre MI, et al. Functional Pdgfra fibroblast heterogeneity in normal and fibrotic mouse lung. JCI Insight. 2023;8(22).

189. Yao L, Rathnakar BH, Kwon HR, et al. Temporal control of PDGFRalpha regulates the fibroblast-to-myofibroblast transition in wound healing. Cell Rep. 2022;40(7):111192.

190. Bisig B, Gaulard P, de Leval L. New biomarkers in T-cell lymphomas. Best Pract Res Clin Haematol. 2012;25(1):13-28.

191. Hollinger JO, Alvarez-Urena P, Ducheyne P, et al. 6.2 Bone Tissue Engineering: Growth Factors and Cytokines ☆. 2017:20-53.

192. Gauthier V, Kyriazi M, Nefla M, et al. Fibroblast heterogeneity: Keystone of tissue homeostasis and pathology in inflammation and ageing. Front Immunol. 2023;14:1137659.

193. McCartney EE, Chung Y, Buechler MB. Life of Pi: Exploring functions of Pi16+ fibroblasts. F1000Res. 2024;13:126.

194. Buechler MB, Pradhan RN, Krishnamurty AT, et al. Cross-tissue organization of the fibroblast lineage. Nature. 2021;593(7860):575-579.

195. Paulsson M. Basement membrane proteins: structure, assembly, and cellular interactions. (1040-9238 (Print)).

196. Plikus MV, Wang X, Sinha S, et al. Fibroblasts: Origins, definitions, and functions in health and disease. Cell. 2021;184(15):3852-3872.

197. Garrity R, Haque A, Kavelaars A, Heijnen C, Shepherd A. Fibroblast-derived PI16 Drives the Physiological Process of Immune Cell Recruitment and Activation During Inflammatory Response. The Journal of Pain. 2024;25(4, Supplement):13.

198. Wang W, Kissig M, Rajakumari S, et al. Ebf2 is a selective marker of brown and beige adipogenic precursor cells. (1091-6490 (Electronic)).

199. Wang H, Eckel RH. Lipoprotein lipase: from gene to obesity. (1522-1555 (Electronic)).

200. Perdomo G Fau - Henry Dong H, Henry Dong H. Apolipoprotein D in lipid metabolism and its functional implication in atherosclerosis and aging. (1945-4589 (Electronic)).

201. Hishida T, Nishizuka M, Osada S, Imagawa M. The role of C/EBPδ in the early stages of adipogenesis. Biochimie. 2009;91(5):654-657.

202. Vassalli G. Aldehyde Dehydrogenases: Not Just Markers, but Functional Regulators of Stem Cells. Stem Cells Int. 2019;2019:3904645.

203. <1479-7364-5-4-283.pdf>.

204. Petrosino JM, Disilvestro D, Ziouzenkova O. Aldehyde dehydrogenase 1A1: friend or foe to female metabolism? Nutrients. 2014;6(3):950-973.

205. Duester G, Mic FA, Molotkov A. Cytosolic retinoid dehydrogenases govern ubiquitous metabolism of retinol to retinaldehyde followed by tissue-specific metabolism to retinoic acid. Chem Biol Interact. 2003;143-144:201-210.

206. Alto LT, Terman JR. Semaphorins and their Signaling Mechanisms. Methods Mol Biol. 2017;1493:1-25.

207. Sadanandam A, Rosenbaugh EG, Singh S, Varney M, Singh RK. Semaphorin 5A promotes angiogenesis by increasing endothelial cell proliferation, migration, and decreasing apoptosis. Microvasc Res. 2010;79(1):1-9.

208. Duan Y, Wang SH, Song J, et al. Semaphorin 5A inhibits synaptogenesis in early postnatal- and adult-born hippocampal dentate granule cells. Elife. 2014;3.

209. Ko PH, Lenka G, Chen YA, et al. Semaphorin 5A suppresses the proliferation and migration of lung adenocarcinoma cells. Int J Oncol. 2020;56(1):165-177.

210. Wei K, Diaz-Trelles R, Liu Q, et al. Developmental origin of age-related coronary artery disease. Cardiovasc Res. 2015;107(2):287-294.

211. Kolander KD, Holtz ML, Cossette SM, Duncan SA, Misra RP. Epicardial GATA factors regulate early coronary vascular plexus formation. Dev Biol. 2014;386(1):204-215.

212. Molkentin JD. The zinc finger-containing transcription factors GATA-4, -5, and -6. Ubiquitously expressed regulators of tissue-specific gene expression. J Biol Chem. 2000;275(50):38949-38952.

213. Lentjes MH, Niessen HE, Akiyama Y, de Bruine AP, Melotte V, van Engeland M. The emerging role of GATA transcription factors in development and disease. Expert Rev Mol Med. 2016;18:e3.

214. Gu C, Rodriguez Er Fau - Reimert DV, Reimert Dv Fau - Shu T, et al. Neuropilin-1 conveys semaphorin and VEGF signaling during neural and cardiovascular development. (1534-5807 (Print)).

215. Suto F, Ito K Fau - Uemura M, Uemura M Fau - Shimizu M, et al. Plexin-a4 mediates axon-repulsive activities of both secreted and transmembrane semaphorins and plays roles in nerve fiber guidance. (1529-2401 (Electronic)).

216. Lefebvre V. The SoxD transcription factors – Sox5, Sox6, and Sox13 – are key cell fate modulators. The International Journal of Biochemistry & Cell Biology. 2010;42(3):429-432.

217. Michibata H, Okuno T, Konishi N, et al. Human GPM6A Is Associated With Differentiation and Neuronal Migration of Neurons Derived from Human Embryonic Stem Cells. Stem Cells and Development. 2008;18(4):629-640.

218. Huang C, Xiang Y, Chen S, et al. Dermokine contributes to epithelial–mesenchymal transition through increased activation of signal transducer and activator of transcription 3 in pancreatic cancer. Cancer Science. 2017;108(11):2130-2141.

219. Cabezas F, Farfán P, Marzolo M-P. Participation of the SMAD2/3 signalling pathway in the down regulation of megalin/LRP2 by transforming growth factor beta (TGF-ß1). PLOS ONE. 2019;14(5):e0213127.

220. Elbitar S, Renard M, Arnaud P, et al. Pathogenic variants in THSD4, encoding the ADAMTS-like 6 protein, predispose to inherited thoracic aortic aneurysm. Genetics in Medicine. 2021;23(1):111-122.

221. Pavlakis E, Chiotaki R, Chalepakis G. The role of Fras1/Frem proteins in the structure and function of basement membrane. The International Journal of Biochemistry & Cell Biology. 2011;43(4):487-495.

222. Sewgobind NV, Albers S, Pieters RJ. Functions and Inhibition of Galectin-7, an Emerging Target in Cellular Pathophysiology. Biomolecules. 2021;11(11).

223. Nilchian A, Johansson J, Ghalali A, et al. CXADR-Mediated Formation of an AKT Inhibitory Signalosome at Tight Junctions Controls Epithelial–Mesenchymal Plasticity in Breast Cancer. Cancer Research. 2019;79(1):47-60.

224. McMahon M, Ye S, Pedrina J, Dlugolenski D, Stambas J. Extracellular Matrix Enzymes and Immune Cell Biology. Front Mol Biosci. 2021;8:703868.

225. Fan C, Tu C, Qi P, et al. GPC6 Promotes Cell Proliferation, Migration, and Invasion in Nasopharyngeal Carcinoma. (1837-9664 (Print)).

226. Feldt J, Schicht M, Garreis F, Welss J, Schneider UW, Paulsen F. Structure, regulation and related diseases of the actin-binding protein gelsolin. Expert Reviews in Molecular Medicine. 2019;20:e7.

227. Samuelov L, Li Q, Bochner R, et al. SVEP1 plays a crucial role in epidermal differentiation. Experimental Dermatology. 2017;26(5):423-430.

228. Powers RM, Hevner RF, Halpain S. The Neuron Navigators: Structure, function, and evolutionary history. Frontiers in Molecular Neuroscience. 2023;15.

229. Pagani F, Tratta E, Dell'Era P, Cominelli M, Poliani PL. EBF1 is expressed in pericytes and contributes to pericyte cell commitment. Histochemistry and Cell Biology. 2021;156(4):333-347.

230. Jimenez MA, Åkerblad P, Sigvardsson M, Rosen ED. Critical Role for Ebf1 and Ebf2 in the Adipogenic Transcriptional Cascade. Molecular and Cellular Biology. 2007;27(2):743-757.

231. Ihunnah CA, Wada T, Philips BJ, et al. Estrogen Sulfotransferase/SULT1E1 Promotes Human Adipogenesis. Molecular and Cellular Biology. 2014;34(9):1682-1694.

232. Inoue A, Aoki J. Phospholipase A1: structure, distribution and function. Future Lipidology. 2006;1(6):687-700.

233. Rassart E, Bedirian A, Do Carmo S, et al. Apolipoprotein D. Biochimica et Biophysica Acta (BBA) - Protein Structure and Molecular Enzymology. 2000;1482(1):185-198.

234. Goodyer WR, Beyersdorf BM, Duan L, et al. In vivo visualization and molecular targeting of the cardiac conduction system. LID - 10.1172/JCI156955 [doi] LID - e156955. (1558-8238 (Electronic)).

235. Peyser R, MacDonnell S, Gao Y, et al. Defining the Activated Fibroblast Population in Lung Fibrosis Using Single-Cell Sequencing. (1535-4989 (Electronic)).

236. Falls DL. Neuregulins: functions, forms, and signaling strategies. Experimental Cell Research. 2003;284(1):14-30.

237. Turner CE. Paxillin and focal adhesion signalling. (1465-7392 (Print)).

238. Hall A. Rho family GTPases. Biochemical Society Transactions. 2012;40(6):1378-1382.

239. Xu J, Zhang W. EZR promotes pancreatic cancer proliferation and metastasis by activating FAK/AKT signaling pathway. Cancer Cell International. 2021;21(1):521.

240. Round JE, Sun H. The adaptor protein Nck2 mediates Slit1-induced changes in cortical neuron morphology. Molecular and Cellular Neuroscience. 2011;47(4):265-273.

241. Dunbar AJ, Goddard C. Structure-function and biological role of betacellulin. The International Journal of Biochemistry & Cell Biology. 2000;32(8):805-815.

242. Sundvall M, Iljin K, Kilpinen S, Sara H, Kallioniemi O-P, Elenius K. Role of ErbB4 in Breast Cancer. Journal of Mammary Gland Biology and Neoplasia. 2008;13(2):259-268.

243. Kumar R, Sanawar R, Li X, Li F. Structure, biochemistry, and biology of PAK kinases. Gene. 2017;605:20-31.

244. Pisanti S, Picardi P, D'Alessandro A, Laezza C, Bifulco M. The endocannabinoid signaling system in cancer. Trends in Pharmacological Sciences. 2013;34(5):273-282.

245. Balcerczak E, Pasz-Walczak G, Kumor P, et al. Cyclin D1 protein and CCND1 gene expression in colorectal cancer. European Journal of Surgical Oncology (EJSO). 2005;31(7):721-726.

246. Tsai Y-C, Huang C-Y, Hsueh Y-M, et al. Genetic variants in MAPK10 modify renal cell carcinoma susceptibility and clinical outcomes. Life Sciences. 2021;275:119396.

247. Kiryushko D, Berezin V Fau - Bock E, Bock E. Regulators of neurite outgrowth: role of cell adhesion molecules. (0077-8923 (Print)).

248. Masi I, Caprara V, Spadaro F, et al. Endothelin-1 drives invadopodia and interaction with mesothelial cells through ILK. Cell Reports. 2021;34(9).

249. Pederick DT, Richards KL, Piltz SG, et al. Abnormal Cell Sorting Underlies the Unique X-Linked Inheritance of PCDH19 Epilepsy. Neuron. 2018;97(1):59-66.e55.

250. Gordon GJ, Rockwell GN, Jensen RV, et al. Identification of Novel Candidate Oncogenes and Tumor Suppressors in Malignant Pleural Mesothelioma Using Large-Scale Transcriptional Profiling. The American Journal of Pathology. 2005;166(6):1827-1840.

251. Castellana B, Escuin D Fau - Peiró G, Peiró G Fau - Garcia-Valdecasas B, et al. ASPN and GJB2 Are Implicated in the Mechanisms of Invasion of Ductal Breast Carcinomas. (1837-9664 (Electronic)).

252. Oliveira J, Gruber A, Cardoso M, et al. LAMA2 gene mutation update: Toward a more comprehensive picture of the laminin-α2 variome and its related phenotypes. Human Mutation. 2018;39(10):1314-1337.

253. Miller WL. Tenascin-X—Discovery and Early Research. Frontiers in Immunology. 2021;11.

254. Wang Y, Tu Z, Zhao W, et al. PLCB1 Enhances Cell Migration and Invasion in Gastric Cancer Via Regulating Actin Cytoskeletal Remodeling and Epithelial–Mesenchymal Transition. Biochemical Genetics. 2023;61(6):2618-2632.

255. Zhou Y, Ling T, Shi W. Current state of signaling pathways associated with the pathogenesis of idiopathic pulmonary fibrosis. (1465-993X (Electronic)).

256. Naderi A. Molecular functions of brain expressed X-linked 2 (BEX2) in malignancies. (1090-2422 (Electronic)).

257. Kamato D, Mitra P, Davis F, et al. Ga(q) proteins: molecular pharmacology and therapeutic potential. (1420-9071 (Electronic)).

258. Lim PS, Sutton CR, Rao S. Protein kinase C in the immune system: from signalling to chromatin regulation. (1365-2567 (Electronic)).

259. Schultheiss TM, James RG, Listopadova A, Herzlinger D. 4 - Formation of the Nephric Duct. In: Vize PD, Woolf AS, Bard JBL. The Kidney. San Diego: Academic Press; 2003.

260. Wu S, Zhang W, Shen D, Lu J, Zhao L. PLCB4 upregulation is associated with unfavorable prognosis in pediatric acute myeloid leukemia. Oncol Lett. 2019;18(6):6057-6065.

261. Wang F, Wang L, Shen M, Ma L. GRK5 deficiency decreases diet-induced obesity and adipogenesis. Biochemical and Biophysical Research Communications. 2012;421(2):312-317.

262. Shi J, Jiang D, Yang S, et al. LPAR1, Correlated With Immune Infiltrates, Is a Potential Prognostic Biomarker in Prostate Cancer. Frontiers in Oncology. 2020;10.

263. Liu L, Arévalo-Martínez M, Rippe C, et al. Itga8-Cre-mediated deletion of YAP and TAZ impairs bladder contractility with minimal inflammation and chondrogenic differentiation. American Journal of Physiology-Cell Physiology. 2023;325(6):C1485-C1501.

264. Wang T, Baron M, Trump D. An overview of Notch3 function in vascular smooth muscle cells. Progress in Biophysics and Molecular Biology. 2008;96(1):499-509.

265. Kolev V, Mandinova A, Guinea-Viniegra J, et al. EGFR signalling as a negative regulator of Notch1 gene transcription and function in proliferating keratinocytes and cancer. Nature Cell Biology. 2008;10(8):902-911.

266. Minnone G, De Benedetti F, Bracci-Laudiero L. NGF and Its Receptors in the Regulation of Inflammatory Response. International journal of molecular sciences. 2017;18(5).

267. Chaiwatanasirikul KA, Sala A. The tumour-suppressive function of CLU is explained by its localisation and interaction with HSP60. Cell Death & Disease. 2011;2(10):e219-e219.

268. Jaberi SA, Cohen A, D'Souza C, et al. Lipocalin-2: Structure, function, distribution and role in metabolic disorders. Biomedicine & Pharmacotherapy. 2021;142:112002.

269. Lazo JS, Pitt BR. Metallothioneins and cell death by anticancer drugs. Annu Rev Pharmacol Toxicol. 1995;35:635-653.

270. Zou L, Feng Y, Li Y, et al. Complement Factor B Is the Downstream Effector of TLRs and Plays an Important Role in a Mouse Model of Severe Sepsis. The Journal of Immunology. 2013;191(11):5625-5635.

271. Kim GS, Harmon E, Gutierrez MC, et al. Single-cell analysis identifies Ifi27l2a as a gene regulator of microglial inflammation in the context of aging and stroke in mice. Nature Communications. 2025;16(1):1639.

272. Takeda E, Nakagawa S, Nakaya Y, Tanaka A, Miyazawa T, Yasuda J. Identification and Functional Analysis of Three Isoforms of Bovine BST-2. PLOS ONE. 2012;7(7):e41483.

273. Ning S, Pagano JS, Barber GN. IRF7: activation, regulation, modification and function. Genes & Immunity. 2011;12(6):399-414.

274. Wang Y, Gu W, Wen W, Zhang X. SERPINH1 is a Potential Prognostic Biomarker and Correlated With Immune Infiltration: A Pan-Cancer Analysis. Frontiers in Genetics. 2022;12.

275. Bi L, Liu Y, Zhang L, Zhang X, Wang D. High expression of SERPINE1 and CTSL in keratinocytes in pressure injury caused by ischemia-reperfusion injury. Tissue and Cell. 2025;93:102746.

276. Yang R, Zheng G, Ren D, et al. The clinical significance and biological function of tropomyosin 4 in colon cancer. Biomedicine & Pharmacotherapy. 2018;101:1-7.

277. Bradshaw AD, Sage EH. SPARC, a matricellular protein that functions in cellular differentiation and tissue response to injury. The Journal of clinical investigation. 2001;107(9):1049-1054.

278. Cano A, Eraso P, Mazón MJ, Portillo F. LOXL2 in Cancer: A Two-Decade Perspective. International journal of molecular sciences. 2023;24(18).

279. Djurec M, Graña O, Lee A, et al. Saa3 is a key mediator of the protumorigenic properties of cancer-associated fibroblasts in pancreatic tumors. Proceedings of the National Academy of Sciences. 2018;115(6):E1147-E1156.

280. Gong L, Si M-S. SLIT3-mediated fibroblast signaling: a promising target for antifibrotic therapies. American Journal of Physiology-Heart and Circulatory Physiology. 2023;325(6):H1400-H1411.

281. Upadhyay G. Emerging Role of Lymphocyte Antigen-6 Family of Genes in Cancer and Immune Cells. Frontiers in Immunology. 2019;10.

282. Ma Z, Sun Q, Zhang C, et al. RHOJ Induces Epithelial-to-Mesenchymal Transition by IL-6/STAT3 to Promote Invasion and Metastasis in Gastric Cancer. (1449-2288 (Electronic)).

283. Nieddu V, Melocchi V, Battistini C, et al. Matrix Gla Protein drives stemness and tumor initiation in ovarian cancer. Cell Death & Disease. 2023;14(3):220.

284. Loats AE, Carrera S, Fleming AF, et al. Cholesterol is required for transcriptional repression by BASP1. Proceedings of the National Academy of Sciences. 2021;118(29):e2101671118.

285. Zhang D, Dai L, Yang Z, Wang X, LanNing Y. Association of STMN1 with survival in solid tumors: A systematic review and meta-analysis. The International Journal of Biological Markers. 2019;34(2):108-116.

286. Pfister KK, Shah PR, Hummerich H, et al. Genetic Analysis of the Cytoplasmic Dynein Subunit Families. PLOS Genetics. 2006;2(1):e1.

287. Chao CCK, Hung F-C, Chao JJ. Gas7 Is Required for Mesenchymal Stem Cell-Derived Bone Development. Stem Cells International. 2013;2013(1):137010.

288. Xie G-f, Zhao L-d, Chen Q, et al. High ACTN1 Is Associated with Poor Prognosis, and ACTN1 Silencing Suppresses Cell Proliferation and Metastasis in Oral Squamous Cell Carcinoma. Drug Design, Development and Therapy. 2020;14(null):1717-1727.

289. Allen-Gondringer A, Gau D, Varghese C, et al. Vascular endothelial cell-specific disruption of the profilin1 gene leads to severe multiorgan pathology and inflammation causing mortality. PNAS Nexus. 2023;2(10):pgad305.

290. Li C, Ma H, Wang Y, et al. Excess PLAC8 promotes an unconventional ERK2-dependent EMT in colon cancer. The Journal of clinical investigation. 2014;124(5):2172-2187.

291. Alquraini A, Jamal M, Zhang L, Schmidt T, Jay GD, Elsaid KA. The autocrine role of proteoglycan-4 (PRG4) in modulating osteoarthritic synoviocyte proliferation and expression of matrix degrading enzymes. Arthritis Research & Therapy. 2017;19(1):89.

292. Xiong Y, Qi Y, Pan Z, et al. Pancancer landscape analysis of the thymosin family identified TMSB10 as a potential prognostic biomarker and immunotherapy target in glioma. (1475-2867 (Print)).

293. Yang Z, Luo J, Zhang M, et al. TMSB4X: A novel prognostic marker for non-small cell lung cancer. Heliyon. 2023;9(11):e21505.

294. Bock-Marquette I, Saxena A, White MD, Michael DiMaio J, Srivastava D. Thymosin β4 activates integrin-linked kinase and promotes cardiac cell migration, survival and cardiac repair. Nature. 2004;432(7016):466-472.

295. Takayama K-i, Horie-Inoue K, Suzuki T, et al. TACC2 Is an Androgen-Responsive Cell Cycle Regulator Promoting Androgen-Mediated and Castration-Resistant Growth of Prostate Cancer. Molecular Endocrinology. 2012;26(5):748-761.

296. Feng J, Pan W, Yang X, et al. RBM3 Increases Cell Survival but Disrupts Tight Junction of Microvascular Endothelial Cells in Acute Lung Injury. Journal of Surgical Research. 2021;261:226-235.

297. Sosne G, Rimmer D, Kleinman HK, Ousler G. Chapter Twelve - Thymosin Beta 4: A Potential Novel Therapy for Neurotrophic Keratopathy, Dry Eye, and Ocular Surface Diseases. In: Litwack G. Vitamins and Hormones. Vol 102: Academic Press; 2016.

298. Olianas A, Serrao S Fau - Piras V, Piras V Fau - Manconi B, et al. Thymosin β4 and β10 are highly expressed at the deep infiltrative margins of colorectal cancer - A mass spectrometry analysis. (2284-0729 (Electronic)).

299. Wellmann S, Truss M, Bruder E, et al. The RNA-Binding Protein RBM3 Is Required for Cell Proliferation and Protects Against Serum Deprivation-Induced Cell Death. Pediatric Research. 2010;67(1):35-41.

300. Glembotski CC, Thuerauf DJ, Huang C, Vekich JA, Gottlieb RA, Doroudgar S. Mesencephalic Astrocyte-derived Neurotrophic Factor Protects the Heart from Ischemic Damage and Is Selectively Secreted upon Sarco/endoplasmic Reticulum Calcium Depletion *. Journal of Biological Chemistry. 2012;287(31):25893-25904.

301. Ho DV, Chan JY. Induction of Herpud1 expression by ER stress is regulated by Nrf1. FEBS Letters. 2015;589(5):615-620.

302. Oh-hashi K, Koga H, Ikeda S, Shimada K, Hirata Y, Kiuchi K. CRELD2 is a novel endoplasmic reticulum stress-inducible gene. Biochemical and Biophysical Research Communications. 2009;387(3):504-510.

303. Li T, Fu J, Cheng J, Elfiky AA, Wei C, Fu J. New progresses on cell surface protein HSPA5/BiP/GRP78 in cancers and COVID-19. Frontiers in Immunology. 2023;14.

304. Stricher F, Macri C, Ruff M, Muller S. HSPA8/HSC70 chaperone protein. Autophagy. 2013;9(12):1937-1954.

305. Bukau B, Weissman J, Horwich A. Molecular Chaperones and Protein Quality Control. Cell. 2006;125(3):443-451.

306. Liu B, Li Z. Endoplasmic reticulum HSP90b1 (gp96, grp94) optimizes B-cell function via chaperoning integrin and TLR but not immunoglobulin. Blood. 2008;112(4):1223-1230.

307. Petrova K, Oyadomari S, Hendershot LM, Ron D. Regulated association of misfolded endoplasmic reticulum lumenal proteins with P58/DNAJc3. The EMBO journal. 2008;27(21):2862-2872-2872.

308. Kim H-Y, Kim Y-M, Hong S. DNAJB9 suppresses the metastasis of triple-negative breast cancer by promoting FBXO45-mediated degradation of ZEB1. Cell Death & Disease. 2021;12(5):461.

309. Cimmino F, Avitabile M, Lasorsa VA, et al. HIF-1 transcription activity: HIF1A driven response in normoxia and in hypoxia. BMC Medical Genetics. 2019;20(1):37.

310. Liu L, Cara DC, Kaur J, et al. LSP1 is an endothelial gatekeeper of leukocyte transendothelial migration. Journal of Experimental Medicine. 2005;201(3):409-418.

311. Drake LY, Kita H. IL-33: biological properties, functions, and roles in airway disease. Immunological Reviews. 2017;278(1):173-184.

312. Wang C, Hayashi H, Harrison R, et al. Modulation of Mac-1 (CD11b/CD18)-Mediated Adhesion by the Leukocyte-Specific Protein 1 Is Key to Its Role in Neutrophil Polarization and Chemotaxis1. The Journal of Immunology. 2002;169(1):415-423.

313. Sun Y, Chen X, Chen L, Bao B, Li C, Zhou YA-OX. MFAP2 promotes HSCs activation through FBN1/TGF-β/Smad3 pathway. (1582-4934 (Electronic)).

314. Kanaan R, Medlej-Hashim M, Jounblat R, Pilecki B, Sorensen GL. Microfibrillar-associated protein 4 in health and disease. Matrix Biology. 2022;111:1-25.

315. Zhu X, Cheng Y, Wu F, et al. MFAP2 Promotes the Proliferation of Cancer Cells and Is Associated With a Poor Prognosis in Hepatocellular Carcinoma. Technology in Cancer Research & Treatment. 2020;19:1533033820977524.

316. Devos H, Zoidakis J, Roubelakis MG, Latosinska A, Vlahou A. Reviewing the Regulators of COL1A1. International journal of molecular sciences. 2023;24(12).

317. Schlosser A, Pilecki B, Hemstra LE, et al. MFAP4 Promotes Vascular Smooth Muscle Migration, Proliferation and Accelerates Neointima Formation. Arteriosclerosis, Thrombosis, and Vascular Biology. 2016;36(1):122-133.

318. Jiang H, Liu Y, Qian Y, et al. CHL1 promotes insulin secretion and negatively regulates the proliferation of pancreatic β cells. Biochemical and Biophysical Research Communications. 2020;525(4):1095-1102.

319. Bassani S, Chrast J, Ambrosini G, et al. Variant-specific pathophysiological mechanisms of AFF3 differently influence transcriptome profiles. Genome Medicine. 2024;16(1):72.

320. Itoh-Nakadai A, Matsumoto M, Kato H, et al. A Bach2-Cebp Gene Regulatory Network for the Commitment of Multipotent Hematopoietic Progenitors. Cell Reports. 2017;18(10):2401-2414.

321. Zwick D, Vo MT, Shim YA-O, Reijonen H, Do JA-O. BACH2: The Future of Induced T-Regulatory Cell Therapies. LID - 10.3390/cells13110891 [doi] LID - 891. (2073-4409 (Electronic)).

322. Mirotsou M, Zhang Z, Deb A, et al. Secreted frizzled related protein 2 (Sfrp2) is the key Akt-mesenchymal stem cell-released paracrine factor mediating myocardial survival and repair. Proceedings of the National Academy of Sciences. 2007;104(5):1643-1648.

323. Levanon D, Brenner O, Negreanu V, et al. Spatial and temporal expression pattern of Runx3 (Aml2) and Runx1 (Aml1) indicates non-redundant functions during mouse embryogenesis. Mechanisms of Development. 2001;109(2):413-417.

324. Britanova O, Lukyanov S, Gruss P, Tarabykin V. The Mouse Laf4 Gene: Exon/Intron Organization, cDNA Sequence, Alternative Splicing, and Expression during Central Nervous System Development. Genomics. 2002;80(1):31-37.

325. Bugg D, Bailey LRJ, Bretherton RC, et al. MBNL1 drives dynamic transitions between fibroblasts and myofibroblasts in cardiac wound healing. Cell Stem Cell. 2022;29(3):419-433.e410.

326. Qi Y, Wang M, Jiang Q. PABPC1——mRNA stability, protein translation and tumorigenesis. Frontiers in Oncology. 2022;12.

327. Pernot M, Jaspard-vinassa B, Abelanet A, et al. Decrease of Pdzrn3 is required for heart maturation and protects against heart failure. Scientific Reports. 2022;12(1):8.

328. Fernández JR, Byrne B, Firestein BL. Phylogenetic Analysis and Molecular Evolution of Guanine Deaminases: From Guanine to Dendrites. Journal of Molecular Evolution. 2009;68(3):227-235.

329. Paiva RS, Ramos CV, Azenha SR, et al. Peptidylprolyl isomerase C (Ppic) regulates invariant Natural Killer T cell (iNKT) differentiation in mice. European Journal of Immunology. 2021;51(8):1968-1979.

330. Nusse R, Clevers H. Wnt/β-Catenin Signaling, Disease, and Emerging Therapeutic Modalities. Cell. 2017;169(6):985-999.

331. Yang B, Bai J, Shi R, et al. TGFB2 serves as a link between epithelial-mesenchymal transition and tumor mutation burden in gastric cancer. International Immunopharmacology. 2020;84:106532.

332. Ward Y, Kelly K. Gem Protein Signaling and Regulation. Methods in Enzymology. Vol 407: Academic Press; 2006.

333. Hori KA-O, Shimaoka K, Hoshino M. AUTS2 Gene: Keys to Understanding the Pathogenesis of Neurodevelopmental Disorders. LID - 10.3390/cells11010011 [doi] LID - 11. (2073-4409 (Electronic)).

334. Sah JP, Hao NTT, Han X, et al. Ectonucleotide pyrophosphatase 2 (ENPP2) plays a crucial role in myogenic differentiation through the regulation by WNT/β-Catenin signaling. The International Journal of Biochemistry & Cell Biology. 2020;118:105661.

335. Drápela S, Bouchal J, Jolly MK, Culig Z, Souček K. ZEB1: A Critical Regulator of Cell Plasticity, DNA Damage Response, and Therapy Resistance. Frontiers in Molecular Biosciences. 2020;7.

336. Xu J, Lamouille S Fau - Derynck R, Derynck R. TGF-beta-induced epithelial to mesenchymal transition. (1748-7838 (Electronic)).

337. Pegtel DM, Ellenbroek Si Fau - Mertens AEE, Mertens Ae Fau - van der Kammen RA, van der Kammen Ra Fau - de Rooij J, de Rooij J Fau - Collard JG, Collard JG. The Par-Tiam1 complex controls persistent migration by stabilizing microtubule-dependent front-rear polarity. (0960-9822 (Print)).

338. Godde NJ, Galea Rc Fau - Elsum IA, Elsum Ia Fau - Humbert PO, Humbert PO. Cell polarity in motion: redefining mammary tissue organization through EMT and cell polarity transitions. (1573-7039 (Electronic)).

339. Wu X, Wang J, Liang Q, et al. Recent progress on FAK inhibitors with dual targeting capabilities for cancer treatment. Biomedicine & Pharmacotherapy. 2022;151:113116.

340. Wu C. Focal adhesion: a focal point in current cell biology and molecular medicine. (1933-6926 (Electronic)).

341. Jin SA-O, Guerrero-Juarez CA-O, Zhang L, et al. Inference and analysis of cell-cell communication using CellChat. (2041-1723 (Electronic)).

342. Merle NS, Singh P, Rahman J, Kemper C. Integrins meet complement: The evolutionary tip of an iceberg orchestrating metabolism and immunity. British Journal of Pharmacology. 2021;178(14):2754-2770.

343. Bajic G, Yatime L, Sim RB, Vorup-Jensen T, Andersen GR. Structural insight on the recognition of surface-bound opsonins by the integrin I domain of complement receptor 3. Proceedings of the National Academy of Sciences. 2013;110(41):16426-16431.

344. Govindaraju P, Todd L, Shetye S, Monslow J, Puré E. CD44-dependent inflammation, fibrogenesis, and collagenolysis regulates extracellular matrix remodeling and tensile strength during cutaneous wound healing. Matrix Biology. 2019;75-76:314-330.

345. Danen EHJ, Yamada KM. Fibronectin, integrins, and growth control. Journal of Cellular Physiology. 2001;189(1):1-13.

346. Su H, Na N, Zhang X, Zhao Y. The biological function and significance of CD74 in immune diseases. Inflammation Research. 2017;66(3):209-216.

347. Stamatelopoulos K, Sibbing D, Rallidis Loukianos S, et al. Amyloid-Beta (1-40) and the Risk of Death From Cardiovascular Causes in Patients With Coronary Heart Disease. JACC. 2015;65(9):904-916.

348. Gagno G, Ferro F, Fluca AL, et al. From Brain to Heart: Possible Role of Amyloid-? in Ischemic Heart Disease and Ischemia-Reperfusion Injury. International journal of molecular sciences. 2020;21(24).

349. Haase N, Herse F, Spallek B, et al. Amyloid-β Peptides Activate α1-Adrenergic Cardiovascular Receptors. Hypertension. 2013;62(5):966-972.

350. Na KY, Bacchini P, Bertoni F, Kim YW, Park Y-K. Syndecan-4 and fibronectin in osteosarcoma. Pathology. 2012;44(4):325-330.

351. Midwood KS, Valenick Lv Fau - Hsia HC, Hsia Hc Fau - Schwarzbauer JE, Schwarzbauer JE. Coregulation of fibronectin signaling and matrix contraction by tenascin-C and syndecan-4. (1059-1524 (Print)).

352. Lacy SE, Bönnemann CG, Buzney EA, Kunkel LM. Identification of FLRT1, FLRT2, and FLRT3: A Novel Family of Transmembrane Leucine-Rich Repeat Proteins. Genomics. 1999;62(3):417-426.

353. Schlueter J, Brand T. Epicardial Progenitor Cells in Cardiac Development and Regeneration. Journal of Cardiovascular Translational Research. 2012;5(5):641-653.

354. Wolfe CM, Fitz NF, Nam KN, Lefterov I, Koldamova R. The Role of APOE and TREM2 in Alzheimer's Disease—Current Understanding and Perspectives. International journal of molecular sciences. 2019;20(1).

355. Mahoney-Sanchez L, Belaidi AA, Bush AI, Ayton S. The Complex Role of Apolipoprotein E in Alzheimer's Disease: an Overview and Update. Journal of Molecular Neuroscience. 2016;60(3):325-335.

356. Matsuoka S, Facchini RA-O, Luis TA-O, et al. Loss of endothelial membrane KIT ligand affects systemic KIT ligand levels but not bone marrow hematopoietic stem cells. (1528-0020 (Electronic)).

357. Vaine CA, Soberman RJ. The CD200-CD200R1 inhibitory signaling pathway: immune regulation and host-pathogen interactions. (1557-8445 (Electronic)).

358. Xie Y, Su N, Yang J, et al. FGF/FGFR signaling in health and disease. Signal Transduction and Targeted Therapy. 2020;5(1):181.

359. Zhang XA-O, Shao S, Li L. Characterization of Class-3 Semaphorin Receptors, Neuropilins and Plexins, as Therapeutic Targets in a Pan-Cancer Study. LID - 10.3390/cancers12071816 [doi] LID - 1816. (2072-6694 (Print)).

360. Li Y, Lua I, French SW, Asahina K. Role of TGF-β signaling in differentiation of mesothelial cells to vitamin A-poor hepatic stellate cells in liver fibrosis. (1522-1547 (Electronic)).

361. Tzavlaki K, Moustakas AA-O. TGF-β Signaling. LID - 10.3390/biom10030487 [doi] LID - 487. (2218-273X (Electronic)).

362. Piek E, Moustakas A Fau - Kurisaki A, Kurisaki A Fau - Heldin CH, Heldin Ch Fau - ten Dijke P, ten Dijke P. TGF-(beta) type I receptor/ALK-5 and Smad proteins mediate epithelial to mesenchymal transdifferentiation in NMuMG breast epithelial cells. (0021-9533 (Print)).

363. Carulli D, de Winter F, Verhaagen J. Semaphorins in Adult Nervous System Plasticity and Disease. Frontiers in Synaptic Neuroscience. 2021;13.

364. Schwarz Q, Waimey Ke Fau - Golding M, Golding M Fau - Takamatsu H, et al. Plexin A3 and plexin A4 convey semaphorin signals during facial nerve development. (1095-564X (Electronic)).

365. Christie SM, Hao J, Tracy E, Buck M, Yu JS, Smith AW. Interactions between semaphorins and plexin-neuropilin receptor complexes in the membranes of live cells. (1083-351X (Electronic)).

366. Huang F, Zhang J, Zhou H, et al. B cell subsets contribute to myocardial protection by inducing neutrophil apoptosis after ischemia and reperfusion. LID - 10.1172/jci.insight.167201 [doi] LID - e167201. (2379-3708 (Electronic)).

367. García-Serna AM, Alcaraz-García MJ, Ruiz-Lafuente N, et al. Dock10 regulates CD23 expression and sustains B-cell lymphopoiesis in secondary lymphoid tissue. (1878-3279 (Electronic)).

368. Mahauad-Fernandez WD, Naushad W, Panzner TD, Bashir A, Lal G, Okeoma CM. BST-2 promotes survival in circulation and pulmonary metastatic seeding of breast cancer cells. Scientific Reports. 2018;8(1):17608.

369. Cohn RD, Henry MD, Michele DE, et al. Disruption of Dag1 in Differentiated Skeletal Muscle Reveals a Role for Dystroglycan in Muscle Regeneration. Cell. 2002;110(5):639-648.

370. Zhang H, Pan Y-z, Cheung M, et al. LAMB3 mediates apoptotic, proliferative, invasive, and metastatic behaviors in pancreatic cancer by regulating the PI3K/Akt signaling pathway. Cell Death & Disease. 2019;10(3):230.

371. Tahara-Hanaoka S, Shibuya K, Onoda Y, et al. Functional characterization of DNAM-1 (CD226) interaction with its ligands PVR (CD155) and nectin-2 (PRR-2/CD112). International Immunology. 2004;16(4):533-538.

372. Bui TM, Wiesolek HL, Sumagin RA-O. ICAM-1: A master regulator of cellular responses in inflammation, injury resolution, and tumorigenesis. (1938-3673 (Electronic)).

373. Shi N, Chen S, Wang D, et al. MDK promotes M2 macrophage polarization to remodel the tumour microenvironment in clear cell renal cell carcinoma. Scientific Reports. 2024;14(1):18254.

374. Sorrelle N, Dominguez ATA, Brekken RA. From top to bottom: midkine and pleiotrophin as emerging players in immune regulation. (1938-3673 (Electronic)).

375. Li Y-Q, Sun F-Z, Li C-X, et al. RARRES2 regulates lipid metabolic reprogramming to mediate the development of brain metastasis in triple negative breast cancer. Military Medical Research. 2023;10(1):34.

376. Yamaguchi J-i, Kusano KF, Masuo O, et al. Stromal Cell–Derived Factor-1 Effects on Ex Vivo Expanded Endothelial Progenitor Cell Recruitment for Ischemic Neovascularization. Circulation. 2003;107(9):1322-1328.

377. Rath D, Chatterjee M, Borst O, et al. Expression of stromal cell-derived factor-1 receptors CXCR4 and CXCR7 on circulating platelets of patients with acute coronary syndrome and association with left ventricular functional recovery. European Heart Journal. 2014;35(6):386-394.

378. Watson J, Francavilla C. Regulation of FGF10 Signaling in Development and Disease. Frontiers in Genetics. 2018;9.

379. Bucala R Fau - Shachar I, Shachar I. The integral role of CD74 in antigen presentation, MIF signal transduction, and B cell survival and homeostasis. (1875-5607 (Electronic)).

380. Farr L, Ghosh S, Moonah S. Role of MIF Cytokine/CD74 Receptor Pathway in Protecting Against Injury and Promoting Repair. Frontiers in Immunology. 2020;11.

381. Zdżalik-Bielecka D, Poświata A, Kozik K, et al. The GAS6-AXL signaling pathway triggers actin remodeling that drives membrane ruffling, macropinocytosis, and cancer-cell invasion. Proceedings of the National Academy of Sciences. 2021;118(28):e2024596118.

382. Gao Y, Li F, Zhang Y, et al. Silencing of ADIPOQ Efficiently Suppresses Preadipocyte Differentiation in Porcine. Cellular Physiology and Biochemistry. 2013;31(2-3):452-461.

383. Aguirre GA, De Ita JR, de la Garza RG, Castilla-Cortazar I. Insulin-like growth factor-1 deficiency and metabolic syndrome. Journal of Translational Medicine. 2016;14(1):3.

384. Heinen A, Nederlof R, Panjwani P, et al. IGF1 Treatment Improves Cardiac Remodeling after Infarction by Targeting Myeloid Cells. (1525-0024 (Electronic)).

385. Nederlof R, Reidel S, Spychala A, et al. Insulin-Like Growth Factor 1 Attenuates the Pro-Inflammatory Phenotype of Neutrophils in Myocardial Infarction. (1664-3224 (Electronic)).

386. Horii N, Sato K, Mesaki N, Iemitsu M. DHEA administration activates transcription of muscular lipid metabolic enzymes via PPARα and PPARδ in obese rats. Hormone and Metabolic Research. 2016;48(03):207-212.

387. Michaud A, Lacroix-Pépin N, Pelletier M, et al. Expression of Genes Related to Prostaglandin Synthesis or Signaling in Human Subcutaneous and Omental Adipose Tissue: Depot Differences and Modulation by Adipogenesis. Mediators of Inflammation. 2014;2014(1):451620.

388. Tsuboi H, Sugimoto Y, Kainoh T, Ichikawa A. Prostanoid EP4 receptor is involved in suppression of 3T3-L1 adipocyte differentiation. Biochemical and Biophysical Research Communications. 2004;322(3):1066-1072.

389. Burns JM, Summers BC, Wang Y, et al. A novel chemokine receptor for SDF-1 and I-TAC involved in cell survival, cell adhesion, and tumor development. Journal of Experimental Medicine. 2006;203(9):2201-2213.

390. Jeansson M, Gawlik A, Anderson G, et al. Angiopoietin-1 is essential in mouse vasculature during development and in response to injury. The Journal of clinical investigation. 2011;121(6):2278-2289.

391. Lee J, Gray A Fau - Yuan J, Yuan J Fau - Luoh SM, Luoh Sm Fau - Avraham H, Avraham H Fau - Wood WI, Wood WI. Vascular endothelial growth factor-related protein: a ligand and specific activator of the tyrosine kinase receptor Flt4. (0027-8424 (Print)).

392. Liu Y, Soto I, Tong Q, et al. SIRPβ1 Is Expressed as a Disulfide-linked Homodimer in Leukocytes and Positively Regulates Neutrophil Transepithelial Migration*. Journal of Biological Chemistry. 2005;280(43):36132-36140.

393. Hu Z, Jin X, Hong W, et al. Dissecting the single-cell transcriptome network of macrophage and identifies a signature to predict prognosis in lung adenocarcinoma. (2211-3436 (Electronic)).

394. Smith LK, Fawaz K, Treanor B. Galectin-9 regulates the threshold of B cell activation and autoimmunity. eLife. 2021;10:e64557.

395. Schuette V, Embgenbroich M, Ulas T, et al. Mannose receptor induces T-cell tolerance via inhibition of CD45 and up-regulation of CTLA-4. Proceedings of the National Academy of Sciences of the United States of America. 2016;113.

396. Cedrés S, Montero Ma Fau - Zamora E, Zamora E Fau - Martínez A, et al. Expression of Wilms' tumor gene (WT1) is associated with survival in malignant pleural mesothelioma. (1699-3055 (Electronic)).

397. Karki S, Surolia R Fau - Hock TD, Hock Td Fau - Guroji P, et al. Wilms' tumor 1 (Wt1) regulates pleural mesothelial cell plasticity and transition into myofibroblasts in idiopathic pulmonary fibrosis. (1530-6860 (Electronic)).

398. Taniguchi T, Tomita HA-O, Kanayama T, et al. Regulation of Mesothelial Cell Fate during Development and Human Diseases. LID - 10.3390/ijms231911960 [doi] LID - 11960. (1422-0067 (Electronic)).

399. Dao T, Scheinberg DA. Peptide vaccines for myeloid leukaemias. Best Practice & Research Clinical Haematology. 2008;21(3):391-404.

400. Toska E, Roberts SG. Mechanisms of transcriptional regulation by WT1 (Wilms' tumour 1). (1470-8728 (Electronic)).

401. Moore AW, McInnes L Fau - Kreidberg J, Kreidberg J Fau - Hastie ND, Hastie Nd Fau - Schedl A, Schedl A. YAC complementation shows a requirement for Wt1 in the development of epicardium, adrenal gland and throughout nephrogenesis. (0950-1991 (Print)).

402. Herzer U, Crocoll A Fau - Barton D, Barton D Fau - Howells N, Howells N Fau - Englert C, Englert C. The Wilms tumor suppressor gene wt1 is required for development of the spleen. (0960-9822 (Print)).

403. Chau YY, Hastie ND. The role of Wt1 in regulating mesenchyme in cancer, development, and tissue homeostasis. (0168-9525 (Print)).

404. Chau YY, Brownstein D Fau - Mjoseng H, Mjoseng H Fau - Lee W-C, et al. Acute multiple organ failure in adult mice deleted for the developmental regulator Wt1. (1553-7404 (Electronic)).

405. Hastie NA-OX. Wilms' tumour 1 (WT1) in development, homeostasis and disease. (1477-9129 (Electronic)).

406. Wilm B, Muñoz-Chapuli R. The Role of WT1 in Embryonic Development and Normal Organ Homeostasis. (1940-6029 (Electronic)).

407. Huff V. Wilms' tumours: about tumour suppressor genes, an oncogene and a chameleon gene. (1474-1768 (Electronic)).

408. Han Y, San-Marina S, Liu J, Minden MD. Transcriptional activation of c-myc proto-oncogene by WT1 protein. Oncogene. 2004;23(41):6933-6941.

409. Wang ZY, Madden Sl Fau - Deuel TF, Deuel Tf Fau - Rauscher FJ, 3rd, Rauscher FJ, 3rd. The Wilms' tumor gene product, WT1, represses transcription of the platelet-derived growth factor A-chain gene. (0021-9258 (Print)).

410. Takeichi M, Nimura K Fau - Mori M, Mori M Fau - Nakagami H, Nakagami H Fau - Kaneda Y, Kaneda Y. The transcription factors Tbx18 and Wt1 control the epicardial epithelial-mesenchymal transition through bi-directional regulation of Slug in murine primary epicardial cells. (1932-6203 (Electronic)).

411. Werner H, Shen-Orr Z Fau - Rauscher FJ, 3rd, Rauscher Fj 3rd Fau - Morris JF, Morris Jf Fau - Roberts CT, Jr., Roberts Ct Jr Fau - LeRoith D, LeRoith D. Inhibition of cellular proliferation by the Wilms' tumor suppressor WT1 is associated with suppression of insulin-like growth factor I receptor gene expression. (0270-7306 (Print)).

412. Hosono S, Gross I Fau - English MA, English Ma Fau - Hajra KM, Hajra Km Fau - Fearon ER, Fearon Er Fau - Licht JD, Licht JD. E-cadherin is a WT1 target gene. (0021-9258 (Print)).

413. Wagner N, Wagner Kd Fau - Xing Y, Xing Y Fau - Scholz H, Scholz H Fau - Schedl A, Schedl A. The major podocyte protein nephrin is transcriptionally activated by the Wilms' tumor suppressor WT1. (1046-6673 (Print)).

414. Drummond IA, Madden SI Fau - Rohwer-Nutter P, Rohwer-Nutter P Fau - Bell GI, Bell Gi Fau - Sukhatme VP, Sukhatme Vp Fau - Rauscher FJ, 3rd, Rauscher FJ, 3rd. Repression of the insulin-like growth factor II gene by the Wilms tumor suppressor WT1. (0036-8075 (Print)).

415. Idelman G, Glaser T, Roberts CT, Jr., Werner H. WT1-p53 Interactions in Insulin-like Growth Factor-I Receptor Gene Regulation *. Journal of Biological Chemistry. 2003;278(5):3474-3482.

416. Essafi A, Webb A Fau - Berry RL, Berry Rl Fau - Slight J, et al. A wt1-controlled chromatin switching mechanism underpins tissue-specific wnt4 activation and repression. (1878-1551 (Electronic)).

417. Martínez-Estrada OM, Lettice LA, Essafi A, et al. Wt1 is required for cardiovascular progenitor cell formation through transcriptional control of Snail and E-cadherin. Nature Genetics. 2010;42(1):89-93.

418. Chau Y-Y, Brownstein D, Mjoseng H, et al. Acute Multiple Organ Failure in Adult Mice Deleted for the Developmental Regulator Wt1. PLOS Genetics. 2011;7(12):e1002404.

419. Zangi L, Oliveira MS, Ye LY, et al. Insulin-Like Growth Factor 1 Receptor-Dependent Pathway Drives Epicardial Adipose Tissue Formation After Myocardial Injury. (1524-4539 (Electronic)).

420. Westcott GP, Emont MP, Li J, Jacobs C, Tsai L, Rosen ED. Mesothelial cells are not a source of adipocytes in mice. Cell Reports. 2021;36(2).

421. Nisticò P, Bissell Mj Fau - Radisky DC, Radisky DC. Epithelial-mesenchymal transition: general principles and pathological relevance with special emphasis on the role of matrix metalloproteinases. LID - 10.1101/cshperspect.a011908 [doi] LID - a011908. (1943-0264 (Electronic)).

422. Kalluri R, Weinberg RA. The basics of epithelial-mesenchymal transition. The Journal of clinical investigation. 2009;119(6):1420-1428.

423. Kalluri R. EMT: when epithelial cells decide to become mesenchymal-like cells. (1558-8238 (Electronic)).

424. Perez-Oquendo MA-O, Gibbons DL. Regulation of ZEB1 Function and Molecular Associations in Tumor Progression and Metastasis. LID - 10.3390/cancers14081864 [doi] LID - 1864. (2072-6694 (Print)).

425. Wang JA-O, Farkas CA-O, Benyoucef A, et al. Interplay between the EMT transcription factors ZEB1 and ZEB2 regulates hematopoietic stem and progenitor cell differentiation and hematopoietic lineage fidelity. (1545-7885 (Electronic)).

426. Bakir B, Chiarella AM, Pitarresi JR, Rustgi AK. EMT, MET, Plasticity, and Tumor Metastasis. Trends in Cell Biology. 2020;30(10):764-776.

427. Meng F, Wu G. The rejuvenated scenario of epithelial–mesenchymal transition (EMT) and cancer metastasis. Cancer and Metastasis Reviews. 2012;31(3):455-467.

428. Derynck RA-O, Budi EA-O. Specificity, versatility, and control of TGF-β family signaling. LID - 10.1126/scisignal.aav5183 [doi] LID - eaav5183. (1937-9145 (Electronic)).

429. Ramachandran AA-O, Vizán P, Das D, et al. TGF-β uses a novel mode of receptor activation to phosphorylate SMAD1/5 and induce epithelial-to-mesenchymal transition. LID - 10.7554/eLife.31756 [doi] LID - e31756. (2050-084X (Electronic)).

430. Prabhu SD, Frangogiannis NG. The Biological Basis for Cardiac Repair After Myocardial Infarction: From Inflammation to Fibrosis. Circ Res. 2016;119(1):91-112.

431. Ruiz-Villalba A, Simón AM, Pogontke C, et al. Interacting Resident Epicardium-Derived Fibroblasts and Recruited Bone Marrow Cells Form Myocardial Infarction Scar. Journal of the American College of Cardiology. 2015;65(19):2057-2066.

432. Benhaiem-Sigaux N, Mina E, Sigaux F, et al. Characterization of Human Pericardial Macrophages. Journal of leukocyte biology. 1985;38(6):709-721.

433. Fatehi Hassanabad A, Fedak Paul WM, Deniset Justin F. Acute Ischemia Alters Human Pericardial Fluid Immune Cell Composition. JACC: Basic to Translational Science. 2021;6(9-10):765-767.

434. Fatehi Hassanabad A, Schoettler FI, Kent WDT, et al. Comprehensive characterization of the postoperative pericardial inflammatory response: Potential implications for clinical outcomes. JTCVS Open. 2022;12:118-136.

Acknowledgements

Axel – It is an honor to grow as a scientist under your guidance and I am deeply grateful for the opportunity to be a part of your team. It has become clear to me how fortunate I was to walk through that door for the very first time. Thank you for your endless patience, your understanding, and for giving the push when it was necessary!

Prof. Dr. rer. nat. Judith (Jojo) Haendeler – Thank you very much for your support as my second supervisor and for reviewing the entire progress over the past years.

HKP Team – Thanks a lot for your constant support and patience! At any moment, your doors were open, and there was always someone to talk to, seek advice from, or get help with any question. You created a cheerful and friendly atmosphere, both in good and in difficult times.

Anne, Sophia & Kathi – The journey towards a PhD can be challenging, but it can also be filled with joy. As you know, when we share our struggle, it gets cut in a half, when we share the joy, it doubles. Thank you very much for being my labmates and for all the experiences we shared over the past years!

Grace – It is said, “Weather at home is the most important,” and work is a second home. Thank you very much for keeping the weather cozy, for the sincere chats, our scientific conversations, and those spontaneous experiments until late, “just out of curiosity.” It was fun, and, hopefully, it will continue!

IRTG1902 – It was a very intensive and colorful time! Thank you for all the activities and fun that nicely balanced our daily routine. We learned a lot, traveled to many places, and got to know plenty of people! Thank you very much for this valuable experience!

Mom, Dad, Vanya – You did everything to make it possible and I am grateful for every quiet sacrifice. Your unconditional love will always be the strongest motivation for my personal as well as professional achievements.

Marius – You played a significant role in this journey, always offering a steady shoulder to lean on and it will never be enough to say thank you for your love, acceptance and for being the calm in every storm!

Anya – Your words always found me when I needed them most. My soulmate, best friend, and sister, I am grateful that 912a brought us together! Thank you very much for your great support during this journey.